



HAL
open science

Numerical modeling and simulation of selective laser sintering in polymer powder bed

Xin Liu

► **To cite this version:**

Xin Liu. Numerical modeling and simulation of selective laser sintering in polymer powder bed. Thermics [physics.class-ph]. Université de Lyon, 2017. English. NNT : 2017LYSEI012 . tel-01920677

HAL Id: tel-01920677

<https://theses.hal.science/tel-01920677>

Submitted on 13 Nov 2018

HAL is a multi-disciplinary open access archive for the deposit and dissemination of scientific research documents, whether they are published or not. The documents may come from teaching and research institutions in France or abroad, or from public or private research centers.

L'archive ouverte pluridisciplinaire **HAL**, est destinée au dépôt et à la diffusion de documents scientifiques de niveau recherche, publiés ou non, émanant des établissements d'enseignement et de recherche français ou étrangers, des laboratoires publics ou privés.



N°d'ordre NNT : 2017LYSEI012

THESE de DOCTORAT DE L'UNIVERSITE DE LYON
opérée au sein de
(Institut National des Sciences Appliquées de Lyon)

Ecole Doctorale N° ED162
(MEGA de Lyon)

Spécialité/ discipline de doctorat :
Thermique et Energétique

Soutenue à huis clos le 28/02/2017, par :
Xin LIU

**Numerical Modeling and Simulation of
Selective Laser Sintering in Polymer
Powder bed**

Devant le jury composé de :

BARRES Claire	Maître de conférences HDR	INSA-Lyon	Examineur
BERGHEAU Jean-Michel	Professeur des Universités	ENISE-St.Etienn	Examineur
REGNIER Gilles	Professeur des Universités	ENSAM-Paris	Rapporteur
SCHMIDT Fabrice	Professeur des Universités	MINES-Albi	Rapporteur
BOUTAOUS M'hamed	Maître de conférences HDR	INSA-Lyon	Directeur de thèse
XIN Shihe	Professeur des Universités	INSA-Lyon	Co-directeur de thèse

Abstract

Many industrial and academic interests concerning the additive manufacturing processes are developed in the last decades. As one of the most promising technique of additive manufacturing, the Selective Laser Sintering (SLS) has been valued by both industry and academic. However, it remains that several phenomena are still not well understood in order to properly model the process and propose quality improvement of parts made.

The goal of this Ph.D. project is to develop a framework of numerical simulation in order to model the SLS process in polymer powder bed, meanwhile understanding multiple physical phenomena occurring during the process and studying the influence of process parameters on the quality of final product.

In contrast to traditional approach, based on the equivalent homogeneous material in numerical modeling of partial differential equations derived from conservation laws, we propose a global model to simulate powder-based additive manufacturing by using the Discrete Element method (DEM). It consists in a coupling between four different physical models: radiative heat transfer, discrete heat conduction, sintering and granular dynamics models.

Firstly, the submodel of radiative heat transfer concerns the interaction between the laser beam and powder bed. Several phenomena are considered, including the reflection, transmission, absorption and scattering. Besides, a modified Monte Carlo ray-tracing method is developed in order to study the influence of scattering on the distribution of the deposited laser energy inside the powder bed. Furthermore, the submodel of discrete heat conduction describes the inter-particles heat diffusion. Moreover, the sintering submodel concerns the phenomena of coalescence and air diffusion. It describes the melting kinetics of grains, driven by surface tension and the release of entrapped gases inside powder bed. Finally, the granular dynamics submodel concerns the motions and contacts between particles when depositing a new layer of powders.

The coupling between these submodels leads to propose a global numerical framework, validated by comparing the results to both simulated and experimental ones from literatures. A parametric study is then proposed for model validation and process analysis. The Influence of different material and process parameters on the evolution of temperature, relative density and materials structure and characteristics are investigated. The results exhibit accurate modeling of the complex phenomena occurring during the SLS process, and the work constitute a great potential in modeling and optimization of additive processes.

Keywords: additive manufacturing, selective laser sintering, polymer, multiphysics modeling, numerical simulation, Discrete Element method, modified Monte Carlo method.

Résumé

La fabrication additive est l'un des secteurs industriels les plus en développement ces dernières années. L'une de ces technologies de fabrication les plus prometteuses est la fusion laser sélective (SLS), et relève d'un intérêt croissant aussi bien industriel que académique. Néanmoins, beaucoup de phénomène mis en jeu par ce procédé demeure non encore bien compris, entravant ainsi son développement pour la production de pièces de bonne qualité pour des applications industrielles.

L'objectif de cette thèse est de développer un cadre de simulation numérique permettant la simulation du procédé SLS pour des poudres de polymère afin de comprendre les multiples et complexes phénomènes physiques qui se produisent lors du frittage laser et d'étudier l'influence des paramètres du procédé sur la qualité du produit final.

Contrairement aux approches classiques de modélisation numérique, basées sur la définition de matériaux homogène équivalents pour la résolution des équations de bilan, nous proposons une simulation globale du procédé du frittage laser de poudres, en utilisant la méthode des Eléments Discrets (DEM). Cela consiste en un couplage entre quatre sous-modèles : transferts radiatif dans le milieu granulaire semi-transparent, conduction thermique dans les milieux discrets, coalescence puis densification.

Le modèle de transferts par rayonnement concerne l'interaction du faisceau laser avec le lit de poudre. Plusieurs phénomènes sont ainsi pris en compte, notamment la réflexion, la transmission, l'absorption et la réfraction. De plus, une méthode de Monte-Carlo couplée à la méthode du Lancer de rayons est développée afin d'étudier l'influence de la réfraction sur la distribution de l'énergie du laser dans le lit de poudre.

Le modèle de conduction dans des milieux discrets décrit la diffusion thermique inter-particules. Finalement, le modèle de frittage décrit les cinétiques de coalescence et de diffusion de l'air dans le polymère et densification du milieu. Cela permet de décrire les cinétiques de fusion des grains, dont l'énergie de surface et la diffusion de l'air sont les deux moteurs principaux.

Le couplage entre les différents modèles nous a permis de proposer un modèle numérique global, validé grâce à des comparaisons à des résultats de simulations théoriques et expérimentales, trouvés dans la littérature.

Une analyse paramétrique est alors proposée pour la validation du modèle et l'étude du procédé. L'influence de différents paramètres aussi bien du procédé que du matériau sur le champ de température, la densité relative du matériau sa structure, etc , est ainsi investiguée.

Les résultats montrent une bonne précision dans la modélisation des différents phénomènes complexes inhérents à ce procédé, et ce travail constitue un potentiel réel pour la modélisation et l'optimisation des procédés de fabrication additive par matériaux granulaires.

Mots clés : fabrication additive, fusion laser sélective, polymères, modélisation multiphysique, simulation numériques, méthode des éléments discrets, méthode de Monte-Carlo Modifiée.

Acknowledgements

Firstly of all, I would like to gratefully thank to the China Scholarship Council, who provides the scholarship for me to achieve my doctoral degree in France.

Moreover, I would like to extend my sincerely gratitude to my supervisor, Prof. M'hamed BOUTAOUS, for his instructive advice and useful suggestions on my work. I am deeply grateful of him help in the completion of this thesis.

Furthermore, high tribute shall be paid to Prof. Shihe Xin and Dr. Zakariaa Refaa, who reviews my thesis and suggests lots of corrections.

Finally, I am indebted to my parents for their continuous supports and encouragements.

Table of Contents

Abstract.....	2
Résumé.....	3
Acknowledgements	4
Table of Contents.....	5
List of Figures	8
List of Tables	11
INTRODUCTION.....	12
Additive Manufacturing	12
Aim and Outline of Thesis	15
References.....	17
Chapter I: Generalities on Additive Manufacturing	18
1.Introduction of Additive Manufacturing (AM)	18
2. Advantages of AM technology	18
3. Technological limitations of AM in industry.....	19
4. Categories of AM technologies	20
5. Domains of AM application.....	22
Reference	24
Chapter II: Introduction of Selective Laser Sintering in Polymer Powder bed	25
1. Overview of SLS in polymer powder bed.....	26
1.1. Influence of properties on SLS	26
1.2. Conventional forming method compared with SLS.....	27
2. Introduction of SLS process	30
3. Influential parameters of SLS process.....	31
4. Experimental researches of SLS process	32
5. Analysis of SLS part qualities.....	36
6. Application of SLS polymer product.....	37
Reference	40
Chapter III: Multiphysical Phenomena and Models Involved in SLS.....	44
1. Multiphysical phenomena involved in SLS	45
2. Global model of SLS	46
3. Radiation heat transfer submodel	47

3.1. Generalities of radiation heat transfer	47
3.2. Thermal radiation in granular medium.....	47
3.3. Review of thermal radiation models in SLS process.....	49
3.4. Monte Carlo method for thermal radiation	50
3.5. Radiation Transfer in SLS process	53
4. Discrete heat conduction submodel	58
4.1. Introduction of granular material	58
4.2. Discrete methods.....	58
4.3. Review of heat conduction model in SLS process	63
4.4. Discrete heat conduction model in SLS process	64
4.5. Validation of discrete heat conduction model	65
4.6. Phase change and boundary conditions	67
5. Sintering submodel.....	68
5.1. Generalities of sintering	68
5.2. Basic of coalescence	70
5.3. Basic of densification.....	78
5.4. Review of numerical simulation of sintering.....	82
5.5. Synthetic of sintering submodel in SLS process.....	82
6. Contact dynamic submodel.....	86
6.1. Review of sphere packing method.....	86
6.2. Dynamic algorithm with elastic contacts.....	86
6.3. Generating new layers during SLS process	88
7. Methodology of synthetic model.....	90
7.1. Particle system definition.....	90
7.2. Boundary conditions.....	90
7.3. Energy deposition	91
7.4. Sintering and connected neck formation	93
7.5. Time step integration	93
7.6. Visualization and post-processing.....	94
7.7. Implementation	94
Reference	95
Chapter IV: Results and Discussions	100
1. Simulation of SLS process without successive layers of powders.....	101
1.1. Model implementation	101

1.2. Influences of scattering on distribution of laser energy	102
1.3. Effects of scattering on thermal diffusion	104
1.4. Validation of global model	109
1.5. Predication of relative density	112
2. Simulation of SLS process with successive layers of powders	115
2.1. Analysis of temperature evolution with successive layers	115
2.2. Prediction of relative density of sintered sheet	121
3. Influence of SLS process parameters	122
3.1. Influence of laser energy density	123
3.2. Effect of preheating temperature	123
3.3. Effect of grain size	124
3.4. Partial conclusion.....	129
4. Applications of global model.....	129
4.1. Simulation of balling phenomenon.....	129
4.2. Test simulation of SLS process	133
5. Conclusions	135
Reference	136

List of Figures

Fig.1. Process of additive manufacturing.....	13
Fig.2. Yearly sale of additive manufacturing units worldwide.....	13
Fig.3. Performance of additive manufacturing with respect to conventional manufacturing.....	14
Fig.4. Growth of directly producing as percentage of total revenues from AM.....	14
Fig.I-1. Examples of extremely complex parts fabricated by AM (Products of EOS Company).....	18
Fig.I-2. Example of topological optimization of a hinge fabricated by AM (Product of Multistation for Airbus Group Innovations).....	19
Fig.I-3. Repairation of a metal part (CLAD process of company BeAM).....	19
Fig.I-4. Schematic diagram of vat polymerization and its application.....	20
Fig.I-5. Schematic diagram of FDM and its application.....	21
Fig.I-6. Schematic SLS machine EOS P700.....	21
Fig.I-7. Schematic diagram of Sheet lamination and its application.....	22
Fig.I-8. Ring fabricated by Photopolymerisation.....	23
Fig.II-1. Balling effect of laser sintered tracks on steel substrate.....	26
Fig.II-2. Forming of line type thermoplastic polymers by a single screw extruder.....	28
Fig.II-3. Illustration of the forming process assisted by pre-stretching punch.....	28
Fig.II-4. Forming of thermoplastic polymer by an injection molding machine.....	29
Fig.II-5. Curves of constraint for PA12 (InnevPA, Exceltec) specimens transformed under different conditions.....	29
Fig.II-6. Crystal morphology of PA12 transformed by laser melting.....	30
Fig.II-7. SLS machine for fabricating thermoplastic.....	29
Fig.II-8. Schematic layout of EOS P700.....	30
Fig.II-9. Microstructure of powders PA6 (a,c,e) and PA12 (b,d,f).....	31
Fig.II-10. Evolution of total porosity with different energy densities E_p	35
Fig.II-11. Variation of flexural modulus with time.....	35
Fig.II-12. Directions of fabrication.....	36
Fig.II-13. Application examples of the selective laser sintering in the medical field.....	37
Fig.II-14. Application examples of the selective laser sintering in the Aeronautic and automotive field	37
Fig.II-15. Application examples of the selective laser sintering in the architecture field.....	37
Fig.II-16. Application examples of the selective laser sintering in the paleontology field.....	38
Fig.II-17. Application examples of the selective laser sintering in the robotic field.....	38
Fig.III-1.1. Synthetic of phenomena and models involved in SLS.....	44
Fig.III-2.1. Structure of global model of SLS process.....	45
Fig.III-3.1. Electromagnetic wave spectrum (for radiation traveling through vacuum).....	46
Fig.III-3.2. Interaction between photons and spherical particles.....	47
Fig.III-3.3. Phase function for (a) $g=0.06$, (b) $g=0.96$	48
Fig.III-3.4. Comparison of Monte Carlo and conventional solution techniques.....	49
Fig.III-3.5. Monte Carlo method applied to approximating the value of π	50
Fig.III-3.6. Flowchart of Monte Carlo ray tracing method.....	51
Fig.III-3.7. Illustration of the luminance within a powder bed.....	53
Fig.III-3.8. General flow chart of ray tracing process based on Monte Carlo method.....	54
Fig.III-3.9. Illustration of photon initialization and scattering direction.....	55
Fig.III-3.10. Comparison of radiative energy distribution in powder layer with given optical thicknesses.....	56
Fig.III-4.1. DEM simulation of the flow of spherical particles in the helical ribbon blender.....	57
Fig.III-4.2. Characteristic length scales and time scales for numerical methods.....	58
Fig.III-4.3. 2D contact particle model.....	59
Fig.III-4.4. Schematic of assumed temperature distribution between particles in contact.....	60
Fig.III-4.5. Temperature evolution of powder bed during selective laser melting process.....	60
Fig.III-4.6. Crack propagation during sintering under residual thermal stresses with a pre-set crack	

notch.....	61
Fig.III-4.7. Evolution of liquid drops on a flat surface at different times.....	62
Fig.III-4.8. Heat conduction between two contacted elastic spheres.....	63
Fig.III-4.9. Temperature distribution in powder bed for increasing scan speed at $P = 50 \text{ W}$	65
Fig.III-4.10. Temperature history of a particle in the laser scan path.....	66
Fig.III-5.1. Schematic evolution of two spheres sintering.....	67
Fig.III-5.2. Equilibrium contact angle in three phases.....	68
Fig.III-5.3. Equilibrium of sintering in solid phase.....	68
Fig.III-5.4. Three evolution stages of sintering.....	68
Fig.III-5.5. The unit cell and the densification process of a cubic pack structure.....	70
Fig.III-5.6. Schematic of two particles contact.....	74
Fig.III-5.7. Different steps of coalescence of two PVDF grains.....	76
Fig.III-5.7. Temperature as a function of time predicted by laser heat source and two relevant transition temperature.....	76
Fig.III-5.9. Illustration of four stages of non-isothermal coalescence.....	77
Fig.III-5.10. Illustration of liquid menisci at the specimen surface and around a pore containing an inter gas of pressure ΔP_p during liquid phase sintering.....	78
Fig.III-5.11. Three distinct regions in powder bed during SLS process.....	80
Fig.III-5.12. Illustration of different sintering stages in the DSC profile of PA12.....	82
Fig.III-5.13. Equivalent air bubble in powder bed.....	83
Fig.III-5.14. Variation of contact region in sintering process.....	83
Fig.III-6.1. Contact between elastic grains simplified as the damping vibration of spring oscillator.....	86
Fig.III-6.2. Flowchart of contact dynamics.....	87
Fig.III-6.3. Schematic of insertion volume.....	87
Fig.III-6.4. Distribution of powder bed in a box.....	88
Fig.III-7.1. Demonstration of the energy deposition methodology in SLS process.....	90
Fig.III-7.2. Distribution of scattered photons inside powder bed.....	91
Fig.III-7.3. Attenuation path of photon k inside powder bed.....	92
Fig.III-7.4. Illustration of the flow of execution in the Fortran90 implementation of DEM framework.....	93
Fig.IV-1.1. Distribution of photon scattering positions.....	101
Fig.IV-1.2. 2D distribution of the normalized laser intensity in powder bed with various optical depths $Z_{op} = \alpha z$ in condition of different laser models.....	102
Fig.IV-1.3. Time-temperature profile at four different points with FEM and DEM heated by single laser scanning.....	104
Fig.IV-1.4. Temperature field in powder bed.....	105
Fig.IV-1.5. Illustration of the position of three points.....	106
Fig.IV-1.6. Time-temperature profile of three different points in FEM and DEM.....	107
Fig.IV-1.7. Draft of the extraction procedure of the sintered lines.....	108
Fig.IV-1.8. Initial powder bed before laser treatment.....	109
Fig.IV-1.9. Top view of a sintered line and measure of the averaged width.....	109
Fig.IV-1.10. Main dimensions of the profile of sintered lines as a function of energy density adopted.....	110
Fig.IV-1.11. Comparisons of main dimensions of sintered lines with and without scattering.....	110
Fig.IV-1.12. Temperature field of regions heated by laser inside powder bed based on different models.....	111
Fig.IV-1.13. Illustration of surface decreasing of powder bed after laser treatment.....	112
Fig.IV-1.14. Illustration of discretisation of sintered region.....	113
Fig.IV-1.15. Illustration of sintered line in powder bed.....	113
Fig.IV-2.1. Illustration of SLS process in powder bed with successive layers.....	114
Fig.IV-2.2. Five points in the diagonal line of powder bed.....	115
Fig.IV-2.3. Temperature evolutions of five positions in diagonal line.....	115
Fig.IV-2.4. Five points in the middle line of powder bed.....	116
Fig.IV-2.5. Temperature evolutions of five positions in middle line.....	116

Fig.IV-2.6. Temperature evolution in different layers at position of point 2.....	117
Fig.IV-2.7. Temperature evolution in different layers at position of point 3.....	119
Fig.IV-2.8. Illustration of PA12 powder bed.....	121
Fig.IV-2.9 Evolution of porosity with different energy densities E_p	121
Fig.IV-3.1. Effects of energy density on peak temperature and relative density.....	122
Fig.IV-3.2. Evolution of relative density with different preheating temperatures.....	123
Fig.IV-3.3. Temperature evolutions of powder bed with different grain sizes.....	124
Fig.IV-3.4. Temperature evolutions of five positions with different grain sizes.....	125
Fig.IV-3.5. Temperature evolution in different layers at position of point 2 with different grain sizes...	126
Fig.IV-3.6. Temperature evolution in different layers at position of point 3 with different grain sizes.....	127
Fig.IV-4.1. Heat diffusion and sintering process in powder bed with the power of 50W and scanning speed of 0.25 m/s.....	129
Fig.IV-4.2. The effect of scanning speed on the balling phenomenon.....	129
Fig.IV-4.3. Effect of scanning speed on width of molten track.....	130
Fig.IV-4.4. Effect of laser power on width of molten track.....	131
Fig.IV-4.5. Effect of surface tension on width of molten track.....	131
Fig.IV-4.6. Effect of viscosity on width of molten track.....	132
Fig.IV-4.7. Illustration of letter "D".....	132
Fig.IV-4.8. Temperature fields of powder bed in different layers for manufacturing process of letter "D".....	133

List of Tables

Table.I-1. List of main materials used in AM.....18
Table.II-1. Influential material properties and process parameters of SLS process.....30
Table.II-2. Influence of parameters on the density of final parts.....31
Table.III-1. Parameters and properties used in modified Monte Carlo method.....55
Table.III-2. Thermo-physical properties and other parameters used in simulation.....65
Table.III-3. Input parameters of grains.....88
Table.IV-1. Initial conditions.....101
Table.IV-2. Initial conditions and material properties.....105
Table.IV-3. Summary of energy densities used in the manufacturing of different series samples.....120

INTRODUCTION

Before detailing the objectives of this thesis, it seems to be interesting to place it in a more general context to appreciate its contributions. Nowadays, a company has to meet a world who is constantly evolving. In other words, it needs to face challenges from the development of market globalization, the acuity of worldwide competition and inventions of new technologies, but also the different demands of customers. Thus, in order to be capable of maintaining and conquering new markets, the company must adapt to market changes. However, in general, the conventional method for the development of products is expensive and long period. Therefore, it is necessary for the company to control the cost, to improve the quality of products and reduce the cycle of product development. The additive manufacturing was born in this background.

Additive Manufacturing

The additive manufacturing (AM) is a special technique of fabrication which is a part of mechanical engineering. Since decades, a variety of rapid prototyping techniques have been developed. such as the selective laser sintering (SLS) [1], the stereo lithography (SLA) [2], the fused deposition modeling (FDM) [3] and the laminated object manufacturing (LOM) [4]. The process of additive manufacturing consists of five steps [5,6]. The Fig.1 illustrates the chain of additive manufacturing.

Creation of CAD part model

The quality of CAD model will strongly impact the product of additive manufacturing. These CAD models are built from the specific software, like CATIA or Pro/Engineer, which are dedicated software for processing technical draws or real objects into 3D digital models.

Tessellation of CAD model

Due to irregular curved surfaces, the approximate description of these surfaces must be effected before the fabrication. In tessellation, the digital data of AM is usually built as STL file. The STL file contains the information of a series of triangles with co-ordinate of vertices, by which various surfaces of a CAD model are piecewise approximated. The mesh is generally governed by the maximum length of triangle's sides. Sometimes, a local correction is necessary for reducing errors of STL file.

Cutting CAD model into layers

Cutting 3D model into 2D layers is the fundamental principle of additive manufacturing. The direction and thickness of cutting layers are two important parameters that influences the quality and cost of AM products. The thickness of layer depends on the required precision and productivity. The layer thickness are usually in the range of 0.05mm to 0.5mm. It is generally chosen a thickness of 0.1mm to obtain a relative smooth surface.

Fabrication and superposition of layers

According to their contours, the fabrication of layers is achieved either by agglomeration of powder material or by cutting sheet material. After formation of a layer, a new layer is spread over it, and then the new layer is processed and attached to the old layer. This process continues until the product is completed.

The post-processing

The additive manufacturing must undergo several manual post-processing operations, such as

sanding, removal of supports, varnishing and even recovery operations to obtain the required precision. Currently, this post-processing is a necessary step for the process of additive manufacturing.

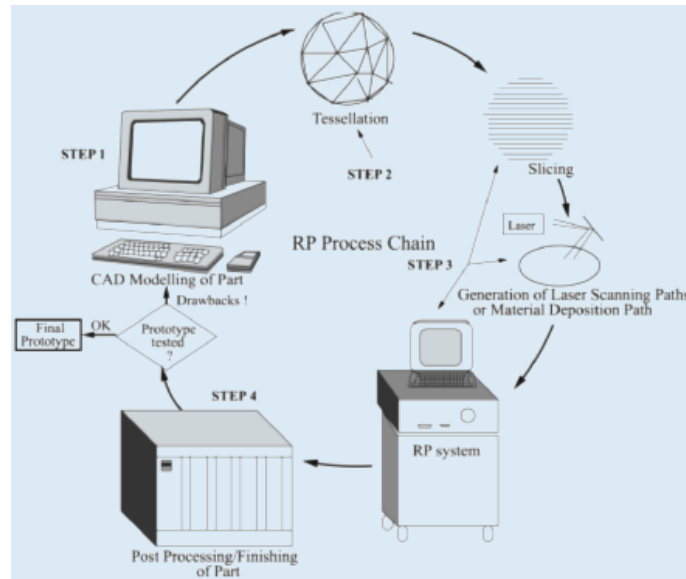


Fig.1. Process of additive manufacturing [6]

The invention of additive manufacturing brings a breakthrough of manufacturing technology and provides huge benefits associated with it. Nevertheless, the additive manufacturing is composite and closely related to other technologies, including computer-aided design, 3D imaging, laser technology and material. Since 1990s, more than 20 different technologies of additive manufacturing have been invented and still expending. The research and development of this technology still remain a very hot state.

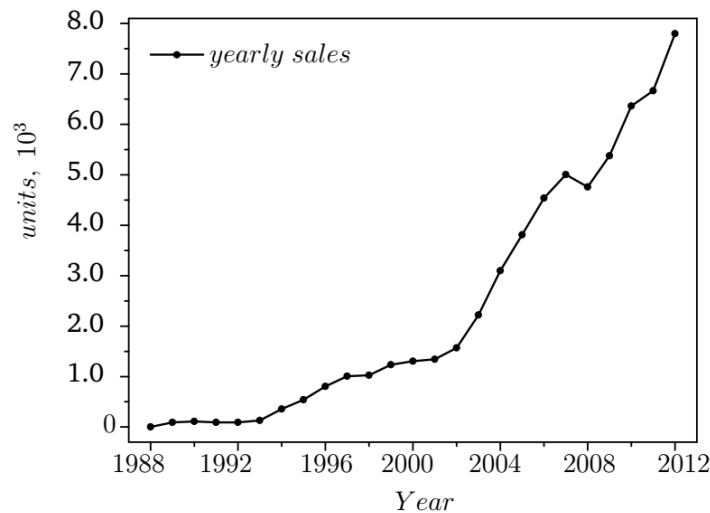


Fig.2. Yearly sale of additive manufacturing units worldwide [7]

Fig.2 shows the exponential growth of sales form additive manufacturing machines around the world, which confirms the growing acceptance of this technology as the new start in industry. Besides the promising future and potential advantages, the additive manufacturing also has some disadvantages. Even though the additive manufacturing has achieved significant improvement in speed, accuracy as well as its ability of processing larger range of materials, it still lags behind in aspects of reproducibility, part volume and production scale [8,9,10]. In the face of conventional manufacturing, the current limitations of additive manufacturing are illustrated in Fig.3, which should be focused to overcome in future.

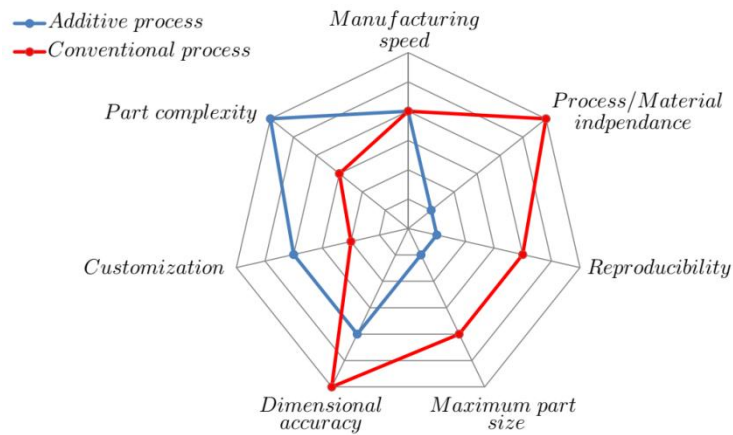


Fig.3. Performance of additive manufacturing with respect to conventional manufacturing [11]

In recent years, the application of AM technologies for directly producing is continuously increased, as shown in Fig.4. However, most of existing AM technologies are currently limited to fabricating prototypes and models. The AM technologies still lack of general application, since it is not capable of processing common engineering materials to meet the functional requirements (such as mechanic properties) [12]. The fusion technologies based on powder bed are most adaptable with not only different types of materials but also applications ranging from aerospace, automotive and medical. The selective laser sintering (SLS) and its variants (selective laser melting (SLM), electron beam melting (EBM)) are such technologies that hold potential as emerging disruptive technology in industry.

The SLS is one of the most modern and innovative AM technologies with general advantages and wide applications, as a non-contact process, which is flexible, automate and easily controlled. This technology of fabrication has been developed by Dr. Carl Deckard in the university of Texas at the end of 1980s. This technique differs from classical manufacturing processes by machines. In effect, successive layers of material are formed by laser sintering, under computer control to create an object. These objects can be of almost any shape or geometry, and the range of available materials expands to metal, ceramic and polymer.

Until now, the SLS technology is still developing and further research is needed in order to improve our understanding of processes [13]. In fact, this technology heavily relies on empirical data obtained from experiments for now. The help from numerical simulation is restricted due to the complexity of physical phenomena involved (such as absorption of laser radiation, heat transfer inside powder, melting, coalescence and consolidation). Therefore, a numerical model, coupling multiple physical phenomena in SLS process, is highly required by both industry and academic.

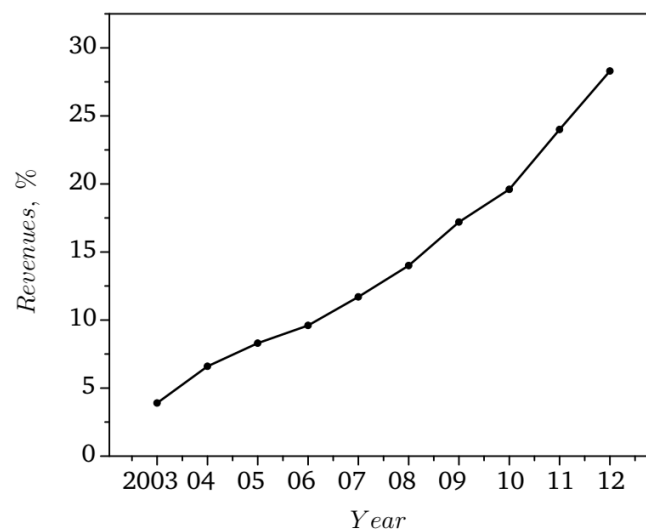


Fig.4. Growth of directly producing as percentage of total revenues from AM [7]

Aim and Outline of Thesis

In this thesis, we focus on developing a numerical model for simulating the SLS process. This numerical model is confirmed by comparing numerical results with experimental data from references. This model will allow the user of SLS machine to predict the influence of parameters on the final work piece, in order to optimize the quality of product, reduce the cost of manufacturing and increase the efficiency of process.

The numerical simulation of this process is developed based on the Discrete Elements Method (DEM) and calculated by Fortran90. Our results are compared with those from the commercial software COMSOL based on the Finite Elements Method (FEM), in order to highlight the difference between granular and homogenous media.

We work on the numerical simulation for polymers and metals. A 3D numerical model based on Discrete Elements method (DEM) was developed. To our knowledge, for the first time, a complicated numerical model is proposed which couples multiple phenomena of the radiation transfer, heat conduction, phase change, coalescence and densification. A discrete heat conduction submodel is established based on Fourier equation, which is able to describe the thermal diffusion in granular medium and makes it possible to estimate the effect of entrapped air inside powder bed. The submodel is confirmed by comparing with the data from published literature. Furthermore, the viscoelastic coalescence theory and air dissolution model are introduced, in order to simulate the phenomena of coalescence and densification, respectively. For highlighting the validation of our work, the numerical result is compared with experimental data from literature. Finally, effects of parameters on the work piece quality are studied.

The comparison between the numerical and experimental results shows that our model has a great potential in modeling the physical phenomena of grains inside powder bed and optimizing parameters of SLS process.

This thesis is divided into four chapters.

Chapter I: Generalities on Additive Manufacturing

This chapter reviews the knowledge of the additive manufacturing (AM) technologies. It proposes a detailed introduction of the background and principles of additive manufacturing, including its advantages, technical limitations, categories and applications.

Chapter II: Introduction of Selective Laser Sintering in Polymers

In the second chapter, we firstly present some properties of polymers related to SLS, and then introduce the advantages of SLS compared to other AM technologies. After a detailed description of SLS process, we review previous researches of SLS process in detail. Based on the comprehensive summarization, we propose a numerical model that is able to simulate the SLS process more practically and accurately.

Chapter III:

In this chapter, firstly, a radiative heat transfer submodel is established by modified Monte Carlo Ray Tracing method, which is able to describe the phenomenon of scattering and makes it possible to estimate the distribution of radiative energy inside the powder bed. Furthermore, a discrete heat conduction submodel is established based on Fourier equation, which is able to describe the thermal diffusion in granular medium and makes it possible to estimate the effect of entrapped air inside powder bed. Moreover, the viscoelastic coalescence theory and air dissolution model are introduced, in order to simulate the phenomena of coalescence and densification, respectively. Finally, the particle dynamics is simulated based on the contact dynamics theory so as to model the SLS process with multiple layers of powders.

Chapter IV:

In the last chapter, the model developed in the previous chapters, which includes four submodels (the radiation heat transfer, discrete heat conduction, sintering and contact dynamics submodels), is applied to simulate the physical phenomena during SLS process. The whole chapter is structured into four main parts. The first part includes the investigation of energy absorption and heat transfer in the powder bed subjected to moving laser source. Two numerical comparisons are proposed, in order to highlight the effect of scattering. Furthermore, the simulated results are compared with experimental data from the literature, so as to validate our model. In second part, the SLS process with successive layers of powders is simulated. The thermal behavior of grains at different positions are investigated in order to observe the variation of temperature within the powder bed during the industrial manufacturing process. Moreover, the relative density of sintered part is predicted and compared with experimental results from the literature. In third part, the influences of parameters on SLS process are deeply analyzed. Finally, in the last part, the model is applied to simulate the balling phenomenon and implement a test simulation so as to present its capability of capturing the spatially and temporally varying distribution of heat and displacement within the additively manufacturingd object, simultaneously, predicting geometric features.

References

- [1] D. Bunnell, D. Bourell, and H. Marcus. Fundamentals of liquid phase sintering related to selective laser sintering. In *Proceeding of the Solid Freeform Fabrication Symposium*, pages 379–385, 1994.
- [2] Gibson, Ian, and Jorge Bártolo, Paulo. "History of Stereolithography." *Stereolithography: Materials, Processes, and Applications*. (2011): 41-43. Web. 7 October 2015.
- [3] Pearce, Joshua M.; et al. "3-D Printing of Open Source Appropriate Technologies for Self-Directed Sustainable Development (*Journal of Sustainable Development*, Vol.3, No. 4, 2010, pp. 17–29
- [4] B Mueller, D Kochan, 1999, Laminated object manufacturing for rapid tooling and patternmaking in foundry industry, *Computers in Industry*, 39: 47–53.
- [5] Greco A. and Maffezzoli A., 2003, Polymer melting and polymer powder sintering by thermal analysis. *Journal of Thermal Analysis and Calorimetry*, 72:1167-1174.
- [6] Pandey P.M, 2010, Rapid prototyping technologies, applications and part deposition planning. IIT Delhi.
- [7] T. Wohlers. Additive manufacturing state of the industry. *Wohlers Report*, 2013.
- [8] J. Kruth, M. Leu, and T. Nakagawa. Progress in additive manufacturing and rapid prototyping. *CIRP Annals-Manufacturing Technology*, 47(1):525–540, 1998.
- [9] G. N. Levy, R. Schindel, and J.-P. Kruth. Rapid manufacturing and rapid tooling with layer manufacturing technologies, state of the art and future perspectives. *CIRP Annals-Manufacturing Technology*, 52(2):589–609, 2003.
- [10] H. Brooks and D. Aitchison. A review of state-of-the-art large-sized foam cutting rapid prototyping and manufacturing technologies. *Rapid Prototyping Journal*, 16(5):318–327, 2010.
- [11] Disruptive technology search for space applications. *Deutsches Zentrum fur Luft-und Raumfahrt (DLR), DST-TN-05(2)*, 2012.
- [12] J. Kruth, G. Levy, F. Klocke, and T. Childs. Consolidation phenomena in laser and powder bed based layered manufacturing. *CIRP Annals - Manufacturing Technology*, 56(2):730–759, Jan. 2007.
- [13] D. L. Bourell, M. C. Leu, and D. W. Rosen. Roadmap for additive manufacturing - identifying the future of freeform processing, 2009.

Chapter I: Generalities of Additive Manufacturing

Additive manufacturing (AM), also known as 3D printing, refers to various processes used to synthesize a three-dimensional object. In AM, successive layers of material are formed under computer control to create an object. These objects can be of almost any shape or geometry and are produced from a 3D model or other electronic data source.

1. Introduction of Additive Manufacturing (AM)

The first AM technique is the stereo-lithography, which was invented in 1984 by Jean Claude André. In effect, the AM is not a new technique, which has been used by industries for more than 20 years, especially for the prototyping [1,2]. In contrast to conventional manufacturing process (involving material removal to achieve final shape), the AM is an additive process wherein the part is built by sequentially fusing thin layers of material one over another.

Depending on the technique of AM, the materials used are mainly in the type of metals, polymers, ceramics and biomaterials. A range of materials used in AM is listed in Table.I-1.

Table.I-1. List of main materials used in AM [3]

Metal	Polymer	Ceramic	Biomaterial
Aluminum	ABS	Alumina	Tissue / Cells
Steel	PLA	Mullite	
Titanium	Nylon	Zirconia	
Inconel	PEEK	Carbide Silicon	
Cobaltchrome	PMMA	Silica	
Copper	PC	Graphite	
	PPSU		

2. Advantages of AM technology

Due to additive build-up principle, AM has an inherent advantage of producing parts of unlimited geometrical complexity offering possibilities for optimization even by geometrical means. The process makes use of sliced CAD data to generate successive layers from bottom to top resulting in the final product. The advantage of AM technology is manifold and listed as below [4-10]:

- Unlimited geometry: the technology allows extremely complex shapes (Fig.I-1), unachievable by traditional techniques;

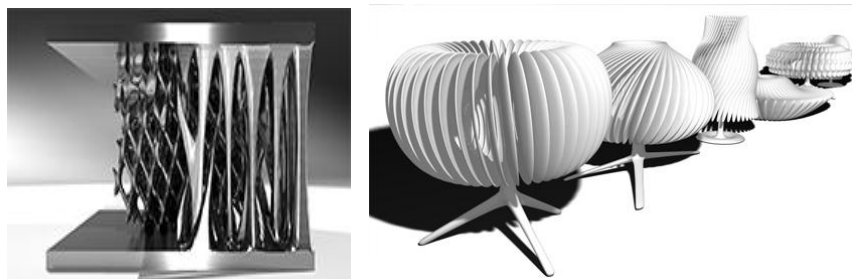


Fig.I-1. Examples of extremely complex parts fabricated by AM (Products of EOS Company)

- Lightening parts: the complexity of the shapes can be used to alleviate already existing parts by topology optimization (Fig.I-2);



Fig.I-2. Example of topological optimization of a hinge fabricated by AM (Product of Multistation for Airbus Group Innovations)

- Repairing parts (Fig.I-3);
- Customization: the technique allows meet the customized requests (custom prostheses in the medical or dental sector, production tooling like molds) [11];

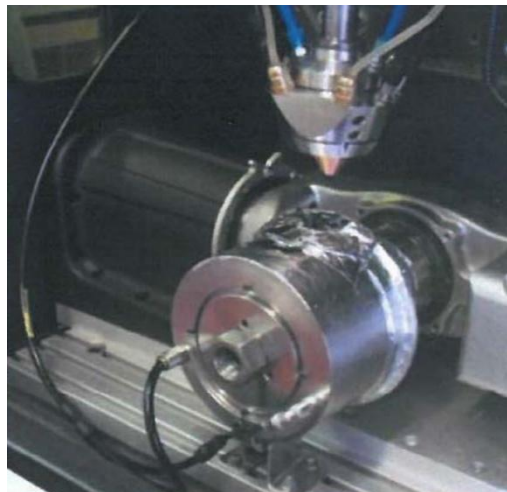


Fig.I-3. Reparation of a metal part (CLAD process of company BeAM)

- Material saving: at the end of the manufacturing process, the unused material is recycled for later use;
- Do not need tools: AM does not require the use of specific tools, such as moulds;
- Ecological and economical: parts can be printed locally by sending the digital model (no transportation, saving space and minimizing losses).

3. Technological limitations of AM in industry

Peoples working in the domain of AM agree that the market in this area is growing very rapidly but not yet mature [12]. The main limitation to the development of this technology comes from the raw material. Industrialists complain about not having enough materials to meet demand and accuse the machine manufacturingrs force the user to use only the materials they sell [12].

Other major limitations of AM are listed as following:

- Uncertain porosity: the porosity of AM product is one of the most important properties, since it is directly related to product quality and mechanical performance. However, until now, the porosity of final product is still hard to measure even not under control [13].

- Requirement of multiple skills: this technology requires multiple skills, hence, it will slow the industry to integrate it into their manufacturing processes;
- Bad surface of final object: the surface condition of final parts is very bad (rough stairs effect) and post-processing requires much more time;
- Lack of reliability: the process is still not fully understood and depends on empirical parameters;
- Small parts only: until now, AM is not capable of fabricating products with large volume.

4. Categories of AM technologies

Although media likes to use the term “3D Printing” as a synonym for all Additive Manufacturing processes, there are actually lots of individual processes which vary in their method of layer manufacturing. Individual processes will differ depending on the material and machine technology used [14].

● VAT Photopolymerisation

Vat polymerization uses a vat of liquid photopolymer resin, out of which the model is constructed layer by layer. An ultraviolet (UV) light is used to cure or harden the resin where required, whilst a platform moves the object being made downwards after each new layer is cured. In this case, support structures will often need to be added. Resins are cured using a process of photo polymerization or UV light, where the light is directed across the surface of the resin with the use of motor controlled mirrors. Where the resin comes in contact with the light, it cures or hardens.

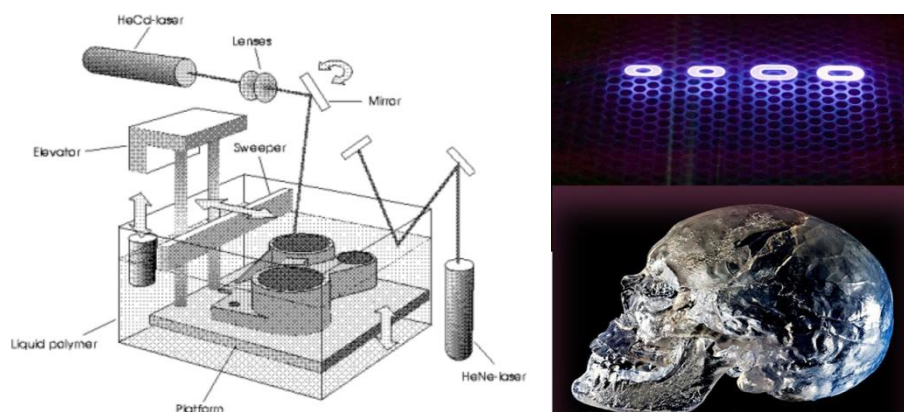


Fig.I-4. Schematic diagram of vat polymerization and its application[14]

● Material Jetting

Material jetting creates objects in a similar method to a two dimensional ink jet printer. Material is jetted onto a build platform using either a continuous or Drop on Demand (DOD) approach. Material is jetted onto the build surface or platform, where it solidifies and the model is built layer by layer. Material is deposited from a nozzle which moves horizontally across the build platform. Machines vary in complexity and in their methods of controlling the deposition of material. The material layers are then cured or hardened using ultraviolet (UV) light. As material must be deposited in drops, the number of materials available to use is limited. Polymers and waxes are suitable and commonly used materials, due to their viscous nature and ability to form drops.

● Binder Jetting

The binder jetting process uses two materials; a powder based material and a binder. The binder acts as an adhesive between powder layers. The binder is usually in liquid form and the build material in powder form. A print head moves horizontally along the x and y axes of the machine and deposits alternating layers of the build material and the binding material. After each layer, the object being printed

is lowered on its build platform. Due to the method of binding, the material characteristics are not always suitable for structural parts and despite the relative speed of printing, additional post processing (see below) can add significant time to the overall process.

- **Material Extrusion**

Fuse deposition modeling (FDM) is a common material extrusion process and is trademarked by the company Stratasys. Material is drawn through a nozzle, where it is heated and is then deposited layer by layer. The nozzle can move horizontally and a platform moves up and down vertically after each new layer is deposited. It is a commonly used technique used on many inexpensive, domestic and hobby 3D printers.

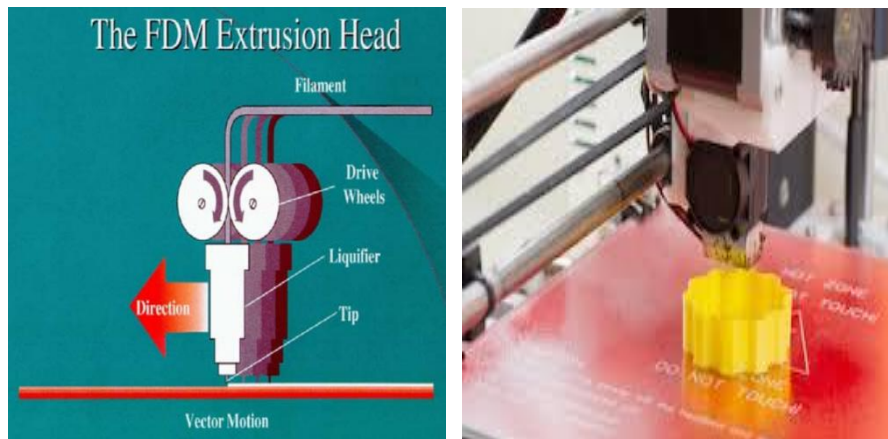


Fig.I-5. Schematic diagram of FDM and its application [14]

- **Powder Bed Fusion**

The Powder Bed Fusion process includes the following commonly used printing techniques: Direct metal laser sintering (DMLS), Electron beam melting (EBM), Selective heat sintering (SHS), Selective laser melting (SLM) and Selective laser sintering (SLS). Powder bed fusion (PBF) methods use either a laser or electron beam to melt and fuse material powder together. Electron beam melting (EBM), methods require a vacuum but can be used with metals and alloys in the creation of functional parts. All PBF processes involve the spreading of the powder material over previous layers. There are different mechanisms to enable this, including a roller or a blade. A hopper or a reservoir below of aside the bed provides fresh material supply. The process sinters the powder, layer by layer. Selective Heat Sintering differs from other processes by way of using a heated thermal print head to fuse powder material together. As before, layers are added with a roller in between fusion of layers. A platform lowers the model accordingly.

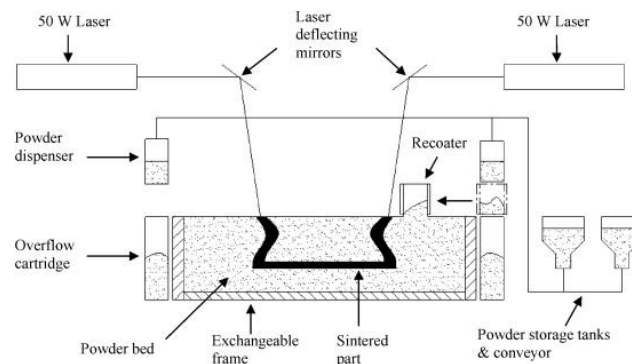


Fig.I-6. Schematic SLS machine EOS P700 [15]

- **Sheet Lamination**

Sheet lamination processes include ultrasonic additive manufacturing (UAM) and laminated object

manufacturing (LOM). The Ultrasonic Additive Manufacturing process uses sheets or ribbons of metal, which are bound together using ultrasonic welding. The process does require additional machining and removal of the unbound metal, often during the welding process. Laminated object manufacturing (LOM) uses a similar layer by layer approach but uses paper as material and adhesive instead of welding. The LOM process uses a cross hatching method during the printing process to allow for easy removal post build. Laminated objects are often used for aesthetic and visual models and are not suitable for structural use. UAM uses metals and includes aluminum, copper, stainless steel and titanium. The process is low temperature and allows for internal geometries to be created. The process can bond different materials and requires relatively little energy, as the metal is not melted.

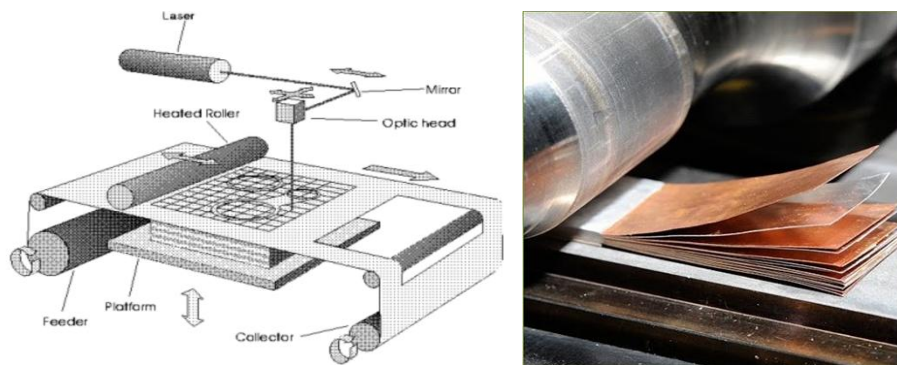


Fig.I-7. Schematic diagram of Sheet lamination and its application [14]

- **Directed Energy Deposition**

Directed Energy Deposition (DED) covers a range of terminology: ‘Laser engineered net shaping, directed light fabrication, direct metal deposition, 3D laser cladding’. It is a more complex printing process commonly used to repair or add additional material to existing components. A typical DED machine consists of a nozzle mounted on a multi axis arm, which deposits melted material onto the specified surface, where it solidifies. The process is similar in principle to material extrusion, but the nozzle can move in multiple directions and is not fixed to a specific axis. The material, which can be deposited from any angle due to 4 and 5 axis machines, is melted upon deposition with a laser or electron beam. The process can be used with polymers, ceramics but is typically used with metals, in the form of either powder or wire. Typical applications include repairing and maintaining structural parts.

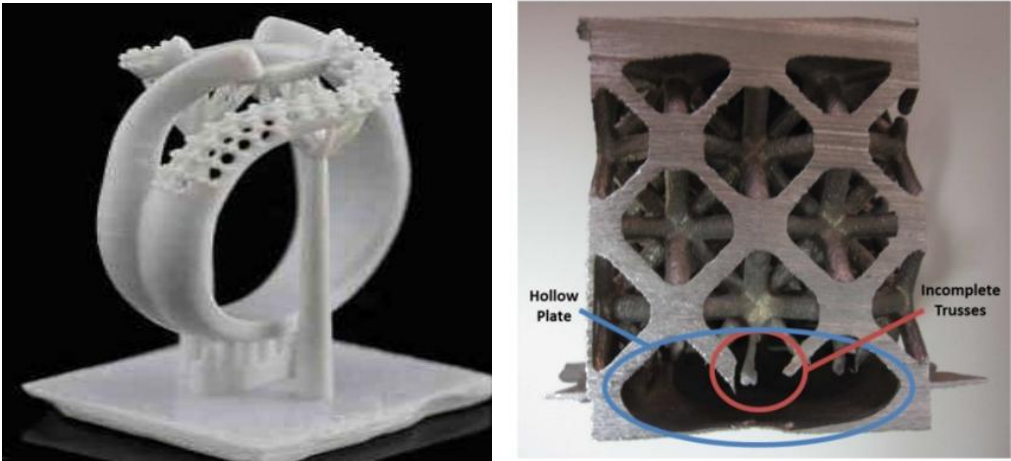
5. Domains of AM application

AM brings a revolution in many domains: aeronautics, aerospace, automotive, dental and medical but also jewelry (Fig.I-8a), sport [16], design and fashion. In the industrial world, the AM was used for prototyping. But now, industry begins to use it to make functional parts. In particular, the AM is used to make cellular structures (Fig.I-8b), also well known as "lattices" structures, in order to lighten parts but also to dissipate heat. For the entire lifecycle of product, the AM is able to help the industry to control the cost, improve the quality of products and reduce the cycle of new product development (from design to final product) [17].

Actually, the AM has been highly developed and widely applied in the medical and dental fields. In the medical field, the AM allows to realize new orthopedic implants (hip prosthesis [18]) and improve the ergonomics of prostheses (hearing aids [19]). In the dental field, it realizes the large-scale production of customized prostheses.

Here, we enumerate a few examples of AM application in the industry: Cirtes company manufacturing aircraft facilities by laminating layers for Airbus [20]. Poly-shape company has many AM machines to work on aerospace projects, particularly, fabricating lightweight solar panels located on satellites [21]. Large industrial companies, such as PSA, use the AM to develop prototypes. The technology allows them to make models on a small-scale production on the purpose of illustrating an innovative design [21]. Safran company uses AM to make functional parts of aircraft engine and rocket. The

technology allows them to lighten aircraft by optimizing the topology of manufacturing parts.



(a)
Fig.I-8. (a) Ring fabricated by Photopolymerisation [12];
(b) Cellular structure fabricated by SLM [22].

Reference

- [1] Dubois P., Aoussat A. et Duchamp R., « Prototypage rapide – Généralités », Dossier Techniques de l'Ingénieur, l'expertise technique et scientifique de référence, BM7017, 10/04/2000.
- [2] Bernard A. et Taillandier G., « Le prototypage rapide », Ed. Hermès, 1998.
- [3] Berchon M. et Bertier L., « L'impression 3D », Serial makers, Eyrolles, 2013, EAN13 : 782212135220.
- [4] Wohlers report: Additive manufacturing and 3D printing state of the industry ; annual worldwide progress report / Tbv1Wohlers Associates ; ID: gnd/6014226-1. Fort Collins, Colorado: Wohlers Associates, 2012, ISBN: 0975442988.
- [5] Lin S.L., Lin C.C., Lin D.Y. et Chuang C.S., "Laser additive manufacturing technology in titanium 64 implant of microstructure fabrication and analysis", 8th Annual IEEE International Conference on Nano/Micro Engineered and Molecular Systems, IEEE NEMS 2013, 2013, 594-597.
- [6] Islam M.N., Boswell B., et Pramanik A., "An investigation of dimensional accuracy of parts produced by three-dimensional printing", Lect. Notes Eng. Comput. Sci., 1 LNECS, 2013, 522-525.
- [7] Meredith B., Morham B. et Gonzalez P., "Application of 3D printing for small UAVs", Int. SAMPE Technical Conference, 2013, 16-33.
- [8] Deckers J., Kruth J.-P., Cardon L., Shahzad K. et Vleugels J., "Densification and geometrical assessments of alumina parts produced through indirect selective laser sintering of alumina-polystyrene composite powder", J. Mech. Eng., 59, 11, 2013, 646-661.
- [9] Rasmussen R., "3D printed electronics: The future is now", SMT Surface Mount Technology Magazine, 28, 62013, 8-11.
- [10] Montfort-Windels F., rapport du Sirris, « Additive manufacturing nouveauté 2012-2013 », juillet 2013.
- [11] Banks J., "Adding value in additive manufacturing: Researchers in the United Kingdom and Europe look to 3D printing for customization", IEEE Pulse, 4, 6, 2013, 22-26.
- [12] Anne-Françoise OBATON, Alain BERNARD, Georges TAILLANDIER et Jean-Marc MOSCHETTA, 2015, Fabrication additive : état de l'art et besoins métrologiques engendrés, DOI: 10.1051/rfm/2015003.
- [13] W. King, A. T. Anderson, R. M. Ferencz, N. E. Hodge, C. Kamath & S. A. Khairallah, 2015, Overview of modelling and simulation of metal powder bed fusion process at Lawrence Livermore National Laboratory, Materials Science and Technology, 31:957-968.
- [14] D.V. Mahindru and Priyanka Mahendru, 2013, Review of Rapid Prototyping-Technology for the Future, Global Journal of Computer Science and Technology, 13:28-33.
- [15] Pham, D., Dotchev, K., Yusoff, W. (2008, November). Deterioration of polyamide powder properties in the laser sintering process. Part C: Journal of Mechanical Engineering Science, 222, 2163-2176.
- [16] Manoharan V., Chou S.M., Forrester S., Chai et G.B.b, Kong P.W., "Application of additive manufacturing techniques in sports footwear", Virtual and Physical Prototyping, 8, 4, 2013, 249-252.
- [17] Meredith B., Morham B. et Gonzalez P., "Application of 3D printing for small UAVs", Int. SAMPE Technical Conference, 2013, 16-33.
- [18] Cronskar M., Backstrom M. et Rannar L.E., "Production of customized hip stem prostheses – A comparison between conventional machining and electron beam melting (EBM)", Rapid Prototyping J., 19, 5, 2013, 365-372.
- [19] Mannoor M.S., Jiang Z., James T., Kong Y.L., Malatesta K.A., Soboyejo W.O., Verma N., Gracias D.H. et McAlpine M.C.a, "3D printed bionic ears", Nano Lett., 13, 6, 2013, 2634-2639.
- [20] 19es Assises européennes de prototypage rapide, Association Française de Prototypage Rapide (AFPR), Châtenay-Malabry, France, 24–26 juin 2014.
- [21] Salon 3D Print « Les rencontres de la fabrication additive », Lyon, France, 17–20 juin 2014.
- [22] N. A. Meisel, C. B. Williams, and A. Druschitz, "Lightweight Metal Cellular Structures via Indirect 3D Printing and Casting," in SFF Symposium, 2012.

Chapter II: Introduction of Selective Laser Sintering in Polymer Powder bed

Compared to other AM technologies, Selective Laser Sintering (SLS) may be one of the most challenging AM technologies to master. But the benefits offered by SLS are worth the effort. SLS provides the freedom to quickly build complex parts that are more durable and offers better functionality over other rapid prototyping technologies. Furthermore, the SLS process is faster, more affordable and can build smaller features more accurately. Additionally, SLS process has a wide selection of material for many different applications.

However, even the industry has made major advances in this area, it remains that several phenomena are still not well understood in order to properly model the process and propose quality improvement of tracks and parts made. This will extend the areas of application for this technology, which promises to be very innovative, especially if we succeed to make parts with structures leading to achieve higher mechanical and thermal characteristics.

1. Overview of SLS in polymer powder bed

Plastic materials represent the developing direction of material science. Due to their reduced densities, special structures and often combined with other materials to give them better mechanical properties. The reduction in costs and energy consumption will provide massive benefits. The progress of our knowledge of polymers (their properties, performance and durability) allows us to apply them in more and more areas, based on their mechanical, thermal and chemical behavior in various environments. Among methods of polymer production, the selective laser sintering (SLS) is a very new technology. In SLS process, successive layers of material are formed by laser sintering, under computer control to create an object. This process allows creating products from a digital geometric models and part with complex geometries without additional tools.

1.1. Influence of properties on SLS

The SLS process with polymers is very different from the case with other materials (metal and ceramic), due to the distinguishing properties and thermal behavior of polymers. The impact of polymer on SLS process will be detailed as following.

Viscosity

During SLS process, to obtain a better quality of product, it is necessary to keep viscosity of molten grains low enough so as to ensure sufficient coalescence between grains. The rheological properties of molten liquid are crucial for the success of the sintering. The viscosity of the liquid-solid mixture is explained as below [1].

The viscosity of liquid is defined as:

$$\eta = \tau / \dot{\gamma}$$

where η is the liquid viscosity, τ is the applied shear stress and $\dot{\gamma}$ is the shear rate.

According to Arrhenius equation, the viscosity is extremely dependent on the temperature:

$$\eta_T = A e^{E/\sigma T}$$

Where η_T is the viscosity at the temperature T , A is the frequency factor (constant for a given material), E is the active energy of viscous flow and σ is the Boltzmann constant.

The viscosity of powder during SLS process includes the viscosity of both solid and liquid phase, which is dependent on characters of solid and liquid. Agarwala et al. [2] demonstrated that the viscosity of the solid-liquid mixture increases with the volume fraction of the solid phase and decreases when the particle size increases. Moreover, the viscosity of the mixture is directly proportional to volume fraction of the liquid phase. One important consequence of melt viscosity is the balling effect in SLS process. Very high melt viscosity at low energy input generates severe balling effect (Fig.II-1), and high energy input with very low melt viscosity results in melt spreading [3]. It appears that precise control of melt pool temperatures and the melt viscosity by process parameter optimization is very critical to improve the quality of product.

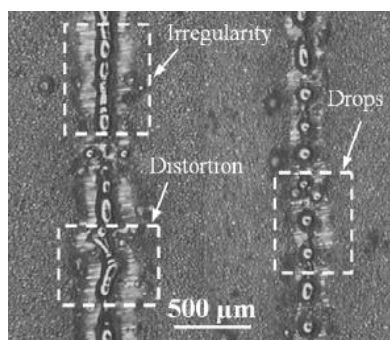


Fig.II-1. Balling effect of laser sintered tracks on steel substrate [3]

Surface tension

When the temperature is higher than the melting point, the liquid phase is formed. The densification of material occurs due to the merger of molten particles and rearrangement of solid particles under the influence of capillary forces. The capillary force during sintering is defined by [4]:

$$\Delta p = 2\gamma_{la}\cos\theta/d$$

Where p is the pressure on particles, γ_{la} is the surface tension between liquid-air interface, θ is the contact angle and d is the distance between particles.

The surface tension between interface of solid and liquid particles is defined as the energy which holds the particles together in order to minimize the superficial energy of powders. During the sintering by SLS, the material is partially melted. If the surface tension between the liquid-air interface (γ_{la}) is higher than that between the solid-liquid interface (γ_{sl}), θ increases and the liquid retracts by spheroidization to minimize the superficial energy. On the other hand, if the surface tension between the solid-liquid interface (γ_{sl}) is higher than that between the liquid-air interface (γ_{la}), the liquid spreads around particles and joins them together. The diffusing capacity of liquid on solid can be expressed by [5]:

$$S_{ls} = \gamma_{sa} - (\gamma_{sl} + \gamma_{la})$$

Where S_{ls} is the diffusion coefficient always positive.

Normally, the surface tension γ_{la} is less than γ_{sa} . Therefore, it should chose materials for SLS whose surface tension γ_{sl} is as small as possible.

Radiative properties

Thermal radiation is emitted at different wavelengths of electromagnetic spectrum, which ranges approximately from 0.1 to 100 microns, including part of the ultraviolet band and total of the visible and infrared bands. All materials emit and receive thermal radiation's energy with different efficiencies because of their distinguishing radiative properties: the emissivity, absorptivity, the reflectivity and transmissivity. These properties are dependent on the wavelength of incident energy, body temperature, surface condition, incidence direction and composition of materials. However, radiative properties are not easy to be obtained from measurements. These properties usually defined as functions of the composition of materials and the wavelength of incident energy [6].

The laser beam is commonly used in SLS process as radiation heat source. The absorptivity of a certain laser beam depends on the wavelength of laser, composition of material, size of grains and temperature of powder bed. In industrial manufacturing, most polymers used for SLS are assumed to be opaque in case of CO₂ laser with the wavelength of 10.6 microns. The transmissivity is zero and non-reflected radiation energy is completely absorbed by a thin layer of material [5].

However, amorphous polymers are not opaque to all wavelength, such as polycarbonate. A part of incident laser can transmit through a layer polycarbonate with thickness of 2.5mm. But, in applications, it is always assumed that all radiation energy is non-reflected and absorbed, because the powder bed is much thicker than 0.25mm. Some crystalline polymers, such as nylon, are opaque in solid phase and transparent when melting. So these materials absorb radiation energy differently depending on their state [7].

The assumption, that polymers used for SLS are opaque, is not realistic. Because the powder bed is a typical granular material. Unlike in the homogenous material, the thermal radiation in granular medium is different which the radiative intensity may be changed by absorption and scattering when a photon interacts with small particles. But, in previous researches, the influence of scattering on radiation energy is ignored.

1.2. Conventional forming method compared with SLS

Compared with conventional forming methods of polymers, the SLS process has lots of advantages. In order to make a comprehensive comparison, the most common forming processes of polymers will be

listed and explained firstly.

Extrusion

The extrusion is the most common way of shaping thermoplastics. It allows to obtain long products through a die such as tubes, profiles, sheets, films, plates, or wires. The material is added continuously in the form of powder or granules and leads to the forming finished or mostly semi-finished products (that is to say still requiring one or more steps to final use), as shown in Fig.II-2:

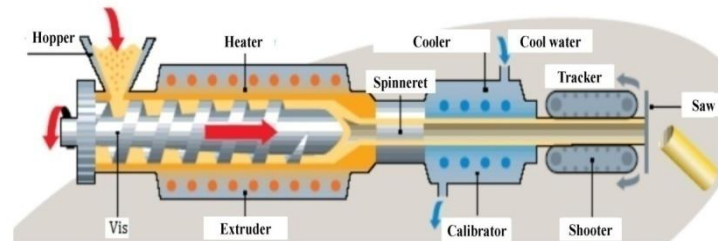


Fig.II-2. Forming of line type thermoplastic polymers by a single screw extruder [8]

Pre-stretching punch

The thermoforming mainly concerns polymers with large diffusion such as polystyrene, polyvinyl chloride, poly (acryl-butadiene-styrene), poly (methylmethacrylate), polycarbonate, polypropylene, polyethylene terephthalate or high-density polyethylene. Thermoforming is a major polymer shaping methods of making sheets or plates, generally extruded or calendared, even concave objects with different dimensions. It involves heating a polymer sheet to a temperature allowing its deformation (for amorphous thermoplastics, the forming phase corresponds to the temperature range above the glass transition; for semi-crystalline thermoplastics, the molding range is smaller and corresponds to the beginning of the melting range), then shaping it into a mold (usually steel or aluminum). After cooling, the desired object is obtained. The illustration of the forming process assisted by pre-stretching punch is presented in Fig.II-3. Because they are ease to be soften, amorphous thermoplastics are the most used[9].

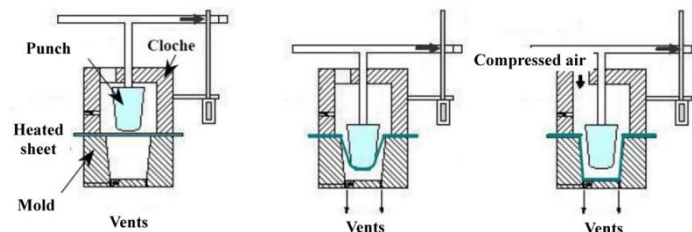


Fig.II-3. Illustration of the forming process assisted by pre-stretching punch [9]

Injection molding

The thermoplastic injection is to get a melted or softened polymer into a cold mold. The polymer then takes the shape of the mold and cools. Once the polymer is cooled, the part is ejected from the mold. This process is reserved for mass production due to the cost of design and manufacturing of mold and injection machine. The forming of thermoplastic polymer by an injection molding machine is shown in Fig.II-4:

The injection blow molding allows the forming of hollow parts from semi-finished products called "preform". In this case, a preform is a hollow which is generally carried out by the injection process. This preform is then heated and stretched inside a gas injection mold. This method is widely used in the manufacturing of PET bottles [11]. The blown film extrusion is to achieve the preform and injection blow in the same step [12].

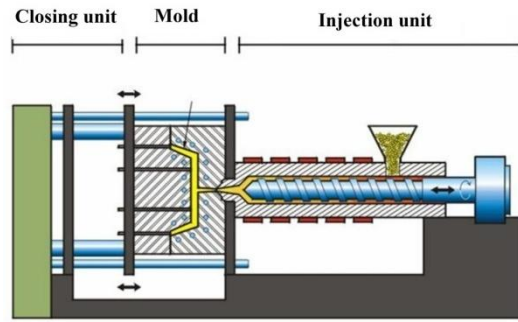


Fig.II-4. Forming of thermoplastic polymer by an injection molding machine [10]

Advantages of SLS

Due to additive build-up principle, SLS has an inherent advantage of producing parts of unlimited geometrical complexity, offering possibilities for optimization even by geometrical means. The process makes use of sliced CAD data to generate successive layers from bottom to top resulting in the final product. The advantages of SLS technology are manifold and listed as below [5-7]: (1) the technology allows extremely complex shape that is unachievable by traditional techniques; (2) the complexity of the shapes can be used to alleviate already existing parts by topology optimization; (3) SLS can be used for repairing injured parts; (4) the technique allows meet the customized requests (custom prostheses in the medical or dental sector, production tooling like molds); (5) at the end of the manufacturing process, the unused material is recycled for later use; (6) SLS does not require the use of specific tools, such as moulds; (7) products can be printed locally by sending the digital model (no transportation, saving space and minimizing losses).

Disadvantages of SLS

The biggest problem of the additive technology is well known that parts fabricated by SLS can be porous and/or have a rough surface depending on the used materials. The porosity of parts will largely reduce their mechanical performance and causes a strong anisotropy of mechanical properties: in the direction of construction (vertical, z), the mechanical strength is lower than in the (x,y) plane. Compared to parts fabricated by conventional process such as injection molding, parts from SLS can have equivalent modules without supercooling (slow cooling allows an increase in the crystallization rate). However, final properties (stresses and strain at break) are much smaller than the injected parts. An illustration of this comparison is presented in Fig.II-5.

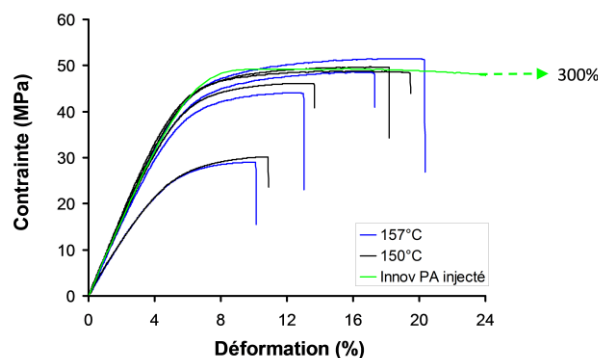


Fig.II-5. Curves of constraint for PA12 (InnevPA, Exceltec) specimens transformed under different conditions: laser fusion with preheating temperatures of 157°C (in blue) and 150°C (in black), respectively; injection molding (in green) [86]

Another problem, mainly for polymer parts, is the thermal distortion, resulting in the shrinking and warping of fabricated parts. This is mainly caused by the thermal residual stresses, due to the anisotropic distribution of temperature gradient. In other words, the microstructure of parts from SLS is complex and heterogeneous: some particles absorbing sufficient energy are fully melted; other particles absorbing

non-sufficient energy are partially even not melted. By the optical microscopy, the crystalline morphology can be observed from Fig.II-6. It can clearly seen the heterogeneous states of particles (full, partial and non molten).

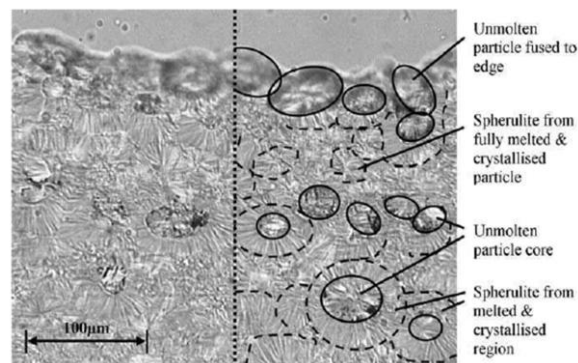


Fig.II-6. Crystal morphology of PA12 transformed by laser melting [87]

Due to the disadvantages above, 47% of manufactures in the USA do not yet trust this technology because of the non-reproducibility of the performances obtained, based on the survey of the Lawrence Livermore National Laboratory (USA) [88]. Hence, there is an urgent need to improve the understanding of the multiple mechanisms involved in the SLS process, and then propose a numerical modeling coupling all these multiphysical phenomena.

2. Introduction of SLS process

The production procedure of parts by SLS is well described in the literature [13] and illustrated in Fig.II-7. During manufacturing, a model of workpiece is created digitally with a design software. The numerical model is operated by processor of the SLS machine which will build the workpiece layer by layer. Before starting production, powders are placed on a plate of SLS machine and a powder bed with certain thickness is established in the production zone. The plate can move along the vertical axis to add new layers of powders and drop the production zone to create successive layers. Two extra plates can remove excess powders by a roller.

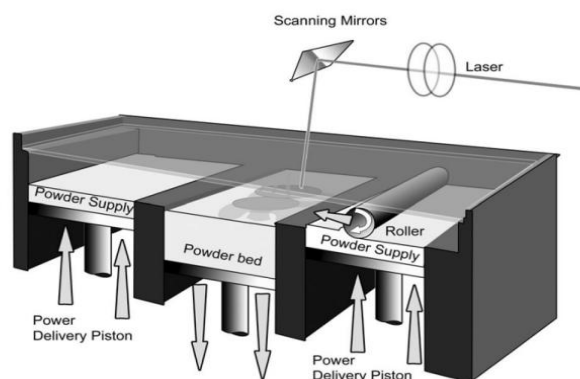


Fig.II-7. SLS machine for fabricating thermoplastic [13]

In SLS machine, powders are pushed by a roller to form a new layer in the production zone. The supply and manufacturing plate are preheating at different temperatures. A radiative system above the production zone (such as infrared ray) can heat up the powder bed. The laser is placed above the production zone and used to merge the specifically powder on the surface of powder bed by means of a mirror system.

In order to add a new layer of powders, the powder is firstly preheated in the supply zone. Then, the supply plate rises to release the powder. Powders are moved by a roller or blade from the supply zone to production zone. Hereafter, the plate of production zone decrease. Meanwhile, excess powders are

removed by the roller from the production zone to supply zone. The powders in production zone are heated up by infrared ray to the aimed temperature. And then, the laser heat a specific area of the new layer. Finally, the laser is interrupted and a new layer is added. Layer after layer, the process is repeated until obtaining the final part.

In the production zone, the temperature of powder bed is well controlled in depth by the plate for taking control of the cooling process of sintered part. At the end of manufacturing, the production zone is filled with unmelted powders which surrounds the solidified part. Thus, it needs to remove the unmelted powders and take out the final product from production zone. After production, the unmelted powders will be recycled for further manufacturing.

Until now, there are two main SLS machine suppliers, EOS GmbH and 3D systems Corporation. Pham et al. [14] described the features of these machines and analyzed the quality of SLS part by using EOS P700 machine. The schematic layout of EOS P700 is presented in Fig.II-8.

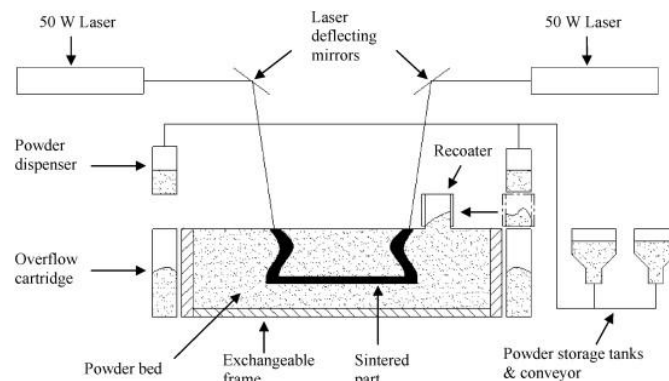


Fig.II-8. Schematic layout of EOS P700 [14]

3. Influential parameters of SLS process

The SLS process involves a large number of material properties and process parameters as listed in Table.II-1. The majority of these parameters are related to the thermal aspect of the process. According to previous researches [5-7,15-19], the key to successfully fabricate parts by SLS is the good control of these parameters.

Table.II-1. Influential material properties and process parameters of SLS process

Material properties	Process parameters
Viscosity	Laser power
Granulometry	Laser velocity
Thermal conductivity	Preheating temperature
Specific heat capacity	Interspace between laser paths
Radiative attenuation coefficient	Diameter of laser beam
Density	Thickness of powder layer
Diameter of grain	Time between successive layers

The quality of final part is highly dependent on the thermal cycle during processing. The importance of various process parameters have been numerically and experimentally studied by previous researches [15-19]. We classify the influences of parameters in Table.II-2.

Table.II-2. Influence of parameters on the density of final parts

Parameters	Influence on density
Laser power	Augmentation with power
Preheating temperature	Augmentation with temperature
Scanning speed	Diminution with speed
Thickness of layer	Diminution with thickness

The laser power is the parameter who plays the main role in the process, particularly strongly impacts the density and deformation stress. The density of parts increases with the laser power, but decreases after a certain limitation when the degradation occurs. Too much laser power can lead powders to melt and merge at the center of the laser beam, causing the Balling Phenomenon.

The preheating temperature is also limited to a few degrees below the melting temperature (thermoplastic material) or glass transition temperature (amorphous material) so as to increase the density of final parts but not to solidify the entire powder bed.

The scanning speed particularly influences the mechanical strength of the parts, but is also limited. Beyond a certain speed, a "balling" effect appears (spheroidization melted regions under the effect of surface tension). This speed is also limited by the frequency of the laser pulses (beyond a certain speed, there is no overlap between the laser spots and the melt surface is heterogeneous).

In fact, all these parameters must be considered as one entirety to achieve the best possible quality of final parts. Besides, for the same material, the parameters inducing higher density are not the same as those inducing maximum modulus.

4. Experimental researches of SLS process

The part treated by laser is often compared to that obtained by the injection process. Salmoria et al.[20] proposed an comparison of microstructure between two kinds of powders (PA6 and PA12) before and after laser treatment, as shown in Fig.II-9.

As presented in Fig.II-9, the powders are not totally densified and porosities are visible. While, PA6 seems more melted. We notice that grains of PA12 just attach to each other, with very little coalescence. Therefore, it indicates that the performance of pieces obtained from SLS will be highly dependent on the state of powder after melting.

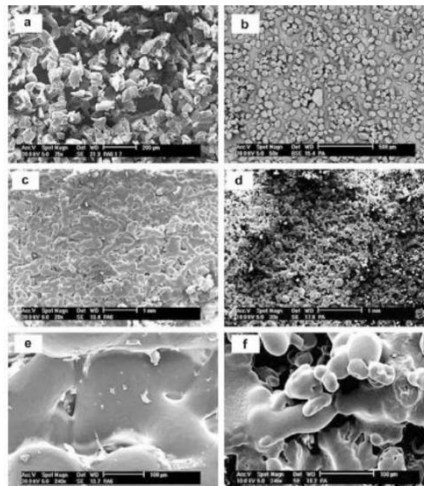


Fig.II-9. Microstructure of powders PA6 (a,c,e) and PA12 (b,d,f) [20]: (a,b) before sintering (a,b); (c,d,e,f) after sintering.

When fabricating pieces by SLS, several important steps take place: the choice of material used, limited preheating of powders, cooling control of production zone, choice of laser and control of its actions. In order to obtain a piece as desired, all these steps above are needed to be mastered. The

detailed description of these steps allows us to deeply understand the various difficulties during the SLS process. Due to many parameters involved in this process, it is difficult to reproduce pieces with the exact same states and properties [19,21].

An overview of previous researches on the selective laser melting process [22-24] allows to highlight the points discussed in this section.

Preheating in supply zone

In SLS process, powders of new layer is brought from supply zone to production zone. The melted powder in production zone will be influenced by powders of new layer. In effect, a cooling process is usually induced by new arrival powders, because they are colder than those molten [19]. Therefore, it is necessary to maintain powders higher than crystallization temperature in the supply zone, in order to prolong the sintering process. This is why the powder is preheated in supply zone. But, the preheating is limited by the melting temperature, so as not to induce a variation of powder state. In the case of PA12, the preheating temperature is recommended as 170-175°C (10-15°C below the melting temperature of the material) by Pham et al. [14].

Castability of powders

The range of grain size commonly used in the SLS process is from 25µm [25] to 250µm [26]. Manufacturing of powders usually offer grains with the size about 60-80µm, which are generally used for studying the process [16,27,28]. Grains with the size of 75-100µm give out good results of density and precision [29]. The thickness of single powder layer is from 100µm to 250µm [16,27,28,30-32].

The castability of powder is influenced by many parameters [33]. Various studies [34-36] propose methods of measurement to determine the Castability of powders, statically and dynamically. In general, the humidity, temperature and grain size will be influential. Seville [37] and Israelachvili [38] show that the Van der Waals forces are negligible when compared to the gravity if the grains are large enough. When the diameter becomes less than 50µm [39,40], the castability of powders is decreased. A narrow size distribution around 60µm for PA12 mixed with a few grains under 10µm gives a good castability [41]. However, the more the grains are large, the more the initial density of the powder bed is low, resulting in weakening parts densities. Furthermore, a higher density of the powder bed induces a shorter distance of penetration of the laser [19], which must be taken into account in the selection of layer thicknesses. Finally, the surface condition of grain also has a strong influence on the castability [42]. The more circularity of the grains, the better castability.

Heating in production zone

The powders in production zone must be maintained to a temperature enabling a good castability. In the case of PA12, the powders of new layer will be heated up to 150°C by the previous powders [19,43]. But new powders must be heated to a temperature closed to its melting temperature ($T_m=184^\circ\text{C}$ for PA12), in order to ensure optimal conditions for maintaining it in a liquid phase after laser treatment. Therefore, the infrared heater is operated for a few seconds before laser treatment, so as to heat the powder to the temperature of about 10°C below its melting temperature. In the case of PEEK, the preheating temperature is about 340°C [31]. Besides, the preheating temperature should be maintained very precisely, because a small variation will induce a lower density of final piece [7].

Choice of laser source

The laser, better absorbed by polymers, is the CO2 laser with the wavelength of 10.6µm [44-46]. Each material has a different absorption for this wavelength. The choice of laser should take into account its absorption, its energy density and its pulse model. It is possible to use the Nd:Yag laser with the wavelength of 1.064µm. In this case, the additive of black carbon is sensitive to the wavelength, allowing a better absorption of laser energy [47,48]. The CO2 laser is generally used with the mode of PWM (Pulse Width Modulation), in other words, by adapting the duty cycle to control the average output power.

Interactions between laser and material

The interaction between the laser and material is dependent on the wavelength of radiation laser,

the chemical composition of material and the temperature [49]. This interaction has been identified and represented by an exponential law named as Beer-Lambert law [44], which indicates the laser intensity decreases along the direction of depth. The Beer-Lambert law is also suitable for either UV or IR radiation, which has been studied by various previous works [49-53]. For a very small penetration depth (powder bed with lower porosity), this model can be reduced to a surface model of heat flow. This is the case, for example, when using a Nd:YAG laser to treat a titanium material which penetrates only 6 μm in depth [54]. Dong et al. [5] used a surface model with Gauss distribution to model the interaction between laser and material.

$$I_{boundary} = (1 - R_e)I_{0b}e^{-\frac{2(r^2)}{w^2}}$$

$$I_{0b} = \frac{2P}{\pi w^2} \quad w = \frac{R_L}{2.146}$$

where R_e is the reflective coefficient on the surface, r is the radial distance from the center of the laser beam, P is the power of the laser beam and R_L is the radius of the laser beam. In the case of polymer powder, the literature provides the average value for the reflectivity of about 4% [55]. Besides, the reflectivity is related to the wavelength of laser.

Melting of material

The laser beam provides the necessary energy to change the phase of material in a depth of several hundred micrometers. This fusion process is very fast about several milliseconds. In the case of polymer, the quantification of temperature rise caused by a CO₂ laser is little known. Dong et al. [56] propose a finite element model of a powder area heated by a surface deposit laser with Gauss intensity distribution. The author estimated that the temperature increases from 398 K before laser passage to 1321 K, for a power of 8 W and a scanning speed of 0.33m/s. Such overheating may cause a degradation of polymers. In fact, the laser-material interaction should be considered as volumetric model, then this increase will be lower. The following year [57] the author proposed new results. The heating obtained for a scanning speed of 1.26m/s and a power of 3.85 W is about 340 °C. Again, the model chosen is a surface heat flux. Lower temperature rise is expected by the Beer-Lambert laws in depth. Some previous work [51,58,59] studied the interaction between the diode laser and ABS-PC and obtained the temperature rise on the surface of material. For $P = 5\text{W}$, $V = 2\text{mm/s}$, temperature rise is about 240°C [51], and $P = 10\text{W}$ and $V = 16\text{mm/s}$, an overheating 90°C is observed [59]. Finally, Franco et al. [60] studied the selective laser melting in polyamide powder bed, which indicates the rise of temperature from 15°C to 180°C for speeds of 0.25m/s to 2.5m/s and laser power of 12.5W 50W. This study analyzed the thicknesses of molten powder and connected this thickness to the given laser energy density. The fusion of layers must be perfectly controlled. Too little energy will not allow to melt the various layers together, too much energy will induce melting of the previous layers that can increase the dimensions of the part manufacturing.

Coalescence of grains

In the liquid state, the powder grains coalesce [61,62], so as to minimize the curvature of the interface of all grains. Coalescence of all grains in the powder bed tends to densify the material and the air present between the grains escaping through even open paths to the surface of the powder bed. Dupin [19] shows that the coalescence of the polymer grains is very fast (a few seconds) relative to the holding time in the polymer of the liquid state (a few tens of seconds) in the SLM process.

Densification of powder bed and diffusion of gases

The literatures show that the final density of parts is mainly determined by the initial density of powder bed [43,63,64], the preheating temperature [65] and parameters of materials. All these parameters have influences on not only the coalescence of grains but also the diffusion of entrapped gases inside powder bed. In fact, during the densification of powder bed, closed pores inside powder bed are formed [66]. This process induces the diffusion of gases [67,68]. Gogos et al. [69] numerically determines the lifetime of nitrogen bubble in a polyethylene at 189°C and its result is consistent with previous studies [70,71]. In the case of an unsaturated polymer, the disappearance time of bubble with the radius of 10-265 μm is from a few milliseconds to fifty seconds. The surface tension has little influence

in this case. However, in the case of a saturated polymer, the time becomes much longer of 10 to 90 minutes for the same bubbles. And then the value of the surface tension governs the kinetics of disappearance time of bubbles. The recent study of Dupin [19] on the laser sintering process shows that the coalescence phenomena are fast and the residual porosity of parts cannot be attributed to this phenomenon alone. Thus, the evolution of the size of closed pores in the material can only be explained by the diffusion of gases in the molten polymer. Therefore, in order to obtain parts with proper densification, it is necessary to allow time for the gas to spread.

Cooling and solidification of material

The molten grains treated by laser undergo different successive cooling process: (1) just after the passage of laser beam, molten grains are rapidly cooled to the temperature of production zone; (2) grains are secondly cooled when adding next layer of powders; (3) the final cooling happens in the manufacturing zone. If the molten grains are cooled too fast to the temperature of surrounding powder bed, it is necessary to remain the temperature higher than the crystallization temperature to guarantee enough time for solidification. According to the different heat conditions, the crystallization time can range from a few seconds to several hours. The aim is to allow molten grains to crystallize as slowly as possible. Firstly, it takes time for gases to diffuse [19], then to limit distortions of parts in depth [16], and finally to obtain a high degree of crystallinity with a good rigidity of parts [72].

Degradation of material

If being maintained in a high temperature environment for hours, the polymer powder will degrade. When manufacturing parts, about 90% of the powder is not melted and recycled. Pham et al. [14] and Dotchev et al. [73] studied the degradation of powder PA12 undergoing several production cycles. They highlight the molecular weight of PA12 is multiplied by 12 after 3 recycles. The viscosity is thus increased and an effect of "orange peel" is measured at the surface of the parts during the use of recycled powder. But, a recycling strategy is possible to replace the full recycled powder by a mixture of new and recycled powder, which can increase the performance of fabrication parts [74,75]. Dupin [19] shows that the PA12 undergoes a post-condensation reaction which increase its molecular weight and finally impacts the crystallization of future parts. A decrease of viscosity has been observed in the powder with more than 4 recycles.

Porosity of workpiece

The porosity of workpiece is one of the most important properties concerned by manufacturing, because it is directly related to the mechanical performance of workpiece. Dupin [19] measured the porosity of PA12 workpiece obtained from SLS process. He studied the relationship between the porosity of workpiece and the energy density E_ρ . The energy density E_ρ is commonly defined as below [76]:

$$E_\rho = \frac{P}{\pi r^2} \frac{2r}{v} \frac{2r}{e}$$

where P is the laser power, r is the radius of laser beam, v is the scanning velocity and e is the space between two successive scanning lasers. In the experiment, different energy densities are obtained by varying the laser power. The space between each scanning laser is set to 0.15mm and the scanning speed is 5m/s.

Finally, Dupin [19] obtained the evolution of total porosity with different energy densities E_ρ , as presented in Fig.II-10. For Innov PA, a sharp decrease of porosity is observed between 1.36J/cm² and 2.04 J/cm². Then the porosity continues slightly decrease to a value of 4%. As Dupin's conclusion, it is noted that the energy density of 2.5 J/cm² is a good choice for manufacturing when considering the energy consuming.

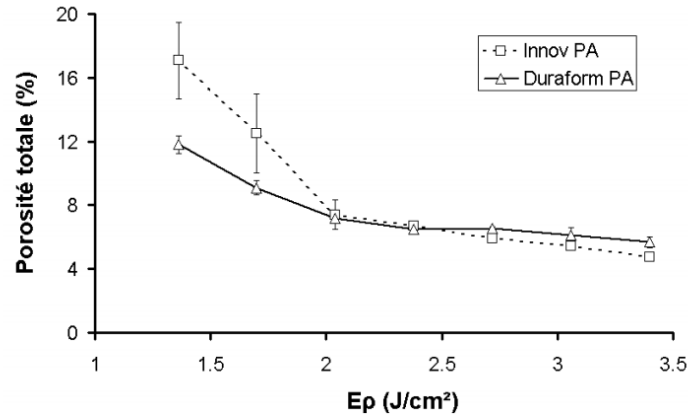


Fig.II-10. Evolution of total porosity with different energy densities E_p [19]

5. Analysis of SLS part qualities

Mechanical properties

Narkis et al. [77] shows that the properties of sintered parts highly depend on the state of densification of the material. At the beginning, the powder grains coalesce with each other and merge quickly. In parallel, the air flows between the grains is released to the surface of powder bed. And then, closed cavities are created and the evolution of densification has a lower kinetic. The analysis of flexural modulus as a function of time shows three different kinds of behavior (Fig.II-11): (1) the module increases rapidly with the rapid expansion of contact zones between grains; (2) the module drops during the creation of closed pores, (3) the module slowly increases again.

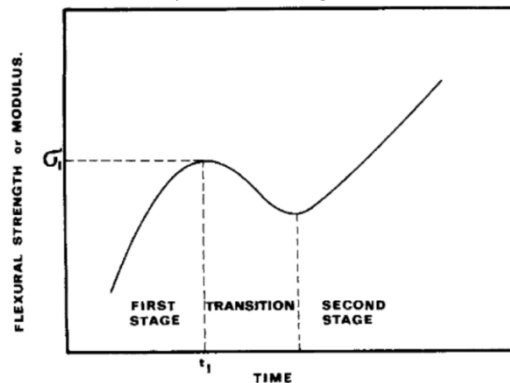


Fig.II-11. Variation of flexural modulus with time [77]

The flexural strength of PEEK parts treated by laser is highly dependent on their density [31]. Thus, a 60% decrease of flexural strength is obtained for a relative density of 0.9, and 90% decrease for a relative density of 0.8. The work of Ajoku et al. [78] researched the effect of the porosity of nylon on its compression behavior. The modulus of the part obtained by laser sintering is 10% lower than that of a molded part, due to the existence of heterogeneously distributed pores. A simulation work confirms the influence of the heterogeneous distribution of pores on the mechanical properties of sintered parts.

The performance of manufacturing parts depends on not only their porosity, but also the organization within the material. The orientation of parts with respect to the three fabrication axis X, Y and Z (Fig.II-12) strongly influences their mechanical strength [17,79,80]. The scan direction Y is the direction in which the best performance is obtained. The strength in the orthogonal direction X is controlled by the welding condition of inter-space between successive lasers. Finally, the strength in the direction Z depends on the thickness of each layer. In general, the performance of sintered parts is highly dependent on the energy supplied to the material and the inter-space between successive lasers [81]. Besides, the mechanical properties of parts also depend on the microscopic characteristics of the material after laser treatment. Thus, increasing the crystallinity of the material can greatly improve mechanical properties [19,72,82].

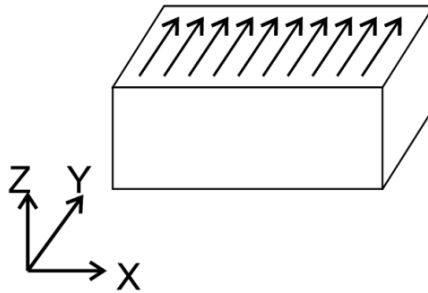


Fig.II-12. Directions of fabrication [83]

Defects of shape

The thermoplastic materials are very sensitive to thermal gradients due to inhomogeneous crystallizations. Because the perfect control of the heat in the manufacturing zone is difficult, the workpieces present shape defects of warping and distortion [16]. These defects, when they appear in the manufacturing zone, can result in the stop of manufacturing because warping may cause a rise of material which can collide with the powder supplying system. To decrease the distortions, it is necessary to maintain the temperature as close as possible to the polymer melting temperature and guaranty the homogeneity to maintain a low and uniform rate of crystallization. Wang et al. [16] concluded the shape defect is directly relative to the laser power. Besides, the thermal conduction can induce the molten of grains closed to the fusion region and increase the size of sintered parts [17,84].

State of surface (Roughness)

The surface condition of parts is characterized in two ways. Firstly, the melting of powders leads to a more or less densification, which can induce a significant roughness. Moreover, the fusion caused by laser generates a specific effect at the edge of workpiece [16]. When the laser arrives at the edge, it will stop or change its direction. Due to the Gauss distribution of laser energy intensity, the laser does not provide enough energy to its periphery. Thus, at the edge of workpiece, the thickness of fusion area is not the same as in the area where the laser makes a complete pass. Finally, the difference of thickness induces a geometry whose edge is not smooth. A staircase effect is always observed at the surface of workpiece.

6. Application of SLS polymer product

The selective laser sintering of polymers is a new technology. Despite this, many applications of additive manufacturing are currently used. In fact, this technology has a great potential in the production of pieces with extremely complex geometry. That is why it has been widely used in the medical, artistic and aeronautic field.

Medical field

The medical field is one of the most consumer areas of parts manufactured by SLS. Furthermore, it is also one of the most hot topics concerned by the academic research for this process. The main reason is the uniqueness of the morphology of each individual.

Most plastic processes use expensive tools for the polymer processing. The cost of a product is almost inversely proportional to the number of parts produced. In the case of the single piece, as is the case for the medical field, the cost of tool would be unacceptable (it takes several thousands of euros for a mold of injection). In another point, this technology can facilitate the medical field by using 3D images and computer aided design software to directly produce pieces. Several applications of polymer SLS pieces in medical field are presented in Fig.II-13.



Fig.II-13. Application examples of the selective laser sintering in the medical field [85]

The two images on the left presents a micro-surgery system developed by polyamide 12. This system can be directly placed on the patient and allows to control the manipulation of surgical instruments with an accuracy below one millimeter. The third image demonstrates another bio-product by SLS. This product shows the possibility in the future that a new biocompatible material can replace human tissue (a bone in this case). The final image is a prosthesis leg manufactured by another machine: 3D Systems.

Aeronautic and automotive field

Due to the confidentiality, it is difficult to find examples of Aeronautic or automotive applications. Nevertheless, some companies are working on research programs. Besides, the U.S. Air Force has funded lots of money on this technology. The 3D Systems company works on strengthening the parts production chain of the F-35. French companies have also invested in the field. In Fig.II-14, we can see a central diffuser of Falcon 7X from Dassault Aviation and the air inlets of PA 12 for vehicle made by E2R. Finally, the FADIPLAST project of France aims to expand the range of usable materials for additive manufacturing applications in the areas of aviation and aerospace.

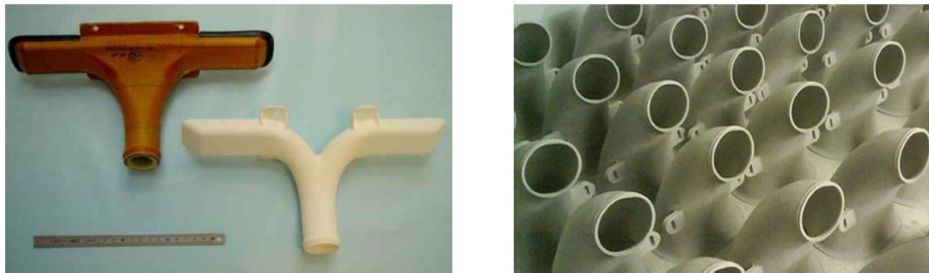


Fig.II-14. Application examples of the selective laser sintering in the Aeronautic and automotive field [85]

Diverse applications

Due to the capability of fabricating piece with complex geometry, a large amount of applications are found in the fields of architecture, jewelry or luxury interior design. So architects can build quickly conception models of their projects, as shown in Fig.II-15.



Fig.II-15. Application examples of the selective laser sintering in the architecture field [85]

More marginal applications are encountered in the field of paleontology, where scientists reconstruct fossil to preserve them from damage of manipulating and to reproduce multiple copies, as presented in Fig.II-16.



Fig.II-16. Application examples of the selective laser sintering in the paleontology field [85]

Researchers, at the Fraunhofer Institute for Manufacturing Engineering and Automation IPA, develop an outer frame robot fabricated by thermoplastic SLS technology in the aim of searching disaster victims, as shown in Fig.II-17.



Fig.II-17. Application examples of the selective laser sintering in the robotic field [85]

Reference

- [1] Agarwala M.K., 1990, Viscosity of suspensions, Master Thesis, University of Alabama at Birmingham.
- [2] Agarwala M.K., Bourell D., Beaman J., Marcus H. and Barlow J., 1995, Direct selective laser sintering of metals, *Rapid Prototyping Journal*, 1:36-44.
- [3] I. Yadroitsev, I. Smurov, 2010, Selective laser melting technology: from the single laser melted track stability to 3D parts of complex shape, *Physics Procedia* 5:551–560.
- [4] Agarwala M.K., 1994, Synthesis: selective laser sintering and post-processing of metal and ceramic composites. PhD. Thesis, University of Texas at Austin, USA.
- [5] L. Dong, 2007, Simulation et Modélisation du Frittage Selectif par Laser Après la Methode des Elements Finis, Ph.D. Thesis, Université Louis Pasteur, Strasbourg, France.
- [6] Nelson J.C., 1993, Selective laser sintering: A definition of the process and an empirical sintering model. PhD Thesis, University of Texas at Austin, USA.
- [7] Denis DEFAUCHY, 2013, "SIMULATION DU PROCEDE DE FABRICATION DIRECTE DE PIECES THERMOPLASTIQUES APR FUSION LASER DE POWDER", Ph.D. Thesis, Arts et Métiers PatisTech, Paris, France.
- [8] Giraud A.. Presentation of Pipe Products. International Technical Symposium, 2000
- [9] Erner Aliza. Étude expérimentale du thermoformage assisté par poinçon d'un mélange de polystyrènes. Sous la direction de Noëlle Billon, Nice Sophia Antipolis, Mines ParisTech, 2005
- [10] Gosselin Ryan. Injection de mousses composites bois/plastiques d'origine postconsommation. Sous la direction de Rodrigue Denis et Riedl Bernard, Laval, Université de Laval, 2005
- [11] Bordival Maxime. Modélisation et optimisation numérique de l'étape de chauffage infrarouge pour la fabrication de bouteilles en PET par injection soufflage. Sous la direction de Fabrice Schmidt et Yannick Le Maout, Albi, Mines ParisTech, 2009.
- [12] Tewfik Ghomari. Contribution à la modélisation 3D volumique de la mise en forme des corps plastiques creux. Sous la direction de R. Ayad et D. E. Kerdal, Reims, Université de Reims Champagne-Ardenne, 2007
- [13] Hopkinson, N., Hague, R., Dickens, P. (2006). *Rapid manufacturing: an industrial revolution for a digit age*. Chichester, UK: John Wiley & Sons.
- [14] Pham, D., Dotchev, K., Yusoff, W., 2008, Deterioration of polyamide powder properties in the laser sintering process. Part C: *Journal of Mechanical Engineering Science*, 222, 2163-2176.
- [15] Ho, H., Gibson, I., Cheung, W. (1999). Effects of energy density on morphology and properties of selective laser sintered polycarbonate. *Journal of Materials Processing Technology*, 89-90, 204-210.
- [16] Wang, P., Li, X., Xiao, J., Zhu, F., Yang, Y. (2006). Research on sintering parameters and prototyping quality of SLS polymer powders, *International Congress on Applications of Lasers and ElectroOptics*, Scottsdale.
- [17] Caulfield, B., McHugh, P., Lohfeld, S. (2007). Dependence of mechanical properties of polyamide components on build parameters in the SLS process. *Journal of Materials Processing Technology*, 182, 477-488.
- [18] Beal, V., Paggi, R., Salmoria, G., Lago, A. (2009). Statistical evaluation of laser energy density effect on mechanical properties of polyamide parts manufacturing by selective laser sintering. *Journal of Applied Polymer Science*, 113, 2910-2919.
- [19] Dupin, S. (2012). Etude fondamentale de la transformation du polyamide 12 par frittage laser: mécanismes physico-chimiques et relations microstructures/propriétés. Thèse de Doctorat, INSA de Lyon.
- [20] Salmoria, G., Leite, J., Paggi, R. (2009). The microstructural characterization of PA6/PA12 blend specimens fabricated by selective laser sintering. *Polymer Testing*, 28, 746-751.
- [21] Leigh, D. (2010). LS production in a multiple platform environment. Additive Manufacturing International Conference, Loughborough University, (UK).
- [22] Kruth, J.-P., Levy, G., Klocke, F., Childs, T. (2007). Consolidation phenomena in laser and powderbed based layered manufacturing. *CIRP Annals - Manufacturing Technology*, 56, 730-759.
- [23] Kruth, J.-P., Levy, G., Schindel, R., Craeghs, T., Yasa, E. (2008). Consolidation of polymer powders by selective laser sintering. *Proceedings of the 3rd International Conference on Polymers and Moulds Innovations*, Gent (B).

- [24] Goodridge, R., Tuck, C., Hague, R. (2012). Laser sintering of polyamides and other polymers. *Progress in Materials Science*, 57, 229-267.
- [25] Tan, K., Chua, C., Leong, K., Cheah, C., Cheang, M., Abu Bakar, M., et al. (2003). Scaffold development using selective laser sintering of polyetheretherketone–hydroxyapatite biocomposite blends. *Biomaterials*, 24, 3115–3123.
- [26] Salmoria, G., Ahrens, C., Klauss, P., Paggi, R., Oliveira, R., Lago, A. (2007). Rapid Manufacturing of Polyethylene Parts With Controlled Pore Size Gradients Using Selective Laser Sintering. *Materials Research*, 10, 2011-214
- [27] Kim, D., Ahn, Y., Bae, S., Kim, C., Kim, H. (2006a). Development of polyamide-6 powders and its effect on the fabrication by selective laser sintering. *International Congress on Applications of Lasers and Electro-Optics*, Scottsdale.
- [28] Kim, D., Ahn, Y., Bae, S., Choi, B., Choi, K. (2006b). A study on the selective dual laser sintering process for the solid freeform fabrication system. *International Congress on Applications of Lasers & Electro-Optics*, Scottsdale.
- [29] Shi, Y., Li, Z., Sun, H., Huang, S., Zeng, F. (2004). Effect of the properties of the polymer materials on the quality of selective laser sintering parts. *Proceedings of the Institution of Mechanical Engineers, Part L: Journal of Materials: Design and Applications*, 218, 247-252.
- [30] Kruth, J., Mercelis, P., Froyen, L., Rombouts, M. (2004). Binding Mechanisms in Selective Laser Sintering and Selective Laser Melting. *15th Solid Freeform Fabrication Symposium*, Austin (TX).
- [31] Schmidt, M., Pohle, D., Rechtenwald, T. (2007). Selective Laser Sintering of PEEK. *CIRP Annals -Manufacturing Technology*, 56, 205-208.
- [32] Bae, S., Kim, D., Choi, K., Yoo, S. (2008). Application and evaluation performance of DMS in the SLS process. *International Congress on Applications of Lasers & Electro-Optics*, Temecula (CA).
- [33] Ganesan, V., Rosentrater, K., Muthukumarappan, K. (2008). Flowability and handling characteristics of bulk solids and powders – a review with implications for DDGS. *Biosystems Engineering*, 101, 425-435.
- [34] Schulze, D. (2008). *Powders and Bulk Solids: Behavior, Characterization, Storage and Flow*. Springer Berlin - Heidelberg – New York – Tokyo.
- [35] Krantz, M., Zhang, H., Zhu, J. (2009). Characterization of powder flow: Static and dynamic testing. *Powder Technology*, 194, 239-245.
- [36] Amado, F., Schmid, M., Levy, G., Wegener, K. (2011). Advances in SLS Powder Characterisation. *International Solid Freeform Fabrication Symposium*, Austin (TX).
- [37] Seville, J., Tüzün, U., Clift, R. (1997). *Processing of Particulate Solids*, Powder Technology. Blackie Academic & Professional.
- [38] Sraelachvili, J. N. (1992). *Intermolecular and Surface Forces*. Boston : Academic Press.
- [39] Condotta, R. (2005a). *Coulabilité des poudres cohésives : Mesure aux faibles contraintes, granulaires humides et application à une poudre industrielle*. Thèse de doctorat, INP Toulouse.
- [40] Condotta, R., De Ryck, A. (2005b). Dilatancy and yield stress of dry and wet beads, 5th International Conference on the Micromechanics of Granular Media: Powders and Grains, Stuttgart.
- [41] Keller, B., Pfeifer, R., Su, W., Eyrer, P. (1998). Temperature dependent optical properties of polymers as a basis for laser process modeling. *Solid Freeform Fabrication Proceedings*, Austin (TX).
- [42] Oshima, T., Zhang, Y.-L., Hirota, M., Suzuki, M., Nakagawa, T. (1995). The effect of the types of mill on the flowability of ground powders. *Advanced Powder Technology*, 6, 35-45.
- [43] Rietzel, D., Drexler, M., Kühnlein, F., Drummer, D. (2011b). Influence of temperature fields on the processing of polymer powders by means of laser and mask sintering technology. *International SFF Symposium – An Additive Manufacturing Conference*, Austin (TX).
- [44] Jacobs, P. (1992). *Rapid Prototyping and Manufacturing - Fundamentals in stereolithography*. Published by the Society of Manufacturing Engineers in cooperation with the Computer and Automated Systems Association of SME.
- [45] Tolochko, N., Khlopkov, Y., Mozharov, S., Ignatiev, M., Laoui, T., Titov, V. (2000). Absorptance of powder materials suitable for laser sintering. *Rapid Prototyping Journal*, 6, 155-161.
- [46] Kruth, J., Wang, X., Laoui, T., Froyen, L. (2003). Lasers and materials in selective laser sintering. *Assembly Automation*, 23, 357-371.
- [47] Wagner, T., Hofer, T., Knies, S., Eyrer, P. (2004). Laser Sintering of High Temperature Resistant Polymers with Carbon Black Additives. *International Polymer Processing*, 19, 395-401.

- [48] Woicke, N., Wagner, T., Eyerer, P. (2005). Carbon Assisted Laser Sintering of Thermoplastic Polymers. Annual Technical Conference, Boston (MA).
- [49] Keller, B. (1998). Rapid Prototyping: Grundlagen Zum Selektiven Lasersintern Von Polymerpulver. Shaker Verlag.
- [50] Riedel, D., Castex, M. (1999). Effective absorption coefficient measurements in PMMA and PTFE by clean ablation process with a coherent VUV source at 125 nm. *Applied Physics A: Materials Science & Processing*, 69, 375-380.
- [51] Ilie, M., Kneip, J., Mattei, S., Nichici, A. (2007a). Simulation du procédé de soudage laser par transparence de polymères thermoplastiques. Congrès Français de Thermique, Île des Embiez (FR).
- [52] Ilie, M., Kneip, J., Mattei, S., Nichici, A., Roze, C., Girasole, T. (2007b). Through transmission laser welding of polymers – temperature field modeling and infrared investigation. *Infrared Physics & Technology*, 51, 73-79.
- [53] Coelho, J. M., Abreu, M. A., Carvalho Rodrigues, F. (2004). Methodologies for determining thermoplastic films optical parameters at 10.6 μm laser wavelength. *Polymer Testing*, 23, 307-312.
- [54] Kolossov, S., Boillat, E., Glardon, R. F., Locher, M. (2004). 3D FE simulation for temperature evolution in the selective laser sintering process. *International Journal of Machine Tools and Manufacturing*, 44, 117-123.
- [55] Sun, M., Beaman, J. (1991). A three dimensional model for selective laser sintering. *Solid Freeform Fabrication Proceedings*, Austin.
- [56] Dong, L., Makradi, A., Ahzi, S., Remond, Y. (2007). Finite element analysis of temperature and density distributions in selective laser sintering process. *Materials Science Forum*, 553, 75-80.
- [57] Dong, L., Makradi, A., Ahzi, S., Remond, Y., Sun, X. (2008). Simulation of the densification of semicrystalline polymer powders during the selective laser sintering process: Application to Nylon 12. *Polymer Science Series A*, 50, 704-709.
- [58] Speka, M., Mattei, S., Pilloz, M., Ilie, M. (2008). The infrared thermography control of the laser welding of amorphous polymers. *NDT & E International*, 41, 178-183.
- [59] Ilie, M., Cicala, E., Grevey, D., Mattei, S., Stoica, V. (2009). Diode laser welding of ABS: Experiments and process modeling. *Optics & Laser Technology*, 41, 608-614.
- [60] Franco, A., Lanzetta, M., Romoli, L. (2010). Experimental analysis of selective laser sintering of polyamide powders: an energy perspective. *Journal of Cleaner Production*, 18, 1722-1730.
- [61] Frenkel, J. (1945). Viscous flow of crystalline bodies under the action of surface tension. *J. Phys.*, 9, 385-391.
- [62] Eshelby, J. (1949). Discussion of 'Seminar on the Kinetics of Sintering'. *Metallurgical Transactions*, 185, 796-813.
- [63] Yan, C., Shi, Y., Hao, L. (2011). Investigation into the Differences in the Selective Laser Sintering between Amorphous and Semi-crystalline Polymers. *International Polymer Processing*, 16, 416-423.
- [64] Rietzel, D., Aquite, W., Drummer, D., Osswald, T. (2011a). Polymer powders for Selective Laser Sintering – Production and Characterization. 44th Conference on Manufacturing Systems, Madison (WI).
- [65] Tontowi, A., Childs, T. (2001). Density prediction of crystalline polymer sintered parts at various powder bed temperatures. *Rapid Prototyping Journal*, 7, 180-184.
- [66] Narkis, M. (1979). Sintering Behavior of Poly(Methyl Methacrylate) Particles. *Polymer Engineering and Science*, 19, 889-892.
- [67] Spence, A., Crawford, R. (1996). The Effect of Processing Variables on the Formation and Removal of Bubbles in Rotationally Molded Products. *Polymer Engineering and Science*, 36, 993-1009.
- [68] Kontopoulou, M., Vlachopoulos, J. (2001). Melting and Densification of Thermoplastic Powders. *Polymer Engineering and Science*, 41, 155-169.
- [69] Gogos, G. (2004). Bubble Removal in Rotational Molding. *Polymer Engineering and Science*, 44, 388-394.
- [70] Spence, A. G. (1994). Analysis of Bubble Formation and Removal in Rotationally Moulded Products. PhD thesis, The Queen's University of Belfast.
- [71] Kontopoulou, M., Vlachopoulos, J. (1999). Bubble dissolution in molten polymers and its role in rotational molding. *Polymer Engineering and Science*, 39, 1189-1198.
- [72] Zarringhalam, H. (2007). Investigation into crystallinity and degree of particle melt in selective laser sintering. PhD Thesis, Loughborough University.

- [73] Dotchev, K., Yusoff, W. (2009). Recycling of polyamide 12 based powders in the laser sintering process. *Rapid Prototyping Journal*, 15, 192-203.
- [74] Gornet, T.J. (2002a). Characterisation of selective laser sintering TM to determine process stability. *Proceeding of Solide Freeform Fabrication*, Austin (TX).
- [75] Gornet, T. (2002b). Improving selective laser sintering consistency. *CAD/CAM publishing*, San Diego (CA).
- [76] R. Morgan, C. J. Sutcliffe, W. O'Neill. Density analysis of direct metal laser re-melted 316L stainless steel cubic primitives. *Journal of Materials Science*, 39, 1195 – 1205, 2004.
- [77] Narkis, M. (1979). Sintering Behavior of Poly(Methyl Methacrylate) Particles. *Polymer Engineering and Science*, 19, 889-892.
- [78] Ajoku, U., Hopkinson, N., Caine, M. (2006a). Experimental measurement and finite element modelling of the compressive properties of laser sintered Nylon-12. *Materials Science and Engineering: A*, 428, 211-216.
- [79] Gibson, I., Shi, D. (1997). Material properties and fabrication parameters in selective laser sintering process. *Rapid Prototyp Journal*, 3, 129-136.
- [80] Ajoku, U., Saleh, N., Hopkinson, N., Hague, R., Erasenthiran, P. (2006b). Investigating mechanical anisotropy and end-of-vector effect in laser-sintered nylon parts. *Proceedings of the Institution of Mechanical Engineers, Part B: Journal of Engineering Manufacturing*, 220, 1077-1086.
- [81] Ho, H., Gibson, I., Cheung, W. (1999). Effects of energy density on morphology and properties of selective laser sintered polycarbonate. *Journal of Materials Processing Technology*, 89-90, 204-210.
- [82] Majewski, C. E., Zarringhalam, H., Hopkinson, N. (2008). Effect of the degree of particle melt on mechanical properties in selective laser sintered Nylon-12 parts. *Proceedings of the Institution of Mechanical Engineers, Part B: Journal of Engineering Manufacturing*, 222, 1055-1064.
- [83] Mercelis, P., Kruth, J.P., Residual stresses in selective laser sintering and selective laser melting, *Rapid Prototyping Journal*, 12, 254-265
- [84] McAlea, K., Forderhasse, P., Booth, R. (1998). Selective laser sintering of polymer powder of controlled particle size distribution. US patent 5817206.
- [85] Emmanuel DUMOULIN, 2013, Fabrication additive de pièces en polymères thermoplastiques hautes performances et en polyamide 12 par le procédé de frittage sélectif par laser, PhD Thesis, l'École nationale supérieure des mines de Paris.
- [86] Dupin S.: "Etude fondamentale de la transformation du polyamide 12 par frittage laser : mécanismes physico-chimiques et relations microstructure-propriétés", Thèse de Doctorat, INSA-Lyon, 2012.
- [87] Zarringhalam H., Hopkinson N., Kampermanb N.F., de Vlieger J.J.: "Effects of processing on microstructure and properties of SLS Nylon 12", *Mater. Sci. Eng. A*, 435-436, 172-180, 2006.
- [88] Mies, D., Marsden, W. & Warde, S. "Overview of Additive Manufacturing Informatics: A Digital Thread" *Integr Mater Manuf Innov* (2016) 5: 6. doi:10.1186/s40192-016-0050-7.

Chapter III: Multiphysical Phenomena and Models Involved in SLS

The selective laser sintering is a new technology that involves multiple physical phenomena, such as the radiation heat transfer, heat conduction, coalescence and densification. In order to optimize the quality of product and control the fabrication, it is necessary to fully understand all physical phenomena involved during the process of selective laser sintering. Even though many researchers have built lots of models concerning the SLS, most of these models only consider part of the physical phenomena during SLS process. In order to deeply and globally understand the SLS process, we propose a synthetic model of SLS process that couples most of these phenomena. The ultimate goal of this model is to explain multiple physical phenomena occurring inside powder bed, and also to predict quantitatively the dimension of final parts.

1. Multiphysical phenomena involved in SLS

In the last chapter, we comprehensively introduced the process of selective laser sintering. During SLS process, a digital model of product is created and operated by process of SLS machine. The product is built cyclically layer by layer under control of computer. This process can be divided into three steps as shown in Fig.III-1.1:

Deposition of new powder layer

Layer by layer deposition of powdered material is a key step in selective laser sintering, yielding a loosely packed irregular structure. This packing structure represents the state of powder before consolidation with sintering. This process involves phenomena of motions and contacts of particles, which is described by the dynamics of particle. The model concerning this process is based on the theory of granular dynamics so as to simulate a randomly generated powder bed. Meanwhile, for modeling purpose, all particles are assumed to have a spherical shape.

Heating by laser

In SLS process, the laser beam is the thermal source. The interaction between laser and particles is described by the theory of laser radiation transfer. Moreover, the powder bed is a granular material. Unlike the homogenous material, the thermal radiation in granular medium is different, because the distribution of laser intensity can be changed by absorption and scattering when photons interact with small particles. Furthermore, due to the granularity of powder bed, the heat conduction is different from the case of continuum medium. The quoted differences between granular and homogenous material requires the development of a model concerning the SLS process considering the characters of granular material [1-5].

Sintering and post process

In SLS process, selected regions of powder bed are rapidly heated through a phase transition of solid-liquid-solid state. When the temperature is higher than the melting point, small molten particles come together and merge into larger particles as a result of surface tension. This phenomenon is called coalescence. Meanwhile, the entrapped air is released from the inside of powder bed that is called the densification. The process, including these two phenomena, is named as sintering. Now, it is established that the performance of SLS product is highly related to the degree of sintering [6-8]. Thus, most of products will be treated by post processing so as to increase the rate of relative density and crystallinity (for semi-crystallization polymers).

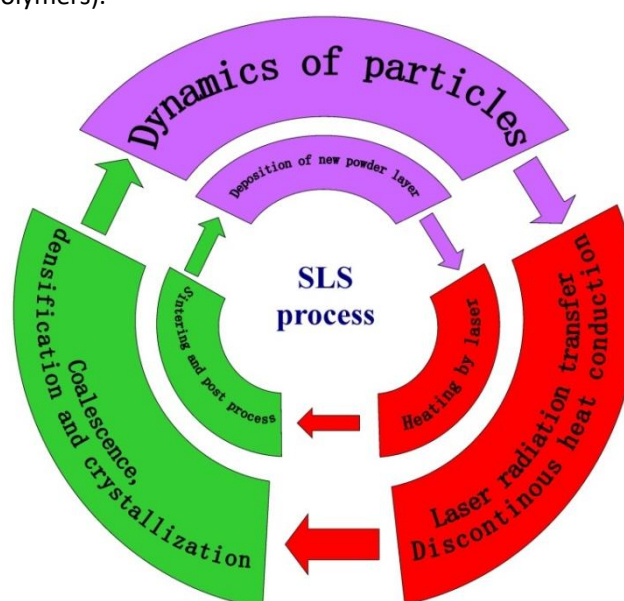


Fig.III-1.1. Synthetic of phenomena and models involved in SLS

2. Global model of SLS

As illustrated in Fig.III-1.1, physical phenomena involved during SLS process are multiple and complex. Therefore, we propose a synthetic model that includes most of physical phenomena during SLS process. Our global model can be separated into four main submodels: the radiation transfer, discrete heat conduction, sintering and particle dynamics. The structure of the global model of SLS is given in Fig.III-2.1.

Fig.III-2.1 shows the operational process of the synthetic model: the submodel of laser radiation transfer uses parameters of laser beam (such as the laser power, scanning speed and radius of laser beam). It also uses the optical properties of material and the geometry of grains so as to calculate the energy absorbed by powder bed. The heat flux from submodel of laser radiation transfer is regarded as the intern heat source in discontinuous heat conduction submodel. The temperature field of powder bed is calculated by discontinuous heat conduction submodel. Using this model, we can obtain the thermal history of each grain inside powder bed. Sintering submodel uses thermal data and rheological properties of particles to estimates the change of geometry of powder bed caused by the coalescence and densification. After finishing the sintering process, the contact dynamic submodel is used to simulate the deposition of successive layer of powders.

The submodel of radiation transfer concerns the interaction between the laser beam and powder bed. Several phenomena are considered in the submodel, including the reflection, transmission, absorption and scattering. The submodel of discrete heat conduction describes the transfer of heat between particles. The phenomena considered by this submodel are the thermal conduction inside powder bed and convection at surface. The sintering submodel concerns the phenomena of coalescence and densification. It describes the merger of melton grains driven by surface tension and the release/diffusion of entrapped gases inside powder bed. The submodel of contact dynamic concerns the motions and contacts between particles when depositing a new layer of powders. All these submodels above will be detailed in the following sections.

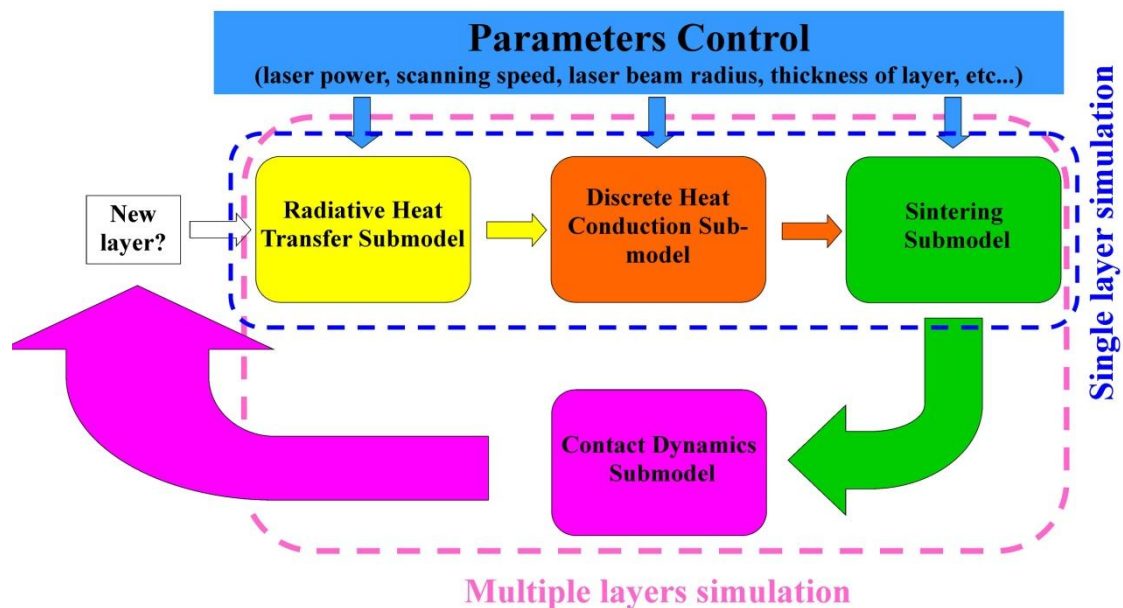


Fig.III-2.1. Structure of synthetic model of SLS process

3. Radiative heat transfer submodel

During SLS process, selected regions of powder bed are heated by laser beam, which is a strong thermal radiation phenomenon. The quality of final product from SLS is directly related to parameters of laser beam (such as laser power, scan speed and radius of laser beam). Therefore, the significance of thermal radiation underlines the need to develop a thermal model to improve our understanding of radiation transfer during SLS process.

3.1. Generalities of radiation heat transfer

The radiation transfer and thermal radiation are commonly used to describe the science of the heat transfer caused by electromagnetic waves. There are so many examples of thermal radiation, such as the heating from sun on a clear day or feeling of hot when facing the fire.

In fact, all materials continuously emit and absorb electromagnetic waves or photons, by lowering or raising their molecular energy levels. The strength and lengths of emission depend on the temperature of the emitting material. The range of wavelengths from 10^{-7} m to 10^{-3} m (ultraviolet, visible and infrared) are much more important and considered as presented in Fig.III-3.1.

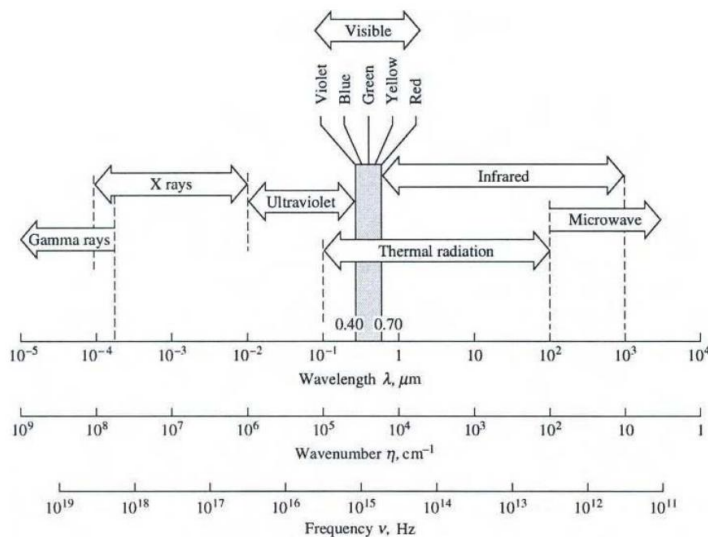


Fig.III-3.1. Electromagnetic wave spectrum (for radiation traveling through vacuum) [10]

The thermal radiative energy can be considered as consisting of electromagnetic waves or as massless energy particles, called photons (particle and wave approaches). Both these two views have been confirmed for describing completely all radiative phenomena that have been observed. In general, the electromagnetic wave theory is more used to radiative properties of liquid, solid and interfaces, while radiative properties of gases are more conveniently obtained from quantum mechanics.

When photons strikes the surface of another medium, the photons may be reflected either partially or totally. And then, the non-reflected part will penetrate into the medium. Photons may become continuously attenuated when passing through the medium. If the attenuation is complete so that no penetrating radiation reemerges, it is known as opaque. If photons passes through a medium without any attenuation, it is termed transparent, while a body with partial attenuation is called semitransparent. Metals are commonly regarded as opaque (like steel 316L), while many polymers are semitransparent, such as Polyether ether ketone (PEEK) and Polyamide 12 (PA12).

3.2. Thermal radiation in granular medium

Unlike in the homogenous material, the thermal radiation in granular medium is different because the radiative intensity may be changed by absorption and scattering when a photon interacts with small

particles. Common examples of this interaction are sunlight being absorbed by a cloud of smoke, scattering of sunshine by the atmosphere resulting in blue sky and red sun. At the beginning, astrophysicists dealt with the radiation scattering by particles due to their interests in the scattering of starlight by interstellar dust. Now, the scattering of electromagnetic waves or photons is concerned by scientists from many other domains: The scattering within the earth atmosphere is concerned by meteorologist; Physics and engineers today use light scattering as diagnostic tools for non-intrusive and non-destructive measurements in gases, liquid and solid. A review of thermal radiation phenomena in granular medium has been given by Tien and Drolen [11].

The new direction and distance of a scattered photon after passing a particle depends on many parameters: the shape of the particle; the material of the particle; the size of the particle and the clearance between particles. The shape of particles is always simplified to be spherical or cylindrical. These simplifying assumptions give generally excellent results [11]. The interaction between photons and spherical particles are shown in Fig.III-3.2.

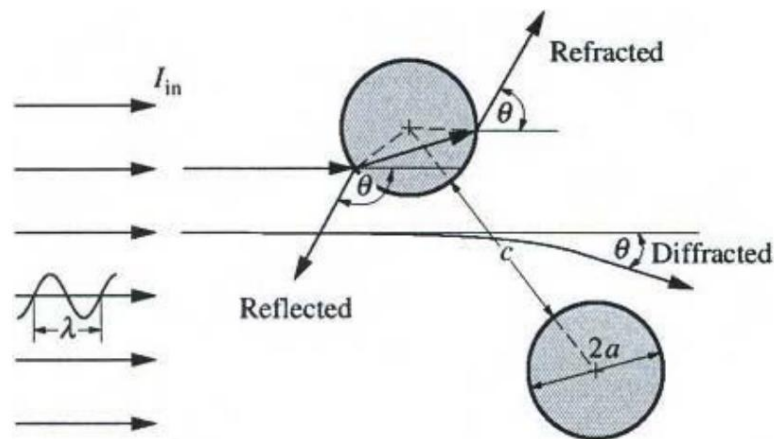


Fig.III-3.2. Interaction between photons and spherical particles [10]

As shown in Fig.III-3.2, an electromagnetic wave or photon passing through the spherical particles will be absorbed or scattered. The scattering is caused by three different phenomena: the diffraction, reflection by a particle and refraction in a particle. In other words, the photon direction of propagation is altered by the presence of the particle, even though it never come into contact with the particle. Furthermore, the photon is reflected from the surface of particle. Moreover, the photon is partially absorbed when penetrate into the particle and then reemerge traveling into a different direction.

The scattering and absorption of radiation by single spheres was first discussed during the later part of the nineteenth century by Lord Rayleigh [12], who obtained a simple solution for spheres whose diameters are much smaller than the wavelength of radiation. This work was followed by the classical paper of Gustav Mie [13] in 1908, who developed an equivalent solution to Maxwell's equations for an electromagnetic wave train traveling through a medium with an imbedded sphere. Generally, the Mie theory must be used when the size of spheres is closed to the wavelength of radiation.

In Mie theory, the amount of scattering and absorption by a particle is usually expressed by the terms of the scattering cross section C_{sca} and absorption cross section C_{abs} . The total amount of absorption and scattering, called extinction, is expressed by the term of extinction cross section:

$$C_{ext} = C_{abs} + C_{sca}$$

Often efficiency factors Q are used instead of cross section, being non-dimensionalized with the projected surface area of the sphere:

$$Q_{abs} = \frac{C_{abs}}{\pi r^2}, \quad Q_{sca} = \frac{C_{sca}}{\pi r^2}, \quad Q_{ext} = \frac{C_{ext}}{\pi r^2}$$

$$Q_{ext} = Q_{abs} + Q_{sca}$$

Radiation interacting with a spherical particle may be scattered away from its original direction by an angle θ . The propagation vector of the photon may be redirected by the scattering angle as shown in Fig.III-3.2. This directional scattering behavior can be described by the average cosine of the scattering angle, known as the anisotropy factor g , and related to the phase function $\Phi(\theta)$ as following:

$$g = \overline{\cos\theta} = \frac{1}{4\pi} \int_0^{4\pi} \Phi(\theta) \cos\theta d\Omega$$

According to the work of Chu and Churchill[14,15], the scattering phase function $\Phi(\theta)$ can be expressed as a series in Legendre polynomials: $\Phi(\theta) = 1 + \sum_{n=1}^{\infty} A_n P_n(\cos\theta)$. The coefficients A_n and P_n are directly related to the Riccati-Bessel functions, which are rather complicated not reproduced here.

The anisotropy factor g takes value ranging from -1 through 0 to 1. When g is equal to -1, it is the backscattering. The propagation vector after scattering is opposite to the original direction. When g is equal to 0, it is the isotropic scattering, which means equal amounts of photons are scattered into all directions. When g is equal to 1, it is forward scattering. The propagation vector after scattering is the same as the original direction. The phase function with different anisotropy factors is presented in Fig.III-3.3.

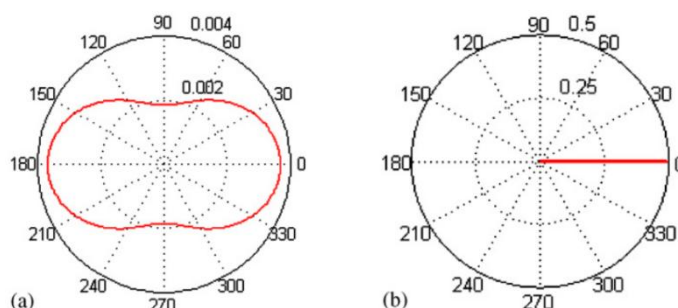


Fig.III-3.3. Phase function for (a) $g=0.06$, (b) $g=0.96$ [16]

3.3. Review of thermal radiation models in SLS process

Unlike traditional technologies, the SLS process fabricates solid objects from powders, a typical granular medium that is very different from the homogenous medium. Until now, all thermal radiation studies in SLS process can be classified as continuum based or discrete particle based approach [17]. In the continuum approach the granular bed is assumed as a homogeneous medium having effective properties, while these properties are modeled separately or obtained experimentally. On the other hand in discrete particle approach, the packed bed is explicitly modeled and the discrete nature of system is taken into account while considering the involved phenomenon.

In the case of continuum approach, the laser beam energy input is often modeled as a heat flux with density described by the Gaussian distribution. Lin et al. [18] developed a three-dimensional finite element based model to predict the temperature and energy density distribution in sintered amorphous polymer powders modeling the heat flux as a boundary heat source on the surface. Labeas et al. [19], Grewell et al.[20] and Defauchy [21] used the Beer-Lambert law to simulate the absorption phenomenon inside the material. Becker and Potent [22] developed a mathematical model considering different energy conditions to join parts with various absorption properties. In all these works, the authors ignored the effect of scattering of the laser intensity distribution inside the semi-transparent material. This assumption is not realistic, in particular given the particulate nature of the powder. Mingliang et al. [23] studied the welding process of polycarbonate (PC), polyamide 6 (PA6) and glass fibers reinforced polyamide 6 (PA6GF), by laser transmission welding (LTM) using both the FEM numerical simulation and experimental measurements to investigate the effect of scattering. They defined global factors to describe the scattering phenomena, by separating the optical extinction coefficient into two contributions: absorption and scattering parts. This global approach is not sufficient to characterize explicitly the scattering phenomena

because the redirection of photon propagation is not taken into consideration.

The granular medium can be regarded as homogenous when the porous medium with porosity smaller than 0.05 [17]. However, most of the powder beds have porosity higher than the specified limit. Therefore, radiative properties of powder bed cannot be predicted from the properties of single particle as homogenous medium.

In case of discrete particle approach, Tien [24] reviewed the radiation heat transfer in granular medium. He concluded the use of discontinuous approach based on Monte Carlo and/or ray-tracing method is found to be a natural choice for predicting radiative heat transfer in granular systems. Mariana et al. [16] used Monte Carlo method based on the Mie theory to analyze the scattering effect on laser beam in a non-absorbent polymer powder bed. Zhou et al. [25] developed a Monte Carlo method based on ray tracing scheme in the granular system to simulate the radiative heat transfer in a bimodal randomly packed structure composed of particles with various size and emissivity. He presents experimental confirmation of his Monte Carlo calculations of the light scattering in the polymeric medium. Andre et al. [26] proposed a numerical method based on ray tracing to simulate the light scattering during laser welding process. In his work, the radiative energy is estimated at the welding interface in order to describe the heat source. Singh and Kaviny [27] used Monte-Carlo method for radiative heat transfer through mono-dispersed powder bed. They proposed a discrete ordinate method based scaling approach so that independent radiative properties can be scaled to obtain effective properties in dependent regime. A ray-tracing model is developed by Wang and Kruth [28] to simulate the energy absorption and penetration during the SLS of metal powders. Their model, which is based on geometrical optics, yields the evolution of the energy absorption in the powder and accordingly predicts the sintering zone dimension. Chan and Tien [29] used discrete model to determine radiative properties of packed bed, they treated particulate medium as regularly packed system and investigated a representative unit cell using ray-tracing techniques. Kudo et al. [30] adopted Monte-Carlo technique for radiation heat transfer in representative unit cell. Yang et al. [31] investigated radiation in randomly packed bed using Monte-Carlo method.

Based on the review of existing thermal radiation models, a discontinuous approach is adopted in our work, based on the Monte Carlo ray tracing method. This model will be the subject of the following section.

3.4. Monte Carlo method for thermal radiation

Problems in thermal radiation concern the energy which travels as photons over relatively long distance along a straight path before interaction with matter. This type of problems is particularly suitable to be solved by a Monte Carlo technique [10]. Solving a thermal radiation problem by Monte Carlo implies tracing the history of a statistically meaningful random sample of photons from their points of emission to their points of absorption. The advantage of the Monte Carlo method is that even the most complicated problem may be solved with relative ease, as schematically indicated in Fig.III-3.4. Nevertheless, for a trivial problem, setting up the appropriate photon sampling technique alone may require more effort than finding the analytical solution. As the complexity of the problem increases, however, the complexity of formulation and the solution effort increase much more rapidly for conventional techniques. For problems beyond a certain complexity, the Monte Carlo solution will be preferable.

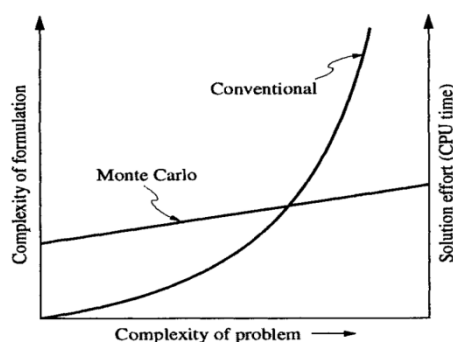


Fig.III-3.4. Comparison of Monte Carlo and conventional solution techniques [10]

3.4.1. Introduction of Monte Carlo method

The Monte Carlo method was invented by a Polish mathematician Stanislaw Ulam, which is named after the principality of Monte Carlo in the south of France. The aim of Monte Carlo method is to solve one or both of the following problems: generating samples from a given probability or/and estimating experiments of functions under this distribution. When the problem is calculating the probability of some random events or the expectation of a random variable, through some kind of "experimental" approach, the frequency or some characteristic variables of such events will be regarded as the solution of the problem. Based on different sampling methods, Monte Carlo methods can be classified as four different methods: importance sampling, rejection sampling, Metropolis method and Gibbs sampling.

Let's consider for a while the area estimation of an irregular geometry, how to use Monte Carlo method to calculate it? Let's imagine that you have a bag of beans. These beans are evenly dispread on the floor. Then we count the number of beans in the geometry. This number is an approach of the area of the geometry. The more and smaller the beans are, the more accurate the result is. Here, we assume there is no overlap between beans. For example, consider a circle inscribed in a unit square. Given that the circle and the square have a ratio of areas that is $\pi/4$, the value of π can be approximated using a Monte Carlo method, as shown in Fig.III-3.5. The difference between the estimation and real value is only 0.07%.

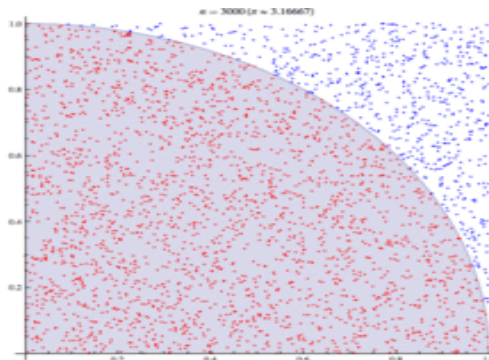


Fig.III-3.5. Monte Carlo method applied to approximating the value of π [32]

3.4.2. Monte Carlo method based on Mie theory

At the beginning of the section 3.4, the Monte Carlo method has been introduced as a useful method for simulating thermal radiation. Mariana et al. [16] proposed a Monte Carlo method based on the Mie theory in order to simulate the scattering effect on laser beam in polymers. In this method, the trajectories of photons are simulated probabilistically through the considered medium until they hit a predefined detecting area. A flowchart is presented in Fig.III-3.6 that illustrates the main steps in the Monte Carlo method based on Mie theory. As shown in Fig.III-3.6, this method includes four main steps: photon initialization, photon scattering, photon propagation and reflection or transmission at the boundary.

Photon initialization

In general, the light is assumed to illuminate on a plane-parallel medium, which infinites in the x and y directions, with a certain thickness in the z direction, containing random distributed spheres with identically size. For each photon, provided from the laser source, the initial position is defined by the radius r and the angle φ in the beam section. The angle φ is uniformly distributed in a range of $[0, 2\pi]$. The radial distribution is assumed to obey to Gaussian distribution. The initial direction of propagation is downward into the participating medium $\vec{u}_0 = (0,0,1)$. So the initial conditions equations are written as following:

$$\begin{cases} x_0 = r \cdot \cos(\varphi) \\ y_0 = r \cdot \sin(\varphi) \\ z_0 = 0 \end{cases} \quad (\text{III-3.1})$$

where $r = R_0 \xi_1$ and $\varphi = 2\pi \xi_2$, R_0 is the radius of laser beam section. ξ_1 and ξ_2 are pseudo-random numbers distributed normally (Gauss) and uniformly over the interval [0,1] respectively.

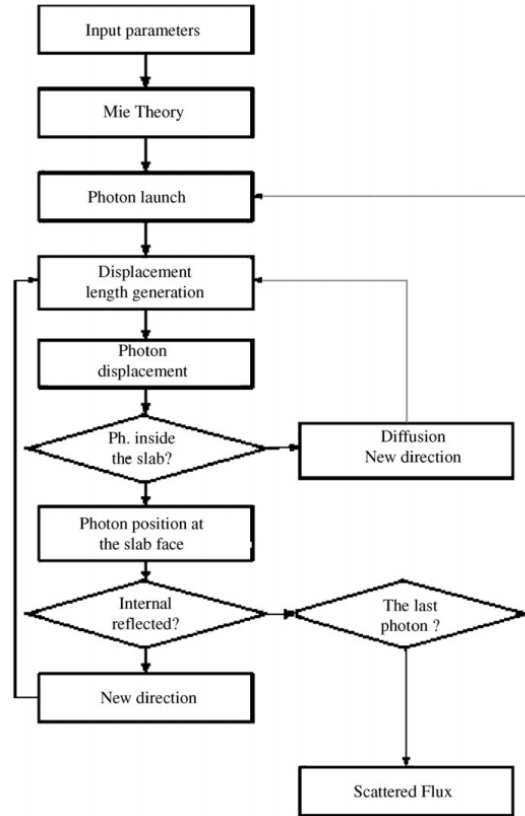


Fig.III-3.6. Flowchart of Monte Carlo ray tracing method [16]

Photon propagation

The propagation of photon at each step is calculated based on the probability distribution of photon's mean free path or displacement [16], given by:

$$l = -\frac{\ln(\xi)}{\alpha_{abs}} \quad (\text{III-3.2})$$

where ξ is a random variable uniformly distributed over the interval [0,1]; α_{abs} is the absorption coefficient, $\alpha = \alpha_{abs} + \alpha_{sca}$ is the total attenuation coefficient and α_{sca} is the scattering coefficient.

Photon scattering

Once the photon hits a particle, it is scattered because the particle is non-absorbent. The scattering direction is chosen according to the normalized phase function provided by Mie theory, which describes the probability density function for the azimuthal and longitudinal angles.

Scattering direction is defined by two angles (θ, ϕ) relatively to the incident direction. Since we consider an unpolarized radiation and spherical particles, the phase function has no azimuthally dependence, so angle ϕ is uniformly distributed between 0 and 2π [16]:

$$\phi = 2\pi\xi \quad (\text{III-3.3})$$

Angle θ is chosen using the phase function, given a pseudo-random number, by inverting the

following integral [16]:

$$\xi = \frac{\int_0^\theta p(\theta) \sin(\theta) d\theta}{\int_0^\pi p(\theta) \sin(\theta) d\theta} \quad (\text{III-3.4})$$

Once the deflection angle θ and the azimuthal angle ϕ are chosen, the new direction for the photon propagation can be calculated using the next formulas [16]:

$$k'_x = \frac{\sin(\theta)}{\sqrt{1-k_z^2}} \cdot (k_x k_z \cos(\phi) - k_y \sin(\phi)) + k_x \cos(\theta) \quad (\text{III-3.5})$$

$$k'_y = \frac{\sin(\theta)}{\sqrt{1-k_z^2}} \cdot (k_y k_z \cos(\phi) - k_x \sin(\phi)) + k_y \cos(\theta) \quad (\text{III-3.6})$$

$$k'_z = -\sin(\theta) \cos(\phi) \sqrt{1-k_z^2} + k_z \cos(\theta) \quad (\text{III-3.7})$$

The direction cosines $k_{x,y,z}$ are the cosines of the angle that the photon's direction makes with each axis in the slab referential.

If the photon is moving over the z-direction, use of the above formulas will lead to a division by zero, since $k_z=1$, so for avoiding this the following formulas have to be used [16]:

$$k'_x = \sin(\theta) \cos(\phi) \quad (\text{III-3.8})$$

$$k'_y = \sin(\theta) \sin(\phi) \quad (\text{III-3.9})$$

$$k'_z = \text{sign}(k_z) \cos(\phi) \quad (\text{III-3.10})$$

Reflection or transmission at the boundary

When photons reach the upper and lower boundaries of the medium, the possibility of a photon being internally reflected is computed according to the Fresnel reflection coefficient $R(\theta_i)$ [16].

$$R(\theta_i) = \frac{1}{2} \left[\frac{\sin(\theta_i - \theta_t)^2}{\sin(\theta_i + \theta_t)^2} + \frac{\tan(\theta_i - \theta_t)^2}{\tan(\theta_i + \theta_t)^2} \right] \quad (\text{III-3.11})$$

where $\theta_i = \cos^{-1}(|u_z|)$ is the angle of incidence at the boundary and θ_t is given by the Snell's law $n_i \sin(\theta_i) = n_t \sin(\theta_t)$, n_i and n_t are incident and transient refraction coefficients, respectively.

By comparing the Fresnel reflection coefficient $R(\theta_i)$ with a pseudo-random number ξ , it is determined whether the photon is internally reflected or transmitted[16]:

For $\xi > R(\theta_i)$, the photon escapes the slab, it is recorded by the detector as the transmitted radiation when it leaves at the bottom or as backscattered one when it leaves from the top.

For $\xi \leq R(\theta_i)$, the photon is internally reflected and its directional cosines are updated by reversing the z component.

3.5. Radiation Transfer in SLS process

According to the work of Gusarov et al. [35], a powder bed with opaque or semi-transparent particles can be approximated by an equivalent homogenous absorbing scattering medium. Therefore, the distribution of the luminance within a powder bed involves three mechanisms: emission, absorption and diffusion, as illustrated in Fig.III-3.7.

When photons pass through a powder bed, part of the flux is absorbed and the rest is scattered in multiple directions. The molecules absorb a part of the flux, in turn, emit photons at their local temperatures, and some of re-emitted flux are absorbed again.

According to literatures [36-38], the reabsorbed energy obtained from the emission is much smaller than the incident part from laser beam. The temperature of laser beam is usually beyond 2000K. Therefore, it is acceptable to assume that the self emission has little effect on the thermal behavior process of SLS and can be ignored [39].

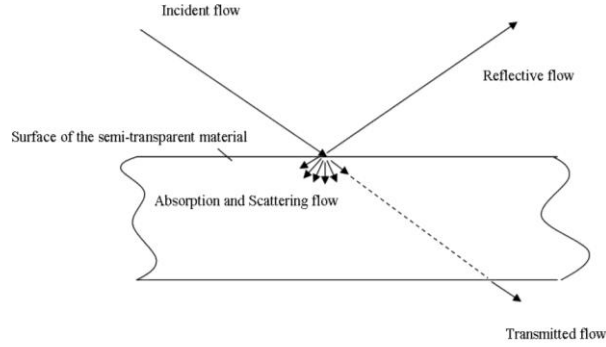


Fig.III-3.7. Illustration of the luminance within a powder bed

In condition of little emission, the radiation transfer equation in the material, giving the laser polymer interaction, can be simplified as follow, it is named as Beer-Lambert Law [40]:

$$I(s) = \int_{\lambda} I_{\lambda 0} e^{-\alpha_{\lambda} s} d\lambda \quad (\text{III-3.12})$$

where α_{λ} is the monochromatic attenuation coefficient, λ the wave length, $I(s)$ is the radiation energy intensity at a given depth s , $I_{\lambda 0}$ is the initial radiation energy intensity. For laser heat source, the radiation wave length is usually unique. So Eq.(III-3.12) can be written as:

$$I(s) = I_0 e^{-\alpha s} \quad (\text{III-3.13})$$

3.5.1 Modified Monte Carlo Ray Tracing method

When a light beam interacts with a particle, it is demonstrated the emission of secondary radiation known as scattering. In condition that the size of particle is less than twenty times of the laser wavelength, Mie theory has been confirmed for modeling the scattering in participating medium by experiments [16,42]. Furthermore, a combination of Monte Carlo and ray tracing method is widely used in multiple scattering topics [33,34], named as the Monte Carlo ray tracing method. In this method, the trajectories of light rays (photons) are simulated probabilistically through the considered medium until they hit a predefined detecting area. Several works [16,43,44] indicate that Monte Carlo method is capable to solve more complex problem in relative cases, and it is widely used in modeling radiative heat transfers in non-homogeneous and non-continuum media.

In the SLS process, the size of particle and laser wavelength are about $40 \mu m$ and $10 \mu m$, respectively. Besides, the powder bed is a granular material that is a typical non-homogenous and non-continuum media. Therefore, the Monte Carlo ray tracing method is very suitable in our case. However, Mariana et al. [16] assumed that polymers are non-absorbent, which is actually partial absorbent in SLS process. Thus, we modify the Monte Carlo ray tracing method by introducing the Beer-Lambert law so as to estimate the attenuation of laser energy inside semi-transparent powder bed. The main calculation steps of the modified method are illustrated in Fig. III-3.8 and details are explained here after.

Most steps of modified Monte Carlo ray-tracing method are identical to that presented in section III-3.4.2. However, it is not easy to calculate the angle θ due to its implicit format in Eq.III-3.4. Therefore, we introduced the Henyey and Greenstein phase function in order to save the computational consuming, which is validated by many researches in case of modeling scattering between light and small particles [42,43,45].

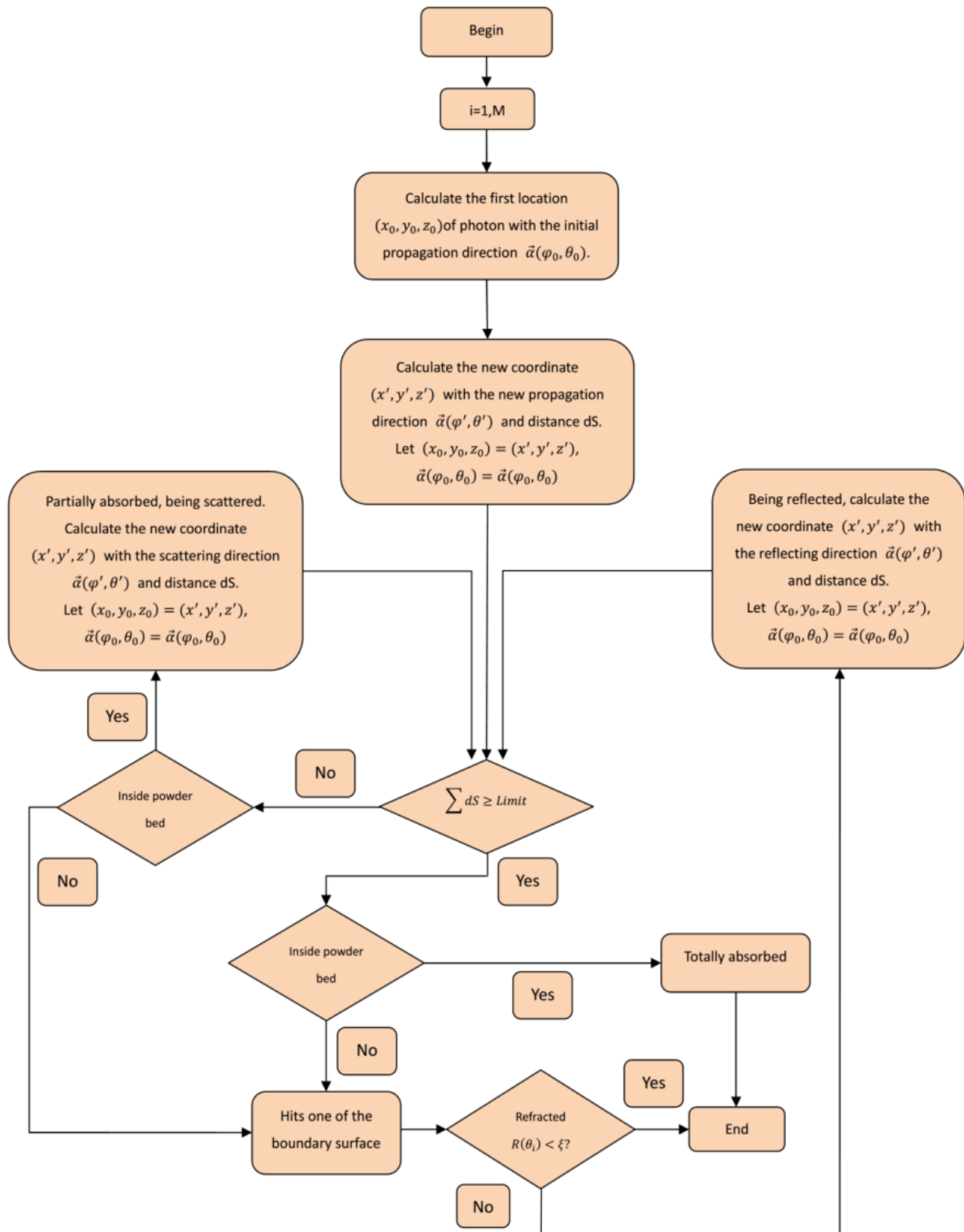


Figure III-3.8. General flow chart of ray tracing process based on Monte Carlo method

Modified photon scattering

The scattering direction is described by the azimuthal and longitudinal angles(ϕ, θ), as illustrated in Fig.III-3.9(b). In our model, we considered an unpolarized radiation and spherical coordinates. Therefore, the phase function has no azimuthally dependence and ϕ is uniformly distributed over the interval $[0, 2\pi]$:

$$\phi = 2\pi\xi \quad (\text{III-3.14})$$

The longitudinal angle θ is characterized by the Henyey and Greenstein phase function [45]:

$$\cos(\theta) = \frac{1}{2g} \left\{ 1 + g^2 - \left[\frac{1-g^2}{1-g+2g\xi} \right]^2 \right\} \quad (\text{III-3.15})$$

where $-1 \leq g \leq 1$ is the anisotropy factor, ranging from backscattering ($g = -1$) through isotropic scattering ($g = 0$) to forward scattering ($g = 1$).

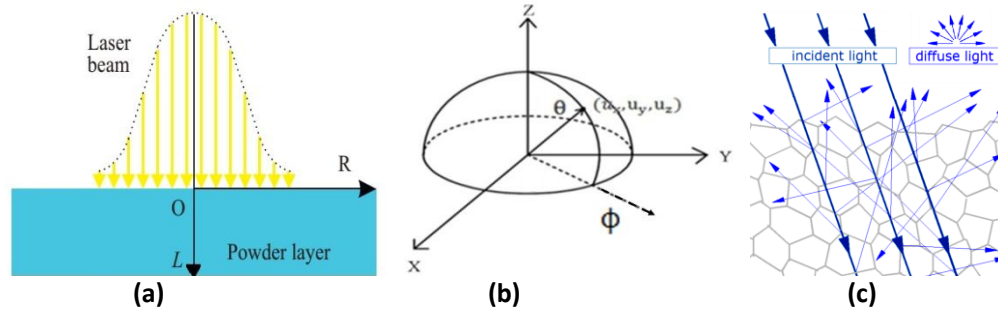


Fig.III-3.9. Illustration of photon initialization and scattering direction:
 (a) Photon initialization at 2D cross section;
 (b) Direction of photon propagation with coordinates (x,y,z)
 (c) Light behavior in STM

3.5.2. Validation of modified Monte Carlo method: case of metallic powder

The coupling of all these previously developed theories of light behavior constitutes the modified Monte Carlo theory, which will now be used to simulate the laser energy distribution in granular medium. Before applying the model to simulate the entire laser sintering process, a validation of the estimated laser heat source distribution within the materials is needed. For this purpose, we compare first the model's estimations to some results from the literature.

Table.III-1. Parameters and properties used in modified Monte Carlo method

Parameter and Property	Value
Diameter of laser beam, D_L [μm]	120
Thickness of powder layer, h [μm]	50
Total attenuation coefficient, α [m^{-1}]	$4e^4$
Anisotropy factor, g	0.88
Single scattering albedo, ρ	0.7, 0.9, 0.95, 0.98

Even there is a lack of similar simulations in the literature, the work of A.V. Gusarov et al. [35] is one interesting and recent published work dealing with radiative heat transfers in granular medium. In order to validate the model, we propose to compare results obtained with our modified Monte Carlo method developed in this paper to those published in the work of A.V. Gusarov et al. [35]. In their work, A.V. Gusarov proposed a 3D (2D Axisymmetric) theoretical model of the radiation transfer equation, with numerical simulation using Discrete Ordinates Method, to calculate the spatial distributions of deposited laser energy on a powder. In their work, they conclude that the scattering of the incident laser beam in the powder layer can considerably affect the distribution of heat source intensity, especially, at the center of the beam. When the number of simulated photons reaches 5×10^6 , the distribution of scattered photons is stable. The parameters chosen for our modified Monte Carlo method are taken from the published data presented in the reference [35] and presented in Table.III-1. The numerical simulation based on Monte

Carlo method is implemented in Matlab.

In Fig.III-3.10, a comparison of 2D radiative energy distribution with different albedo is presented. The radiation fluxes are normalized by the maximum incident radiation flux q_0 as $\bar{q}_z = q_z/q_0$ in a dimensionless coordinates $\tau_r = \alpha r$ and $\tau_z = \alpha z$, ($\tau_z = 0$ meaning at the surface). The single scattering albedo $\rho = \frac{\alpha_{sca}}{\alpha}$ characterizes the effect of scattering on radiation transfer. When $\rho = 0$, there is no scattering and the entire radiative flux is absorbed by particles. The comparison shows that results of Monte Carlo method are in good agreement with those from the published work. We can observe in Fig.III-3.10(a), that the value of \bar{q}_z is negative when $\tau_r > 2$ implying that photons are completely reflected back on the surface of powder bed. This situation is due to the assumption of the existence of back scattering on the upper surface, which is not considered in our model, where no negative energy is predicted. In both figures, the energy distribution presents a bell shape, with a maximum energy concentration at the region close to the center of laser beam. Far from the surface, as the beams penetrates through the bottom of the material, and also for higher albedo values (high scattering), the maximum peak of radiative flux is decreasing at the center of laser beam, because the light always changes travelling direction when scattering.

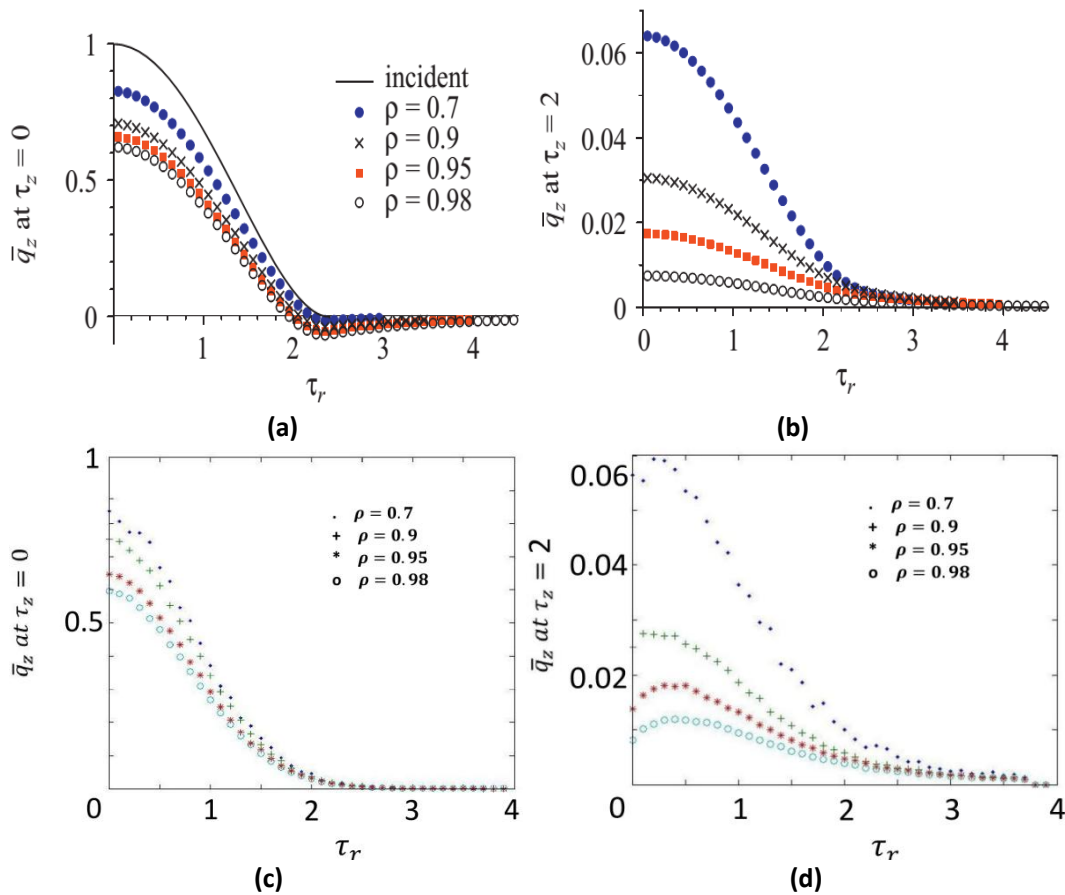


Fig.III-3.10. Comparison of radiative energy distribution in the powder layer with given optical thicknesses $\tau_z=0$ (upper surface) and $\tau_z=2$ (lower surface or bottom) with various single scattering albedo ρ : (a) (b) results of A.V. Gusarov [35]; (c) (d) results of modified MC method.

If we compare the energy distribution at the upper surface ($\tau_z = 0$) and at the bottom ($\tau_z = 2$), the difference of radiation flux distribution is about 75% for $\rho = 0.7$, indicating that the radiative energy is considerably absorbed by the region close to the surface. Both longitudinal energy fluxes at the surface and bottom decreases with increasing the albedo ρ , because of a stronger effect of scattering. Hence, the phenomenon of scattering has a strong effect on the propagation of radiative flux. It is responsible of the energy distribution in laser sintering, and it defines the shape of the energy distribution within the granular medium. It must be exactly estimated, indeed it is a key factor in simulating the laser sintering process and for its optimization.

4. Discrete heat conduction submodel

The SLS process is multiphysical, in which most of phenomena are either purely or partially thermal induced. Given the difference between homogenous medium and granular material (powder bed), it is crucial to develop a thermal conduction model to improve the understanding of SLS process.

4.1. Introduction of granular material

A granular medium is a heterogeneous system made of solid particles with its void filled with fluids (like air and liquid), which behaves differently from any of other standard and familiar forms of matters (solid, liquid and gas). Granular materials are ubiquitous in our daily lives that can be naturally formed (rocks and sands) or fabricated (powders and insulations). Therefore, the range of particle sizes is vast and can be in the range from 10nm (atom size) to 1m (rock size). The granular material plays a very important role in many domains, such as mining, agriculture, civil engineering and pharmaceutical manufacturing.

In the field of pharmaceutical manufacturing, the mixing of granular and powder materials is a vital component. A DEM(Discrete Element Method)-based model was proposed by Bertrand et al. [48] in order to simulate the flow behavior of granular material in mixing systems. In his works, the flow behavior of spherical particles is studied under different types of mixers and blenders.

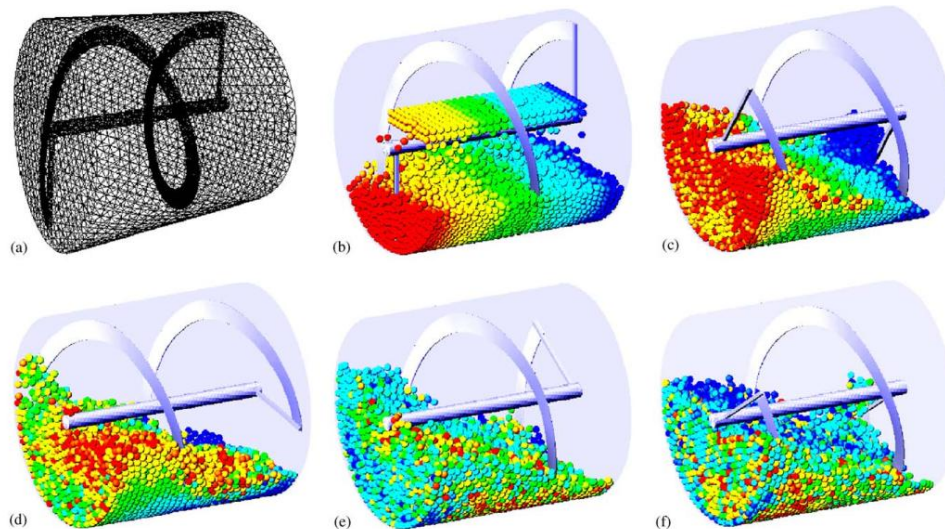


Fig.III-4.1. DEM simulation of the flow of spherical particles in the helical ribbon blender[48]:
(a) triangular discretization of the boundary surfaces; (b) filling step at $t = 0$ s;
(c–f) position of the particles after 1, 2, 5 and 6 s.

4.2. Discrete methods

All numerical methods can be classified into continuous methods and discrete methods. These methods have been used over the years to simulate and solve a large number of mechanical problems at different scales from microscopic to macroscopic [49]. In the case of microscopic, about 10^{-6} m, the interaction between atoms is governed by empirical inter-atomic potentials. The movement of atoms is obtained from classic Newton mechanics. In the mesoscopic scale, about 10^{-4} m, only large scale entities are considered. The interaction between particles is also described by classic Newton mechanics. In case of macroscopic scale, about 10^{-2} m, most physical systems are regarded as continuous material. The physical behavior is described by constitutive laws. Typically, at the macroscopic scale, most of materials can be treated as continuous medium even though they consist of smaller discrete grains. Thus, the continuous methods can be used in this scale without problems. However, in the other three scales, the length of material is at the same order of magnitude of discontinuous space, which causes inappropriate application of continuous methods. Thus, discrete methods are more commonly used in these three

scales.

In general, discrete methods studied materials consisting of a set of discrete elements with different shapes and sizes. These elements interact with each other by contact laws and/or cohesive bonds. Knowing forces and torques applied on the displacements and rotations computed using classic Newton mechanics. The classification and application of discrete methods are given in the coming section.

4.2.1. Classification of discrete methods

According to the scale, the discrete methods can be classified into three groups: quantum mechanical methods (QMMs), atomistic methods (AMs) and mesoscopic methods (MDMs), as shown in Fig.III-4.2.

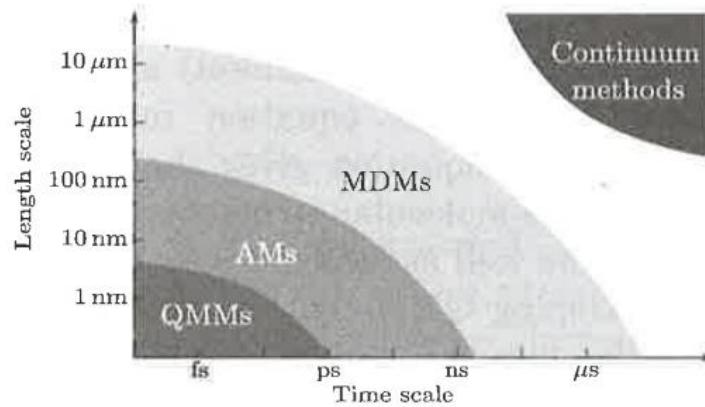


Fig.III-4.2. Characteristic length scales and time scales for numerical methods [49]

Quantum mechanical methods

The scale used by the quantum mechanical methods is about 10^{-9} m. In this scale, the molecules are treated as collections of nuclei and electrons whose interaction is directly controlled by their quantum mechanical state without any reference to chemical bonds. These methods are all based on the Schrodinger equation proposed in 1925 as below [49].

$$\left[-\frac{\hbar}{2m^p} (\nabla^2 + \Phi(r^p, t)) \right] \Psi(r^p, t) = i\hbar \frac{\partial \Psi(r^p, t)}{\partial t}$$

where m^p is the mass of particle, r^p is the position vector of particle, Φ is an external field, ∇^2 is the Laplacian, \hbar is Plank's constant divided by 2π , i is the square root of -1 and Ψ is the wave function which characterizes the particle motion.

In general, the quantum mechanical methods are accurate in modeling particle/electron motions [50,51]. However, the cost of simulations based on these methods is very high. Besides, these methods can be only applied in very small domains of nano-scale.

Atomistic methods

The atomic methods are used for modeling material at the microscopic scale (about 10^{-6} m). In this scale, the electronic motions are ignored. The interaction laws between particles can be described by empirical inter-atomic potentials that encapsulate the effects of bonding between them [52,53]. The Lennard-Jones potential is more practical and realistic in modeling some physical interactions, such as the Van der Waals interaction:

$$\Phi(l_{pq}) = 4\varepsilon \left[\left(\frac{l_m}{l_{pq}} \right)^{12} - 2 \left(\frac{l_m}{l_{pq}} \right)^6 \right]$$

where ε is the depth of the potential well, l_m is the distance at which the potential reaches its

minimum and l_{pq} is the distance between two particles p and q.

Compared to the quantum mechanical methods, the atomic methods are less accurate but relatively inexpensive. These methods are able to simulate the atomic process involving considerably large systems of up to 10^9 atoms [54]. But dynamic simulation based on atomic methods is generally limited to the timescales of a few nanoseconds, which can be a flaw for the simulation of realistic mechanical problems.

Mesoscopic methods (Discrete Elements methods)

In order to overcome limitations of quantum and atomic methods, another discrete method has been developed: mesoscopic discrete methods. The scale used by the mesoscopic mechanical methods is about 10^{-4} m. At this scale, the material is too small to be regarded as a continuum and too large to be simulated effectively using quantum or atomic methods. The mesoscopic scale can be treated as an intermediate scale at which the microscopic phenomena can be assumed in mechanical equilibrium, but cannot be described by continuum mechanics. In these methods, only large scale particles are modeled. Originally, this class of methods (Discrete Elements methods) was firstly developed to model movements within granular materials in rock mechanics [55].

Now, the mesoscopic methods have presented an alternative method to study realistic complex problems, for which continuous assumption is not valid, or problems with discontinuities that cannot easily be treated by continuous methods [49]. In mesoscopic methods, the contact particle method is very commonly used. In this method, elements with masses and volumes are considered to interact through contact laws, as shown in Fig.III-4.3.

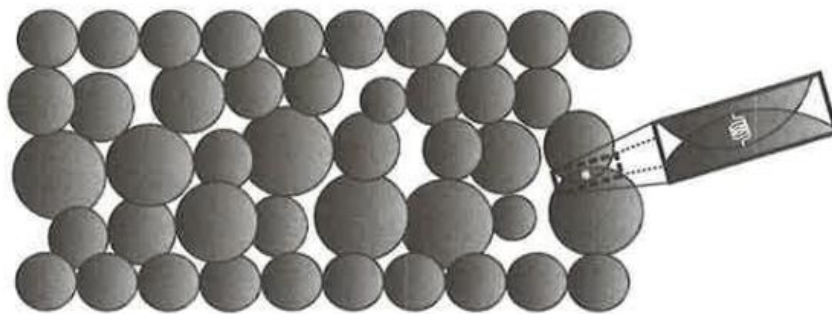


Fig.III-4.3. 2D contact particle model[4]

4.2.2. Applications of Discrete Elements methods (DEM)

As we discussed previously, the Discrete Elements methods (DEM) are widely used in modeling physical phenomena at mesoscopic scale, which is inconvenient for continuous methods. Here, we present several applications of DEM as following.

Heat conduction in granular medium

Unlike in a homogeneous medium, the heat conduction in granular medium, such as powder bed, is defined as the transfer of heat flux through physical contacts of particles, which is strongly dependent on the nature of contact between the particles [56]. The traditional continuum model of heat conduction is not suitable in case of laser sintering process. Vargas and McCarthy [120] has developed a thermal particle dynamic approach for heat conduction in granular medium. They assumed the temperature inside particles remains uniform because the contact thermal resistance between particles is significantly larger than the thermal resistance in the particles. The temperature gradient only exists near the contact points as shown in Fig.III-4.4.

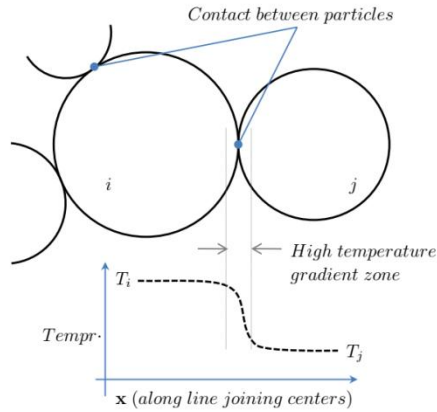


Fig.III-4.4. Schematic of assumed temperature distribution between particles in contact [58]

Under these assumptions, the net heat transferred to a particle due to conduction with its neighbor particles is given by [58]:

$$Q_i = \sum_{j=1}^N C_{ij}(T_j - T_i)$$

where N is the number of neighbor particles in contact with particle i and C_{ij} is contact conductance between the pair ij . The conductance C_{ij} depends on the contact force between the particles, which is obtained using Hertz's theory.

$$C_{ij} = 2\lambda_e \left(\frac{3F_n R_e}{4E_Y} \right)^{\frac{1}{3}}$$

where λ_e is the effective thermal conductivity of the particles. F_n is the normal contact force between particles, R_e is the effective radius of contact pair and E_Y is effective Young's modulus.

This approach has been used by Ram [58] to simulate the heat conduction during selective laser melting process in metallic powder bed as presented in Fig.III-4.5.

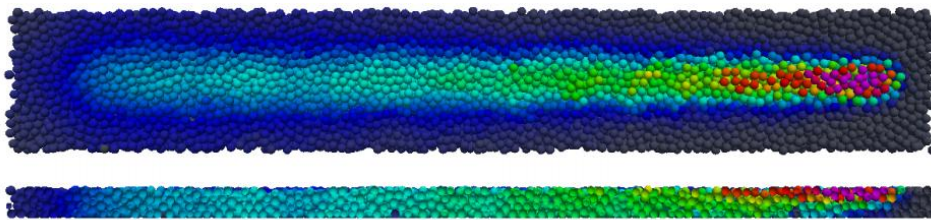


Fig.III-4.5. Temperature evolution of powder bed during selective laser melting process [58]

Thermal Sintering and crack propagation

Nearly all production processes of powder technology include a sintering step at a high temperature [62]. Some of the constitutive sintering models used in the framework of continuum-mechanics were derived from micromechanical models on a grain scale [59,60,61]. These approaches are based on the Taylor–Bishop–Hill assumption [62,63], which states that the velocity of each grain is uniquely prescribed by the macroscopic strain rate. The discrete elements method (DEM) is a promising tool for overcoming the limitations of the Taylor–Bishop–Hill assumption. In contrast to continuum mechanical models, this model offers the advantage that the effect of grain rearrangement are considered by design. It also allows access to mesoscopic properties such as the position, velocity, contact area and coordination number of every grain.

In case of solid state sintering, particles are driven by the sintering force given by polynomial approximations [64]:

$$F_s = \frac{\pi^{\frac{2}{3}} R \gamma_s}{3^{\frac{1}{6}} (1-f)^{\frac{2}{3}}} Y(f, \psi)$$

$$f = 1 - \pi \sqrt{3} (R/d_{ij})^3$$

where $Y(f, \psi)$ is a polynomial function of the porosity f and the dihedral angle ψ . R is the identical radius of particle, γ_s is the specific surface energy and d_{ij} is the mid-point distance between two particles.

Besides the normal sintering force, a tangential force presenting a viscous resistance against sliding is also used[65]:

$$F^t = \eta A ((v_{ij} - v_{ij}^n r_{ij}) + \frac{r_{ij}}{2} \times (\omega_i + \omega_j))$$

where η is the viscosity, A is the grain contact area, v_{ij} is the relative grain-grain velocity, r_{ij} is the unit vector in the direction perpendicular to the contact area.

Henrich et al. [66] used this approach to study the crack propagation during sintering under residual thermal stresses, as shown in Fig.III-4.6. He concluded that the DEM is well suited for treating sintering process and offers many advantages over traditional, continuous-mechanics approaches or analytical models.

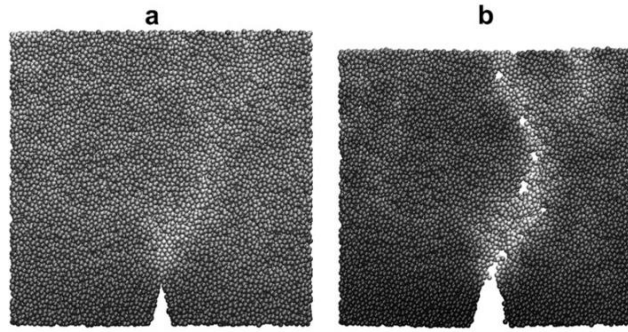


Fig.III-4.6. crack propagation during sintering under residual thermal stresses with a pre-set crack notch: (a) initial and (b) final configuration [66]

Surface tension and wetting effect

At small length scales of the order of nano and micrometers, surface tension plays an important role in free-surface and multiphase flows. In contrast to macroscopic length scales, the influence of inertial forces on the flow is greatly reduced, resulting in greater impact of surface tension forces on the shape and properties of the flow. This effect can be observed in many natural phenomena, such as the wetting of water drops on the leaves of the Lotus plant or in transpiration flow in the xylem tissues in plants. For now, a discrete elements method has been developed, which is more efficient than continuous methods for modeling structure-fluid and fluid-fluid interactions from the nano to macroscopic scales based on the Navier-Stokes (NS) equations.

$$\frac{\partial \rho}{\partial t} = -\rho \nabla v$$

$$\frac{D \nabla v}{Dt} = \frac{1}{\rho} (-\nabla p + \eta \nabla^2 v + F) + g$$

where ρ is fluid density, η is dynamic viscosity, v is velocity and p is pressure, respectively. g corresponds to external body forces such as gravity.

Breinlinger et al. [67] used this approach to simulate the shape variation of water drops caused by surface tension which includes special boundary conditions for fluids in contact with solid walls as shown in Fig.III-4.7. His works shows that the discrete elements method gives accurate results for the solution of the Young-Laplace equation even at comparably low resolutions. Besides, this method is also capable of

reproducing more complex wetting phenomena such as the pinning effect.

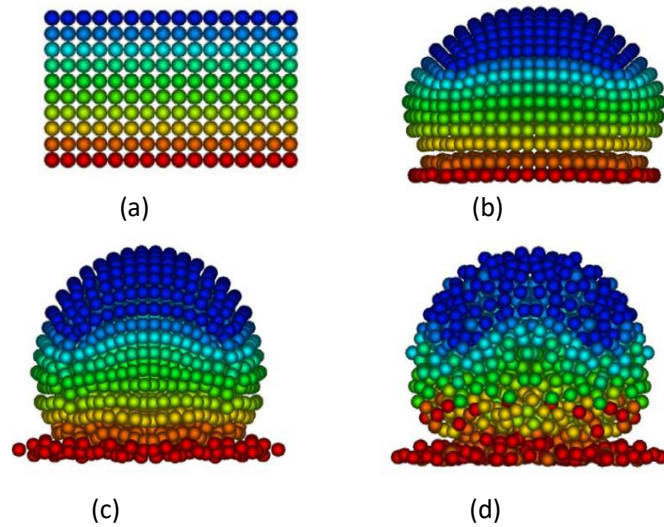


Fig.III-4.7. Evolution of liquid drops on a flat surface at different times [67]:
(a) $t=0$; (b) $t=0.05s$; (c) $t=0.25s$; (d) $t=1.0s$.

4.3. Review of heat conduction model in SLS process

The numerical models of heat conduction for selective laser sintering process can be classified as continuum or discrete based approach, such as the finite elements method (FEM) and discrete elements method (DEM). In continuum approach the granular bed is assumed as a homogeneous medium having effective properties, while these properties are modeled separately or obtained experimentally. On the other hand in discrete particle approach, the packed bed is explicitly modeled and discrete nature of system is taken into account while considering the involved phenomenon.

According to the literatures, most of studies about heat conduction in granular media are proposed by FEM and the powder bed is regarded as equivalent homogenous media: Roberts et al. [68] built a 3D numerical model based on FEM to simulate the temperature distribution in a powder bed. He developed an innovative simulation technique as element birth and death, but, without considering the effect of scattering in participating medium. A SLS process in the metallic powder bed with two components is studied by Chen and Zhang [69]. They developed a 3D model and investigated the shape of heat affected zone inside the powder bed. The accurateness of their work relies on empirical values of thermal properties. However, the variation of density and conductivity are intricate to be measured and predicted during SLS process. Donghua and Dongdong [70] developed a numerical simulation based on finite volume method to study densification mechanisms of WC/Cu powder system during SLS process. They also regarded the powder bed as a homogenous medium and estimated the variation of material properties by empirical equations, resulting in that numerical results are always higher than those from experiments. Fischer et al. [71] proposed a 2D thermal model to predict the instationary temperature distribution in the powder bed, which is treated by periodic laser pulses during SLS process. The influence of pulse frequency on temperature in powder bed is studied, but the phase change of particles is not taken into consideration. Zhang Y.W. et al. [72] developed a 3D thermal model of SLM in a metal powder bed, which contains a mixture of two powders with significantly different melting points. The simulation results based on FEM are compared with the data from experiments. However, local boundaries of sintered areas from actual and predicted results are different, because they underestimated differences between thermal properties of homogenous and granular mediums. Several literatures [73-76] developed complex models based on FEM which coupled multiple phenomena, such as the radiation transfer, heat conduction and sintering. However, the validation and accuracy of their models are based on empirical values of physical properties, which are intricate to be measured and predicted during laser treatment. In Schultz's thesis[77], he built a 3D continuum numerical model of selective laser sintering in the polymer powder bed, including heat transfer, phase change and densification. However, his model is not able to simulate the variation of

volume caused by air evaporation in SLS process.

All literatures above assumed the powder bed as a homogenous medium and estimated the variation of material properties by empirical equations, underestimating the effect of the air between grains in the laser sintering process. In fact, the powder bed is always treated as a homogeneous medium instead of discrete granular system which is an assembly of many discrete solid particles interacting with each other due to dissipative collisions. Numerical models of granular medium based on Finite Element Method (FEM) are born with several limitations: it is not possible to capture the physical phenomena of grains inside powder bed; its accuracy relies on empirical values of material properties which are hard to be measured and predicted during sintering process; it is not able to describe the phenomena of densification caused by the escape of entrapped air bubbles between grains. Compared to the Finite Element method, the discrete elements method (DEM) is particularly useful for modeling phenomena in materials that undergo discontinuous connections, which is possible to capture almost all the physical phenomena linked to the particles interactions and the granular characteristics of the materials. In spite of that, the dedicated heat transfer studies in granular medium for application to laser sintering are rather rare [78].

In view of what we have discussed earlier, we propose a heat conduction model based on the discrete elements method to model the heat conduction in SLS process. This model will be detailed in the following section.

4.4. Discrete heat conduction model in SLS process

The heat conduction in granular medium, such as powder bed, is defined as the transfer of heat flux through physical contacts of particles. The traditional continuum model of heat conduction is not suitable in the case of laser sintering process. Therefore, a discrete model is needed to describe the thermal diffusion inside powder bed. The heat conduction between two elastic particles is illustrated in Fig.III-4.8.

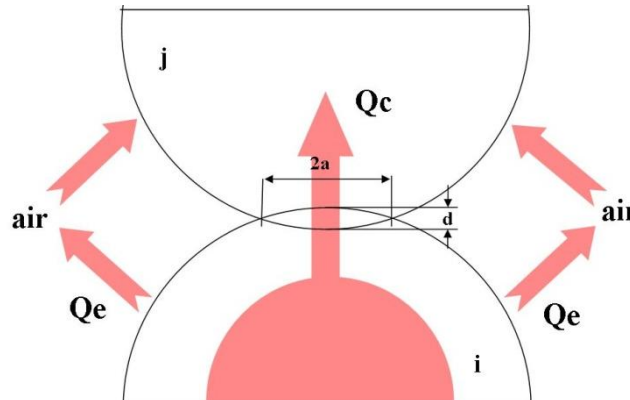


Fig.III-4.8. Heat conduction between two contacted elastic spheres

As shown in Fig.III-4.8, the heat flux consists of two parts: the heat conduction through contact area Q_c and by air Q_e . Therefore, the entire heat flux between two particles i and j is written as below:

$$Q_{ij} = Q_{cij} + Q_{ej} \quad (\text{III-4.1})$$

Given that Q_c is relative to the contact area, Q_c can be given based on the Fourier equation:

$$Q_{cij} = -k_c Area_c \frac{dT_{ij}}{dx} \quad (\text{III-4.2})$$

where $k_c = \frac{2k_i k_j}{k_i + k_j}$ [80] is the harmonic mean of the conductivity of two particles [J/(K·s·m)] and $Area_c = \pi a^2$ is the contact area between two particles [m^2].

Because the size of two particles i and j are very small, usually less than $50\mu m$, we can assume that the thickness of contact region d can be approached by the thickness of thermal conduction:

$$\frac{dT_{ij}}{dx} \approx \frac{\Delta T_{ij}}{d} \quad (\text{III-4.3})$$

Therefore, Eq.(III-4.2) can be modified as:

$$Q_{cij} = -\frac{k_c Area_c}{d} \Delta T_{ij} = H_c \Delta T_{ij} \quad (\text{III-4.4})$$

$$H_c = -\frac{k_c Area_c}{d} = -\frac{\pi k_c a^2}{d} \quad (\text{III-4.5})$$

where $\Delta T_{ij} = T_i - T_j$ [K], H_c is the heat transfer coefficient [J/(K·s)].

According to Hertz contact theory [78], the radius of contact area of two elastic spheres is defined as

$$a = \sqrt{Rd} \quad (\text{IV-4.6})$$

where d is the thickness of contact region, $R = \frac{1}{\frac{1}{R_1} + \frac{1}{R_2}}$ is the effective radius, R_1 and R_2 are radii of two contact spheres, respectively.

Substituting Eq.(III-4.6) into Eq.(III-4.5), the heat transfer coefficient can be modified as:

$$H_c = -\pi k_c \frac{r_i r_j}{r_i + r_j} \quad (\text{III-4.7})$$

where r_i and r_j are the radii of particle i and j respectively.

The heat flux by air Q_e is given by [79]:

$$Q_e = H_e \Delta T_{i,air} \quad (\text{III-4.8})$$

$$H_e = -k_{air} \left[\frac{2\pi \left[1 - \frac{1}{2} \left(\frac{a}{r} \right)^2 \right] (r-a)}{2 - \frac{\pi}{4}} \right] \quad (\text{III-4.9})$$

Where $\Delta T_{i,air} = T_i - T_{air}$, k_{air} is the conductivity of air and r is the radius of particle.

In a multiple contacts model, we assume that each particle shares the same size of area contacted with air. If the particle i is contacted by N particles, the heat flux between particles i and others is modified as below:

$$\sum_{j=1}^N Q_{ij} = N Q_{cij} + Q_e \quad (\text{III-4.10})$$

With the assumption that the temperature within each particle is uniform, the heat conduction between particles in contact is calculated according to equations below:

$$\dot{q}_{pi-pj} = Q_{ij} \quad (\text{III-4.11})$$

$$m_p C_p \frac{dT_{pi}}{dt} = \sum_{cont i-j} \dot{q}_{pi-pj} + \dot{q}_{pisource} + \dot{q}_{piconv} \quad (\text{III-4.12})$$

where m_p is the mass of single particle, $A_{cont i-j}$ is the contact area between particle i and j , $\sum_{cont i-j} \dot{q}_{pi-pj}$ represents the heat conduction by contacts, $\dot{q}_{pisource}$ represents the heat source and \dot{q}_{piconv} is the heat flux corresponding to convection.

4.5. Validation of discrete heat conduction model

Before applying the model to simulate the entire laser sintering process, a validation of the estimated heat conduction within powder bed is needed. Thus, we propose to compare our model's estimations to some results from the literature concerning metallic laser sintering. In this part, we validate the discrete heat conduction model developed in this paper by comparing the results with Ram [58], who proposed a 3D discrete heat conduction model. The SLS process is numerically simulated by a Discrete Elements Method, in order to obtain the temperature field in powder bed. For confirming our model, we proposed

a simulation under the same conditions as Ram [58]. The powder bed consists of stainless steel grains. The properties of powder material is listed in Table.III-2.

Table.III-2. Thermo-physical properties and other parameters used in simulation [58]

Property	Value
Melting point (T_{mp})	1673.0 K
Enthalpy of fusion (H_f)	285.0 kJ · kg ⁻¹
Specific heat (C_p)	500.0 J · kg ⁻¹ · K ⁻¹
Density (ρ)	7800.0 kg · m ⁻³
Thermal conductivity (λ)	40.0 W · m ⁻¹ · K ⁻¹
Emissivity (ϵ)	0.2
Size distribution	mono-dispersed
Grain size	30 μ m
Laser beam size	140 μ m

Considering the phase change during metallic SLS process, the conductive heat transfer equation Eq.(III-4.12) can be modified as:

$$\frac{dH_{pi}}{dt} = \sum_{cont i-j} \dot{q}_{pi-pj} + \dot{q}_{pi source} + \dot{q}_{pi conv} \quad (III-4.13)$$

$$T_{pi} = \begin{cases} \frac{H_{pi}}{m_{pi}C_{spi}}, & H_{pi} \leq m_{pi}C_{spi} * T_m \\ T_m, & m_{pi}C_{spi} * T_m < H_{pi} < m_{pi}C_{spi} * T_m + H_m \\ T_m + \frac{H_{pi}-C_{spi}*T_m-H_m}{m_{pi}C_{lpi}}, & H_{pi} \geq m_{pi}C_{spi} * T_m + H_m \end{cases} \quad (III-4.14)$$

where the volumetric enthalpy H_{pi} is related with temperature T by the thermal equation of phase state. C_{spi} and C_{lpi} are the specific heats in solid and liquid phases, respectively. T_m is the melting point, H_m is the latent heat of melting.

The top view of temperature field in powder bed with different scanning velocity are illustrated in Fig.III-4.9. The temperature history of a certain particle in the laser scan path is shown in Fig.III-4.10. In both Fig.III-4.9 and 4.10, it shows that results of our simulations are in good agreement with that from Ram [58]. In Fig.III-4.10, the scan velocity of 0.6 m/s, with a power of 50 W, is sufficient to melt the particles in the laser scan path to form a continuous melted track. The peak temperature in powder bed is about 2000K, which is significantly above the melting point. The temperature history of a certain particle in the scan path with different power is shown in Fig.III-4.10. The results show that increasing power will raise up the peak temperature of particles, which is mutually opposite with the observed trends from Fig.III-4.10 when increasing the scan velocity. This suggests that the ratio between the power and scan speed can play an important role to characterize thermal behavior of heated particles in powder bed.

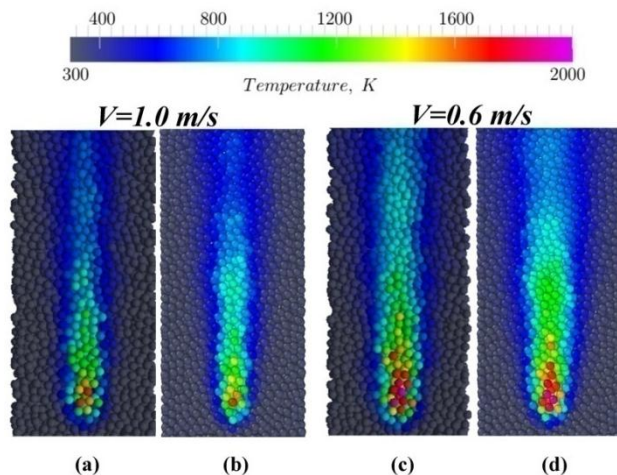


Fig.III-4.9. Temperature distribution in powder bed for increasing scan speed at P = 50 W: (a)(c) Results from Ram [58]; (b)(d) Results from our simulations.

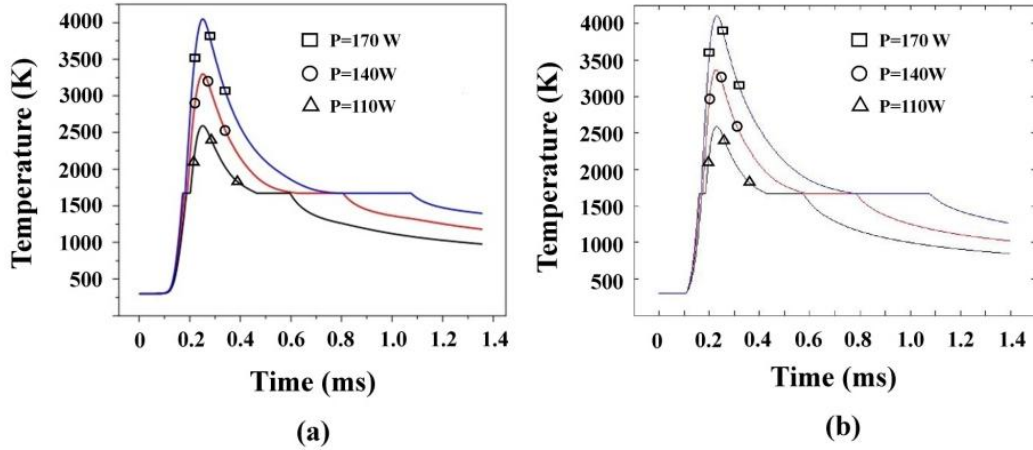


Fig.III-4.10. Temperature history of a particle in the laser scan path: (a) Results from Ram[58]; (b) Results from our simulations.

4.6. Phase change and boundary conditions

Due to differences between thermal properties of metal and polymer, both Eq.(III-4.13) and Eq.(III-4.14) are not suitable to describe the process of phase change in polymer powder bed. But the mechanism of heat conduction by contacts is effective in the case of polymer. Therefore, we can modify Eq.(III-4.13) and take into account the variation of thermal properties during phase change of polymer:

$$m_p C_p^* \frac{dT_{pi}}{dt} = \sum_{cont i-j} \dot{q}_{pi-pj} + \dot{q}_{pi source} + \dot{q}_{pi conv} \quad (III-4.15)$$

The modified heat capacity integrating solid-liquid phase transformation C_p^* is given as following [9]:

$$C_p^* = C_p(T) + \frac{\Delta H_m}{\sqrt{\pi(T_{mf}-T_{ms})^2}} \exp\left(-\frac{(T-T_{ms})^2}{(T_{mf}-T_{ms})^2}\right) \quad (III-4.16)$$

where T_{ms} and T_{mf} are the temperatures of melting onset and end respectively, H_m is the latent heat of melting and $C_p(T)$ is considered as a constant.

Besides, the heat conductivity k and density ρ of a single particle are also determined by its phase:

$$k = \begin{cases} k_s & \text{if solid} \\ k_l & \text{if liquid} \end{cases} \quad \rho = \begin{cases} \rho_s & \text{if solid} \\ \rho_l & \text{if liquid} \end{cases} \quad (III-4.17)$$

At the powder upper surface, the energy lost by the radiation and convection can be expressed as below[5]:

$$-k \frac{\partial T}{\partial z} |_{surf} = h(T_a - T|_{surf}) + \varepsilon_R \sigma (T_a^4 - T|_{surf}^4) \quad (III-4.18)$$

where T_a is the ambient temperature, h is the convective heat transfer coefficient, ε_R is the surface emissivity of the material, σ is the Stefan-Boltzmann constant and k is the thermal conductivity.

At the bottom of the powder bed, the boundary condition satisfies the requirement that no heat is lost through the bottom of the powder bed:

$$-k \frac{\partial T}{\partial z} |_{bottom} = 0 \quad (III-4.19)$$

5. Sintering submodel

During the SLS process, selected regions of the powder bed are rapidly heated through a phase transition of solid-liquid-solid state, which is called the sintering phenomenon. Now, it is well known that the performance of product from SLS is highly related to the degree of sintering [6-8]. In order to predict the degree of sintering, it is important to develop a sintering model.

5.1. Generalities of sintering

Sintering is a heat treatment that can transfer one material from the state of powder to a solid material. The treatment takes place at the temperature when all the ingredients of the powder remains in the solid state. The consolidation is realized by the growing of the contact area between particles due to molecular diffusion. The driving force is the large interfacial energy of the system powder. Like the system tends to move to a state with lower energy, the interfaces with more energy, such as solid-gas type, are reduced to those with lower energy as solid-solid type. At the thermodynamic equilibrium, two particles are converted into one single spherical particle, as the illustration in Fig.III-5.1.

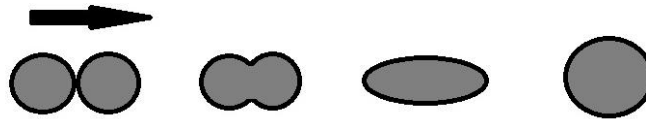


Fig.III-5.1. Schematic evolution of two spheres sintering

In the following paragraphs, we will describe the basics of the sintering in solid/liquid phase, including the variation of interface energy, mechanisms of transportation and different stages of the microstructure evolution.

5.1.1. Interfacial energy and superficial tension

The stress required for separating two media (solid, liquid or gas) is known as the surface tension. In the case of solid phase sintering, the energy consists of a contribution of solid-gas interfaces with an area of S_{sg} and interfacial free energy γ_{sg} , also a contribution of solid-solid interfaces with an area of S_{ss} and interfacial free energy γ_{ss} [81].

$$E = \gamma_{sg}S_{sg} + \gamma_{ss}S_{ss} \quad (\text{III-5.1})$$

When two surfaces are intersected, a stress will be exerted along the line of intersection. The stress imposes an equilibrium contact angle, as shown in the Fig.III-5.2. In the case that surfaces are associated with different states (either solid- liquid - gas), the equilibrium angle is known as the wetting angle and satisfies the following equation:

$$\gamma_{sg} = \gamma_{sl} + \gamma_{lg} \cos \theta_e \quad (\text{III-5.2})$$

where γ_{sg} , γ_{sl} and γ_{lg} are interfacial tension of solid-gas, solid-liquid and liquid-gas respectively. When γ_{sg} is much larger than the summary of γ_{sl} and γ_{lg} , the equilibrium is impossible and the liquid will flow on the surface of solid.

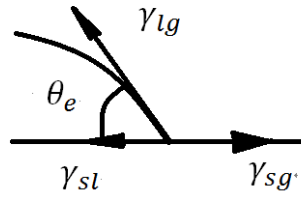


Fig.III-5.2. Equilibrium contact angle in three phases

Similarly to the sintering in solid phase, at the intersection of three surfaces, two solid grains into contact with a gaseous phase, it may define a dihedral angle Ψ_e balance as shown in Fig.III-5.3:

$$\gamma_{ss} = 2\gamma_{sg} \cos (\Psi_e/2) \quad (\text{III-5.4})$$

When γ_{ss} is larger than $2\gamma_{sg}$, the equilibrium is impossible and it cannot form the grain's joint, that is to say the natural sintering system is impossible.

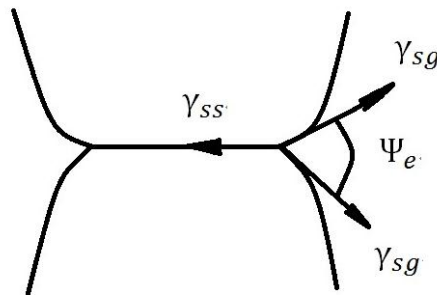


Fig.III-5.3. Equilibrium of sintering in solid phase[81]

The consolidation of ceramic is mostly caused by sintering in solid phase [81]. But the liquid sintering is dominant in the SLS process. Although the coalescence of molten grains is contributed by the surface tension between solid-liquid-gas interfaces, the precise modeling is difficult and costs lots of computational source [128,129]. In order to simulate the sintering process in case of massive grains, many researchers proposed simplified models that replace the surface tension by sintering angle or sintering force [83,85-89]. These simplified models will be introduced in this chapter.

5.1.2. Stages of sintering

The reduction of system interfacial energy during sintering is related to the growth of neck joining particles in thermodynamic equilibrium, which causes a micro-structural evolution. According to the formation of porosity, the sintering has been divided into three stages by Coble et al. [82]. In the initial state of sintering, particles are assumed to be in point contact. The three stages of sintering are shown in Fig.III-5.4.

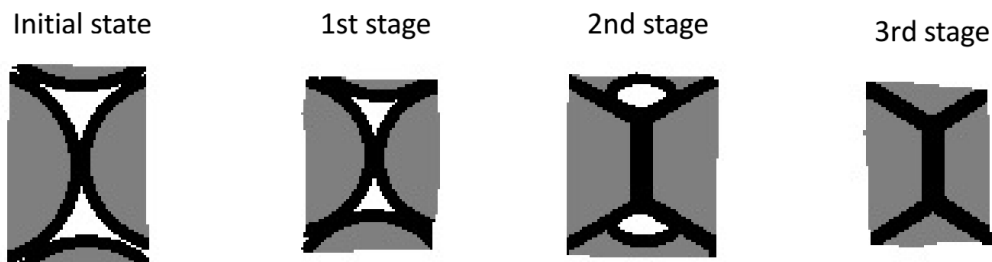


Fig.III-5.4. Three evolution stages of sintering [82]

The first stage of sintering is related to the formation and growth of necks between particles. In the second stage, the volume of the network of pores is reduced gradually. Finally, during the third stage, the spherical and isolated pores are eliminated.

1st stage of sintering

The first stage of sintering is normally completed during the heating period, before reaching the melting temperature of particles. During this stage, contacts between the particles are expanding and necks begin to grow. The growth of necks reduces the interfacial energy more than 50%. The first stage ends when the ratio of the contact radius to particle radius is about 0.3 for particles with the same size. But it could also be determined by considering other parameters such as the pressure, the area of the free surface or density.

2nd stage of sintering

The second sintering stage is particularly associated with the densification and enlargement of grains. At the end of the second stage, pores become spherical and are mainly located in the periphery grain boundaries. The elimination of small grains causes coalescence of pores progressively being attached to the corners of the grain boundaries. The growth of large pores depends on the smaller ones which uses the grain boundaries as transport paths.

3rd stage of sintering

The third stage of sintering begins when the boundary is closed, approximately when the porosity falls to 8%. Pores continue to be filled by the transporting material from the grain boundaries or center of the grain. The third stage is relatively slow compared to previous stages. There may be a phenomenon of separation between pores and grain boundaries.

5.1.3. Driving force and basic phenomena

The driving force of sintering is the reduction of the total interfacial energy. The total interfacial energy of a powder compact is expressed as γA , where γ is the specific surface (interface) energy and A is the total surface area of the compact. The reduction of the total energy can be expressed as [81]

$$\Delta(\gamma A) = \Delta\gamma A + \gamma \Delta A \quad (\text{III-5.5})$$

The variation of interfacial energy $\Delta\gamma$ is due to the densification and the change of interfacial area ΔA is relative to the coalescence. In other words, there are two main phenomena in the sintering process: ***Coalescence*** and ***Densification***.

5.2. Basic of coalescence

5.2.1. Mechanisms of coalescence

Reduction of interfacial energy is achieved by mass transportation at contacts, where necks between particles form. The mechanisms of sintering are generally classified into 4 categories: viscous model, viscous-elastic model and grain diffusion model.

Shrinking cube model

The theory of viscous sintering was explored by Frenkel. The primary concept of his theory is the balance of energy between the work done by surface tension P_t and viscous dissipation P_v during the particle deformation [83]:

$$P_t = P_v \quad (\text{III-5.6})$$

$$P_t = - \int_S \Gamma \frac{dS}{dt} dS \quad (\text{III-5.7})$$

$$P_v = \int_V \tau : DdV \quad (\text{III-5.8})$$

where V is the volume of the sintering system, S is the surface of the sintering system, D is the deformation tensor, τ is the stress and Γ is the surface tension

Based on Frenkel theory, Sun et al. [84] built a sintering model for powder bed under the assumption that the unit cell is spherical and regarded as incompressible Newton fluid. The unit cell and the densification process of a cubic pack structure are illustrated in Fig.III-5.5.

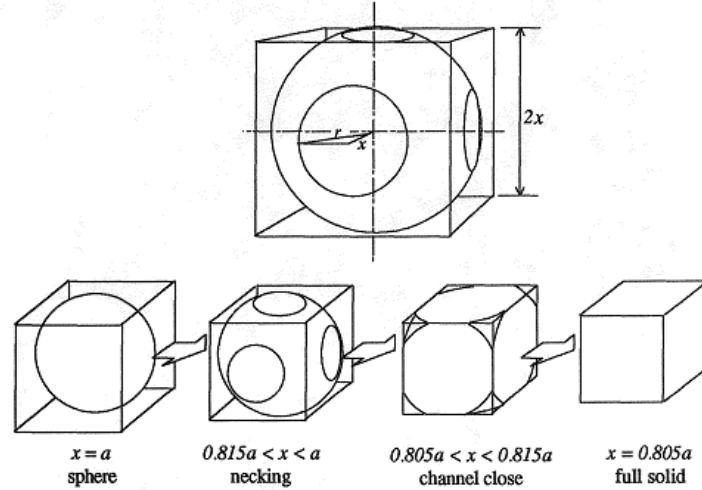


Fig.III-5.5. The unit cell and the densification process of a cubic pack structure [84]

During the densification process, the volume of sphere is conservative:

$$V_a = \frac{4\pi}{3} a^3, \quad V_x = \frac{4\pi}{3} r^3 - 6 * \left(\frac{\pi}{3} x^3 - \pi r^2 x + \frac{2\pi}{3} r^3 \right)$$

$$V_a = V_x$$

Therefore, the x and r satisfy the equation as below:

$$3x^3 - 9r^2x + 4r^3 + 2a^3 = 0 \quad (\text{III-5.9})$$

A critical point in the densification process is when $r = \sqrt{2}x$, where the flat circular area on each side of the cell connect, in other words the channels connecting the void space between the particles close, and the voids are separated. The value of x at this point is $0.8156a$.

After x becomes less than $0.8156a$, the isolated void keeps decreasing in its size until $x = 0.805a$ at which time the void vanishes and the structure becomes full solid. The volume conservation does not hold in this period since the contact area between two particles is not an exact circle.

For a sintered particle, the contact area vanishes and the remained surface area of the deformed particle in a unit cell is as below:

$$A_S = 12\pi r x - 8\pi r^2 \quad (\text{III-5.10})$$

For an unsintered particle, the contact area remains as a boundary between particles, and the surface area of the deformed particle is as following:

$$A_U = 12\pi r x - 2\pi r^2 - 6\pi x^2 \quad (\text{III-5.11})$$

Now we define a factor ξ as the function of sintered particles. ξ ranges between 0 and 1. When no sintering occurs between particles $\xi = 0$.

With the factor ξ , the effective surface area of a partially sintered particle is

$$A = \xi A_S + (1 - \xi) A_U \quad (\text{III-5.12})$$

Under this assumption, Sun simplified Frenkel's energy balance equation as following[84]:

$$\gamma \dot{A} + \eta_b \dot{\varepsilon}^2 V = 0 \quad (\text{III-5.13})$$

where γ is the surface tension of the material, η_b is the bulk viscosity of the porous structure, $\dot{\varepsilon}$ is the volumetric strain rate of the structure and V is the volume of the unit cell.

The surface area rate \dot{A} can be derived from Eq.(III-5.12) as following

$$\dot{A} = 12\pi(\dot{r}x + x\dot{r}) - 2(6\xi + 2)\pi r\dot{r} - 12(1 - \xi)\pi x\dot{x} \quad (\text{III-5.14})$$

In Eq.(III-5.14), the bulk viscosity η_b is a function of the viscosity of the material and the relative density. Skorohod's model directly relates viscosity η_b to the relative density ρ .

$$\eta_b = \frac{4\eta\rho^3}{3(1-\rho)} \quad (\text{III-5.15})$$

where $\rho = \frac{\pi a^3}{6x^3}$.

The volumetric strain of the unit cell is by definition

$$\varepsilon = 3\left(1 - \frac{x}{a}\right) \quad (\text{III-5.16})$$

Substituting Eq.(III-5.12,13,15,16) into Eq.(III-5.14), the final sintering rate equation can be derived as

$$\dot{x} = -\frac{\pi\gamma a^2}{6\eta_b x^3} \left\{ r - (1 - \xi)x + \left[x - \left(\xi + \frac{1}{3} \right) r \right] \frac{9(x^2 - r^2)}{18rx - 12r^2} \right\} \quad (\text{III-5.17})$$

Viscous coalescence model

Frenkel's model has been used by many researchers in describing the kinetics of Newtonian sintering. However the model is valid only in the early stage of sintering. Pokluda et al. [85] developed a sintering model using a similar approach to that of Frenkel and Eshelby but considering the variation of the particle radius with time. The following equation can be easily obtained based on the conservation of volume:

$$V_0 = V_t \quad (\text{III-5.18})$$

$$V_0 = \frac{4\pi}{3} r_0^3 \quad (\text{III-5.19})$$

$$V_t = \frac{4\pi}{3} r^3(t) - \left[\frac{2\pi}{3} r^3(t)(1 - \cos\theta) - \frac{\pi}{3} r^3(t)\cos\theta\sin^2\theta \right] \quad (\text{III-5.20})$$

$$r(t) = r_0 \left(\frac{4}{(1 + \cos(\theta(t)))^2 (2 - \cos(\theta(t)))} \right)^{1/3} \quad (\text{III-5.21})$$

Thus, the total surface of particles varies with the angle θ according to the following formula

$$S = 4\pi r^2(1 + \cos(\theta)) = \frac{8\pi r_0^2 2^{1/3}}{(1 + \cos(\theta))^{5/3} (2 - \cos(\theta))^{2/3}} \quad (\text{III-5.22})$$

From Frenkel's theory, the sintering rate equation is derived from the energy balance equation that the surface energy reduction rate is equal to the viscous dissipation rate during the deformation. For each unit cell, the equation is

$$W_s = W_v \quad (\text{III-5.23})$$

$$W_s = - \int_S \Gamma \frac{dS}{dt} dS \quad (\text{III-5.24})$$

$$W_v = \int_V (\tau : D) dV \quad (\text{III-5.25})$$

where W_s represents the work done by surface tension and W_v represents viscous dissipation of energy during the particle deformation, respectively.

$$D = \frac{1}{2}(\nabla u + (\nabla u)^T) \quad (\text{III-5.26})$$

$$\text{Where } \nabla u = \begin{bmatrix} 2\dot{\epsilon} & 0 & 0 \\ 0 & -\dot{\epsilon} & 0 \\ 0 & 0 & -\dot{\epsilon} \end{bmatrix}$$

And the extra-stress tensor of Newtonian fluid can be defined as follows:

$$\tau = 2\eta D \quad (\text{III-5.27})$$

Consequently, substituting Eq.(III-5.26,27) into Eq.(III-5.25), the surface energy reduction can be written as follows:

$$W_V = \int_V 12\eta\dot{\epsilon}^2 dV \quad (\text{III-5.28})$$

Following Frenkel, the strain rate is approximated by

$$\dot{\epsilon} = \frac{\partial u_x(A)}{\partial x} \approx \frac{u_x(A) - u_x(0)}{a} \quad (\text{III-5.29})$$

Where $u_x(A)$ is the velocity with which point A moves towards point O. The term $u_x(0)$ is the velocity of the fluid at the plane of contact of the two particles and is equal to zero. The term $u_x(A)$ is defined as follows

$$u_x(A) = \frac{d}{dt}(r\cos(\theta)) = -\frac{2^{5/3}r_0\sin(\theta)}{(1+\cos(\theta))^3(2-\cos(\theta))^{4/3}}\dot{\theta} \quad (\text{III-5.30})$$

Consequently,

$$\dot{\epsilon} = \frac{u_x(A)}{r_0} = \frac{2^{2/3}r_0\sin(\theta)}{(1+\cos(\theta))^3(2-\cos(\theta))^{4/3}}\dot{\theta} \quad (\text{III-5.31})$$

And the formula of dissipated energy is

$$W_V = \frac{32\pi r_0^3 \eta (1-\cos(\theta))}{(1+\cos(\theta))(2-\cos(\theta))^2} (\dot{\theta})^2 \quad (\text{III-5.32})$$

The work of surface tension W_s is defined as

$$W_s = -\Gamma \frac{dS}{dt} \quad (\text{III-5.33})$$

where Γ is the coefficient of surface tension and S is the surface of the sintering system.

Modifying Eq.(III-5.22), the term $\frac{dS}{dt}$ can be derived

$$\frac{dS}{dt} = \frac{dS}{d\theta} \frac{d\theta}{dt} = -\frac{8\pi r_0^2 2^{1/3} \sin(\theta) \cos(\theta)}{(1+\cos(\theta))^{4/3} (2-\cos(\theta))^{5/3}} \dot{\theta} \quad (\text{III-5.34})$$

Thus the expression for the work of surface tension becomes

$$W_s = \Gamma \frac{8\pi r_0^2 2^{1/3} \sin(\theta) \cos(\theta)}{(1+\cos(\theta))^{4/3} (2-\cos(\theta))^{5/3}} \dot{\theta} \quad (\text{III-5.35})$$

After some manipulations, Pokluda et al.[85] obtained

$$\theta' = \frac{\Gamma}{\eta r_0} \frac{2^{-\frac{5}{3}} \cos(\theta) \sin(\theta) (2 - \cos(\theta))^{1/3}}{(1 - \cos(\theta))(1 + \cos(\theta))^{1/3}} \quad (\text{III-5.36})$$

With the initial condition

$$\theta(0) = 0 \quad (\text{III-5.37})$$

The evolution of the sintering neck radius with time is given by

$$\frac{h}{r} = \sin(\theta) \quad (\text{III-5.38})$$

Viscoelastic coalescence model

The present viscoelastic sintering model is based on Frenkel's approach [83] and its subsequent correction by Eshelby et al. [86] and modification by Pokluda et al. [85]. The convected Maxwell constitutive equation is used to introduce viscoelastic behavior in the description of the sintering process.

The convected Maxwell model can be written as follows:

$$\lambda \dot{\tau} + \tau = 2\eta D \quad (\text{III-5.39})$$

Where λ is defined as the material relaxation time and $\dot{\tau}$ represents a general form of the invariant derivative of the extra-stress tensor:

$$\dot{\tau} = \frac{D\tau}{Dt} - \omega \cdot \tau + \tau \cdot \omega - \alpha(D \cdot \tau + \tau \cdot D) \quad (\text{III-5.40})$$

where $\frac{D\tau}{Dt}$ is the substantial derivative of the extra-stress tensor and ω is the rotational tensor. α corresponds to the upper, lower and co-rotational derivative for values α equal to -1, 1 and 0, respectively.

The flow field in the sintering system is defined to be extensional and the rotational tensor ω is therefore equal to zero. Assuming quasi-steady state flow as a first approximation:

$$\tau + \lambda \alpha (D \cdot \tau + \tau \cdot D) = 2\eta D \quad (\text{III-5.41})$$

The principal components of the extra-stress tensor can be defined as

$$\tau_{xx} = \frac{-4\eta \dot{\epsilon}}{1 - 4\alpha \lambda \dot{\epsilon}} \quad (\text{III-5.42})$$

$$\tau_{yy} = \tau_{zz} = \frac{2\eta \dot{\epsilon}}{1 - 4\alpha \lambda \dot{\epsilon}} \quad (\text{III-5.43})$$

Thus, the work of viscous forces W_v can be expressed as

$$W_v = \iiint_V \tau : D dV = \frac{32\pi a_0^3 \eta \dot{\epsilon}^2}{(1 - 4\alpha \lambda \dot{\epsilon})(1 + 2\alpha \lambda \dot{\epsilon})} \quad (\text{III-5.44})$$

For the initial stage of sintering ($a = a_0$) the strain rate and the work of the surface tension can be defined as follows, as proposed by Frenkel et al. [83] and Eshelby et al. [86]:

$$\dot{\epsilon} = \frac{1}{4} (\theta^2)' \quad (\text{III-5.45})$$

$$W_s = 2\Gamma \pi a_0^2 (\theta^2)' \quad (\text{III-5.46})$$

where $(\theta^2)'$ is defined as $\frac{\partial \theta^2}{\partial t}$. The energy dissipated by viscous flow is balanced by the energy from the reduction of the surface.

Without the assumption that $a = a_0$, a non-linear differential equation is obtained by equating the energy dissipated by viscous flow, as described in Eq.(III-5.44). Substituting Eq.(III-5.42,43) into Eq.(III-5.44)

with some manipulations, a non-linear differential equation is obtained by the balance of energies dissipated:

$$8(\alpha\lambda K_1\theta')^2 + \left(2\alpha\lambda K_1 + \frac{\eta\alpha_0 K_1}{\Gamma K_2}\right)\theta' - 1 = 0 \quad (\text{III-5.47})$$

Where

$$K_1 = \frac{\sin(\theta)}{(1 + \cos(\theta)(2 - \cos(\theta)))}$$

$$K_2 = \frac{2^{-5/3} \cos(\theta) \sin(\theta)}{(1 + \cos(\theta))^{4/3} (2 - \cos(\theta))^{5/3}}$$

A numerical solution for θ is obtained from Eq.(III-4.48). The initial boundary condition is fixed as Eq.(III-5.37).

After some manipulations, a quadratic expression in term of $(\theta^2)'$ is obtained, and with the assumption that $(\theta^2)'$ is always positive, which is also well known as Bellehumour Law:

$$\frac{d(\theta^2)}{dt} = \frac{-\alpha\lambda - 2\frac{\eta\alpha_0}{\Gamma} + [(3\alpha\lambda)^2 + 4\alpha\lambda\frac{\eta\alpha_0}{\Gamma} + 4(\frac{\eta\alpha_0}{\Gamma})^2]^{1/2}}{2(\alpha\lambda)^2} \quad (\text{III-5.48})$$

where $\sin(\theta) = h/r$ is the sinter angle, h is the radius of sintering neck, r is the radius of particle, λ is defined as the relaxation time, η is the viscosity, Γ is the surface tension, the value α is equal to -1, 1 and 0, corresponding to the upper, lower and co-rotational derivative, respectively.

Grain-Boundary diffusion model

D. Bouvard and R.M. McMeeking [87] developed a grain-boundary diffusion sintering model to simulate the coalescence of metal and polymer powders under certain conditions.

A plane, circular join between two identical particles of initial radius R is considered as shown in Fig.III-5.6. The system is axially symmetric about the axis perpendicular to the neck.

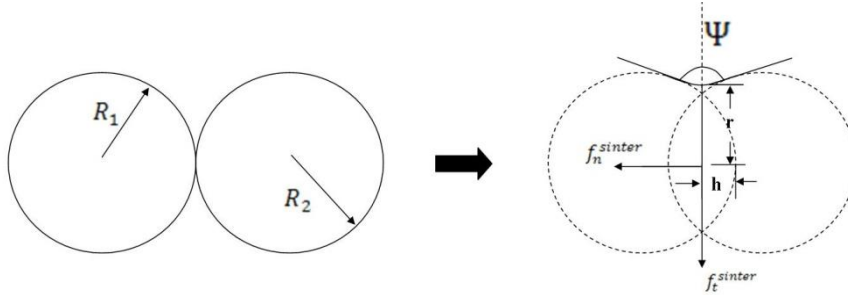


Fig.III-5.6. Schematic of two particles contact [87]

The gradient of chemical potential in the neck, which is treated as a grain boundary, results in a diffusion flux. The classical analysis of Johnson[88] shows that at the edge of the neck, the flux feeding the surface diffusion is:

$$j_r(r) = \frac{4D_g\Omega}{rkT} \left[\sigma + \gamma_s K(r) - 2\frac{\gamma_s}{r} \sin\left(\frac{\Psi}{2}\right) \right] \quad (\text{III-5.49})$$

where $j_r(r)$ is the volume of material passing out of the grain boundary at r through unit area in unit time, D_g is the diffusivity in the grain boundary, Ω is the atomic volume, k is the Boltzmann's constant, T is the absolute temperature, σ is the average compressive stress on the neck, γ_s is the energy of the free surface and $K(r)$ is the sum of the principal curvatures at the edge of the neck. Curvature is defined to be positive when the center of curvature is outside of the particle. The total volume of material delivered to the edge of the neck in unit time is $2\pi r\delta_g j_r(r)$ where δ_g is the thickness of the grain boundary. The shrinkage rate \dot{w} can be expressed as

$$\dot{w} = \delta_g \frac{j_r(r)}{r} \quad (\text{III-5.50})$$

Defining V_n as the velocity of approach of one particle toward the other.

$$V_n = 2\dot{w} = \frac{8D_b}{r^2} [\sigma + \gamma_s K(r) - 2 \frac{\gamma_s}{r} \sin(\frac{\Psi}{2})] \quad (\text{III-5.51})$$

where $D_b = \frac{D_g \delta_g \Omega}{kT}$ is the effective grain boundary diffusivity.

The sum of the curvatures is expressed as

$$K(r) = -\frac{1}{s} + \frac{1}{r} \sin \frac{\Psi}{2} \quad (\text{III-5.52})$$

where s is the radius of free surface curvature in the meridional plane just at the edge of the grain boundary. Coble et al. [82] assumed that two particles can be modeled as intersecting spheres jointed by neck segments with constant s meeting at a dihedral angle Ψ . When $s \leq r \leq R$, preservation of volume to first order gives

$$\frac{1}{s} = \frac{4R[1 - \cos \frac{\Psi}{2}]}{r^2} \quad (\text{III-5.53})$$

Substituting Eq.(III-5.52,53) into Eq.(III-5.51), the approach velocity can be written as

$$V_n = \frac{8D_b}{r^2} \sigma - \frac{8D_b \gamma_s}{r^4} [4R \left(1 - \cos \frac{\Psi}{2}\right) + r \sin \left(\frac{\Psi}{2}\right)] \quad (\text{III-5.54})$$

The average compressive stress on the neck σ is defined by the normal force on the inter-particle grain boundary.

$$\sigma = \frac{f_n^{sinter}}{\pi r^2} \quad (\text{III-5.55})$$

Combining Eq.(III-5.54) and (III-5.55), we can finally get the expression of normal sintering force:

$$f_n^{sinter} = \frac{\pi r^2}{8D_b} V_n - \pi \gamma_s [4R \left(1 - \cos \frac{\Psi}{2}\right) + r \sin \left(\frac{\Psi}{2}\right)] \quad (\text{III-5.56})$$

As the neck grows, particles are not free to slide. Thus, a tangential force, opposed to sliding has to be implemented. Swinkels and Ashby[89] showed that when sliding resistance is driven by diffusion, this can be expressed as a viscous force, proportional to the sliding velocity. Hence, the tangential force is given as below:

$$f_t^{sinter} = -\eta \frac{\pi r^2 R^2}{8D_b} V_t \quad (\text{III-5.57})$$

where η is the viscosity, V_t is the tangential velocity and $R = R_1 R_2 / (R_1 + R_2)$ as the equivalent radius for two particles of radius R_1 and R_2 .

Bouvard and McMekking[87] have simplified the normal and tangential sintering force for the numerical calculation convenience:

$$f_n^{sinter} = \frac{\pi r^4}{2\beta D_b} V_n - \frac{\alpha}{\beta} \pi R \gamma_s \quad (\text{III-5.58})$$

$$f_t^{sinter} = -\eta \frac{\pi r^2 R^2}{2\beta D_b} V_t \quad (\text{III-5.59})$$

The parameters α and β should depend on the ratio of the grain-boundary diffusion to the surface diffusion:

$$\xi_d = \frac{\delta_b D_b}{\delta_s D_s} \quad (\text{III-5.60})$$

The numerical simulations on pairs of particles of Bouvard are well fitted with $\beta = 4$ for all values of ξ_d and with $\alpha = 9/2$ for $\xi_d = 2$, $\alpha = 3$ for $\xi_d = 0.2$ and $\alpha = 5/2$ for $\xi_d = 0.02$. Bouvard and McMeeking have shown that the value of the dihedral angle has only a limited effect on α and β .

5.2.2. Coalescence of polymer powder bed during SLS process

5.2.2.1. Coalescence of fusion polymer grains

Unlike the Newtonian fluid as water, the coalescence of fusion polymer grains is very different due to their distinguishing rheological properties. The isothermal coalescence of two PVDF grains was observed by Tcharkhtchi [90]. The process takes more than 180s from melting of grains into a larger one, as shown in Fig.III-5.7.

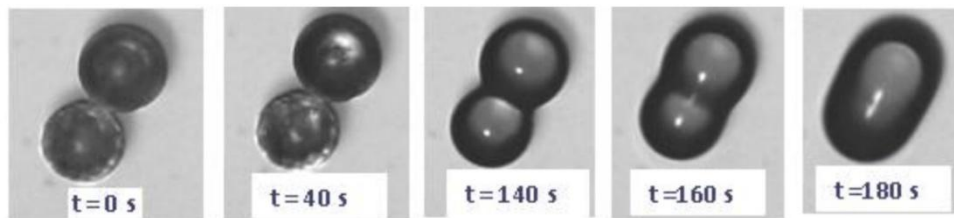


Fig.III-5.7. Different steps of coalescence of two PVDF grains [90]

However, the SLS process is not isothermal. According to the work of Schultz [91] who simulated the temperature evolution of PEEK powder bed, the grains lasts less than 1s in the molten state as shown in Fig.III-5.8. Compared to the isothermal coalescence in Fig.III-5.7, the effective time of coalescence of polymer grains is very insufficient in SLS process.

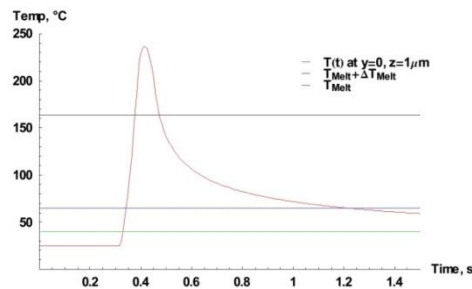


Fig.III-5.7. Temperature as a function of time predicted by laser heat source and two relevant transition temperature [91]

Based on the discussion of section III-5.1.2, the coalescence process can be regarded as the first stage of sintering, in which contact areas between grains are expanding and necks begin to grow. The lack of effective time of coalescence will constrain the growing of necks and expanding of contact areas, finally resulting in a high porosity of product. Therefore, an extra post-processing is required in case of the SLS process in polymer powder bed [19]: it is necessary to maintain the chamber temperature higher than crystallization temperature for hours after laser scanning, so as to guarantee enough time for sintering.

5.2.2.2. Non-isothermal coalescence during SLS process

The SLS process is a non-isothermal process. Therefore, the coalescence process can be divided into four stages (from thermal behavior point of view) as illustrated in Fig.III-5.9.

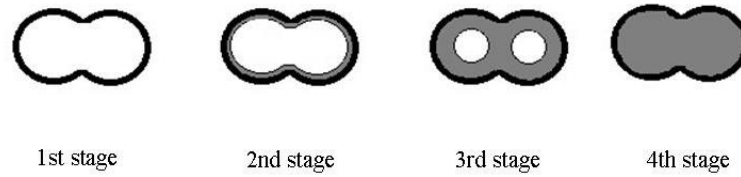


Fig.III-5.9. Illustration of four stages of non-isothermal coalescence

The first stage

In the first stage, the temperature of particles is above the melting temperature T_m^0 . In other words, there is no crystallization phenomenon in this stage. The mechanism of growth rate of neck radius is the same with the isothermal coalescence with the temperature above T_m^0 .

The second stage

At this stage, the temperature of particles begins to decrease below T_m^0 . That means there is possible crystallization phenomenon at this stage. It is naturally assumed that the grain begins to crystallize from the surface of particle. The liquid part of particle still obeys the viscous sintering model. Because the crystallinity is very small at the beginning, the crystallization has little effect on the coalescence process. Therefore, the mechanism of growth rate of neck radius is the same with that in the first stage.

The third stage

In this stage, the temperature of particles is much lower than T_m^0 . The volume of crystallized part grows larger. Meanwhile, there is no relative movement between the two particles. The coalescence ceases and there is only the crystallization mechanism.

The fourth stage

In the final stage, major part of particle is fully crystallized. The volume of crystallization part still grows until the volume of liquid phase is null. There is still no relative movement between the two particles.

5.2.2.3. Coalescence model for SLS process in polymer powder bed

The shrinking cube model is based on the ideal assumption. But, in fact, the grain won't shrink into a cube. This model cannot simulate the displacement of grain due to the coalescence. The molten polymer is a typical viscoelastic material. Therefore, the viscous coalescence model is not suitable in our case. The grain-boundary diffusion model is capable to simulate the displacement of molten grain due to the coalescence. However, this model requires many parameters (i.e. material properties) which are difficult to obtain. In conclusion, the viscoelastic coalescence model is more suitable in our case, because it can describe the change of geometry of polymer powder bed.

5.3. Basic of densification

The phenomena of densification can be distinguished into two different stages [81]:

The first stage corresponds to the fast increase in density. In this stage, gains are not stuck yet. The air between grains can escape rapidly through the freeways between grains because of the high mobility of particles in liquid phase. This stage is directly controlled by the coalescence and its kinetic depends on the viscosity of material.

The second stage corresponds to the formation and release of the entrapped gases. After coalescence, interfaces between grains are not free and the air cannot escape from this way anymore. So the air is trapped in the molten polymer and forms the bubbles. The migration of the air towards outside will be performed by the diffusion of gas in molten grains.

Given that the first stage of densification is caused by the rearrangement of grains due to the coalescence, this stage of densification can be explained by the model of coalescence, as we have discussed in the last section. For now, it is necessary to pay more attention to the understanding of the second stage, and two models are introduced as following.

5.3.1. Mechanisms of densification

Pore filling theory

When the gas pressure in an isolated pore is different to that outside the compact, pore filling is either retarded with an excess internal pressure or accelerated with an excess external pressure. Fig.III-5.10 is a schematic showing the compact surface and the internal surface of a pore containing insoluble gases [82]. Since a hydrostatic pressure is maintained in a liquid, the bulk liquid pressure at the surface is the same as that at the pore surface.

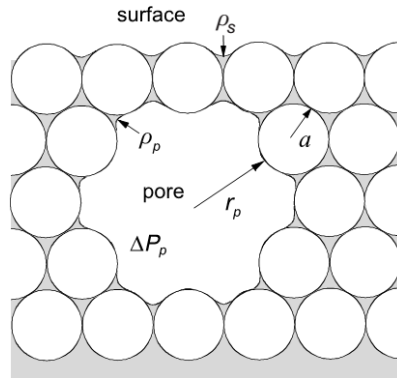


Fig.III-5.10. Illustration of liquid menisci at the specimen surface and around a pore containing an inter gas of pressure ΔP_p during liquid phase sintering [82]

$$\Delta P = P_s - P_l = \frac{2\Gamma_l}{\rho_s} \quad (\text{III-5.60})$$

$$P_l = \Delta P_p + P_s - \frac{2\Gamma_l}{\rho_p} \quad (\text{III-5.61})$$

where P_l is the liquid pressure, P_s is the sintering atmosphere pressure, ΔP_p is the difference in gas pressure between the pore and the atmosphere, ρ_s and ρ_p are the radii of liquid menisci at the pore and at the compact surface, respectively. And ρ_s is linearly proportional to the grain radius a .

$$\rho_s(t) \propto a(t) \quad (\text{III-5.62})$$

if $\Delta P_p \neq 0$, ρ_p is equal to r_p at the critical condition for the wetting of a pore surface. Let $a(\Delta P_p)$ and $a(0)$ be the critical grain sizes under $\Delta P_p \neq 0$ and $\Delta P_p = 0$, respectively. Then,

$$\frac{a(\Delta P_p)}{a(0)} = \frac{\rho_s(\Delta P_p)}{\rho_s(0)} = \frac{\rho_s(\Delta P_p)}{r_p} \quad (\text{III-5.63})$$

and

$$\frac{a(\Delta P_p)}{a(0)} = \frac{1}{1 - \frac{r_p \Delta P_p}{2\Gamma_l}} \quad (\text{III-5.64})$$

Substituting Eq.III-5.63 into Eq.III-5.64, the variation of grain radius vers time is written as

$$\dot{a} = a(\Delta P_p) \frac{\frac{r_p \Delta P_p}{2\Gamma_l}}{1 - \frac{r_p \Delta P_p}{2\Gamma_l}} \quad (\text{III-5.65})$$

Bubble dissolution theory

M. Kontopoulou et al. [93] have studied the bubble growth and collapse in viscous or viscoelastic fluids and given the conclusion that the bubble's dynamics are mainly controlled by pressure differences and fluid viscosity.

By conservation of mass, the inverse-square law requires that the radially outward velocity $u(r, t)$ must be inversely proportional to the square of the distance from the origin (the center of the bubble). Therefore, letting $F(t)$ be a function of time:

$$u_r(r, t) = \frac{F(t)}{r^2} \quad (\text{III-5.66})$$

In the case of zero mass transport across the bubble surface, the velocity at the interface must be

$$u_r(R, t) = \frac{dR}{dt} = \frac{F(t)}{R^2} \quad (\text{III-5.67})$$

which gives that $F(t) = R^2 dR/dt$

In the case where mass transport occurs, the rate of mass increase inside the bubble is given by:

$$\frac{dm_V}{dt} = \rho_V \frac{d(4\pi R^3/3)}{dt} = 4\pi \rho_G R^2 \frac{dR}{dt} \quad (\text{III-5.68})$$

with V being the volume of the bubble.

If u_L is the velocity at the interface between liquid and bubble, then mass entering the bubble is given by

$$\frac{dm_L}{dt} = \rho_L S u_L = \rho_L (4\pi R^2) u_L \quad (\text{III-5.69})$$

with S being the surface area of the bubble.

Now by conservation of mass $\frac{dm_V}{dt} = \frac{dm_L}{dt}$, hence

$$u_r(R, t) = \frac{dR}{dt} - u_L = \left(1 - \frac{\rho_G}{\rho_L}\right) \frac{dR}{dt} \quad (\text{III-5.70})$$

In most cases, the liquid density is much greater than the bubble density. So the mass transfer can be neglected. The velocity $u(r, t)$ is expressed as below:

$$u_r(r, t) = \frac{R^2}{r^2} \frac{dR}{dt} \quad (\text{III-5.71})$$

The dynamics of the system are governed by the conservation of momentum in the radial direction, the Navie-Stokes equation in spherical coordinate:

$$\rho \left(\frac{\partial u_r}{\partial t} + u_r \frac{\partial u_r}{\partial r} \right) = - \frac{\partial P}{\partial r} + \frac{1}{r^2} \frac{\partial}{\partial r} (r^2 \tau_{rr}) - \frac{\tau_{\theta\theta} + \tau_{\phi\phi}}{r} \quad (\text{III-5.72})$$

Since the fluid is highly viscous, the inertia terms can be neglected and integrate Eq.(III-5.72) from the bubble wall to infinity. So Eq.(III-5.72) becomes as below

$$P(R) - P(\infty) + \tau_{rr}(\infty) - \tau_{rr}(R) - 2 \int_R^\infty \frac{\tau_{\theta\theta} + \tau_{\phi\phi}}{r} dr = 0 \quad (\text{III-5.73})$$

A force balance at the bubble-liquid interface gives:

$$2\pi R\Gamma + \pi R^2 (P(R) - \tau_{rr}(R)) = \pi R^2 (P_G - \tau_{rr,G}) \quad (\text{III-5.74})$$

Since the normal stress due to a low viscosity gas can be neglected, $\tau_{rr,G} = 0$. Eq.(III-5.74) can be

expressed as following:

$$P(R) = \tau_{rr}(R) + P_G - \frac{2\Gamma}{R} \quad (\text{III-5.75})$$

where P_G is the average gas pressure within the bubble.

Substituting Eq.(III-5.75) into Eq.(III-5.73) and assuming that the dynamic stress is zero at infinity, $\tau_{rr}(\infty) = 0$. Hence, Eq.(III-5.73) can be simplified as below:

$$P_G - P(\infty) - \frac{2\Gamma}{R} + 2 \int_R^\infty \frac{\tau_{\theta\theta} + \tau_{\varphi\varphi}}{r} dr = 0 \quad (\text{III-5.76})$$

The rate of deformation tensor in spherical coordinates is

$$\Delta = \begin{bmatrix} 2 \frac{\partial u_r}{\partial r} & 0 & 0 \\ 0 & 2 \frac{u_r}{r} & 0 \\ 0 & 0 & 2 \frac{u_r}{r} \end{bmatrix} \quad (\text{III-5.77})$$

$$\tau_{ij} = \eta \Delta_{ij} \quad (\text{III-5.78})$$

Substituting Eq.(III-5.73,76,78) into Eq.(III-5.76), we can get the relationship between the pressure inside the bubble to the rate of dissolution of the bubble:

$$\dot{R} = \frac{1}{4\eta} [(P_G - P(\infty))R - 2\Gamma] \quad (\text{III-5.79})$$

5.3.2. Densification of polymer powder bed during SLS process

In SLS process, the powder bed can be separated into three distinct regions, due to the non-uniform distribution of laser intensity, as illustrated in Fig.III-5.11. In the first region, the temperature of polymer grains are higher than the melting point T_m . All grains are totally melted. Therefore, molten polymer grains in this region can be regarded as liquid. After laser treatment, there are some air bubbles entrapped inside this region. The bubble dissolution theory is suitable to model the release of entrapped gases inside fusion polymer. In the second region, the temperature of polymer grains is between the equilibrium melting point T_{m0} and melting point T_m . Grains with two phase of solid and liquid both exist in this region, because they are partially molten. In this region, partially molten grains are lack of nobilities and cannot provide sufficient liquid flow. Therefore, we assume that the phenomenon of densification in this region is negligible. In the third region, the temperature of grains is lower than the equilibrium melting point T_{m0} . All grains are in solid state and there is no densification in this region.

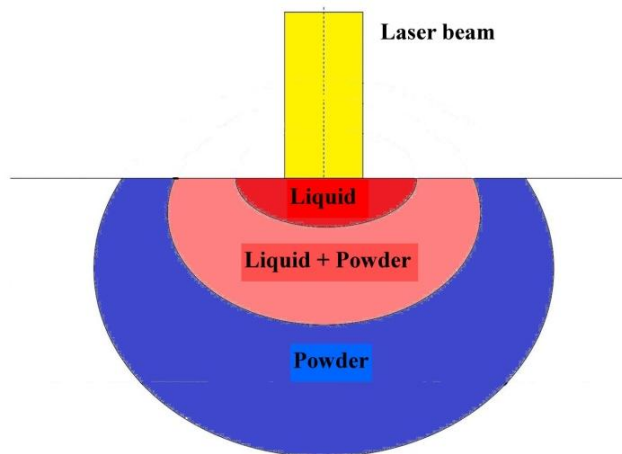


Fig.III-5.11. Three distinct regions in powder bed during SLS process

5.4. Review of numerical simulation of sintering

Although the selective laser sintering is a new technique, the sintering is actually one of the oldest human technologies, originating in the prehistoric age with the firing of pottery. Compared to its long history, the research concerning numerical simulation of sintering in SLS process is rather few.

The first numerical simulation of sintering we found is proposed by Ross et al.[94], who studied the sintering of infinite line of cylinders. Jagota et al. [95] simulated the viscous sintering of two spheres, using an axis-symmetric finite element method. Martínez-Herrera & Derby[96] proposed an axisymmetric finite element model showing the influence of grain size on the kinetic of coalescence. The first 3D numerical simulation was proposed by Zhou and Derby [97], who developed a finite element model to study the viscous sintering of three connected particles and concluded that it remained lots of work for understanding the phenomena occurring during the sintering of real powder compacts. Walkley et al. [98] developed a method with 3D finite element remeshing that is able to simulate fluid flow with consideration of surface tension. The same authors [99] also discussed the numerical difficulties in simulation of the sintering, in particular, the mesh distortion problems in case of large deformation fluids. In order to overcome the difficulties, a new finite elements method, called the Boundary Integral Method, has been commonly used for modeling the sintering of two spheres [100-106].

However, the problem mentioned by using these methods is strongly sensitive to the number of nodes, inducing significantly computational limitation in the case of 3D modeling. Therefore, until now, no numerical simulation based on finite element method has modeled the sintering phenomenon in an area consisting of plenty randomly arranged grains with non-isothermal conditions, such as the selective laser sintering. For achieving that, a new numerical method based on Discrete Elements method (DEM) is proposed. Compared to the finite elements method, the Discrete Elements method is particularly useful for modeling phenomena in materials with evolving discontinuous connections. The DEM makes it possible to capture almost all the physical phenomena linked to interacting particles and the granular characteristics of the materials, such as the coalescence and densification.

For the last decade, several authors have presented their works of numerical simulation of sintering based on discrete element method. Martin and Bordia [107] studied the sintering process among several grains on a substrate. Martin et al. [108] and Henrich et al. [109] have focused on the influence of rearrangement of grains on the kinetic of sintering. Wang and Chen [110] studied the evolution of forces and contact networks among grains during sintering. Martin et al. [111] and Wonisch et al. [112] implemented the basic grain growth models. Wonisch et al. [112] compared the simulation results to the experimental data of the anisotropy induced by stress. Then, a couple of synchrotron X-ray microtomography studies have pointed out the ability of this method to get accurate data on the micro-structure evolution [113,114]. Olmos et al. [115,116] also used this approach to validate the discrete element model. Hence, DEM simulation appears to be a suitable method to simulate the sintering phenomenon in SLS process.

Based on the discussion above, we propose a sintering model based on the discrete elements method for modeling sintering phenomenon in SLS process. This model will be detailed in the coming section.

5.5. Synthetic of sintering submodel in SLS process

The sintering process of polymer powder bed can be separated into three periods: initial, intermediate and final stage. As shown in Fig.III-5.12, when the temperature of powder bed is higher than melting temperature T_m , fusion grains begin to coalesce and necks between molten grains are created at the initial stage of sintering. In SLS process, the period of initial stage is very short, usually less than 1 second [90]. When the temperature of powder bed is lower than T_m but higher than crystallization temperature T_c , considerable densification occurs during the period of intermediate and final stage of sintering, because lots of entrapped air escapes from powder bed. The period of intermediate and final stage depends on the preheating temperature of powder bed, usually much longer than that of initial stage. Finally, the sintering process ceases when the temperature is lower than T_c .

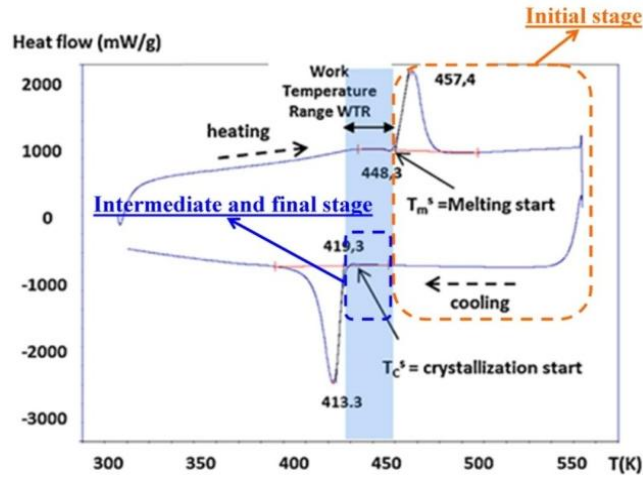


Fig.III-5.12. Illustration of different sintering stages in the DSC profile of PA12 [117]

5.5.1. Initial stage sintering

In order to simplify the sintering of powder with complex shaped particles, the spherical particles are assumed to have the same size. In the initial stage of sintering, the neck growth can be explained by the coalescence model. For polymers like PA12 or PEEK, the coalescence only exists among molten particles.

As the discussion in the section 5.2.2, the viscoelastic coalescence model is suitable in the case of polymer laser sintering [85]:

$$\frac{d(\theta^2)}{dt} = \frac{-\alpha\lambda - 2\frac{\eta r}{\Gamma} + [(3\alpha\lambda)^2 + 4\alpha\lambda\frac{\eta r}{\Gamma} + 4(\frac{\eta r}{\Gamma})^2]^{1/2}}{2(\alpha\lambda)^2} \quad (\text{III-5.82})$$

$$r(t) = r_0 \left(\frac{4}{(1 + \cos(\theta(t)))^2 (2 - \cos(\theta(t)))} \right)^{1/3} \quad (\text{III-5.83})$$

5.5.2. Intermediate and final stage

In the intermediate and final stage of sintering, the densification is mainly caused by evaporation and release of entrapped air inside powder bed. As discussed in the section 5.3.2, the evaporation and the release of entrapped air can be modeled by the bubble dissolution theory in the case of polymer laser sintering [93]:

$$\dot{R} = \frac{1}{4\eta} [(P_G - P(\infty))R - 2\Gamma] \quad (\text{III-5.84})$$

where P_G is the average gas pressure within the bubble, $P(\infty)$ is assumed as the pressure atmospheric, R is the radius of air bubble.

The pressure inside air bubble is given out by Perason et al. [118]:

$$P_G = P_0 - \rho g \Delta h \quad (\text{III-5.85})$$

where P_0 is used as the reference pressure atmospheric, ρ is the density of molten polymer, g is the acceleration of gravity, Δh is the distance between the surface of molten region of powder bed and the center of air bubble.

As presented in Fig.III-5.13(a), in a powder bed with homogeneous distribution, we assume that the entrapped gases are replaced by an equivalent air bubble. In case of single particle with multiple air bubble around as shown in Fig.III-5.13 (b), we assume the kinetic of particle inflating is equal to the average kinetic of air bubbles shrinkage:

$$\frac{4}{3}\pi R_0^3 = (2r)^3 - \frac{4}{3}\pi r^3 \quad (\text{III-5.86})$$

$$\dot{r} = -\frac{\sum_1^n \dot{R}}{n} \quad (\text{III-5.87})$$

where R_0 is the initial value of bubble radius R and n is the number of contacted air bubble.

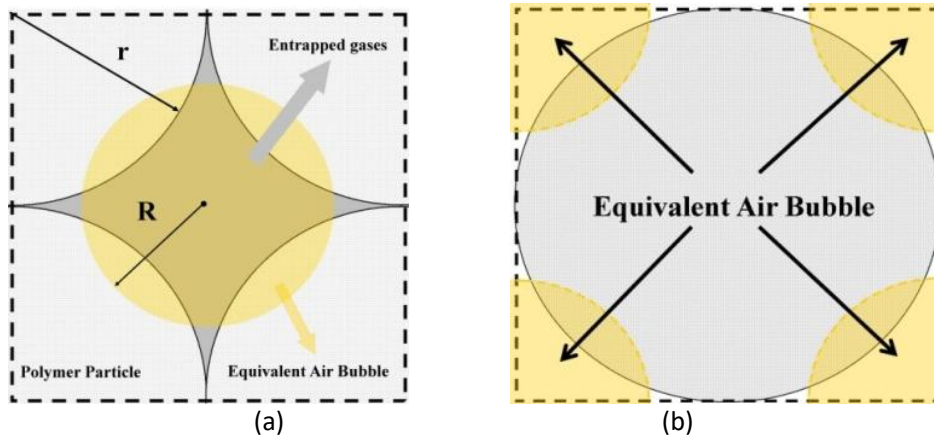


Fig.III-5.13. Equivalent air bubble in powder bed

The particle on the surface of powder bed does not inflate because there is no difference of pressure. During the process of densification, the room of entrapped gases is gradually filled by molten polymer. Therefore, the volumetric variation of equivalent air bubble is equal to that of fusion particle closed to surface, assuring the volume conservation.

5.5.3. Effect of sintering on heat conduction

As the derivation in the last chapter IV, the heat conduction model is validated when all grains are assumed to be elastic spheres with rigid contacts. However, when introducing the phenomenon of sintering, relative positions of grains are not constant and necks between grains are formed as illustrated in Fig.III-5.14. Therefore, the area of contact regions between grains is function of time.

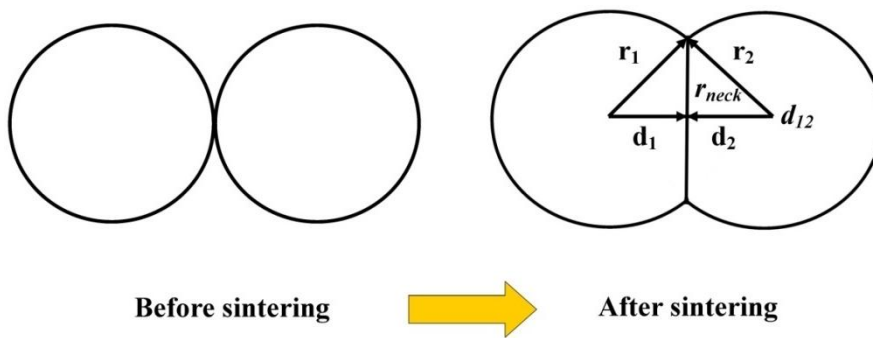


Fig.III-5.14. Variation of contact region in sintering process

Based on the basic rules of geometry, we can obtain the relationships as below:

$$d_1 + d_2 = d_{12} \quad (\text{III-5.88})$$

$$r_1^2 - d_1^2 = r_2^2 - d_2^2 = r_{neck}^2 \quad (\text{III-5.89})$$

where d_1 is the distance from the center of particle 1 to the interface of contact region, d_2 is the distance from the center of particle 2 to the interface of contact region, d_{12} is the distance between two centers of two particles, r_{neck} is the radius of neck of contact region, r_1 and r_2 are radiuses of particle 1 and particle 2, respectively.

Substituting Eq.III-5.88 into Eq.III-5.89, we can obtain as following:

$$d_1 = \frac{d_{12}}{2} + \frac{r_1^2 - r_2^2}{2d_{12}} \quad (\text{III-5.90})$$

$$d_2 = \frac{d_{12}}{2} - \frac{r_1^2 - r_2^2}{2d_{12}} \quad (\text{III-5.91})$$

Thus, the area of contact region after sintering is written as:

$$Area_c = \pi r_{neck}^2 = \pi \times \left[r_1^2 - \left(\frac{d_{12}}{2} + \frac{r_1^2 - r_2^2}{2d_{12}} \right)^2 \right] \quad (\text{III-5.92})$$

During numerical simulation based on DEM, we can obtain the position and radius of each particle at each time step, and then it is easy to calculate the area of contact region. After substituting Eq.III-5.92 into Eq.III-4.4, we can get the new heat transfer coefficient H_c after sintering as below.

$$H_c = -\frac{k_c \pi}{d_{12}} \left[r_1^2 - \left(\frac{d_{12}}{2} + \frac{r_1^2 - r_2^2}{2d_{12}} \right)^2 \right] \quad (\text{III-5.93})$$

6. Contact dynamic submodel

In the case of numerical simulation of SLS process, the powder bed is usually assumed as a homogenous sheet [1-7,9]. However, this simplification neglects the characters of powder bed as a granular medium, resulting in limitations for analyzing the variation of porosity inside powder bed during SLS process. In fact, the porosity has been confirmed as a very important factor that is directly related to the performance of SLS product [5-9]. Thus, we need to model the geometry of powder bed so as to simulate the SLS process more precisely. The purpose of contact dynamic submodel is to simulate a randomly generated powder bed of poly-dispersed particles. Powder material may be single-component or multi-component mixture. Powder grains are simply assumed to be spherical. Using this assumption, the model is simplified significantly, because only the coordinates of centre and radius of a sphere are needed to define a sphere completely, whereas a non-spherical surface may need a number of parameters to define it. Moreover, it is difficult to estimate overlaps between non-spherical surfaces.

6.1. Review of sphere packing method

As discussed in section III-4.2, discrete methods is highly suitable for modeling the dynamics of granular medium. In general, discrete methods studied materials consisting of a set of discrete elements with different shapes and sizes. These elements interact with each other by contact laws and/or cohesive bonds. Knowing forces and torques applied on the discrete elements, displacements and rotations can be computed using classic Newton mechanics. A review of various sphere packing algorithms reveal that existing models can be broadly classified into three types:

1. Ballistic or sequential addition algorithms[119-121]
2. Collective rearrangement algorithms[122,123]
3. Dynamic algorithms[124,125]

Ballistic and rearrangement algorithms are purely mathematical means to generate a model of disorderly packed structure. These algorithms, although simple, yet fail to take into account the mechanical interactions between the particles in their modeling approach. On the other hand in dynamic algorithms, the motion of individual particles is governed by Newtonian mechanics. These algorithms incorporate energy losses (due to friction, collision, deformation etc.) during packing process to obtain the final packing. For the present work we have chosen dynamic packing method to model the geometry of packed bed since it is derived based on mechanics of particle interactions during packing. In the following subsection the details of this method are provided.

6.2. Dynamic algorithm with elastic contacts

After laser treatment, a new layer of powders will be added into the production area. At this moment, all grains are solid and can be considered as rigid spheres. Thus, the process of adding new layer of powders can be simulated by the elastic contact model.

Cundall and Strack [124] firstly proposed a simplified discrete numerical model which calculates the contact force only based on the normal and tangential displacement. This model has a smaller computational intension without significant error, which is suitable in our case.

In this model, the contact between elastic grains is simplified as the damping vibration of spring oscillator as shown in Fig.III-6.1 [124]:

$$m\ddot{x} + \eta\dot{x} + kx = 0 \quad (\text{III-6.1})$$

where x is the distance deviated from equilibrant position, m is the mass of the grain, η and k are damping and elastic coefficient respectively.

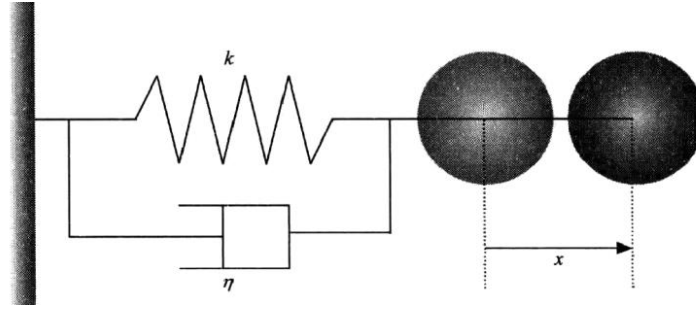


Fig.III-6.1. Contact between elastic grains simplified as the damping vibration of spring oscillator[124]

According to Hertz theory, the normal contact force on the particle i F_{nij} is written as [124]:

$$\mathbf{F}_{nij} = (-k_n \alpha^{\frac{3}{2}} - \eta_{ni} \mathbf{G} \mathbf{n}) \mathbf{n} \quad (\text{III-6.2})$$

where α is the normal overlap displacement, $\mathbf{G} = \mathbf{v}_i - \mathbf{v}_j$ is the relative velocity from particle i to particle j , \mathbf{n} is the unit vector from the center of particle i to particle j , k_n and η_{ni} are the normal elastic and damping coefficient respectively.

Similarly, the tangential force \mathbf{F}_{tij} is written as below:

$$\mathbf{F}_{tij} = -k_t \boldsymbol{\delta} - \eta_{tj} \mathbf{G}_{ct} \quad (\text{III-6.3})$$

where k_t and η_{tj} are the tangential elastic and damping coefficient respectively, \mathbf{G}_{ct} is the slip velocity at the contact point, $\boldsymbol{\delta}$ is the slip displacement at the contact point.

In multiple particles system, particle i can contact with several particles at the same time. Therefore, the resultant force on the particle i can be written as:

$$\mathbf{F}_i = \sum_j (\mathbf{F}_{nij} + \mathbf{F}_{tij}) \quad (\text{III-6.4})$$

In our case, the diameter of particle is about $50 \mu\text{m}$ and the velocity is very small. So the effect of tangential force can be neglected. Therefore, Eq.III-6.4 can be simplified as:

$$\mathbf{F}_i = \sum_j \mathbf{F}_{nij} + \mathbf{g} \quad (\text{III-6.5})$$

where \mathbf{g} is the force of gravity.

With the assumption that the contact force is constant in the period of one time step Δt , the velocity and displacement of one particle i can be estimated by Euler integration [124]:

$$\mathbf{v}_i(t + \Delta t) = \mathbf{v}_i(t) + \frac{1}{m_i} \mathbf{F}_i \Delta t \quad (\text{III-6.6})$$

$$\mathbf{s}_i(t + \Delta t) = \mathbf{s}_i(t) + \mathbf{v}_i \Delta t \quad (\text{III-6.7})$$

where \mathbf{v}_i is the velocity of particle i , m_i is the mass of particle i and \mathbf{s}_i is the displacement of particle i .

For simulating the motion of grain, the velocity and displacement are accumulated step by step, as illustrated in Fig.III-6.2.

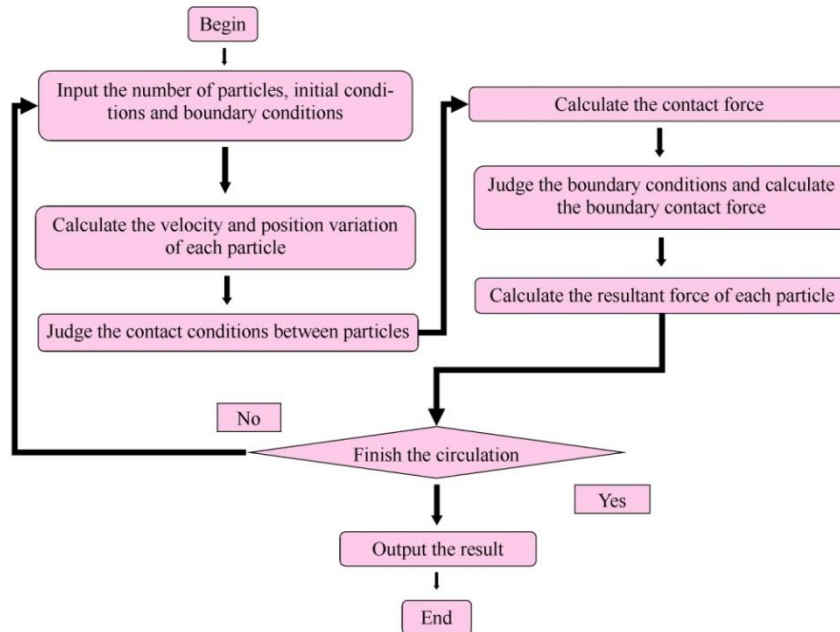


Fig.III-6.2. Flowchart of contact dynamics

The growth of the particle bed in the model starts by dropping the particles from a fixed height. This is achieved by inserting a group of particles of desired size distribution into a relatively small volume above the bed (Fig.VI-5) and allowing them to fall under the influence of gravity. The spatial distribution of particles in this insertion volume is random. When a group of inserted particles fall out of the insertion volume, another group of particles is inserted. This insertion continues at regular intervals until the desired fraction of total volume is filled with particles. However, the simulation stops only when all the particles settle down resulting in a randomly packed structure. The total kinetic energy of the particles is used as a measure of the dynamic state of the system. The particles lose their kinetic energy due to dissipation during each collision (inelastic). The particulate system is thus considered static when its kinetic energy becomes negligible, and the resulting packing structure is ready for further analysis.

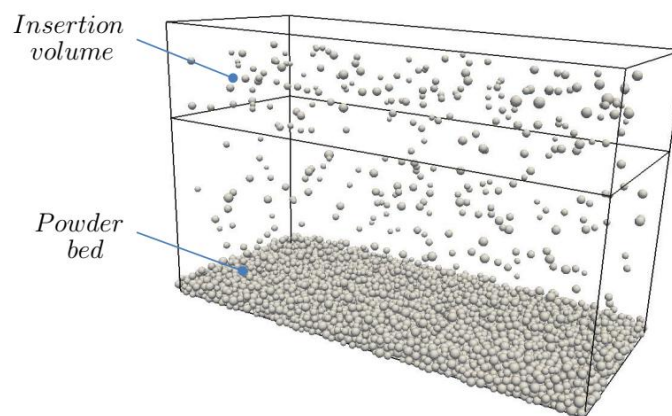


Fig.III-6.3. Schematic of insertion volume [8]

6.3. Generating new layers during SLS process

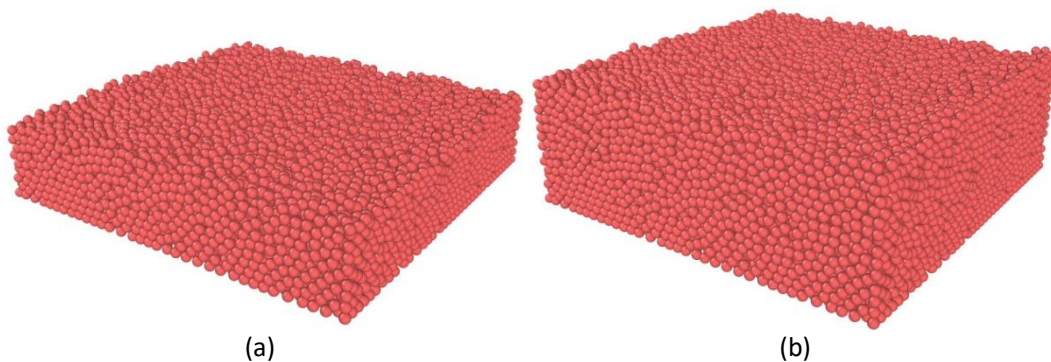
For ensuring the random distribution of particles, the granular package in LAMMPS has been used to generate the initial powders bed of spherical particles of a given size. LAMMPS is a freely-available open-source code, developed by Sandia National Laboratories of USA. Adding a new layer of grains starts by dropping the particles from a fixed height. This is achieved by inserting a group of particles of desired size distribution into a relatively small volume above the powder bed and allowing them to fall under the

influence of gravity. The spatial distribution of particles in the box is random. The process of adding new layer of powders is simulated by Fortran90.

Table.III-6.1 Input parameters of grains [8]

Input parameter	Value	Unit
Gravity	9.8	m/s ²
Young's modulus	800	MPa
Density	1030	kg/m ³
Elastic coefficient	800	kg/s ²
Damping coefficient	0.012	kg/s
Dropping velocity	0	m/s
Poisson ratio	0.38	

For example using LAMMPS, we generate a package of PA12 grains in a given box with the dimension of $2\text{ mm} \times 2\text{ mm} \times 2\text{ mm}$, as illustrated in Fig.VI-6(a). The number of grains is 16000 and they have the same size $50\ \mu\text{m}$. The input parameters needed for generating new layer of powders are listed in Table.III-3. In our case, we assume that all grains are randomly distributed with the same size in a given box. New added grain freely fall under the influence of gravity. After adding a new layer with the thickness of $300\ \mu\text{m}$, the distribution of new package of powders is shown in Fig.III-6.4(b).



(a) (b)
 Fig.III-6.4. Distribution of powder bed in a box:
 (a) initial powder bed from LAMMPS;
 (b) new powder bed after adding grains from Fortran90.

7. Methodology of synthetic model

Based on the discussion of analytical and numerical models presented in the previous sections, it is clear that the synthetic model must link these submodels to each other. In order to achieve this goal, we developed a numerical framework based on DEM for the simulation of SLS process, the details regarding different aspect of this framework, the constituent algorithms and implementation are given in the following sections.

7.1. Particle system definition

In this thesis, a DEM particle system is used which occupies a volume $\Omega \in \mathbb{R}^3$ with a boundary Γ , in Cartesian spatial coordinate (x,y,z) . The single particle is defined by the position of its center and radius R_i . The corresponding vectors of particle acceleration, velocity, displacement and force are denoted as \mathbf{a}_i , \mathbf{v}_i , \mathbf{x}_i and \mathbf{f}_i , respectively. The particle mass is m_i and its radius is r_i , the temperature is represented by T_i and the heat flux by q_i .

In the present work, we define the volume Ω to be a regular box with parallelepiped boundary such as $0 \leq x \leq x_{max}$, $0 \leq y \leq y_{max}$ and $0 \leq z \leq z_{max}$. We assume the gravity to act in the -z direction with a magnitude of 9.81 m/s^2 .

The simulation time variable is t , if $t=0$ corresponding to the introduction of the first laser scanning in the box. In other words, the first layer of powder bed is predefined and its consuming time is neglected. The discrete simulation time step is Δt , and n_t is the total number of such time steps in the simulation. For stability, we request $\Delta t < \Delta t_{max}$, which is a max time step determined from the particle system stiffness. A satisfactory approximation of the max time step is given in the reference [126]

$$\Delta t_{max} \simeq \sqrt{\frac{m_{min}}{k_n}} \quad (\text{III-7.1})$$

where m_{min} is the minimum particle mass and k_n is the normal stiffness of the particles from Eq.III-6.2. In most cases, satisfactory efficiency can be achieved simply by taking $\Delta t = \Delta t_{max}/10$.

7.2. Boundary conditions

In this work, the plane boundary conditions are assumed to be stationary. Additionally, these plane boundaries can be classified as two types of collision and thermal boundary.

In case of collision boundary, if particle i impinges on boundary plane k , it experiences a force normal to the plane [126]

$$\mathbf{f}_{bn_{i,k}} = k_b c_i \mathbf{n}_k \quad (\text{III-7.2})$$

$$c_i = \begin{cases} 0 & \text{if } r_i - \delta_b \leq 0 \\ r_i - \delta_b & \text{if } r_i - \delta_b > 0 \end{cases}$$

where k_b is the boundary stiffness and δ_b is the distance between the particle i boundary plane k and \mathbf{n}_k is the unit normal vector of boundary plane k .

In case of thermal boundary, it is assumed that planes are thermal isolation. If a particle i is in contact with a boundary plane k , its heat flux is adjusted

$$\nabla \cdot \mathbf{q}_{i,k} = 0 \quad (\text{III-7.3})$$

At the powder upper surface, the energy lost by the emission and convection can be discretized as below:

$$\dot{q}_{piconv} = -2\pi R_i^2 [h(T_i - T_a) + \varepsilon_R \sigma (T_i^4 - T_a^4)] \quad (\text{III-7.4})$$

where \dot{q}_{pconv} is the convection heat flux from Eq.III-4.12, T_i is the temperature of particle i at the surface of powder bed, T_a is the ambient temperature, h is the convective heat transfer coefficient, ε_R is the surface emissivity of the material and σ is the Stefan-Boltzmann constant

7.3. Energy deposition

In additive manufacturing, the advantageous aspects are derived from the highly directed energy which is transferred to the material. A laser or electron beam is usually used as the heat source in powder-based additive manufacturing systems. The position and orientation of heat source is controlled by a computer-control device. The geometric complexity observed in existing additive manufacturing processes dictates that the pattern of heat deposition into the selected powder will be highly non-uniform in terms of both the spatial and temporal variables.

In physical SLS process, the laser heat source moves along a predefined path in order to transfer energy to the selected powder. In the DEM simulation, this path is captured and interpreted by a discrete function of time that gives the spatial coordinate of the laser center as presented in Fig.III-7.1. This function is expressed as below.

$$X(t) = \begin{cases} X_1(t) & 0 \leq t \leq \Delta t \\ X_2(t) & \Delta t \leq t \leq 2\Delta t \\ \dots & \dots \\ X_n(t) & (n-1)\Delta t \leq t \leq n\Delta t \end{cases} \quad (\text{III-7.5})$$

where $X_i(t)$ corresponds to the Cartesian spatial position of laser center at time step i . For the period of time in which the laser is turned off, $X_i(t)$ is equal to the position of the last time step, but the power of laser introduced is null.

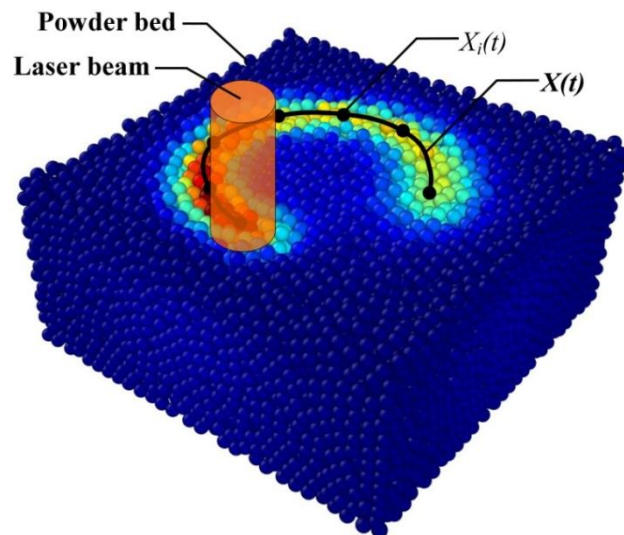


Fig.III-7.1. Demonstration of the energy deposition methodology in SLS process

The path of laser beam as presented above is predefined before the DEM simulation begins. Therefore, the position of the heat source is known at each time step. With this information, the radiation heat transfer submodel (section III-3) is connected to the discrete heat conduction submodel (section III-4) by computing the laser energy transferred to the particles proximal to this location. Based on the radiation transfer submodel, we can obtain the distribution of laser energy as shown in Fig.III-7.2. Every point represents the scattered position of a photon that occupies a part of laser energy absorbed by particle.

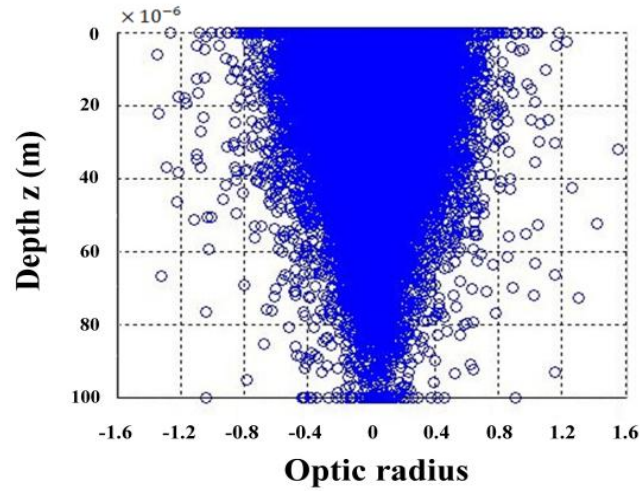


Fig.III-7.2. Distribution of scattered photons inside powder bed

Therefore, the laser energy absorbed by a certain particle can be expressed as

$$\begin{aligned} \dot{q}_{p\text{source}} &= \sum_{j=1}^{N_i} A_j(x, y, z, t) \quad (\text{III-7.5}) \\ (x - x_i)^2 + (y - y_i)^2 + (z - z_i)^2 &\leq R_i^2 \end{aligned}$$

where $\dot{q}_{p\text{source}}$ represents the heat source of Eq.III-4.12, $A_j(x, y, z, t)$ corresponds to laser intensity absorbed by the scattered position, N_i is the number of scattered position inside the particle i , (x_i, y_i, z_i) corresponds to the position of center of particle i and R_i is its radius.

As discussed in the section III-3.5, the Beer-Lambert law is introduced in order to model the attenuation of laser energy inside powder bed. We assume that the laser energy is totally absorbed by particles and ignore the absorption of air inside powder bed. Thus, the attenuation path of a photon is composited of a series of scattered positions, as shown in Fig.III-7.3. The initial laser energy carried by a photon is the accumulation of laser energy absorbed by these scattered positions.

$$\begin{aligned} I^{k,0} &= A^{k,1} + A^{k,2} + A^{k,3} + \dots + A^{k,n-1} + A^{k,n} \quad (\text{III-7.6}) \\ I^{k,0} &= \frac{P}{N} \end{aligned}$$

where $I^{k,0}$ is the initial laser energy carried by photon k , P is the power of laser beam and N is the number of photons used in Monte Carlo simulation. The photon is totally absorbed by particles after being scattered by n times.

Due to the discretization of scattered position, the Beer-Lambert law is discretized as

$$\begin{aligned} I^{k,q} &= I^{k,q-1} \cdot e^{-\alpha_{abs} \cdot l} \\ A^{k,q} &= \begin{cases} I^{k,q-1} - I^{k,q} & \text{if } I^{k,q-1} > 0.05I^{k,0} \\ I^{k,q-1} & \text{if } I^{k,q-1} \leq 0.05I^{k,0} \end{cases} \quad (\text{III-7.7}) \end{aligned}$$

where $I^{k,q}$ represents the transmitted energy carried by the photon k at the scattered step q , $A^{k,q}$ represents the absorbed energy by the scattered portion of photon k at the scattered step q , α_{abs} is the absorption coefficient of powder bed and l is the mean free path of photon (Eq.III-3.2). The photon is demanded to be totally absorbed if its energy is smaller than 5% of the initial energy.

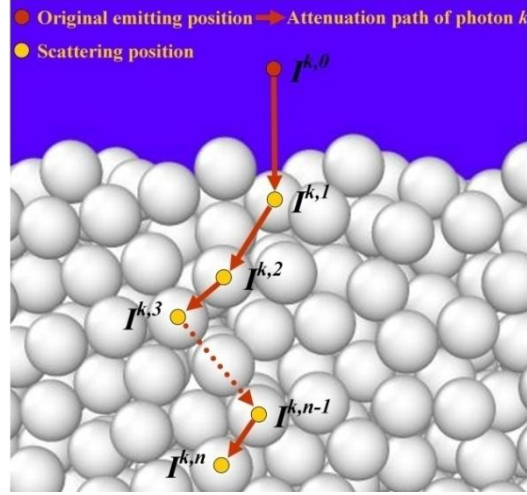


Fig.III-7.3. Attenuation path of photon k inside powder bed

7.4. Sintering and connected neck formation

From a numerical simulation perspective, the most complex aspect of the SLS is the modeling of sintering procedures associated with inter-particle actions. For the simplification, the geometrical variation of particle is neglected in most of researches. Furthermore, the coalescence caused by surface tension is assumed to be driven by the so-called sintering forces [86-89,126].

In this work, we use the relative displacement caused by so-called sintering forces in order to model the sintering interaction between particles. This interaction requires a condition of sufficient temperature and physical contacts.

$$\mathbf{u}_i^t = \sum_{j=1}^{n_c} \mathbf{u}_{i,j}^t \quad (\text{III-7.8})$$

$$\mathbf{u}_{i,j}^t = \begin{cases} R_i [\cos(\theta_{i,j}^{t-\Delta t}) - \cos(\theta_{i,j}^t)] \mathbf{n}_d & \text{if } T_i, T_j \geq T_m, R_i + R_j \leq |\mathbf{d}_{i,j}| \\ 0 & \text{otherwise} \end{cases} \quad (\text{III-7.9})$$

where \mathbf{u}_i^t corresponds to the displacement of particle i caused by sintering, $\mathbf{u}_{i,j}^t$ is the relative displacement between particle i and j , $\theta_{i,j}^t$ represents the sintering angle from Eq.III-5.83, $\mathbf{d}_{i,j}$ is the vector from the center of particle i to particle j , \mathbf{n}_d is the unit vector of $\mathbf{d}_{i,j}$ and T_m is the melting point. According to the discussion of section III-5.5, the coalescence only occurs in the initial stage sintering that is relatively weak. Therefore, the variation of radius caused by coalescence is neglected here.

7.5. Time step integration

In the synthetic model, the classic Euler explicit integration scheme is used, even though lots of integration schemes have been developed for DEM [127]. At each time step, the force, displacement and heat flux have been calculated by submodels introduced in previous sections. The update scheme applied is presented by

$$\mathbf{v}_i^{t+\Delta t} = \mathbf{v}_i^t + \frac{\mathbf{f}_i^t}{m_i} \Delta t \quad (\text{III-7.10})$$

$$\mathbf{x}_i^{t+\Delta t} = \mathbf{x}_i^t + \mathbf{v}_i^t \Delta t + \mathbf{u}_i^t \quad (\text{III-7.11})$$

$$T_i^{t+\Delta t} = T_i^t + \frac{q_i^t}{m_i C p_i} \Delta t \quad (\text{III-7.12})$$

$$q_i^t = \sum_{\text{cont}i-j} \dot{q}_{pi-pj} + \dot{q}_{pisource} + \dot{q}_{piconv} \quad (\text{III-7.13})$$

where \mathbf{u}_i^t corresponds to the displacement caused by coalescence, $C p_i$ is the specific heat capacity and q_i^t represents the total heat flux from Eq.III-4.12.

7.6. Visualization and post-processing

Normally, it involves millions of particles or more during a typical additive manufacturing. But, considering the limitation of computational performance, we usually proposed the DEM simulations in condition with less than 50 thousands particles. The visual depiction of the particle system is provided by the open source software OVITO from Dr. Stukowski's team, in order to develop, debug, calibrate and use the DEM simulation. Furthermore, the procedures outlined in the previous sections were implemented in the Fortran90 programming language. Therefore, we can access to all information of each particle at every time step for further analysis, such as the position x_i^t , the velocity v_i^t , the contact force f_i^t and the temperature T_i^t .

7.7. Implementation

The procedures presented in the previous sections are implemented by the Fortran90 programming language. The flow of execution of this implementation is shown in Fig.III-7.4. Several information of particles, such as the position of center, radius and temperature, are exported as results of simulation. These results are saved in the data file which can be directly read by the visualization software.

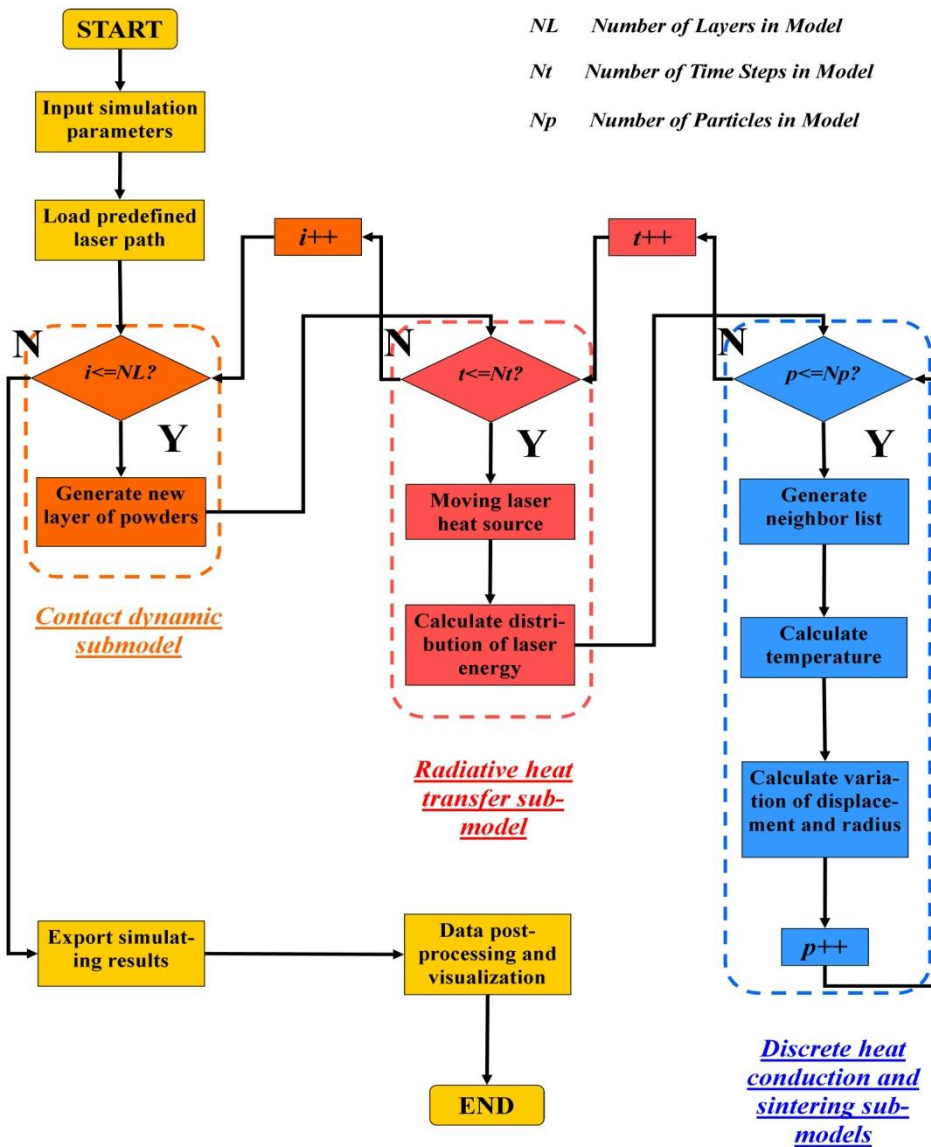


Fig.III-7.4. Illustration of execution in the Fortran90 implementation of DEM framework

Reference

- [1] Gabriel Bugada, Miguel Cervera and Guillermo Lombera, 1999, "Numerical prediction of temperature and density distributions in selective laser sintering processes", *Rapid Prototyping Journal*, 5(1):21-26.
- [2] Chen T.B., Zhang Y.W., 2007, "Thermal modeling of laser sintering of two component metal powder on top of sintered layers via multi-line scanning", *Applied Physics A*, Vol. 86, pp. 213-220.
- [3] THC Childs, M Berzins, G. R. Ryder and A. Tontowi, 1999, "Selective laser sintering of an amorphous polymer-simulations and experiments", *Proceedings of the Institution of Mechanical Engineers, Part B : Journal of Engineering Manufacturing*, 213: 333-349.
- [4] Donghua Dai, Dongdong Gu, 2014, "Thermal behavior and densification mechanism during selective laser melting of copper matrix composites: Simulation and experiments", *Materials and Design*, Vol. 55, pp. 482-491.
- [5] Dong Lin, A. Makradi, S. Ahzi, Y. Remond, 2009, "Three-dimensional transient finite elements analysis of the selective laser sintering process", *Journal of Materials Processing Technology*, Vol. 209, pp. 700-706.
- [6] Denis DEFAUCHY, 2013, "SIMULATION DU PROCEDE DE FABRICATION DIRECTE DE PIECES THERMOPLASTIQUES APR FUSION LASER DE POWDER", Ph.D. Thesis, Arts et Métiers PatisTech, Paris, France.
- [7] Dong Lin, 2007, "SIMULATION ET MODELISATION DU FRITTAGE SELECTIF PAR LASER PAR LA METHODE DES ELEMENTS FINIS", Ph.D. Thesis, Université Louis Pasteur, Strasbourg, France.
- [8] Ram Dayal aus Jodhpur, 2014, "Numerical Modelling of Process Governing Selective Laser Sintering", Ph.D. Thesis, Darmstadt, German.
- [9] Patrice Peyre, Yann Rouchausse, Denis Defauchy and Gilles Regnier, 2015, "Experimental and numerical analysis of the selective laser sintering (SLS) of PA12 and PEEK semi-crystalline polymers", *Journal of Materials Processing Technology*, 225:326-336.
- [10] Michael F. Modest, 2003, radiative heat transfer: 2nd edition, Elsevier Science, USA.
- [11] Tien, C. L., and B. L. Drolen, "Thermal radiation in particulate media with dependent and independent scattering," in Annual Review of Numerical Fluid Mechanics and Heat Transfer, vol. 1, Hemisphere, New York, pp. 1-32,1987.
- [12] Rayleigh, L.: "On the light from the sky, its polarization and colour," *Philos. Mag*, vol. 41, pp. 107-120,274-279, 1871 (reprinted in Scientific Papers by Lord Rayleigh, vol. I: 1869-1881, no. 8, Dover, New York, 1964).
- [13] Mie, G. A.: "Beitrage zur Optik triiber Medien, speziell kolloidaler Metallosungen," *Annalen der Physik*, vol. 25, pp.377-445,1908.
- [14] Chu, C. M., and S. W. Churchill: "Representation of the angular distribution of radiation scattered by a spherical particle," *Journal of the Optical Society of America*, vol. 45, no. 11, pp. 958-962, 1955.
- [15] Clark, G. C , C. M. Chu, and S. W. Churchill: "Angular distribution coefficients for radiation scattered by a spherical particle," *Journal of the Optical Society of America*, vol. 47, pp. 81-84,1957.
- [16] Mariana Iliea, Jean-Christophe Kneip, Simone Mattei,, Alexandru Nichici, Claude Roze, Thierry Girasole, 2007, Laser beam scattering effects in non-absorbent inhomogenous polymers, *Optics and Lasers in Engineering*, 45: 405-412.
- [17] M. Kaviany. Principles of Heat Transfer in Porous Media. Mechanical Engineering Series. Springer New York, New York, NY, 1995.
- [18] L. Dong, A. Makradi, S. Ahzi, Y. Remond, 2009, Three-Dimensional Transient Finite Elements Analysis of the Selective Laser Sintering Process, *Journal of Materials Processing Technology*, Vol. 209, pp. 700-706.
- [19] G.N. Labeas, G.A. Moraitis, C.V. Katsiropoulos, 2010, "Optimization of Laser Transmission Welding Process for Thermoplastic Composite Parts using Thermo-Mechanical Simulation", *J. Composite Materials*, Vol. 44, pp. 113-130.
- [20] D.A. Grewell and A.Benatar, 2003, *Plastics and Composites: Welding Handbook*, Hanser Verlag.
- [21] D. Defauchy, 2013, *Simulation du Procédé de Fabrication Directe de Pièces Thermoplastiques Apr Fusion Laser de Poudre*, Ph.D. Thesis, Arts et Métiers PatisTech, Paris, France.
- [22] F. Becker, H. Potente, 2002, A Step Towards Understanding the Heating Phase of Laser Transmission Welding in Polymers, *Polymer Engineering and Science*, Vol. 42, pp. 365-374.
- [23] C. Mingliang, 2009, Gap Bridging in LTW of Thermoplastics, Ph.D. Thesis, Queen's University, Kingston

Ontario, Canada.

- [24] C. L. Tien. Thermal radiation in packed and fluidized beds. *ASME J. Heat transfer*, 110:1230–1242, November 1988
- [25] J. Zhou, Y. Zhang and J.K. Chen, 2009, Numerical Simulation of Laser Irradiation to a Randomly Packed Bimodal Powder Bed, *Int. J. Heat Mass Transfer*, Vol. 52, pp. 3137-3146.
- [26] A. Chateau, A. Asseko, B. Cosson, M. Deleglise, F. Schmidt, Y. Le Maoutl and E. Lafranche, 2013, Analytical and Numerical Modeling of Light Scattering in Composite Transmission Laser Welding Process, *Int. J. Material Forming*, Vol. 8, pp. 127-135.
- [27] B. Singh and M. Kaviany. Modelling radiative heat transfer in packed beds. *International Journal of Heat and Mass Transfer*, 35(6):1397–1405, June 1992.
- [28] X. Wang and J.-P. Kruth. A simulation model for direct selective laser sintering of metal powders. In *International conference on engineering computational technology*, pages 57– 71, 2000.
- [29] C. K. Chan and C. L. Tien. Radiative transfer in packed spheres. *ASME J. Heat transfer*, 96:52–58, 1974.
- [30] K. Kudo, W. J. Yang, H. Taniguchi, and A. H. Hayasaka. Radiative heat transfer in packed spheres by monte carlo method. In *Heat Transfer in High Technology and Power Engineering Conference*, pages 529–540, 1985.
- [31] Y. S. Yang, J. R. Howell, and D. E. Klein. Radiative heat transfer through a randomly packed bed of spheres by the monte carlo method. *ASME J. Heat transfer*, 105(2):325– 332, 1983.
- [32] Helmut G. Katzgraber, 2011, Introduction of Monte Carlo method, Department of Physics and Astronomy, Texas A&M University, USA.
- [33] Girasole T, Roze C, Maheu B, Gre han G, Me nard J. Distances of visibility in a foggy atmosphere: comparisons between lighting installations by means of a Monte Carlo simulation. *Int J Light Res Tech* 1998;30(1):29–36.
- [34] Lavigne C, Roblin A, Outters V, Langlois S, Girasole T, Roze C. Comparison of iterative and Monte Carlo methods for calculation of the aureole about a point source in the Earth's atmosphere. *Appl Opt* 1999;38(30):6237–46.
- [35] A.V. Gusarov, I. Smurov, 2010, Radiation Transfer in Metallic Powder Beds Used in Laser Processing, *J. Quantitative Spectroscopy & Radiative Transfer*, Vol. 111, pp. 2517-2527.
- [36] Y. Marco, 2003, Caractérisation Multi-Axiale du Comportement et de la Microstructure d'un Semi-Cristallin: Application au Cas du PET, Ph.D. Thesis, Ecole Normale Supérieure de Cachan, ENS Cachan, France.
- [37] P. Lebaudy and J. Grenet, 2001, Heating Simulation of Multilayer Performs, *Applied Polymer Science*, Vol. 80, pp. 2683-2689.
- [38] A. Denis, 1995, Etude Expérimental et Modélisation du Chauffage par Rayonnement Infrarouge de Polymères Semi-Cristallins: Influence des Centres Diffusants", Ph.D. Thesis, Université du Rouen, Rouen, France.
- [39] L. Dong, 2007, Simulation et Modélisation du Frittage Selectif par Laser Apr ès la Methode des Elements Finis, Ph.D. Thesis, Université Louis Pasteur, Strasbourg, France.
- [40] R. West, D. Gibbs, L. Tsang and A.K. Fund, 1994, Comparison of Optical Scattering Experiments and the Quasy-Crystalline Approximation for Dense Media, *J. Optics A*, Vol. 11, pp. 1854-1858.
- [41] Prah SA, Keijzer MR. Dosimetry of laser radiation in medicine and biology. A Monte Carlo model of light propagation in tissue, *SPIE Insitute Series*, vol IS 5 Publications, 1989. p. 102–11.
- [42] L. Wang, S. L. Jacques and L. Zheng, 1995, MCML-Monte Carlo Modeling of Light Transport in Multi-Layered Tissues, *Computer Methods and Programs in Biomedicine*, Vol. 47, pp. 131-146.
- [43] T. Girasole, C. Rozé, B. Maheu, G. Gréhan and J. Ménard, 1998, Distances of Visibility in a Foggy Atmosphere: Comparisons Between Lighting Installations by Means of a Monte Carlo Simulation, *Int. J. Light Res. Tech.*, 30(1), pp. 29–36.
- [44] C. Lavigne, A. Roblin, V. Outters, S. Langlois, T. Girasole and C. Rozé, 1999, Comparison of iterative and Monte Carlo methods for calculation of the aureole about a point source in the Earth's atmosphere, *Appl. Opt.*, 38(30.), pp. 6237–46.
- [45] S.A. Prah, M. Keijzer and S.L. Jacques, 1989, A Monte Carlo Model of Light Propagation in Tissue, *Astrophysical J.*, Vol. 93, pp. 70-83.
- [46] Heinrich M. Jaeger and Sidney R. Nagel, 1996, Granular solids, liquids, and gases, *Reviews of Modern Physics*, 68: 1259-1273.

- [47] Simone A. Zavattoni, Maurizio C. Barbato, Andrea Pedretti, Giw Zanganeh, 2011, CFD SIMULATIONS OF A PEBBLE BED THERMAL ENERGY STORAGE SYSTEM ACCOUNTING FOR POROSITY VARIATIONS EFFECTS, Conference of SolarPACES, 20–23 September 2011, Granada (Spain).
- [48] F. Bertrand, L. A. Leclaire, G. Levecque, 2005, DEM-based models for the mixing of granular materials, *Chemical Engineering Science* 60: 2517–2531.
- [49] M. Jebahi, D. Andre, I. Terreros and I. Iordanoff, *Discrete elements Method to Model 3D Continuous Materials*, 2015, Wiley, London, UK.
- [50] Hohenberg P., Kohn W., 1964, Inhomogeneous electron gas, *Physical Review B*, 136:864-871.
- [51] Payne M., Teter M., Allan D., 1992, Iterative minimization techniques for ab initio total-energy calculation: molecular dynamics and conjugate gradients, *Reviews of Modern Physics*, 64:1045-1097.
- [52] Alder B., Wainwright T., 1957, Phase transition for a hard sphere system, *Journal of Chemical Physics*, 27:1208-1209.
- [53] Alder B., Wainwright T., 1959, Studies in molecular dynamics: General method, *Journal of Chemical Physics*, 31:459-466.
- [54] Abraham F.F., Walkup R., Gao H., 2002, Simulating materials failure by using up to one billion atoms and the world's fastest computer: brittle fracture, *Proceedings of the National Academy of Sciences of the United States of America*, 99:5777-5782.
- [55] Cundall P.A., 1971, Computer model for simulating progressive large scale movements in blocky rock systems, *Proceedings of the Symposium of the International Society of Rock Mechanics*, Nancy, France.
- [56] P. Furmanski, 1992, Effective macroscopic description for heat conduction in heterogeneous materials. *International Journal of Heat and Mass Transfer*, 35(11):3047–3058.
- [57] Y. Zhang, A. Faghri, C. Buckley, and T. Bergman. Three-dimensional sintering of two component metal powders with stationary and moving laser beams. *Journal of heat transfer*, 122(1):150–158, 2000.
- [58] Ram Dayal Jodhpur, 2014, "Numerical Modelling of Process Governing Selective Laser Sintering", Ph.D. Thesis, Darmstadt, Germany.
- [59] Svoboda J, Riedel H. *Acta Metall Mater* 1995;43:1.
- [60] Riedel H, Blug B. A comprehensive model for solid state sintering and its application to silicon carbide. In: Chuang TG, Rudnicki JW, editors. *Multiscale deformation and fracture in materials and structures*, The James R. Rice 60th Anniversary Volume. Dordrecht: Kluwer; 2001. p. 49–70.
- [61] Kraft T, Riedel H. *J Eur Ceram Soc* 2004;24:345.
- [62] Taylor GI. *J Inst Metal* 1938;63:307.
- [63] Bishop JFW, Hill R. *Philos Mag* 1951;42:414.
- [64] Svoboda J, Riedel H, Zipse H. *Acta Metall Mater* 1994;42:435.
- [65] Riedel H, Zipse H, Svoboda J. *Acta Metall Mater* 1994;42:445.
- [66] B. Henrich, A. Wonisch, T. Kraft, M. Moseler, H. Riedel, 2007, Simulations of the influence of rearrangement during sintering, *Acta Materialia*, 55:753–762.
- [67] Thomas Breinlinger, Pit Polfer, Adham Hashibon, Torsten Kraft, 2013, Surface tension and wetting effects with smoothed particle hydrodynamics, *Journal of Computational Physics*, 243:14–27.
- [68] I.A. Roberts, C.J. Wang, R. Esterlein, M. Stanford, D.J. Mynors, 2009, "A three-dimensional finite element analysis of the temperature field during laser melting of metal powders in additive layer manufacturing", *International Journal of Machine Tools & Manufacturing*, Vol. 49, pp. 916-923.
- [69] Chen T.B., Zhang Y.W., 2007, "Thermal modeling of laser sintering of two component metal powder on top of sintered layers via multi-line scanning", *Applied Physics A*, Vol. 86, pp. 213-220.
- [70] Donghua Dai, Dongdong Gu, 2014, "Thermal behavior and densification mechanism during selective laser melting of copper matrix composites: Simulation and experiments", *Materials and Design*, Vol. 55, pp. 482-491.
- [71] P. Fischer, N. Karapatis, V. Romano, R. Glardon, H.P. Weber, 2002, "A model for the interaction of near-infrared laser pulses with metal powders in selective laser sintering", *Applied Physics A*, 467-474.
- [72] Yuwen Zhang, A. Faghri, C. W. Buckley, T. L. Bergman, 2000, "Three-dimensional sintering of two component metal powders with stationary and moving laser beams", *Journal of heat transfer*, 122(1):150-158.
- [73] A. V. Gusarov, T. Laoui, L. Froyen and V. Titov, 2003, "Contact thermal conductivity of a powder bed in selective laser sintering", *International Journal of Heat and Mass Transfer*, 131(7):072101.

- [74] THC Childs, M Berzins, G. R. Ryder and A. Tontowi, 1999, "Selective laser sintering of an amorphous polymer-simulations and experiments", *Proceedings of the Institution of Mechanical Engineers, Part B : Journal of Engineering Manufacturing*, 213: 333-349.
- [75] Nelson J.C., Xue S., Barlow J. W., Beaman J.J., Marcus H.L., and Bourell D.L., 1993, "Model of the selective laser sintering of bisphenol-A polycarbonate", *Industrial & Engineering Chemistry Research*, 34(5): 1641-1651.
- [76] Gabriel Bugada, Miguel Cervera and Guillermo Lombera, 1999, "Numerical prediction of temperature and density distributions in selective laser sintering processes", *Rapid Prototyping Journal*, 5(1):21-26.
- [77] Jeffrey P. Schuktz, 2003, "Modeling heat transfer and densification during laser sintering of viscoelastic polymers", Ph.D. Thesis, Virginia Polytechnic Institute, Blacksburg, VA.
- [78] Hanaor, D. A. H.; Gan, Y.; Einav, I. (2015). "Contact mechanics of fractal surfaces by spline assisted discretisation". *International Journal of Solids and Structures* 59: 121–131
- [79] Waston L. Vargas, J.J. McCathy, 2002, Conductivity of granular media with stagnant interstitial fluids via thermal partial dynamics simulation, *Journal of Heat and Mass transfer*, 45:4847-4856.
- [80] Bodhisattwa Chaudhuri, Fernando J. Muzzio, M. Silvina Tomassone, 2006, Modeling of heat transfer in granular flow in rotating vessels, *Chemical Engineering Science*, 61 :6348 – 6360.
- [81] Suk-Joong L. Kang, 2005, "Sintering: densification, grain growth and microstructure", Elsevier, Oxford, UK.
- [82] R. L. Coble, 1961, Sintering Crystalline Solids. I. Intermediate and Final State Diffusion Models, *J. Appl. Phys.* 32, 787.
- [83] Frenkel, J., 1945, Viscous flow of crystalline bodies under the action of surface tension. *J. Phys.*, 9, 385-391.
- [84] Sun, M., Beaman, J., 1991. A three dimensional model for selective laser sintering. *Solid Freeform Fabrication Proceedings*, Austin.
- [85] Pokluda, O., Bellehumeur, C., Vlachopoulos, J., 1997. Modification of Frenkel's Model for Sintering. *AIChE Journal*, 43, 3253-3256.
- [86] Eshelby, J. (1949). Discussion of 'Seminar on the Kinetics of Sintering'. *Metallurgical Transactions*, 185, 796–813
- [87] D. Bouvard, R. M. McMeeking, 1996, Deformation of Inter-particle Necks by Diffusion Controlled Creep, *Journal of the American Ceramic Society*, 79, 666-672.
- [88] Johnson, K., Kendall, K., Roberts, A. (1971). Surface Energy and the Contact of Elastic Solids. *Proceedings of the Royal Society of London*, 324, 301-313.
- [89] F.B. Swinkels, M.F. Ashby, 1981, A second report on sintering diagrams, *Acta Metallurgica*, 29:259-281.
- [90] Abbas Tcharkhtchi, Rotomoulage de pièces en matière thermoplastique, AM3 706-1, *Techniques de l'Ingénieur*.
- [91] Jeffrey P. Schultz, 2003, Modeling Heat Transfer and Densification during Laser Sintering of Viscoelastic Polymers, PhD Thesis, Blacksburg, VA, USA.
- [92] W.J. Huppmann, H. Riegger, 1975, MODELLING OF REARRANGEMENT PROCESSES IN LIQUID PHASE SINTERING, *Acta Metall.*, 23: 965–971.
- [93] M. Kontopoulou, J. Vlachopoulos, 1999, Bubble dissolution in molten polymers and its role in rotational molding, *Polymer Engineering and Science*, 39:1189-1198.
- [94] Ross, J., Miller, W., Weatherly, G. (1981). Dynamic computer simulation of viscous flow sintering kinetics. *Journal of Applied Physics*, 52, 3884-3888.
- [95] Jagota, A., Dawson, P. R. (1990). Simulation of the Viscous Sintering of Two Particles. *Journal of the American Ceramic Society*, 73, 173-177.
- [96] Martinez-Herrera, J. I., Derby, J. J. (1994). Analysis of capillary driven viscous flows during the sintering of ceramic powders. *A.I.Ch.E. Journal*, 40, 1794-1803.
- [97] Zhou, H., Derby, J. (1998). Three-dimensional finite-element analysis of viscous sintering. *Journal of the American Ceramic Society*, 81, 533-540.
- [98] Walkley, M., Gaskell, P., Jimack, P., Kelmanson, M., Summers, J. (2005). Finite Element Simulation of Three-Dimensional Free-Surface Flow Problems. *Journal of Scientific Computing*, 24, 147-162.
- [99] Zhou, H., Derby, J. (2001). An assessment of a parallel, finite element method for three-dimensional, moving-boundary flows driven by capillarity for simulation of viscous sintering. *International Journal for Numerical Methods in Fluids*, 36, 841-865.

- [100] Hiram, Y., Nir, A. (1983). A Simulation of Surface Tension Driven Coalescence. *Journal of Colloid and Interface Science*, 95, 462-470.
- [102] Van der Vorst, G., Mattheij, R., Kuiken, H. (1992). A boundary element solution for two-dimensional viscous sintering. *Journal of Computational Physics*, 100, 50-63.
- [103] Van der Vorst, G. (1993). Integral method for a two-dimensional Stokes flow with shrinking holes applied to viscous sintering. *Journal of Fluid Mechanics*, 257, 667-689.
- [104] Van der Vorst, G. (1994). Modelling and numerical simulation of viscous sintering. PhD thesis, Eindhoven University of Technology.
- [105] Garabedian, R., Helble, J. (2001). A Model for the Viscous Coalescence of Amorphous Particles. *Journal of Colloid and Interface Science*, 234, 248-260.
- [106] Garabedian, R., Helble, J. (2007). Modeling coalescence in multiple-particle systems. *Journal of Aerosol Science*, 39, 71-81.
- [107] C. Martin, R. Bordia, *Acta Mater.* 57 (2009) 549–558.
- [108] C.L. Martin, H. Camacho-Montes, L. Olmos, D. Bouvard, R.K. Bordia, *J. Am. Ceram. Soc.* 92 (2009) 1435–1441.
- [109] B. Henrich, A. Wonisch, T. Kraft, M. Moseler, H. Riedel, *Acta Mater.* 55 (2007) 753–762.
- [110] C. Wang, S. Chen, *Comput. Mater. Sci.* 69 (2013) 14–21.
- [111] C. Martin, L. Schneider, L. Olmos, D. Bouvard, *Scripta Mater.* 55 (2006) 425–428.
- [112] A. Wonisch, O. Guillon, T. Kraft, M. Moseler, H. Riedel, J. Rödel, *Acta Mater.* 55 (2007) 5187–5199.
- [113] A. Vagnon, J. Rivière, J. Missiaen, D. Bellet, M. Di Michiel, C. Josserond, D. Bouvard, *Acta Mater.* 56 (2008) 1084–1093.
- [114] O. Lame, D. Bellet, M. Di Michiel, D. Bouvard, *Acta Mater.* 52 (2004) 977–984.
- [115] L. Olmos, C.L. Martiin, D. Bouvard, D. Bellet, M. Di Michiel, *J. Am. Ceram. Soc.* 92 (2009) 1492–1499.
- [116] L. Olmos, C.L. Martin, D. Bouvard, Selection of Papers from the Symposium Powder Science and Technology – Powders and Sintered Material STP-PMF 2007 190, 2009, pp. 134–140.
- [117] Patrice Peyre, Yann Rouchausse, Denis Defauchy and Gilles Regnier, 2015, "Experimental and numerical analysis of the selective laser sintering (SLS) of PA12 and PEEK semi-crystalline polymers", *Journal of Materials Processing Technology*, 225:326-336.
- [118] Glen Pearson, Stanley Middleman, 1977, Elongational flow behavior of viscoelastic liquids: Part I. Modeling of bubble collapse, *AIChE Journal*, 23: 714-718.
- [119] C. H. Bennett. Serially deposited amorphous aggregates of hard spheres. *Journal of applied physics*, 43(6):2727–2734, 1972.
- [120] W. L. Vargas and J. J. McCarthy. Heat conduction in granular materials. *AIChE Journal*, 47(5):1052–1059, May 2001.
- [121] W. M. Visscher and M. Bolsterli. Random packing of equal and unequal spheres in two and three dimensions. *Nature*, 239:504–507, 1972.
- [122] W. Jodrey and E. Tory. Computer simulation of isotropic, homogeneous, dense random packing of equal spheres. *Powder Technology*, 30(2):111–118, 1981.
- [123] B. D. Lubachevsky. How to simulate billiards and similar systems. *Journal of Computational Physics*, 94(2):255–283, 1991.
- [124] P. A. Cundall and O. D. L. Strack. A discrete numerical model for granular assemblies. *Géotechnique*, 29(1):47–65, Jan. 1979.
- [125] H. Zhu, Z. Zhou, R. Yang, and A. Yu. Discrete particle simulation of particulate systems: theoretical developments. *Chemical Engineering Science*, 62(13):3378–3396, 2007.
- [126] John C. Steuben, Athanasios P. Iliopoulos, John G. Michopoulos, 2016, Discrete element modeling of particle-based additive manufacturing processes, *Comput. Methods Appl. Mech. Engrg.* 305: 537–561.
- [127] E. Rougier, A. Munjiza, N.W.M. John, Numerical comparison of some explicit time integration schemes used in DEM, FEM/DEM and molecular dynamics, *Internat. J. Numer. Methods Engrg.* 61 (6) (2004) 856–879.
- [128] Jorge I. Martínez-Herrera, Jeffrey J. Derby, 1995, Viscous sintering of spherical particles via finite element analysis, *Journal of the American Ceramic Society*, 78:645-649.
- [129] Hua Zhou, Jeffrey J. Derby, 1998, Three dimensional finite element analysis of viscous sintering, *Journal of the American Ceramic Society*, 81:533-540.

Chapter IV: Results and Discussions

In this chapter, the model developed in the previous chapters is used to simulate the physical phenomena during SLS process. The present chapter is structured into four principle parts. The first part is dedicated to the investigation of energy absorption and heat transfer in the powder bed subjected to moving laser source. Two comparisons are then proposed, in order to highlight the effect of scattering. Furthermore, the simulated results are also compared with experimental data from the literature, so as to confirm the validation of the synthetic model. In the second part, the SLS process with successive layers of powders is simulated. At different positions, the thermal behavior of grains is investigated so as to observe the variation of temperature inside powder bed in the real manufacturing process. Moreover, based on the model, the relative density of sintered part is predicted and compared with experimental results from the literature. In the third part, the influences of parameters on SLS process are deeply analyzed. Finally, in the last part, the model is applied to simulate the balling phenomenon and implement a test simulation, so as to present its capability of capturing the spatially and temporally varying distribution of heat and displacement within the additively manufacturingd object, meanwhile, predicting geometric features.

1. Simulation of SLS process without successive layers of powders

To our knowledge, most numerical studies of SLS [1-5] deal with the process in a certain powder bed without successive layers of powders. Therefore, in this section, 3D numerical simulations of SLS process without successive layers of powders are proposed. Firstly, in order to highlight the effect of scattering on the thermal diffusion in SLS process, the energy distribution and the temperature evolution with different types of laser heat sources are simulated in two different SLS processes. Furthermore, the model is applied to predict main dimensions of sintered lines. The results predicted are compared with experimental results from literature so as to confirm the validity of model. Finally, the model is used to estimate the relative density of sintered part.

1.1. Model implementation

In order to simulate the thermal diffusion in SLS process, the model includes two part: laser radiation submodel and heat conduction submodel. For laser radiation submodel, in most researches of SLS process [3-5], the laser beam is usually assumed as a boundary or a volumetric heat source, without taking into account the phenomenon of scattering. If considering the scattering, the modified Monte Carlo ray tracing method is suitable to simulate the interaction between laser and semi-transparent medium (section III-3.4).

Boundary heat source:

In Lin's thesis [1], the powder bed is considered as an opaque medium, where the interaction between laser and grains only occurs at the surface of powder bed. He used a boundary heat source model to describe the laser energy distribution at the surface of powder bed, given by:

$$I_{boundary} = (1 - R_e)I_{0b}e^{-\frac{2(r^2)}{w^2}} \quad (IV-1.1)$$
$$I_{0b} = \frac{2P}{\pi w^2} \quad w = \frac{R_L}{2.146}$$

where R_e is the reflective coefficient on the surface, r is the radial distance from the center of laser beam, P is the power of laser beam, R_L is the radius of laser beam.

Volumetric heat source without scattering

In the same situation, in order to simulate interaction between laser and semitransparent polymers, Defauchy [3] assumed a volumetric heat source applied in the powder bed. The evolution within the thickness is modeled using the Beer-Lambert Law with a material attenuation factor:

$$I_{body} = (1 - R_e)\alpha I_{0bd}e^{-\frac{2(r^2)}{w^2}}e^{-\alpha z} \quad (IV-1.2)$$
$$I_{0b} = \frac{2P}{(1 - e^{-2*2.146^2})\pi w^2} \quad w = \frac{R_L}{2.146}$$

Volumetric heat source with scattering

When considering the scattering, the distribution of laser energy inside powder bed is obtained from the simulation based on modified Monte Carlo Ray Tracing method, which has been deeply explained in section III-3.5. The link between heat conduction model and modified Monte Carlo Ray Tracing method is also explained in section III-7.3.

For heat conduction submodel, two different numerical methods (FEM and DEM) are introduced so as to highlight the granular character of powder bed and its influence on thermal diffusion. The heat conduction submodel based on DEM has been fully explained in section III-4.

1.2. Influences of scattering on distribution of laser energy

To our knowledge, until now, few literature concerning the SLS process takes the influence of scattering into consideration. However, each parameter of laser beam (like laser power, beam radius and scanning velocity) is very crucial and can even determine the performance of final product. Based on the previous researches [25-28], it is well known that the scattering will strongly impacts the distribution of laser energy in case of laser-granular interaction. Therefore, the importance of scattering is equivalent to other parameters of laser beam. So the first results of our works will research the influence of scattering on distribution of laser energy inside powder bed.

In order to highlight the effect of scattering on the distribution of laser energy, three different models are implemented by Matlab: (1) theoretical volumetric model, which is directly derived from Beer-Lambert law and obeys Gaussian distribution at the surface; (2) volumetric model without scattering, which is implemented by modified Monte Carlo Ray Tracing method. But the scattering direction is fixed as total forward and non scattering; (3) volumetric model with scattering, which is directly obtained from the modified Monte Carlo Ray Tracing method, which has been fully explained in section III-3.5.

To compare results of these different models, a simulation of laser-particle interaction is implemented in a powder bed with dimension of $200\mu\text{m} \times 200\mu\text{m} \times 100\mu\text{m}$. The radius of incident laser beam is $50.8\mu\text{m}$ with the power of 10W. The reflectivity of powder bed surface R_e is 0.04 and the particle diameter is $10\mu\text{m}$. Values of anisotropy factor g range normally from 0.3 to 0.98 for a high scattering medium, but it is commonly taken equal to 0.9 for high wavelengths [29], as is the case for a CO_2 laser. The initial conditions for our modified Monte Carlo method are listed in Table IV-1.1. The radiation fluxes are normalized by the maximum incident radiation flux q_0 as $\bar{q} = q/q_0$ with dimensionless coordinates as optic radius $\tau_r = \alpha r$, where r is the distance from the position to the center of laser beam.

Table IV-1.1. Initial conditions

Number of photons	5E+6
Initial scattering direction u_0	(0,0,1)
Anisotropy factor g	0.9
Attenuation coefficient α [m^{-1}]	20000

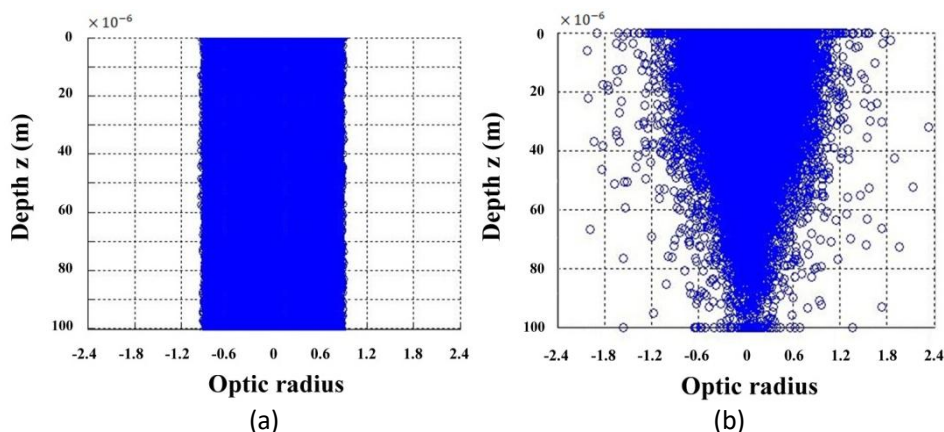


Fig.IV-1.1. Distribution of photon scattered positions:
(a) volumetric model without scattering; (b) volumetric model with scattering.

Fig.IV-1.1 presents the distribution of photon scattering positions obtained from different volumetric models. Each blue point represents that a photon is scattered at that position. In case without scattering as illustrated in Fig.IV-1.1(a), all photons are constrained in the laser beam area with a cylindrical shape

because photons propagate together forward as a whole. However, when considering the scattering as illustrated in Fig.IV-1.1(b), the distribution area of photons is much larger than that in Fig.IV-1.1(a). Besides, most of the radiative energy is concentrated near the surface and the distribution area of photons shrinks with increasing depth. In fact, the direction of photon propagation is random and not longitudinal. This leads to a heated zone at the surface larger than that at the bottom as it can be naturally expected from optical considerations.

Clearly, the rearrangement of photon distribution is caused by scattering: much larger distribution area and more concentration of radiative energy near the surface as illustrated in Fig.IV-1.1. In order to make a more precise comparison and to highlight the scattering effect, a 2D distribution of normalized laser intensity with different optical depths is shown in Fig.IV-1.2. Two different distributions of normalized intensity without considering scattering are shown in Fig.IV-1.2(a) and (b), where the intensity distribution is modeled based on the same model but obtained from different numerical methods: the theoretical volumetric model via Beer- Lambert law as in Defauchy [3] is directly derived from its analytical solution. While, the volumetric model without scattering is also based on Beer-Lambert law but obtained from modified Monte Carlo Ray Tracing method in case of fully forward scattering. Of course, the volumetric model without scattering should be equivalent to the theoretical model. This is confirmed by Fig.IV-1.2(a) and (b), where the differences of laser intensity distributions are negligible and the extinction of laser intensity is in accordance with the Beer-Lambert law. Besides, the laser energy is only distributed in the area of the incident beam because photons totally propagate forward without any scattering.

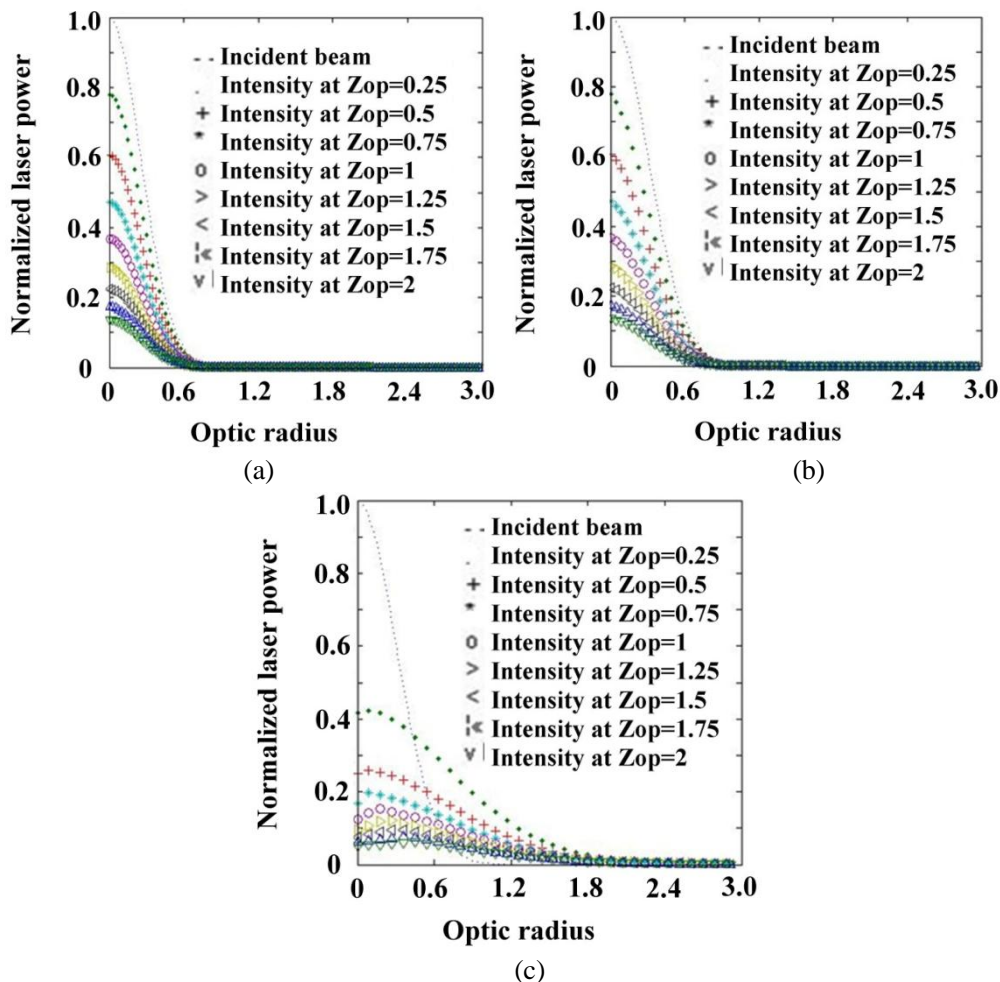


Fig.IV-1.2. 2D distribution of the normalized laser intensity in powder bed with various optical depths $Z_{op} = az$ based on different heat source models: (a) theoretical volumetric model; (b) volumetric model without scattering; (c) volumetric model with scattering

When the scattering is taken into consideration as shown in Fig.IV-1.2(c), the distribution area of

laser intensity becomes much larger than that in others of Fig.IV-1.2 and the major part of laser intensity becomes concentrated in an area with depth less than 1 optical thickness. This is because photons change their propagation direction when travelling inside the powder bed due to the effect of scattering. These results are consistent with those from Fig.IV-1.1. In other words, the effective radius of laser beam is enlarged due to the influence of scattering. This phenomena has been experimentally confirmed by Defauchy [3]. Generally, the effect of scattering is not negligible because it will cause a strong rearrangement of laser intensity that will finally largely affects the size and depth of the heated region in the powder bed.

1.3. Effects of scattering on thermal diffusion

As we mentioned in section IV-1.1, the scattering phenomenon has a great influence on the thermal radiation in granular medium. Therefore, in this section, we deeply analyze the effect of scattering on thermal diffusion during SLS process. In the case of polymeric material, many researchers have studied the energy absorption and heat transfer in SLS process based on Finite Element Method (FEM) [1,3-5]. Nevertheless, little research has been devoted to simulate the thermal behavior in SLS process based on Discrete Element Method (DEM). Thus, firstly, we implemented numerical simulations based on FEM that repeat the works of Lin [1] and Defauchy [3]. And then, other models are proposed at the same conditions based on different approaches of laser source and DEM. New results are compared with the previous one so as to highlight the influence of scattering on thermal diffusion and limitations of FEM when applied to granular material.

1.3.1. Results and discussion

1.3.1.1. Single laser scanning

In this section, the effect of scattering in case with single laser scanning is studied. Firstly, we repeated the work of Defauchy [3] based on FEM. Then, the result is compared to those obtained from models based on the modified Monte Carlo ray tracing method and DEM. Since the heat source model used by Defauchy [3] is volumetric without scattering, the model of boundary heat source is not introduced in this section.

In FEM modeling, the SLS process is simulated in a cuboid box with the dimension of $900\mu\text{m} \times 900\mu\text{m} \times 1000\mu\text{m}$. The finite elements mesh is built by COMSOL software and consisting in 1646264 domain elements, 29710 boundary elements, and 552 edge elements. The maximal size of element is $55\mu\text{m}$. We build our own program of numerical model based on DEM implemented by Fortran90. 13988 PEEK particles with diameter of $24\mu\text{m}$ are deposited in a box with the dimension of $900\mu\text{m} \times 900\mu\text{m} \times 1500\mu\text{m}$. The total mass of grains in DEM is the same as that of powder bed used in FEM. During SLS process, the laser beam scans powder bed in the longitudinal direction ($v_x = 0.5 \text{ m/s}$) for a total length of $600\mu\text{m}$. The initial temperature of powder bed is 573.15K . The temperature of air around the box is 323.15K . The diameter and power of laser beam is $300\mu\text{m}$ and 5W , respectively. The extinction coefficient is 7500m^{-1} . The density of neat polymer is 1327kg/m^3 . The thermal conductivity is $0.25 \text{ W/m} \cdot \text{K}$. The specific heat capacity is $1320 \text{ J/kg} \cdot \text{K}$. The convective heat transfer coefficient with air is $15 \text{ W/m}^2 \cdot \text{K}$. The starting melting temperature T_{mS} and total melting temperature are 552.15K and 611.15K , respectively. According to Defauchy [3], the thermal-physic properties are assumed to be independent from the temperature. To analyze the thermal diffusion in the powder bed, we pick four points at different location in the bed thickness ($0\mu\text{m}$, $250\mu\text{m}$, $500\mu\text{m}$, $750\mu\text{m}$), which are perpendicular to the laser beam path at the center of powder bed.

In Fig.IV-1.3, for both methods, the shape of the temperature evolution curves is similar: the powder bed is heated very quickly and its temperature sharply increases at the very beginning of the simulation. But we can clearly observe that the peak temperatures are different in Fig.IV-1.3(a) and (b). These two results are obtained in the same conditions and implemented by FEM but based on different heat source models. In Fig.IV-1.3(a), the results is directly obtained from Defauchy [3] and the influence of scattering is not considered. The results presented in Fig.IV-1.3(b) is obtained based on the volumetric heat source

with scattering. When considering the scattering, the peak temperature is higher at surface (thickness = 0 μm) but lower at deeper locations. That is because the major part of laser energy is absorbed by the region closed to the surface, as confirmed in section IV-1.1. The equilibrium temperature is still identical at the end of simulation.

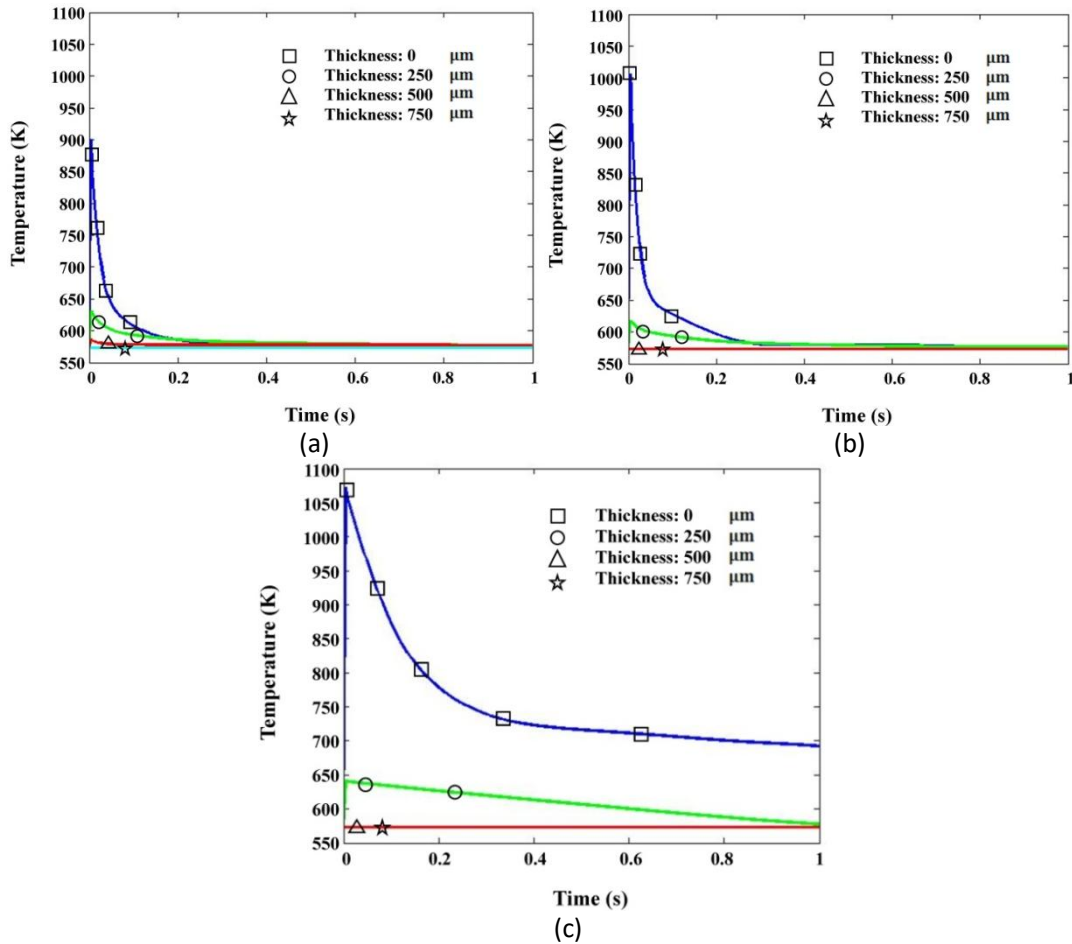


Fig.IV-1.3. Time-temperature profile at four different points in the thickness based on FEM and DEM:
 (a) FEM results with volumetric heat source from Defauchy[3];
 (b) FEM results with volumetric heat source with scattering;
 (c) DEM results with volumetric heat source with scattering.

In Fig.IV-1.3(c), the result is obtained based on Discrete Element Method(DEM) and its value of peak temperature at surface is higher than the other two results. This is because, in case of DEM, the laser energy is totally absorbed by particles and the heat diffusion in the air between particles is neglected due to its low heat conductivity. However, in case of FEM, partial laser energy is absorbed by the air inside powder bed. Besides, the effective heat conductivity of powder bed is smaller than homogenous material as mentioned in section III-4. Therefore, the equilibrium temperature within the whole powder bed is reached much later.

1.3.1.2. Double laser scanning

Previously, we studied the laser-powder interaction with a single scan. Now, we propose to apply our model to analyze the heat diffusion occurring in the powder bed caused by the laser with two scans. For the need of comparison with the work of Lin et al. [4], the SLS process in polycarbonate powder bed is simulated. All the physical properties and initial conditions, needed for numerical simulation, are listed in Table.IV-2. We firstly repeated the work of Lin et al. [4] and then compare the results to those obtained from different heat source models and DEM.

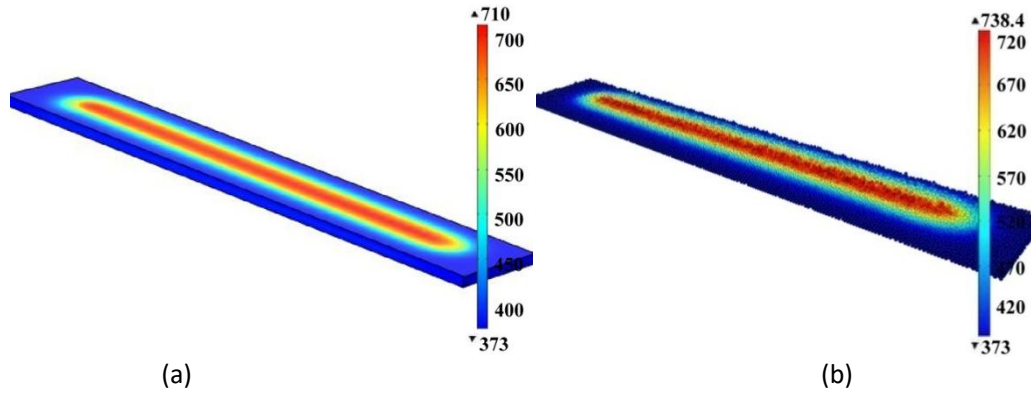


Fig.IV-1.4. Temperature field in powder bed: (a) FEM (b) DEM

The conductive heat diffusion in SLS process is simulated by both finite elements method (FEM) and discrete elements method (DEM) as illustrated in Fig.IV-1.4. The SLS process is simulated in a cuboid specimen with the dimension of $5000 \times 800 \times 100 \mu\text{m}$. For DEM, 27631 particles with diameter of $25 \mu\text{m}$ are deposited in a box with the dimension of $5000 \mu\text{m} \times 800 \mu\text{m} \times 200 \mu\text{m}$. The total mass of grains in DEM is the same as that of the specimen used in FEM. During SLS process, the laser beam double scans the specimen (powder bed) in the longitudinal direction ($v_x = v, v_y = 0$) for a total length of 4 mm. To analyze the thermal diffusion in the powder bed, the laser beam scans two adjacent lines with a hatch spacing of $76.2 \mu\text{m}$. We analyzed the temperature evolution of three points at different thicknesses as shown in Fig.IV-1.4. The laser displacement is defined as a function of time:

$$\begin{cases} x_L = x_0 + v_x t \\ y_L = y_0 + v_y t \end{cases} \quad (\text{IV-1.3})$$

where (x_L, y_L) is the position of laser beam center, v_x and v_y are the beam velocities in x and y directions.

Table.IV-2. Initial conditions and material properties

Property	Value	Property	Value
Preheating temperature, T_a [K]	373	Reflectivity of powder surface, R_e	0.04
Glass transition temperature, T_g [K]	418	Attenuation coefficient, α [m^{-1}]	20000
Initial powder density, ρ_0 [kg/m^3]	600	Convective coefficient, h [$\text{J}/\text{sm}^2\text{K}$]	25
Initial porosity, β_0	0.5	Surface emissivity, ϵ_R	0.8
Fully material density, ρ_{max} [kg/m^3]	1200	Activation energy, E [kJ/mol]	149.66
Laser beam radius, R_L [mm]	0.508	Velocity of laser beam, v [m/s]	1.64
Arrhenius coefficient, A_r [s^{-1}]	8.84×10^{16}	Power of laser beam, P [W]	10

According to the work of Lin et al. [4], the material transformation from the powder phase to the solid phase is accompanied by the variation of the material local density ρ . The rate of density evolution of the powder bed is given by the following differential equation:

$$\frac{d\rho}{dt} = (\rho_{max} - \rho) \cdot A_r \cdot \exp\left(-\frac{E}{RT}\right)$$

where A_r is the Arrhenius coefficient, E is the activation energy, ρ_{\max} is the density of the solid material and R is the universal gas constant.

The heat conductivity and heat capacity of polycarbonate powder are proposed by Lin et al. [4]:

$$k_e = k_s(1 - 0.2\beta - 1.73\beta^2)$$

$$k_s = 0.02504 + 0.0005T$$

$$C_p = \begin{cases} -20.56 + 4.103 \times T & T \leq T_g \\ 935.34 + 2.284 \times T & T > T_g \end{cases}$$

where k_e is the effective heat conductivity, k_s is the heat conductivity of solid polycarbonate, T is the temperature and T_g is the glass transition temperature.

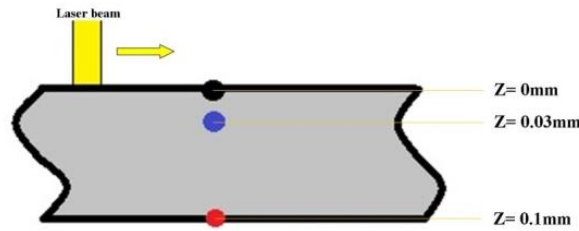
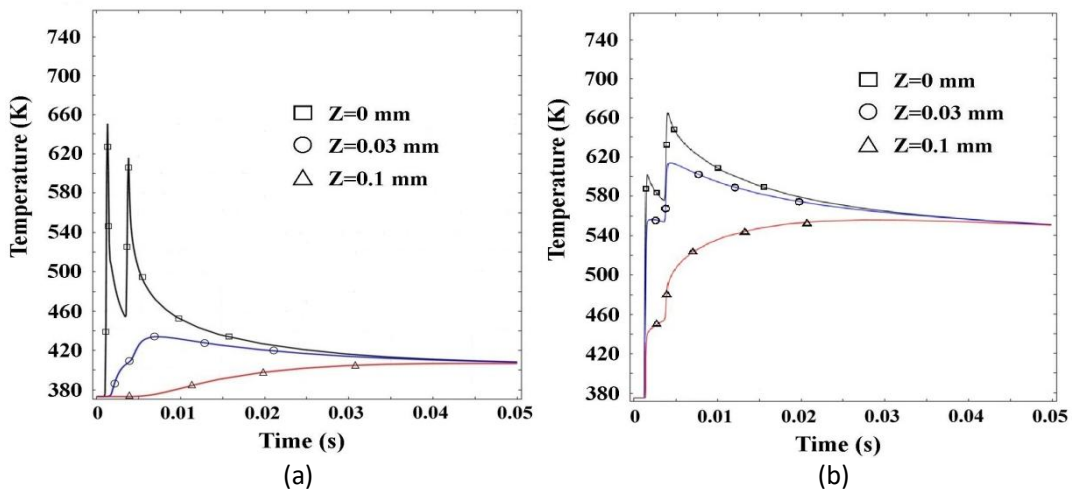


Figure IV-1.5. Illustration of the position of three points

In Fig.IV-1.6, we present a comparison between the results of three different heat source models. The first peak of temperature corresponds to the first laser passage and the second peak is attributed to the passage of the adjacent line. Only in Fig.IV-1.6(a), the second peak of temperature is lower than the first one. It is attributed to the case considering only surface energy distribution. In this case, the first laser beam scanning causes the phase change and increase of the relative density at specimen surface proposed by Lin et al. [4], which leads to a higher effective heat capacity per mass and results in decreasing of temperature at surface for the second scan. In Fig.IV-1.6(b) and (c), peak temperatures of two points near surface are higher when considering the scattering (based on modified Monte Carlo method). Because, due to the effect of scattering, major part of laser intensity is absorbed by the area closed to the surface as confirmed in section IV-1.1. For the same reason derived from Fig.IV-1.3, the peak temperature near surface in Fig.IV-1.6(d) is higher than those in Fig.IV-1.4(a),(b) and (c). Because, in case of DEM, we assume that the total energy is absorbed by particles. The absorption of air inside powder bed is ignored. But, the effective heat conductivity of powder bed is smaller than that of homogeneous material. Thus, the temperature homogenization need more time to be reached. The homogeneity of temperature in the whole material is reached after about four times of needed time in case of homogeneous material (0.2s instead of 0.05s) as presented in Fig.IV-1.6(e).



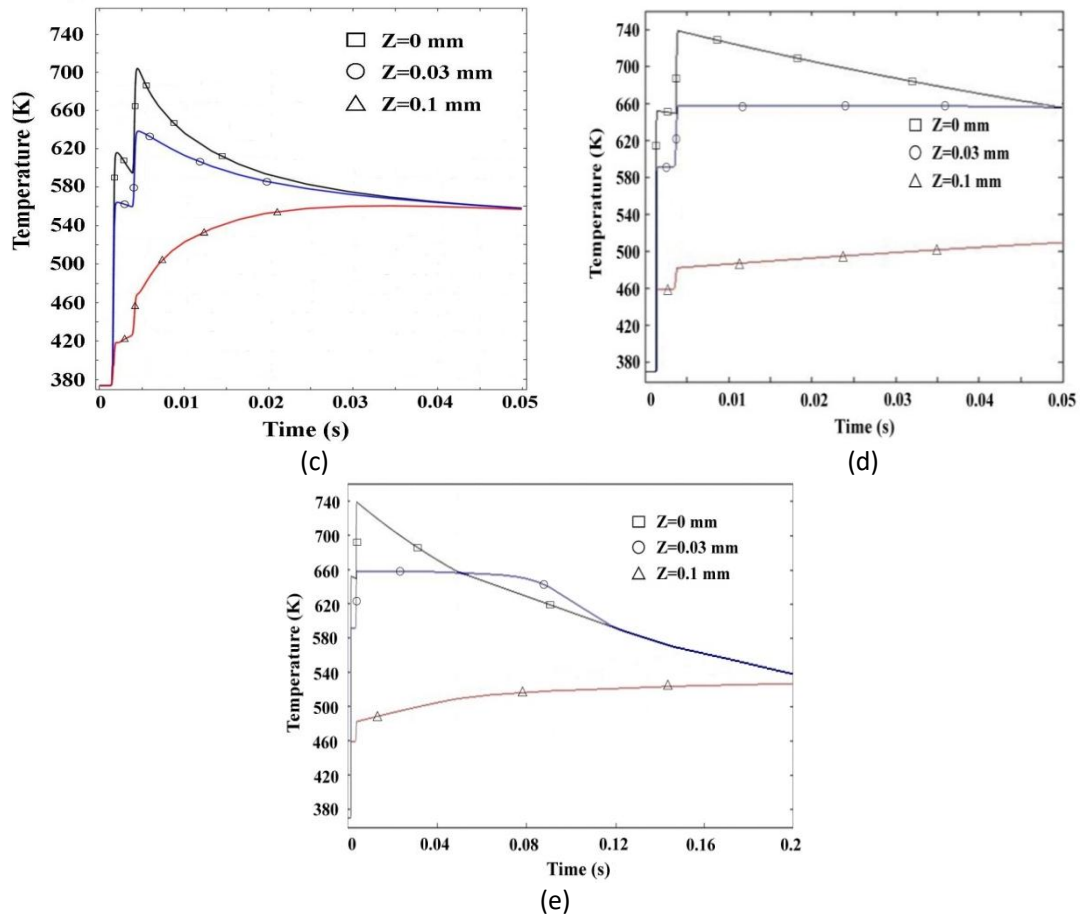


Figure IV-1.6. Time-temperature profile of three different points in FEM and DEM:
 (a) FEM results based on boundary heat source from Lin et al. [4];
 (b) FEM results based on volumetric heat source without scattering;
 (c) FEM results based on volumetric heat source with scattering;
 (d) DEM results based on volumetric heat source with scattering;
 (e) DEM results based on volumetric heat source with scattering in case of longer simulation time.

1.3.3. Partial conclusion

In this section, numerical simulations are proposed in the case of radiative heat transfer inside granular media. Typically, this phenomenon occurs in processes of additive manufacturing, as in selective laser sintering of metals or polymers. One important aspect of the problem is to obtain an precise estimation of the laser power distribution inside the granular medium, which highlights the influence of scattering on the interaction between laser and semi-transparent material.

A 3D numerical model based on Discrete Elements Method is established, in order to investigate the effect of scattering on the radiative heat transfer and heat diffusion in polymer powder bed during laser sintering process. To our knowledge, for the first time, a comprehensive model concerning SLS process is proposed in the case of polymer. It couples phenomena of the absorption, scattering, reflection, convection and heat conduction.

Based on two different numerical methods (FEM and DEM), the energy distribution and the temperature evolution obtained by using different types of heat sources are simulated in two cases with single and double scan. The results showed that the scattering has a strong effect on the distribution of laser intensity in semi-transparent powder bed. Moreover, in the comparison between FEM (homogeneous material) and DEM (granular material), we clearly showed that regarding the powder bed as homogeneous material is not very practical. In other words, the introduction of discrete element method for modeling granular medium is suitable. Thus, for the aim of SLS process optimization, DEM is a more natural and accurate numerical method than FEM.

1.4. Validation of global model

A 3D global numerical model based on DEM has been proposed in chapter III, which includes four different submodels (radiation heat transfer, discrete heat conduction, sintering and contact dynamic). Without the inherent limitations of FEM when simulating physical behavior of granular medium, the model based on DEM help us to step further and allows to predict the precise size of sintered part. Hence, we proposed to compare simulated results of global model and experimental results from the literature.

1.4.1. Model implementation

To our knowledge, most of numerical studies working on SLS process is implemented in condition with one single layer of powders[1-6]. Meanwhile, we want to firstly confirm the global model in this section and then continue to simulate the SLS process with successive layers of powders in the later section. Thus, the contact dynamic submodel is not introduced here. The global model in this section is composed of three submodels: radiation heat transfer, discrete heat conduction and sintering.

For *radiation heat transfer submodel*, the modified Monte Carlo ray tracing method is applied to simulate the interaction between laser beam and powder bed (section III-3.5). For *discrete heat conduction submodel*, a heat transfer model based on DEM is developed to simulate the heat conduction in granular material (section III-4.4). For *sintering submodel*, the viscoelastic coalescence model and bubble dissolution theory are used to describe the behavior of grains during laser sintering (section III-5.5).

1.4.2. Comparison of numerical and experimental results

Due to the limitations of thermal measurements during SLS process, it is difficult to obtain an ideal experimental results of temperature evolution inside powder bed. Even though obtaining the temperature evolution by thermal camera, it turns out that there is a large difference between the simulated and experimental results[7]. Unlike existing models [1-6], our model has the potentiality to predict the precise size of sintered product. Therefore, it is interesting to validate our model by comparing the size of sintered region predicted by numerical simulation to that obtained from experiments.

For the validation of our model, the results predicted are compared with the experimental works from Franco et al. [7], who used a SLS machine to produce sintered lines with different levels of energy density. The PA12 powder has been selected because of its thermal properties which are representative of the typical range of most thermoplastics used for rapid prototyping. In Franco's work, basic sintered structures fabricated by scanning 80mm long lines on the powder bed are showed in Fig.IV-1.7, which were separated from the non-sintered polymer by emptying the powder container from bottom holes, as illustrated in Fig.IV-1.7. Before starting this procedure, the sintered lines were glued to the supporting parts of the container by a single drop of acrylic resin. As final step, non-sintered grains, which could affect the measuring process were removed by positioning the container on a vibrating device.

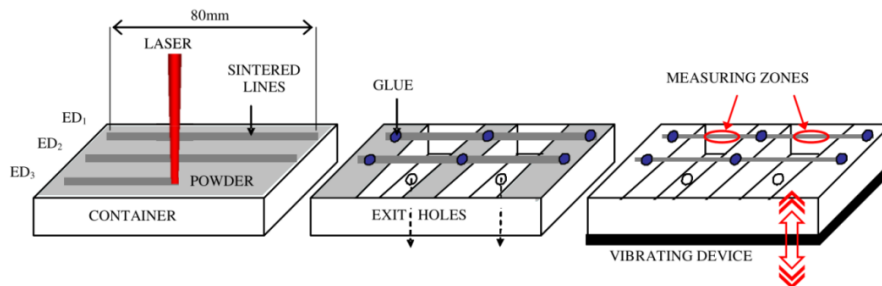


Fig.IV-1.7. Draft of the extraction procedure of the sintered lines [7]

In the simulation, 20308 particles with diameter of $50\mu\text{m}$ are randomly deposited in a box with the dimension of $2000\mu\text{m} \times 1000\mu\text{m} \times 1200\mu\text{m}$ as shown in Fig.IV-1.8. The laser beam single scans the powder

bed in the longitudinal direction with several velocities. The diameter of laser beam ϕ is 0.7mm with a power $P=50W$. The initial temperature T_0 of powder bed and room temperature T_a are the same as 293.15K. The density of particle ρ is 1030kg/m³. The conductivity k is 0.13W/m · K. The specific heat C_{p0} is 2500J/kg · K. The latent heat of melting ΔH_m is 90.8KJ/kg. The effective heat capacity C_p is dependent on the temperature and explained in section III-4.6. The starting melting temperature T_{ms} and total melting temperature are 448K and 507K, respectively. The extinction coefficient of Beer-Lambert law α is 9000m⁻¹.

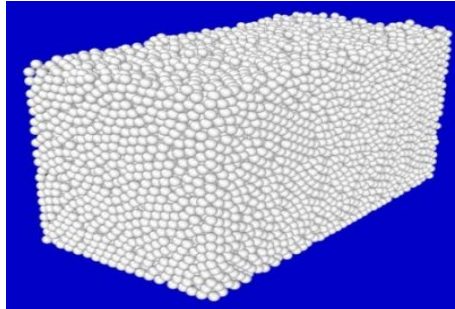


Fig.IV-1.8. Initial powder bed before laser treatment

After being single scanned by laser beam, the obtained sintered line of powder bed is shown in Fig.IV-1.9. The experimental result of Franco et al. [7] is presented in Fig.IV-1.9(a) with the average width of 320μm. In the same conditions of the experiments, the result of numerical simulation is shown in Fig.IV-1.9(b). The average width of sintered line (grains with white color) is 327.98μm, which is very close to the experimental result. Thus, the comparison of simulated and experimental average width of sintered line is very successful. However, only one successful comparison is not enough to validate the model. Therefore, more comparisons will be performed as following.

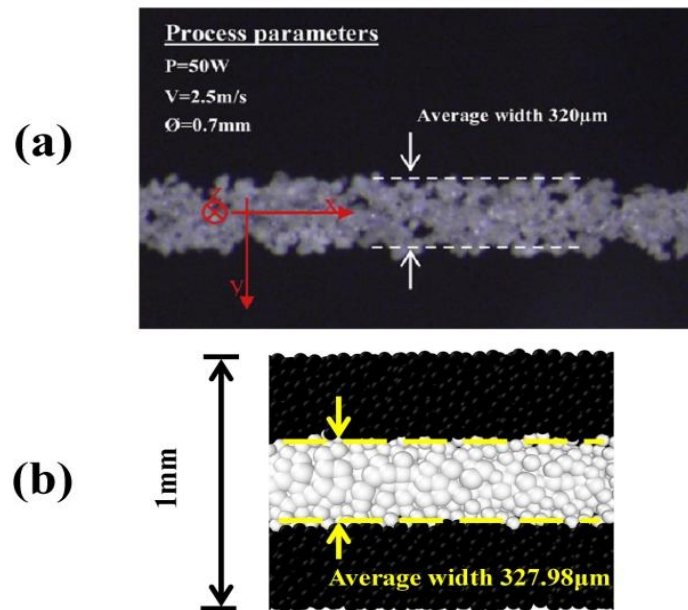


Fig.IV-9. Top view of a sintered line and measure of the averaged width: (a) Experimental result [7]; (b) Simulation result

In order to highlight the reliability and accuracy of simulated results, more comparisons are shown in Fig.IV-1.10 for five energy density ($ED=P/v\phi$). As shown in Fig.IV-1.10, both the width and depth of sintered line increase with the energy density. The increase of width is limited when the energy density is higher than 0.15 J/m². This can be attributed to the laser beam diameter, which restricts laser energy localized inside the irradiated region. The differences between simulated and experimental results can be explained by two possibilities: (1) the size of grain is not uniform in experiments. But we assume that the

size of each grain is identical for simplification. This dissimilarity of particle size can affect the final dimension of sintered line. (2) in SLS process, all grains randomly distribute in a certain volume, leading to the irregular shape of sintered line. The dissimilarity of grain distribution is impossible to be eliminated, which can also result in the difference between simulated and experimental results. However, in general, the average difference between simulated and experimental results is smaller than the average size of one grain, which indicates that the numerical results are acceptable and reasonable. Based on the comparison above, we can conclude that the model has a great potential in industrial applications, which is capable of predicting the geometry of product and helping to optimize parameters of SLS process.

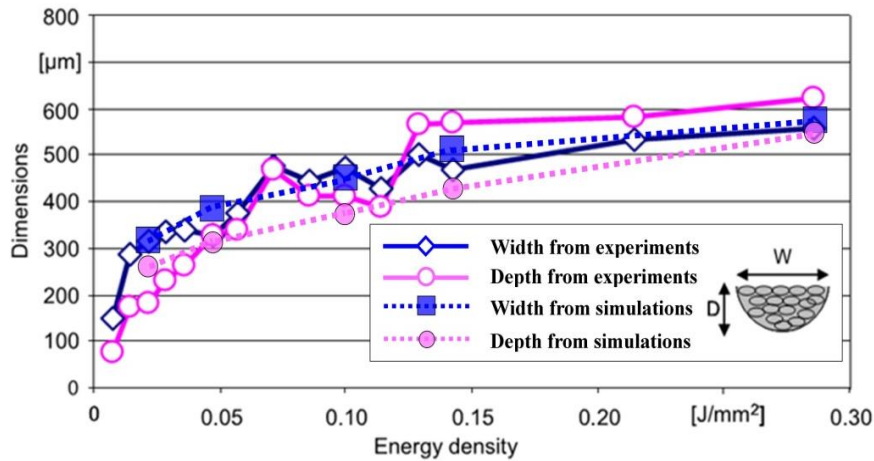


Fig.IV-1.10. Main dimensions of the profile of sintered lines as a function of energy density

1.4.3. Influence of scattering on dimension of sintered line

As mentioned in section III-3.3, the phenomenon of scattering in SLS process is rarely considered in literatures [1-6]. In the section IV-1.1, we have concluded that the scattering will largely affect the laser energy distribution and temperature evolution inside powder bed. Hence, it will also have a strong influence on the dimension of sintered line. A comparison of results obtained from synthetic models with and without considering the scattering is proposed in Fig.IV-1.11, so as to investigate the effect of scattering on the dimension of sintered lines. The volumetric laser source of Defauchy [3] is selected as the input power (without considering scattering).

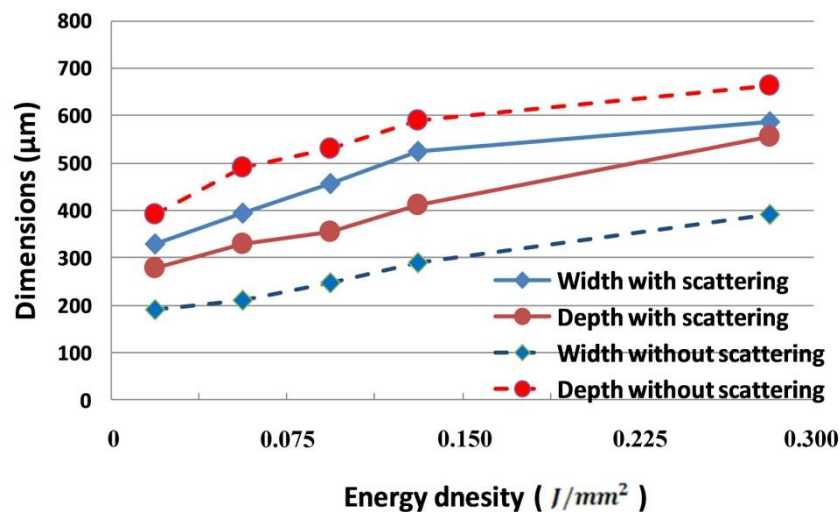


Fig.IV-1.11. Comparisons of main dimensions of sintered lines with and without scattering

The main dimensions (width and depth), in both cases with and without scattering, increase with the increasing of laser energy density as shown in Fig.IV-1.11. However, the width of sintered line is always

larger when considering the scattering. This can be attributed to the influence of scattering that largely rearranges the distribution of laser energy as confirmed in section IV-1.1. Due to the effect of scattering, most of laser energy concentrates in the region closed to the surface as illustrated in Fig.IV-1.1. On the contrary, the depth is larger when not considering the scattering as shown in Fig.IV-1.11. That is because, at the center of laser beam, more laser energy reaches deeper positions of powder bed in case without scattering (also presented in Fig.IV-1.1). A more precise analysis is illustrated in Fig.IV-1.12 derived from section IV-1.1, where the attenuation of normalized laser power deposited inside powder bed is presented. At the center of laser beam (optic radius=0), the deposited laser power is larger when not considering the scattering ($P_1 > P_2$). Therefore, the depth of sintered line is larger without scattering. When the position is close to the edge of laser beam (optic radius=0.4), the deposited laser power is larger when considering the scattering ($P_3 > P_4$). Thus, the width of sintered line is larger with scattering.

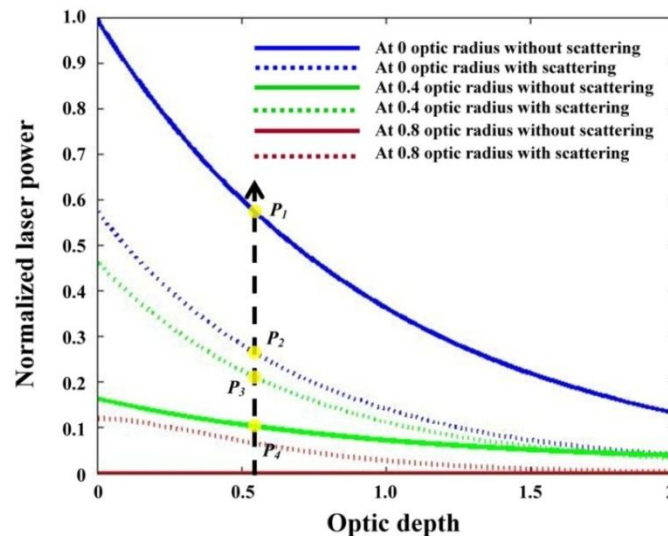


Fig.IV-1.12. Deposited laser power at different optic radius along depth

1.4.4. Partial conclusion

In this section, a 3D synthetic model is proposed, which couples almost all physical phenomena of SLS process, such as radiative heat transfer, scattering, heat conduction, coalescence and densification. In order to validate our model, simulated results have been compared to experimental data from the literature. It turns out that the simulated results are in good agreement with experiments, which confirms the potential of this model to predict the precise geometric features of product fabricated by SLS process.

In order to highlight the influence of scattering and confirm our previous conclusions in section IV-1.1, we proposed another comparison between the simulated results in cases with and without considering the scattering. And the numerical result with scattering has been confirmed by experimental data. Finally, this comparison shows a large difference between results obtained based on different heat source models. It indicates that the scattering has a strong influence on the main dimension (width and depth) of sintered lines, further, confirming its effect on the distribution of laser intensity and temperature evolution of powder bed.

1.5. Predication of relative density

The relative density of product fabricated by SLS process is one of the most important properties concerned by manufacturing. Because it is directly related to the product quality and largely affects its mechanical performance. However, very few works [8-10] studied the relative density of sintered piece. Besides, all these literatures only did the experimental measurements and analyzed effects of several parameters (like laser power and scanning speed) on the relative density of the final product.

Until now, to our knowledge, no research has proposed a numerical model capable of predicting the

relative density. Compared with FEM, DEM has potential in modeling physical phenomena in SLS process, which is possible to capture almost all the physical phenomena linked to grains interactions and the granular characteristic of material. Hence, we modeled the SLS process based on the global model, in order to predict the relative density of the sintered region.

1.5.1. Definition of relative density of sintered region

The granular media, such as powder bed, is a typical porous system. After treated by laser beam, the sintering will cause a large variation of the porosity of powder bed, finally resulting in the evolution of relative density. As we have discussed in the section III-5.3, the evolution of relative density can be distinguished into two different stages. In the first stage, necks between grains are just formed and gases inside powder bed can escape rapidly through the freeways between grains. This stage is directly controlled by the phenomenon of coalescence. The second stage is related to the formation and release of the entrapped bubbles. After coalescence, interfaces between grains are not free. So gases are in trapped in molten grains and forms bubbles. The migration of gases towards outside will be realized by the dissolution of bubbles in molten polymer. This stage is known as the densification phenomenon. Generally, both stages will lead to the shrinkage of powder bed volume. This can be observed in terms of surface decreasing during SLS process, as shown in Fig.IV-1.10(a). Unlike previous models based on FEM [1-6], the model based on DEM is able to simulate this phenomenon during SLS process, as shown in Fig.IV-1.10(b).

The relative density A can be naturally defined as following:

$$A = \rho / \rho_s \quad (IV-1.4)$$

where ρ_s is the density of solid material and ρ is the density of sintered region.

The density of sintered region ρ is defined as:

$$\rho = M / V \quad (IV-1.5)$$

where $M = N_{particle} * M_{particle}$ is the sum of particle mass in the sintered region, V is the volume of the sintered region. $N_{particle}$ is the number of grains in the sintered region, $M_{particle}$ is the mass of a single grain.

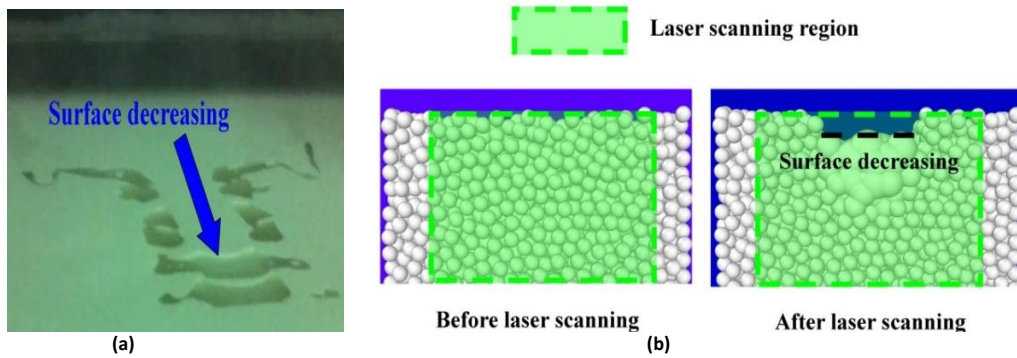


Fig.IV-1.10. Illustration of surface decreasing of powder bed after laser treatment:
(a) Experimental result; (b) Simulation result.

Thus, substituting Eq.IV-1.5 into Eq.IV-1.4, the relative density is given as:

$$A = \frac{M}{V * \rho_s} \quad (IV-1.6)$$

During laser sintering process, the mass of powder bed is constant. However, the volume of powder bed in the sintered region varies as results of the densification and coalescence phenomena. As illustrated in Fig.IV-1.11, the surface is not regular. In order to get the volume of the powder bed, we discretize the box into many meshes and assume that the volume of sintered region V is equal to the accumulation of

mesh volumes as defined by followings:

$$V = \sum_{i=1}^{N_{particle}} d_i^2 * h_{mxa,i} \quad (IV-1.7)$$

where $h_{mxa,i}$ is the distance between the top of the highest particle and the bottom of powder bed in mesh i , d_i is the width of mesh i .

In fact, the powder bed is usually larger than the sintered region. That is because the laser cannot affect all grains if the powder bed is thick enough. Additionally, only a part of the region heated by the laser becomes sintered due to the Gauss distribution of laser intensity. Thus, the geometric features of sintered region only depends on the scanning route of laser beam.

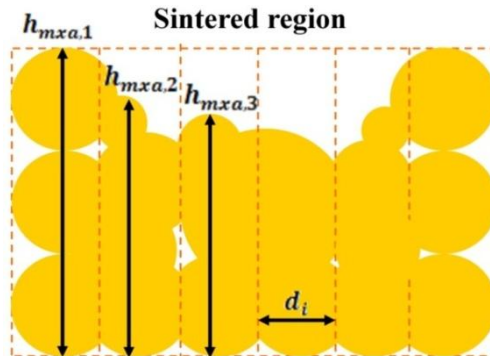


Fig.IV-1.11. Illustration of discretisation of sintered region

1.5.2. Prediction of relative density of sintered line

Due to the limitation of computational performance, we take the process of single laser scanning as example for elaborating the calculation procedures of the relative density prediction. Based on the work of Franco et al. [7], we try to predict the relative density of sintered lines. In the simulation, all parameters and properties of grains are the same as those from Franco. The laser beam with the power of 50W and scanning speed of 0.714m/s is selected as the input power.

As shown in Fig.IV-1.12, the phenomenon of surface decreasing in powder bed is clearly observed after scanned by laser. It indicates there is a strong densification phenomenon inside the powder bed resulting in large evolution of the relative density. After analyzing the simulated results, we finally obtained the relative density is up to 83.47% which was about 55% before laser sintering. In fact, it is nearly impossible to measure the relative density of single sintered line. Thus, there is no experimental results which can confirm this result of prediction. But, we will simulate the fabrication of a sintered part by SLS process in the later section. And the prediction of relative density is going to be compared with experimental results from the literature.

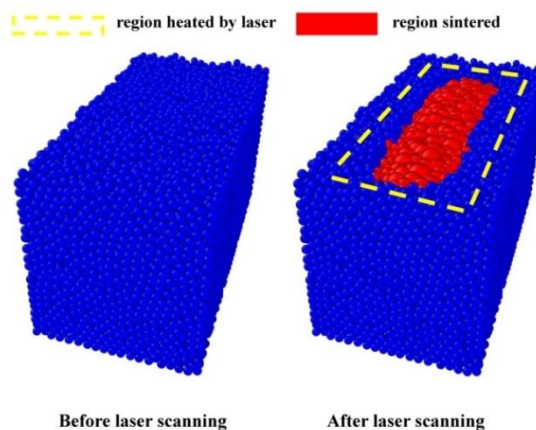


Fig.IV-1.12. Illustration of sintered line in powder bed

2. Simulation of SLS process with successive layers of powders

Until now, most of numerical studies about SLS process only simulate the thermal diffusion inside a predefined powder bed[1-6]. But, successive layers of powders are formed by laser sintering in industrial manufacturing. Few studies have modeled the SLS process with successive layers. In order to simulate the SLS process with additional layers of powders, the numerical model is proposed based on DEM (chapter III). In this section, the applied model includes four submodels: the *radiation heat transfer*, *discrete heat conduction*, *sintering* and *contact dynamic submodel*. The first three submodels are the same used in section IV-1.2. The contact dynamic submodel is introduced so as to model the granular dynamic when adding new layers of powders. Firstly, the evolution of temperature at different positions of powder bed is analyzed. The thermal history of different layers is also studied. Then, the synthetic model is applied to simulate the fabrication process of a sintered sheet and meanwhile predict its relative density, which is compared to experimental results from the literature.

2.1. Analysis of temperature evolution with successive layers

According to literatures [11-13], there is a large deformation of polymer product fabricated by SLS. It indicates the existence of thermal residual stress during SLS process, which is caused by the difference of temperature gradients inside powder bed. Therefore, the analysis of temperature evolution in powder bed is very important. It can explain the mechanism of deformation caused by thermal residential stress and then help in the parameter optimization of SLS process. In this section, we only aim to study the temperature evolution of powder bed with successive layers, so the sintering submodel is not taken into account.

Due to the limitation of computational performance of computer, a numerical simulation of SLS process with successive layers is accomplished inside a relative small volume as shown in Fig.IV-2.1. In the initial powder bed, 16000 PA12 grains with size of $50\mu\text{m}$ are randomly deposited in a box with the dimension of $2000\mu\text{m} \times 2000\mu\text{m} \times 2000\mu\text{m}$. Four successive layers of powders are added into the box. For each layer, it contains 3200 grains with the same size. The laser beam scans the powder bed for four times in the longitudinal direction with the velocity of 0.5m/s . The diameter of laser beam is 0.5mm . The power of laser is 3W . The space between each scanning laser is 0.5mm . The initial temperature T_0 of powder bed and ambient temperature T_a are 443K and 373K , respectively. The density of particle ρ is 1030kg/m^3 . The conductivity k is $0.13\text{W/m} \cdot \text{K}$. The specific heat C_{p0} is $2500\text{J/kg} \cdot \text{K}$. The latent heat of melting ΔH_m is 90.8kJ/kg . The effective heat capacity C_p is dependent on the temperature and explained in section III-4.6. The extinction coefficient of Beer-Lambert law α is 9000m^{-1} . The convective heat transfer coefficient with air is $15\text{W/m}^2 \cdot \text{K}$. The starting melting temperature T_{ms} and total melting temperature T_{mf} are 448K and 507K , respectively. The extinction coefficient of Beer-Lambert law α is 9000m^{-1} .

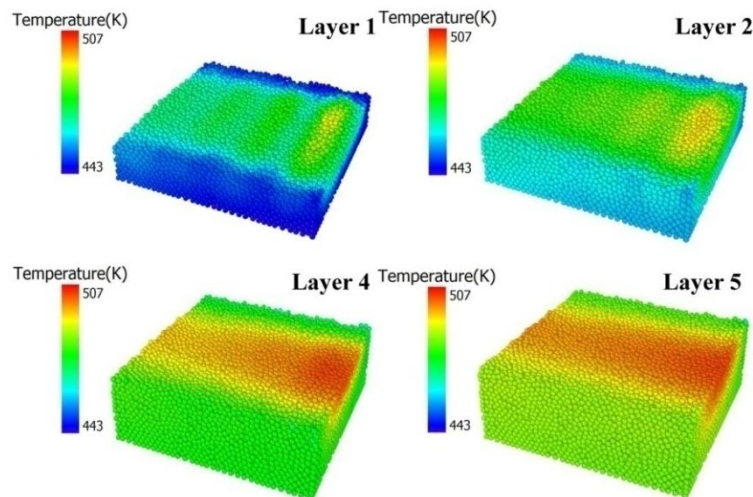


Fig.IV-2.1. Illustration of SLS process in powder bed with successive layers

In the simulation, we assumed that the process of adding new powders is instantaneous and neglect its influence on the thermal diffusion. Considering that SLS process is very fast, we assumed that the process of thermal diffusion lasts 0.1 second in each layer before adding new powders. In order to investigate the difference of temperature between the start and the end position of laser scanning, we selected five points in the diagonal line of first layer of powder bed as shown in Fig.IV-2.2.

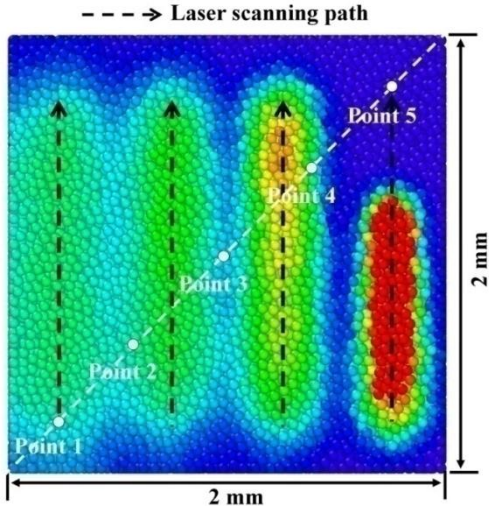


Fig.IV-2.2. Five points in the diagonal line of powder bed

The temperature evolutions of five selected positions are presented in Fig.IV-2.3. At each position, the peak temperature decreases when adding new powders, while the equilibrium temperature increases. Besides, when adding new layer of powders, the temperature firstly decrease, because the temperature of new layer is lower. The difference of peak temperature between the positions at the center and the edge(point 1 and 2) of laser beam is about 100 degree. Moreover, when the laser beam reaches the point 5, the molten grain in point 1 is already cooled. The largest temperature difference between start and end position of laser scanning($t=0.02s$) is about 200 degree. These large differences of temperature can raise the temperature gradient at surface of powder bed, resulting in the existence of thermal residual stress inside sintered region during SLS process.

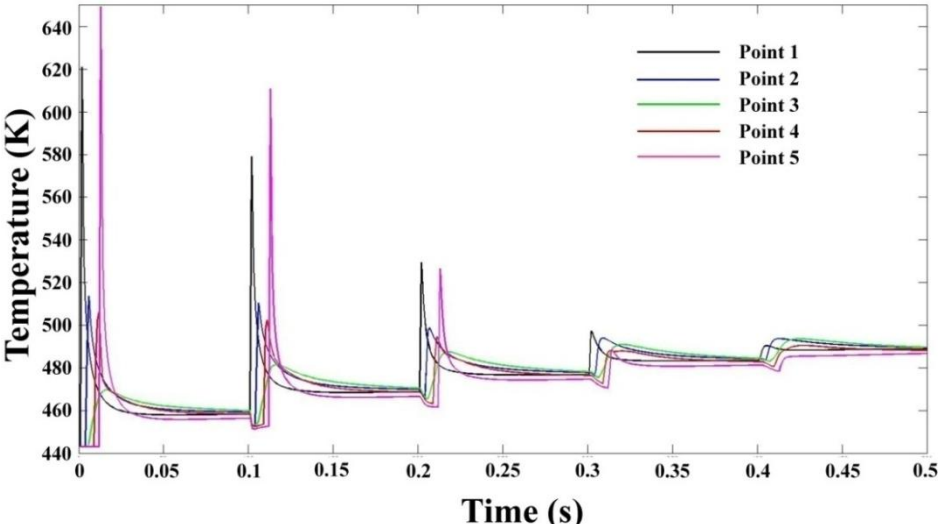


Fig.IV-2.3. Temperature evolutions of five positions in diagonal line

In order to highlight the temperature evolution at the center and the edge of laser beam, another five points are selected as presented in Fig.IV-2.4. These five points are in the middle line of first layer of powder bed. Three points (1,3 and 5) are at the edge of laser beam. Two points (2 and 4) are at the center of laser beam.

The temperature evolution at five points is shown in Fig.IV-2.5. For the points at the center of laser beam (Points 2 and 4), the peak temperature decreases when adding new powders, while the equilibrium temperature increases. For the points at the edge of laser beam (Points 1, 3 and 5), both the peak and equilibrium temperature increases slightly when adding new powders. The different thermal history at these two types points is caused by the Gaussian distribution of laser intensity. Thus, reducing the interspace of scanning laser path is a good way to decrease the temperature gradient. Furthermore, grains at the path of laser beam (points 2 and 4) totally melted for four times (higher than the melting point of 507K). But, grains at the edge of laser beam (points 1,3 and 5) never become molten during SLS process. This can explain the existence of non-molten grain core inside sintered part as found in the literature[14]. This apparent difference of physical phase in powder bed will result in the strong thermal residual stress in sintered region. Thus, reducing the input energy intensity is also a good way to decrease the thermal residual stress.

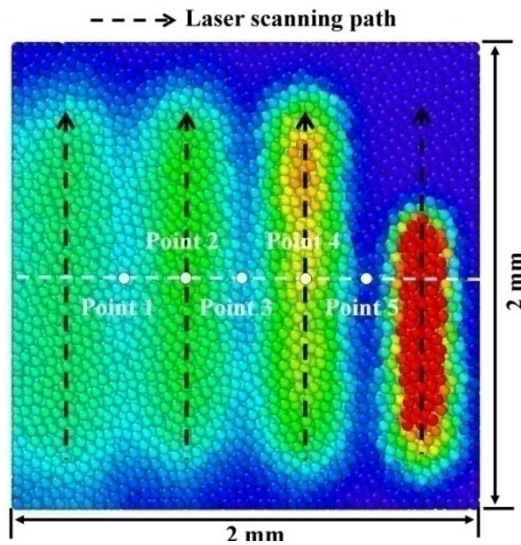


Fig.IV-2.4. Five points in the middle line of powder bed

Based on the discussion above, we can conclude that the temperature gradient is relatively high in the same layer of powder bed. It leads to the existence of strong thermal residual stress in sintered region, inducing the deformation of sintered part. For the next step, we want to investigate whether there is also high temperature gradient between two successive layers of powder bed. In order to study the temperature evolutions in different layers, we selected two typical positions (points 2 and 3 in Fig.IV-2.4) and obtained the thermal histories of grains in different layers as shown in Fig.IV-2.6 and Fig.IV-2.7.

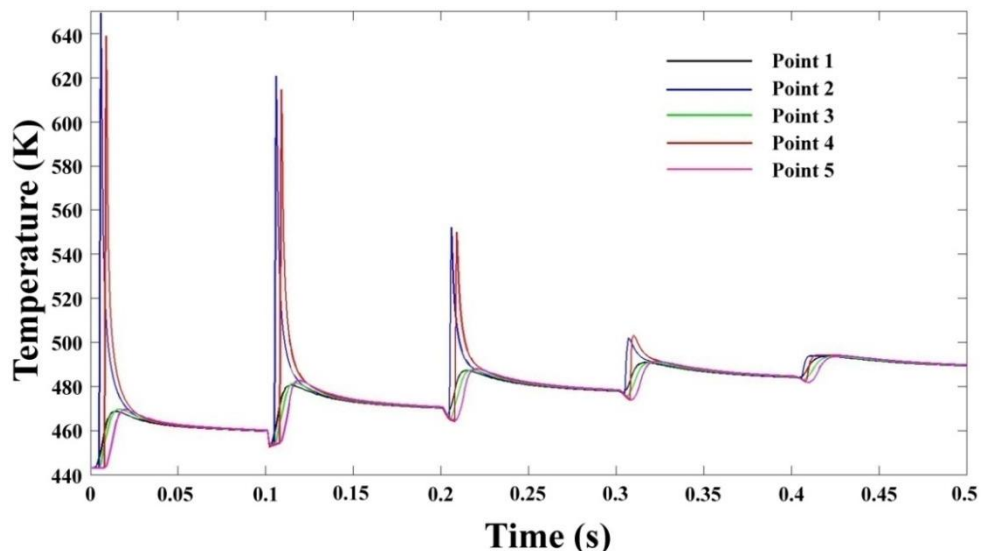


Fig.IV-2.5. Temperature evolutions of five positions in middle line

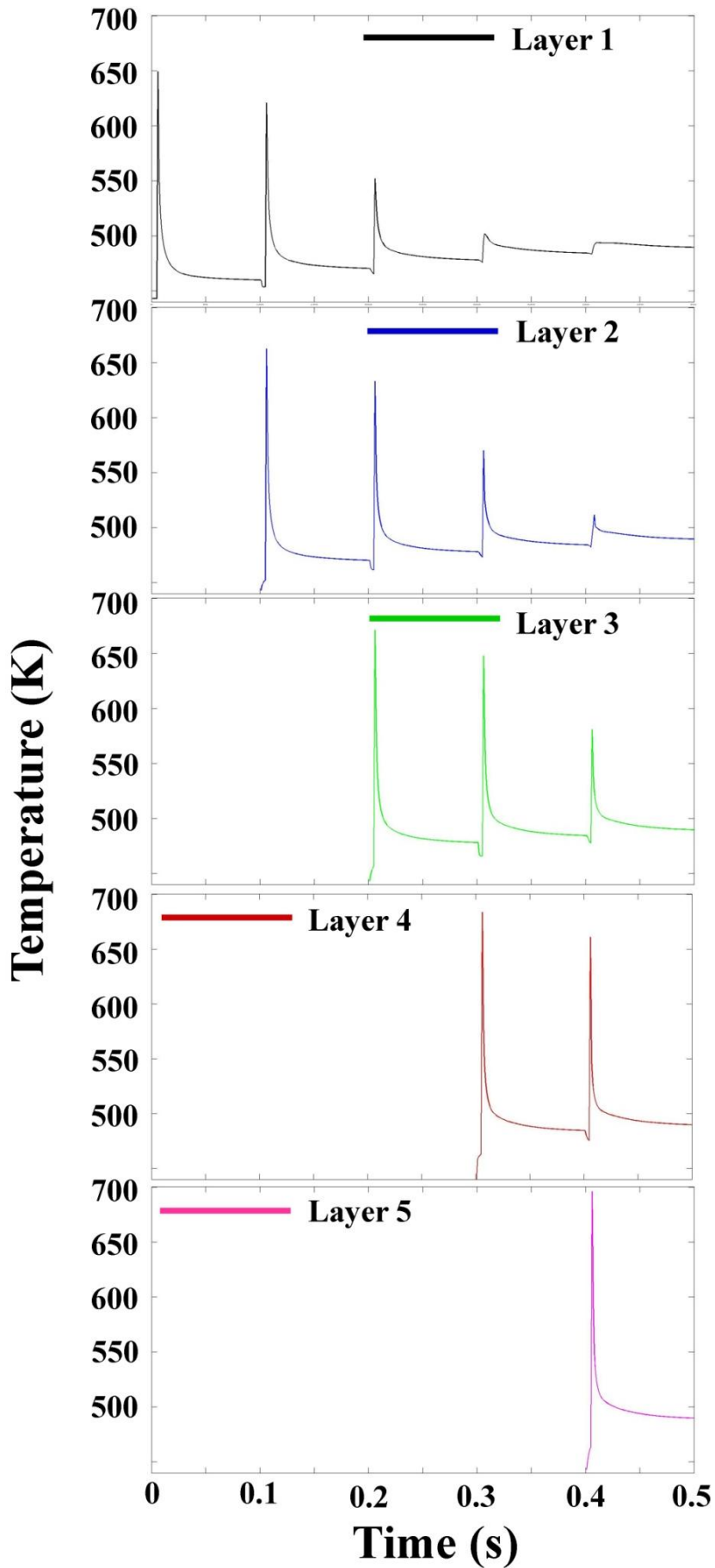


Fig.IV-2.6. Temperature evolution in different layers at position of point 2

Fig.IV-2.6 presents the temperature evolution in different layers of point 2 (at the center of laser beam). The shape of the temperature evolution curves in different layers is very similar. Comparing the peak temperature at the same time, it is higher in the upper layer than that in the lower layer. This is because new adding grains are already heated by old powders through heat conduction before laser treatment. But, in industrial manufacturing, the interval time before adding new powders is usually much longer than 0.1 second and old powders reach the preheating temperature. Thus the slight difference of peak temperature can be neglected. Actually, the successive layer repeats the thermal history of the last layer. Moreover, the evolution of temperature gradient in different layers is nonlinear which behaves as the non-uniform distribution in the direction of depth. When closed to the upper surface (layers 4 and 5), the temperature gradient is small. However, when inside powder bed (layers 2 and 3 or layers 3 and 4), the temperature gradient becomes larger. Finally, when the powders is deep enough (layers 1 and 2), the temperature gradient becomes small again. Therefore, from the surface to the bottom, the temperature gradient firstly increases and then decreases. The peak temperature gradient along depth is in the middle of the region that is directly heat by laser. Due to the high temperature at surface, the sintered region consists of a zone with tensile stress, followed by a large zone of compressive stresses. Mercelis et al. [11] obtained the same conclusion when studying the residual stress in SLS process with metallic powders.

Fig.IV-2.7 presents the temperature evolution in different layers at position of point 3 (at the edge of laser beam). The result shows the same behavior as Fig.IV-2.6: similar shape of temperature evolution curves and higher peak temperature in upper layer. Still, the successive layer actually repeats the thermal history of the last layer. However, the peak temperatures of each layer are only little higher than the equilibrium temperature. Besides, the temperature gradient in the direction of depth is very small. Thus, there is less thermal residual stress in the direction of depth at the edge of laser beam.

Comparing the results of Fig.IV-2.6 and Fig.IV-2.7, in different layers, grains at the center of laser beam (points 2) totally melted for four times (higher than the melting equilibrium temperature 507K). But, grains at the edge of laser beam (points 3) never becomes melted during SLS process. This result is the same observed in Fig.IV-2.5. During cooling process, the evolution of temperature gradient in direction of depth is nonlinear at the path of laser beam, resulting in a tensile-compressive stresses in sintered region. But, at the edge of laser beam, the temperature gradient is much lower. Therefore, the thermal residual stress is mostly concentrated in the zone near the center of laser beam.

Based on the analysis of temperature evolution above, we can conclude the non-homogeneity of temperature gradient mainly display in two aspects: in case of the same layer, the temperature gradient is much higher in the zone close to the center of laser beam. Besides, grains near the center of laser beam are totally melted for several times. But, those at the edge of laser beam will be not fully melted for even one time. This divergence of phase can also cause the residual stress inside powder bed. In case of different layers, the distribution of temperature gradient is also non-uniform, leading to a tensile-compressive stress distribution. Generally, these two types divergence of temperature gradient cause the residual stress in powder bed, finally resulting in the deformation of final product.

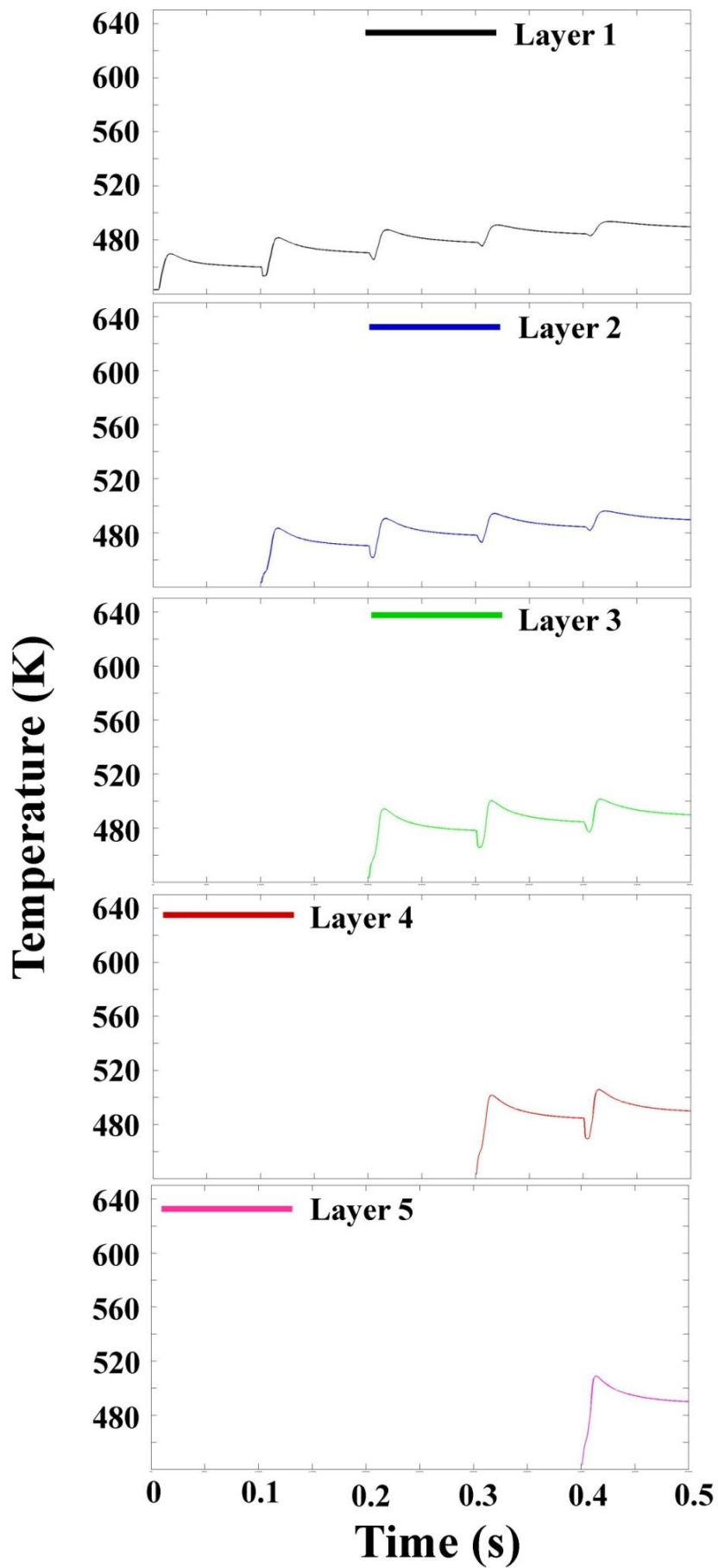


Fig.IV-2.7. Temperature evolution in different layers at position of point 3

2.2. Prediction of relative density of sintered sheet

In the section 1.3 of this chapter, we have defined and predicted the relative density of sintered line. Now, we want to predict the relative density of sintered sheet fabricated through successive layers of powders. Dupin [10] experimentally studied the SLS process in the PA12 powder bed and measured the relative density of the sintered product for different energy density. Therefore, we simulate the SLS process in the same conditions. Then we predicted the relative density of sintered sheet and compared it to the experimental results from Dupin [10].

In the thesis of Dupin, several specimen are fabricated using different energy density E_ρ . The energy density is defined as below [10]:

$$E_\rho = \frac{P}{\pi r^2} \frac{2r}{v} \frac{2r}{e} \quad (\text{IV-2.1})$$

where P is the laser power, r is the radius of laser beam, v is the scanning velocity and e is the space between two successive scanning lasers.

In the experiment, different energy densities are obtained by varying the laser power. The space between each scanning laser is set to 0.15mm and the scanning speed is 5m/s. The energy density used is listed in Table.IV-2.

Table.IV-2. Summary of energy densities used in manufacturing of different samples [10]

Sample	1	2	3	4	5	6	7
Laser power (W)	8	10	12	14	16	18	20
E_ρ (J/cm ²)	1.36	1.7	2.04	2.38	2.72	3.06	3.4

Due to the limitation of computational performance, we simulate the SLS process in a small volume with the dimension of 1.5mm×0.85mm×1mm. The size of grain is assumed to be identical as 50 μ m. The initial thickness of powder bed is 200 μ m. During SLS process, four successive layers of powders are added into the volume. The thickness of each layer is 100 μ m. The preheating temperature of powder bed is 150°C. The initial temperature of successive powders is 130°C. The ambient temperature is 173°C. During the experiment, Dupin [10] maintained the powder bed for several hours after laser treatment, so as to allow enough time for densification and crystallization. However, due to the problem of time consuming, we assumed that the processing time is 0.2s for each layer. Thus, the total process time is 1s for the whole SLS process in our simulation.

The Fig.IV-2.8 presents the powder bed in different conditions: with and without laser treatment. From Fig.IV-2.8, we can clearly observe that the volume of powder bed with laser treatment is smaller than that without treatment by laser, due to the coalescence and densification. After laser scanning, the size of grain increases, which is caused by the combination of coalescence and densification(explained in chapter III). In fact, during the sintering process, small grains will merge into big grain. Furthermore, the gases inside powder bed will be released when grains are molten. In Fig.IV-2.8(b), the size of grain is much larger in the zone closed to the bottom of powder bed. It is because the successive layer of powders is added layer by layer. Therefore, it allows more time for the first layer (near the bottom) to coalesce and to densify.

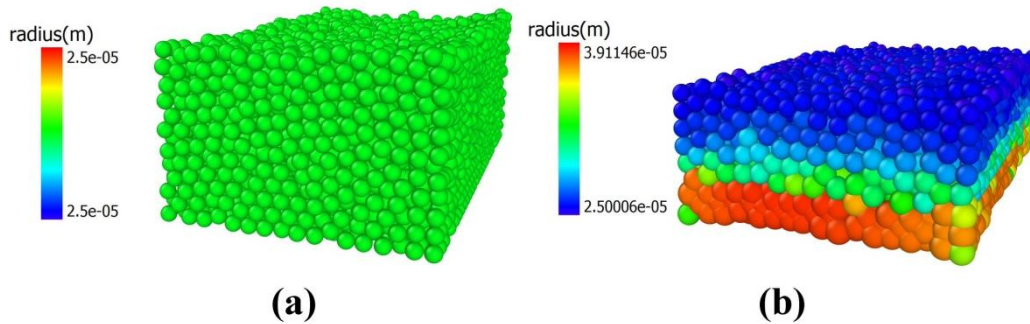


Fig.IV-2.8. Illustration of PA12 powder bed:
 (a) without laser treatment; (b) with laser treatment.

Fig.IV-2.9 presents the evolution of porosity with different energy densities. The porosity is defined as 1 minus the relative density of powder bed, which has been predefined in section IV-1.4. In the case of experiment, a sharp decrease of porosity is observed between 1.36 J/cm² and 2.04 J/cm². Then the porosity continues slightly decrease to a value of 5%. In the case of simulation, a sharp decrease of porosity is observed between 1.36 J/cm² and 2.38 J/cm². Then the porosity continues slightly decrease to a value of 12%. This is because it is more difficult to decrease the porosity when the powder bed approaches to full consolidation (porosity=0). Generally, the curve of simulation results have the similar shape of experimental results. But, the predicted porosity is always higher than the experimental result about 7% of difference in porosity. This difference can be explained by the post-processing. During the experiment, Dupin maintained the powder bed at preheating temperature for several hours, which allows enough time for densification and crystallization. However, due to the problem of time consuming, we assumed that the processing time is 0.2s for each layer. Thus, the total process time is 1s for the entire SLS process in the simulation.

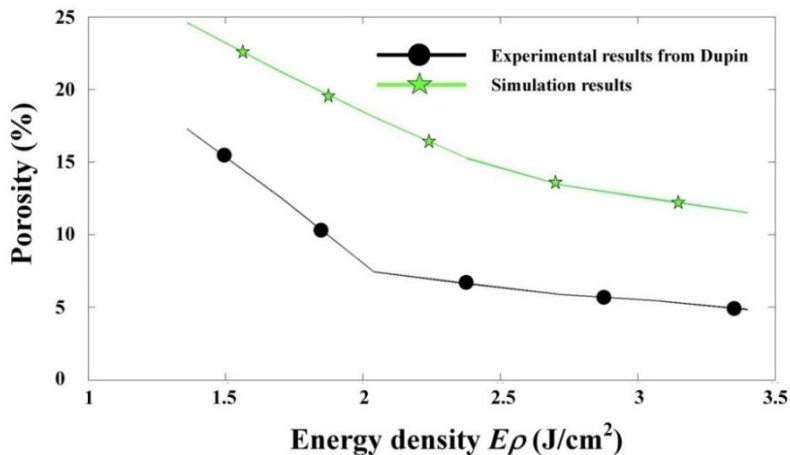


Fig.IV-2.9 Evolution of porosity with different energy densities E_p

3. Influence of SLS process parameters

Physical phenomena involved in SLS process are multiple and complex. In other words, the SLS process is controlled by many parameters, such as the laser power, scanning speed, preheating temperature, grain size and so on. Based on what has been discussed in the former sections, we have developed and validated a 3D numerical model for simulating the SLS process. Thus, we apply the same model used in the section IV-2 to analyze the influence of parameters on the final product. These results can help the user of SLS machine to optimize the quality of product, reduce the cost of manufacturing and increase the efficiency of SLS process.

3.1. Influence of laser energy density

The energy density ($ED=P/v\phi$) is a parameter commonly used in literatures [15-18] to express parameters of SLS process in energetic terms. This parameter involves the laser power P , scanning speed v and diameter of laser beam ϕ . The laser power and scanning speed are two of the most important parameters in SLS process, because they have a strong and direct influence on the quality of product and are easily controlled by manufacturing.

In order to investigate the influence of energy density on the peak temperature and relative density, the PEEK powder has been selected due to its representative thermal properties used for rapid prototyping. We modeled the SLS process in the same conditions as in the work of Peyre et al. [6]. In the simulation, 20308 particles with diameter of $50\mu\text{m}$ are randomly deposited in a volume with the dimension of $2000\mu\text{m}\times 1000\mu\text{m}\times 1200\mu\text{m}$. The laser beam single scans the powder bed in the longitudinal direction with several velocities. The preheating temperature T_0 and the ambient temperature T_a are 520K and 473K, respectively. Simulations based on the integrated model were repeated over times with different input powers (10W, 15W, 25W and 50W) and scanning speeds (0.5m/s, 0.714m/s, 1.25m/s and 2.5m/s). The simulated results are shown in Fig.IV-3.1 as below.

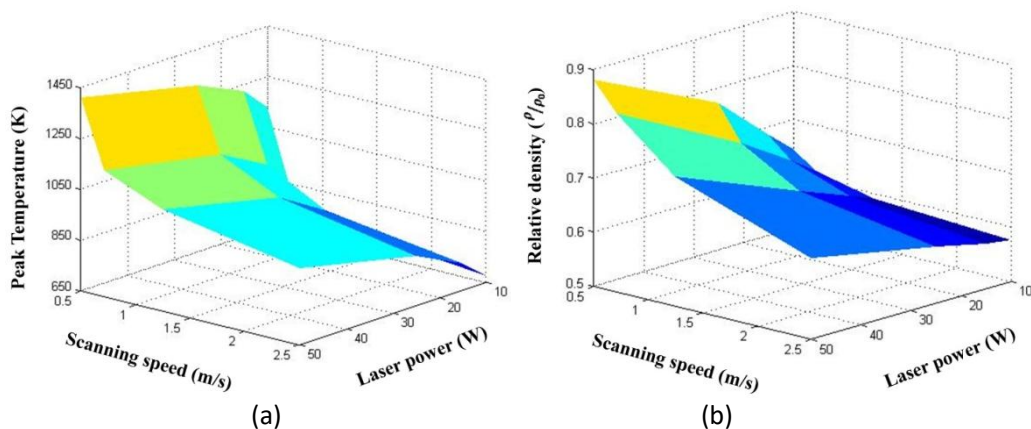


Fig.IV-3.1. Effects of energy density on peak temperature and relative density

In Fig.IV-3.1(a), the peak temperature of powder bed increases with the decreasing of scanning speed and increasing of laser power. When the laser power is larger than 10W, the average value of peak temperature becomes higher than 800K. According to the study of Peyre et al.[6], polymer grain transforms its state from non degradation to partial degradation (even full degradation). Therefore, the laser power of 10W or less is more suitable for laser sintering of PEEK. In fact, the range of laser power used in industrial manufacturing is usually between 1W and 6W [3]. Thus, our conclusion and the industrial practice leads to the same recommendation. As presented in Fig.IV-3.1(b), the relative density increases with decreasing of the scanning speed and increasing of the laser power. Therefore, this indicates that higher input power or lower scan speed could provide larger range and greater flexibility in choosing process parameters for producing high quality parts. But, the laser power cannot be too large in order to avoid the degradation of polymer grain. Besides, based on the definition of energy density ED (section IV-1.4.2), there is a significant positive correlation between the energy density ED and relative density of sintered line. This conclusion can be also found in other works [10,19].

3.2. Effect of preheating temperature

The preheating temperature is one of the important parameters of SLS process [10,20]. In the case of polymer powder bed, it is usually maintaining powders higher than the crystallization temperature in industrial manufacturing, so as to prolong the sintering process [3]. In order to understand deeply the influence of preheating temperature on SLS process, we studied the relationship between final relative density and preheating temperature by numerical simulation.

The SLS process is simulated based on the model with the same conditions as that of the section

IV-2.2. We simulate the SLS process of PA12 in a small volume with the dimension of $1.5\text{mm}\times 0.85\text{mm}\times 1\text{mm}$. The size of grain is assumed to be identical as $50\mu\text{m}$ from Dupin[10]. The initial thickness of powder bed is $200\mu\text{m}$. During SLS process, four successive layers of powders are added into the volume. The thickness of each layer is $100\mu\text{m}$. In order to study the influence of preheating temperature on relative density of product, we pick seven different values of the preheating temperature between the room temperature and the melting point of PA12 (20°C , 50°C , 80°C , 105°C , 130°C , 150°C and 170°C). Due to the problem of time consuming, we assumed that the processing time is 0.2s for each layer. Thus, the total process time is 1s for the whole SLS process in our simulation.

The evolution of relative density with different preheating temperatures is shown in Fig.IV-3.2. The relative density almost linearly increases with the increasing of preheating temperature in range between room temperature and melting point of PA12. According to the fitting curve of relative density's evolution, there is no increase of the relative density when the preheating temperature is smaller than 0°C . This is because there is no sintering occurring if both the preheating temperature and the laser energy density are very small. When the preheating temperature is higher than the melting point, the relative density theoretically continues to increase until fully consolidated (relative density reaches 1). However, the preheating temperature must be smaller than melting point during manufacturing. Otherwise, the entire powder bed will be molten even without heated by laser, which means it is impossible to obtain the designed product.

To conclude, based on the analysis above, the suitable preheating temperature will be the one that is near but smaller than the melting point. In fact, in the case of PA12, the preheating temperature is recommended as $170\text{-}175^\circ\text{C}$ ($10\text{-}15^\circ\text{C}$ below the melting temperature of the material) by Pham et al.[20]. Therefore, our conclusion based on numerical simulation is in good agreement with the recommendation of experimental research.

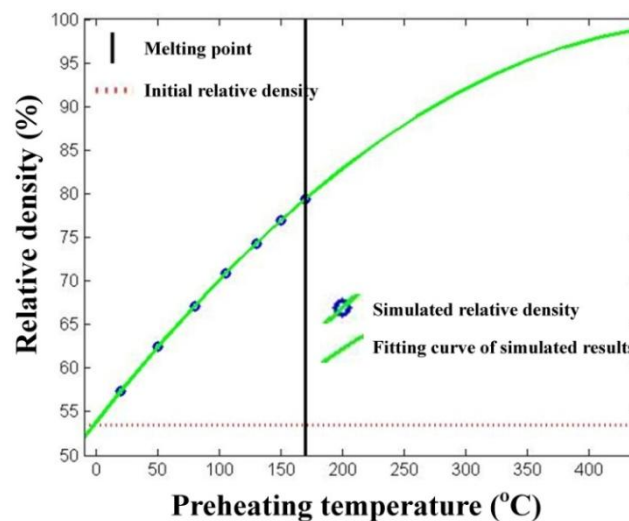


Fig.IV-3.2. Evolution of relative density with different preheating temperatures

3.3. Effect of grain size

In DEM, the grain is the basic unit like the element in FEM (Finite Elements Method). The mesh density in a finite elements model is an important topic because of its relationship to accuracy and numerical cost. Thus, the size of grain is also very critical in DEM. In order to be able to determine a good initial grain size for the subsequent discrete element computations, we proposed another two simulations to study the effect of grain size on the thermal diffusion. The simulations are in the same conditions as the section IV-2.1 with two different grain sizes ($25\mu\text{m}$ and $100\mu\text{m}$) as shown in Fig.IV-3.3. The total mass of powder bed is the same for two different sizes. Thus, the number of grain with the size of $25\mu\text{m}$ is 64 times of $100\mu\text{m}$. Due to the limitation of computational performance, we only simulate the SLS process in the powder bed with three layers in the case of $25\mu\text{m}$.

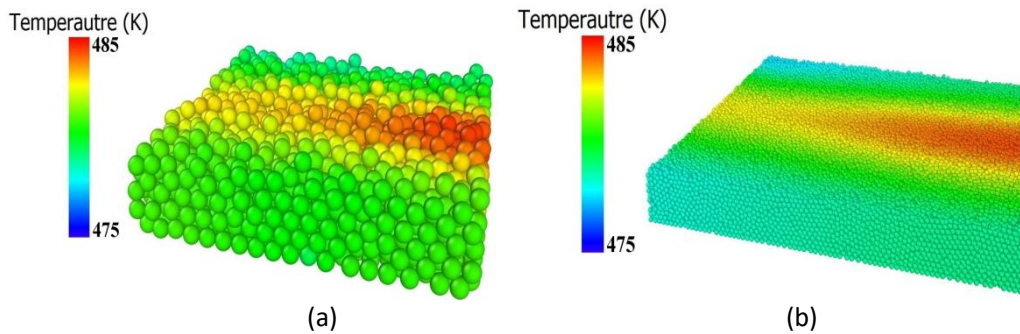
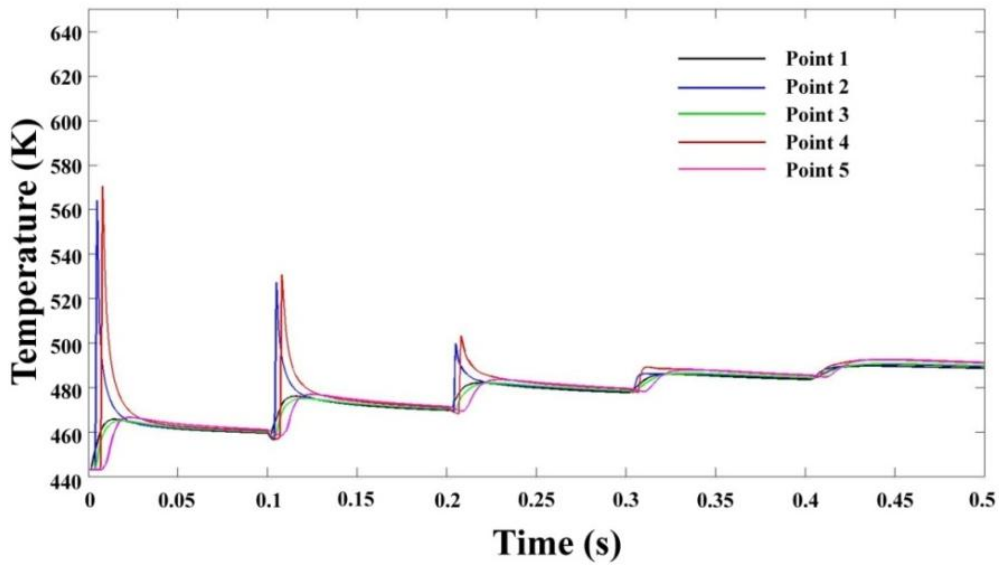


Fig.IV-3.3. Temperature evolutions of powder bed with different grain sizes:
(a) 100µm (b) 25µm

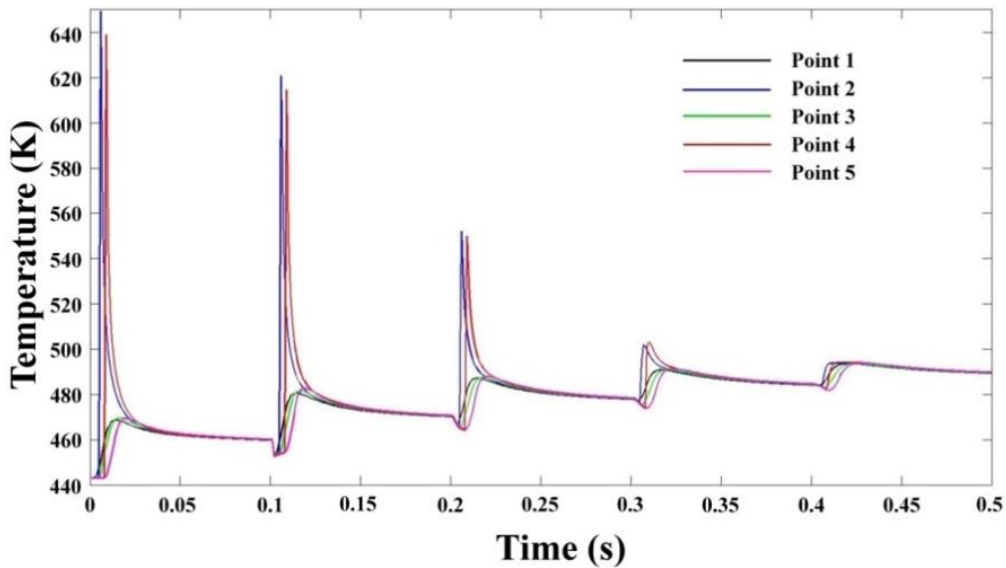
In order to compare the results in the case of 50µm, the same five positions are selected as shown in Fig.IV-2.4. Temperature evolutions of these five positions are presented in Fig.IV-3.4. For all these three cases, the peak temperature decreases when adding new layers of powders, while the equilibrium temperature increases at the center of laser beam (Points 2 and 4). However, both the peak and equilibrium temperatures increase slightly when adding new layers of powders at the edge of laser beam (Points 1, 3 and 5). Furthermore, the equilibrium temperatures in these three cases are the same. It indicates that the size of grain does not affect the mean temperature of powder bed. However, in the case of 100µm, the peak temperature is much smaller than those in other two cases. The bigger grain can be regarded as a group of many smaller grains. Thus, the temperature of bigger grain is equal to the average temperature of those smaller grains. Therefore, it is logical and reasonable that the peak temperature in case of bigger grain is smaller. In the cases of 25µm and 50µm, the temperature evolutions are almost the same. It indicates that the numerical results are stable and the grain size of 50µm is a good choice for numerical simulation when considering the computational cost. However, as shown in Fig.IV-3.3, the volume of powder bed with 25µm is smaller than that with 100µm. The total mass of powder bed in these two cases is the same, which indicates that the initial relative density with smaller size is higher than that with bigger size. In other words, the powder bed with smaller size grains can increase the relative density of final product.

Based on the discussion above, we can conclude that the grain size only affects the peak temperature of grains in the same layer of powder bed. For the next step, we want to investigate whether the grain size has a strong effect on SLS process with successive layers of powders. Still, we selected the two same positions (Points 2 and 3) and obtained their temperature evolutions in different layers.

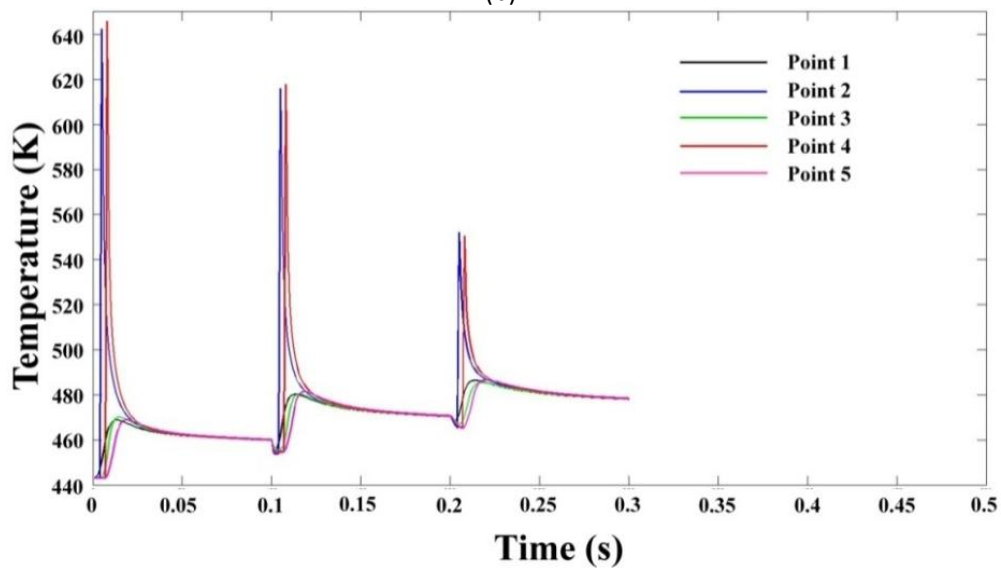
As shown in Fig.IV-3.5, in the center of laser beam, the temperature evolutions have the same tendency: shapes of temperature evolution curves are similar in different layers of powder bed; the peak temperature is higher in the upper layer than that in the lower layer. In the case of 100µm, the peak temperature is still much smaller than those of the other two cases. In the cases of 25µm and 50µm, the temperature evolutions are almost the same. This conclusion is the same as that in case of the same layer. When at the edge of laser beam as presented in Fig.IV-3.6, the temperature evolutions have the same tendency as obtained results in Fig.IV-2.7. The effect of grain size on temperature evolution is much small. Furthermore, the equilibrium temperature is always the same in all these three cases with different grain sizes. Therefore, in case of different layers, we conclude that the grain size only affects the peak temperature of grain. When the size is smaller than 50µm, the numerical results are still stable. Additionally, according to the experimental studying [10], the average size of PA12 grain normally used in industrial manufacturing is also 50µm. Thus, the size of 50µm is a good choice for numerical simulation when considering the accuracy and cost.



(a)



(b)



(c)

Fig.IV-3.4. Temperature evolutions of five positions with different grain sizes:
 (a) 100µm (b) 50µm (c) 25µm

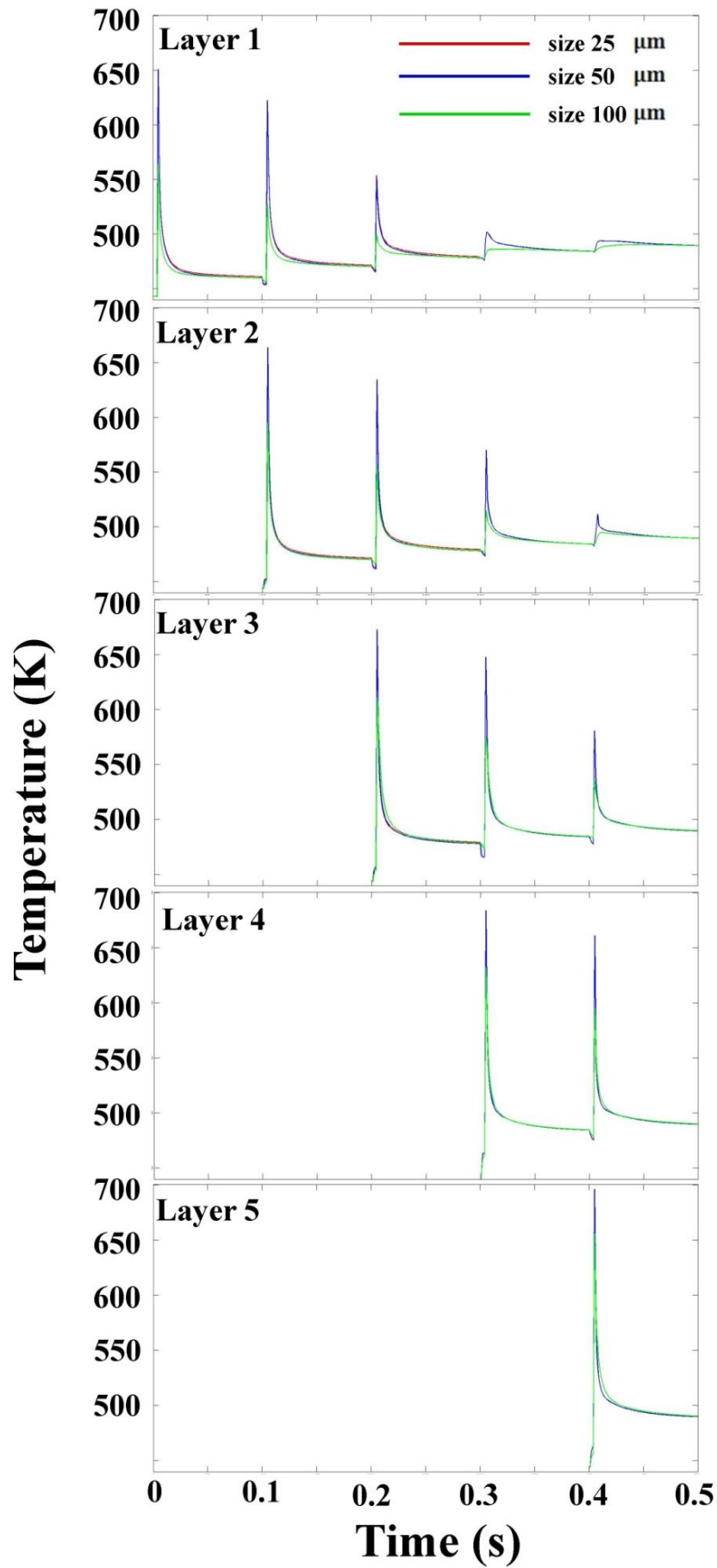


Fig.IV-3.5. Temperature evolution in different layers at position of point 2 with different grain sizes

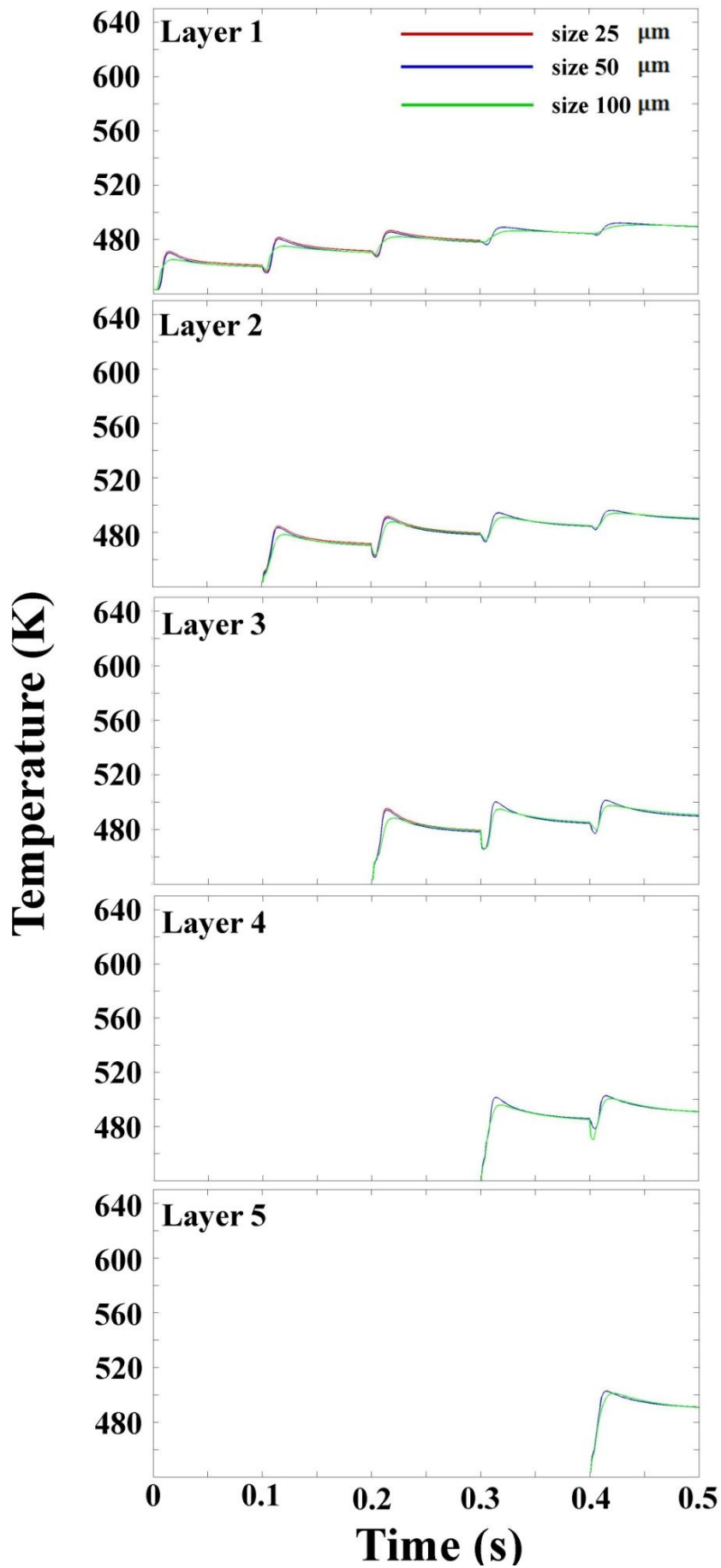


Fig.IV-3.6. Temperature evolution in different layers at position of point 3 with different grain sizes

3.4. Partial conclusion

In this section, the influences of different parameters on SLS process are studied. As well known, the relative density is directly related to the performance and quality of product obtained from SLS. Therefore, the suitable parameters of SLS process are those that can achieve higher relative density of product. Based on our numerical simulation and conclusion from literatures [1,3-6,10], the relative density is positively correlated to the laser energy density and preheating temperature, but negatively correlated to the size of grain. However, each parameter is also restricted by manufacturing conditions or has its own limitations. For example, too high energy density of laser will result in the degradation of polymer. If the preheating temperature is higher than the melting point of polymer, it is impossible to obtain designed product due to melting of the whole powder bed. Furthermore, the decreasing of grain size will reduce its castability and also raise the production cost. Briefly, suitable parameters of SLS process with polymer powders should be: high laser energy density without causing degradation; high preheating temperature but smaller than melting point of polymer; the size of grain as small as possible but affordable.

4. Applications of global model

Based on the works we have presented previously, a numerical model of SLS process has been developed based on DEM and confirmed by comparison with experimental works from literatures. With our model, it is possible to capture almost all physical phenomena inside powder bed linked to the particles interactions and the granular characteristics of the materials, such as the radiative transfer, heat conduction, coalescence and densification. The principle aim of our project is to help manufacturing to optimize the quality of products, reduce the cost of manufacturing and increase the efficiency of process. Thus, we present several applications of the synthetic model in order to illustrate its capabilities.

4.1. Simulation of balling phenomenon

In SLS process, when parameters are not correctly chosen, these powders are either not sintered at all or completely melted, finally joining into rather large drops [21,22]. Usually the drops quickly spread out and their size can exceed the diameter of the laser spot. This process of droplet formation is called balling phenomenon. Due to the difference of rheological property, the balling phenomenon is more commonly observed in metallic SLM process. In order to study effects of parameters on the balling phenomenon, we proposed a simulation of metallic SLM process. In case of metallic powder, fusion grains are assumed as viscous flows. Therefore, we replace the viscoelastic coalescence model by viscous coalescence model in the sintering submodel. Besides, in order to model the phase change of metallic powders, the Eq.III-4.14 is introduced into the discrete heat conduction submodel.

In the simulation, 13909 particles with diameter of $130\mu\text{m}$ are deposited in a box with dimensions of $8\text{mm}\times 4\text{mm}\times 4\text{mm}$. For solid particles, the density is 8470 kg/m^3 , specific heat is $444\text{ J/kg}\cdot\text{K}$ and conductivity is $14.9\text{ W/m}\cdot\text{K}$. For molten particles, the density is 7880 kg/m^3 , specific heat is $611\text{ J/kg}\cdot\text{K}$ and conductivity is $27.5\text{ W/m}\cdot\text{K}$. The melting point of Ni-alloy is 1475 K . The latent heat of melting is 2.516 GJ/m^3 . The surface tension and viscosity of Ni-alloy at the melting point are 1850 mN/m and $5\text{ mPa}\cdot\text{s}$, respectively. The power of input heat flux is 50 W and the radius of laser beam is 0.65 mm . In SLS process, the laser beam scans the powder bed in the longitudinal direction with various scanning speeds. The entire numerical simulation of laser sintering process in Ni-alloy powder bed is calculated by Fortran 90.

4.1.1 Results and discussion

Fig.IV-4.1 illustrates the numerical results of heat diffusion and sintering process in powder bed with laser treatment. The top view of the molten tracks and the calculated temperature distribution on the top of powder surface are presented (Fig.IV-4.1). There is no molten particle at the beginning of sintering process because of insufficient input heat flux (Fig.IV-4.1(a)). Particles start melting with increasing input

laser energy (Fig.IV-4.1(b)), and molten particles combine with each other and grow into larger grains through coalescence, Fig.IV-4.1(c). After laser spot has passed, the temperature of the molten region decreases because of the heat diffusion and the convection at surface.

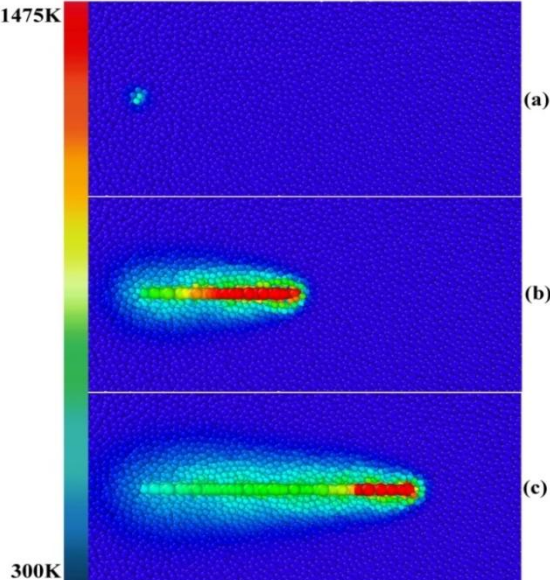


Fig.IV-4.1. Heat diffusion and sintering process in powder bed with the power of 50W and scanning speed of 0.25 m/s: (a) time=0.0001s; (b) time=0.001s; (c) time=0.002s.

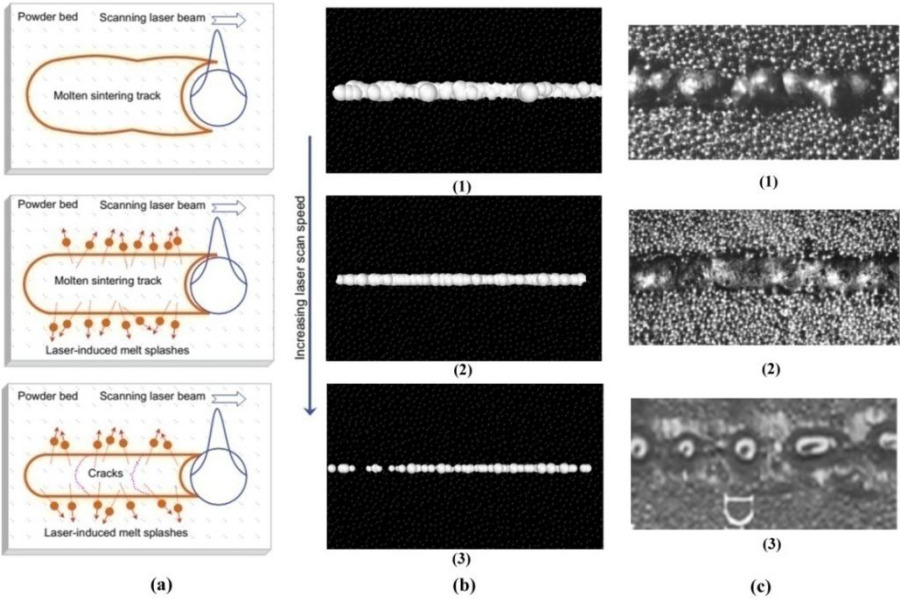


Fig.IV-4.2. The effect of scanning speed on the balling phenomenon: (a) Conclusion from Gu et al. [23]; (b) Results of simulation with the power of 50W and various scanning speeds: 0.15 m/s, 0.25 m/s, 0.65 m/s; (c) Experimental results from Tolochko et al. [22] and Yadroitsev et al. [24].

The effect of scanning speed on the balling phenomenon is presented in Fig.IV-4.2. When the scanning speed is low, the width of the molten track is in a highly unstable state because the amount of molten particles generated is excessive, Fig.IV-4.2(b-1). The surface energy of molten particles will keep decreasing in order to get a final equilibrium state as explained by Gu et al. [23], and as represented in Fig.IV-4.2(a). With increasing scanning speed, the absorbed heat flux decreases leading to the shrinkage of the molten region. If the scanning speed is too high, the molten region becomes unstable resulting in the break-up of the molten track as illustrated in Fig.IV-4.2(b-3).

Fig.IV-4.2 provides the evidence that the simulation methodology presented in this work is quite good as confirmed by comparison with experimental findings in literatures [22,24]. We conclude that the discrete numerical model of metallic laser sintering developed in this work is useful in predicting the suitable input power and scanning speed for the laser melting process to avoid the generation of strong balling process.

4.1.2. Influences of parameters on balling phenomenon

In order to quantitatively analyze the effect of scanning speed on balling phenomenon, the width of molten track are presented in Fig.IV-4.3. When the scanning speed is too low (0.15 m/s), the average width of molten track is largest. But, the shape of molten track is in high irregularity. When the scanning speed is too high (0.65 m/s), the average width of molten track is smallest and break-ups of molten track occur (width is zero). The laser power is also a very important parameter in SLM process. In order to study the effect of laser power on balling phenomenon, we simulated the SLM process with constant scanning speed (0.25 m/s) and different laser powers (20 W, 50W and 80 W). As shown in Fig.IV-4.4, the average width of molten track is largest when laser power is too high (80 W). Besides, the shape of molten track is still in high irregularity. When the laser power is too low (20 W), the average width of molten track is smallest and molten track breaks up.

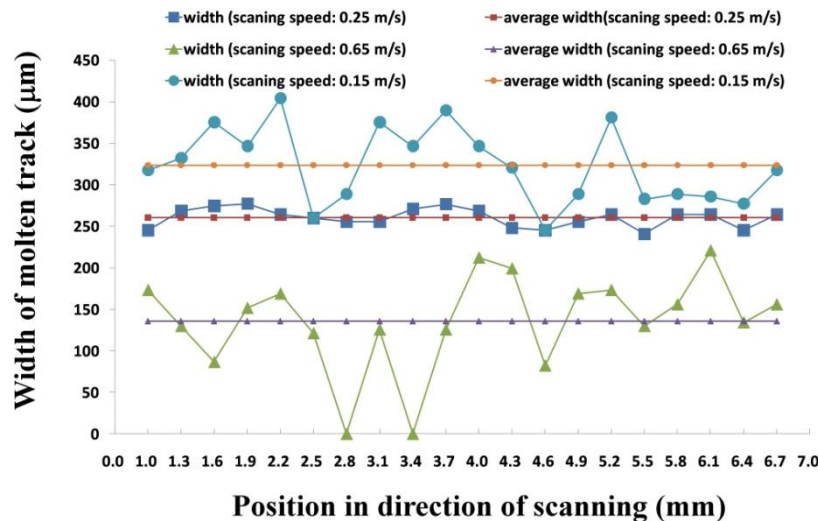


Fig.IV-4.3. Effect of scanning speed on width of molten track

Based on discussions above, the influences of scanning speed and laser power are opposite. This is because the relationship between these two parameters and laser energy density $ED (ED=P/v\phi)$ is a parameter commonly used in the literatures [30-32] to express the SLS process parameters in energetic terms. This parameter involves the laser power P , scanning speed v and diameter of laser beam ϕ . If ED is too high, there are too many grains are melted resulting in the state of high distortion and irregularity. This is because the surface energy of liquid molten track will keep decreasing in order to obtain a final equilibrium. If ED is too slow, the formation of molten grains is limited resulting in the unstable state and occurrence of break-ups.

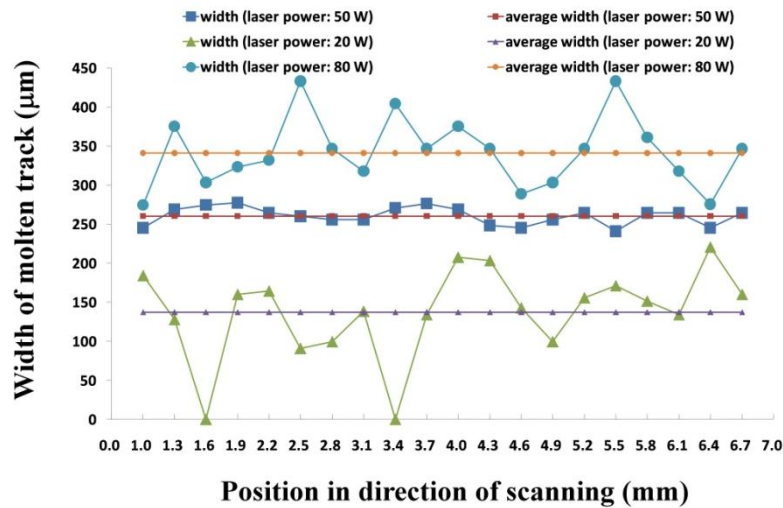


Fig.IV-4.4. Effect of laser power on width of molten track

According to Frenkel's model (Eq.III-5.36), the coalescence kinetic of molten grain is directly controlled by surface tension and viscosity. In order to study the influence of these two properties on balling phenomenon, we simulated SLM processes with constant parameters (laser power 50 W and scanning speed 0.25 m/s) and different properties (surface tension 1350 mN/m, 1850 mN/m, 2350 mN/m and viscosity 3.75 mPa · s, 5 mPa · s, 6.25 mPa · s).

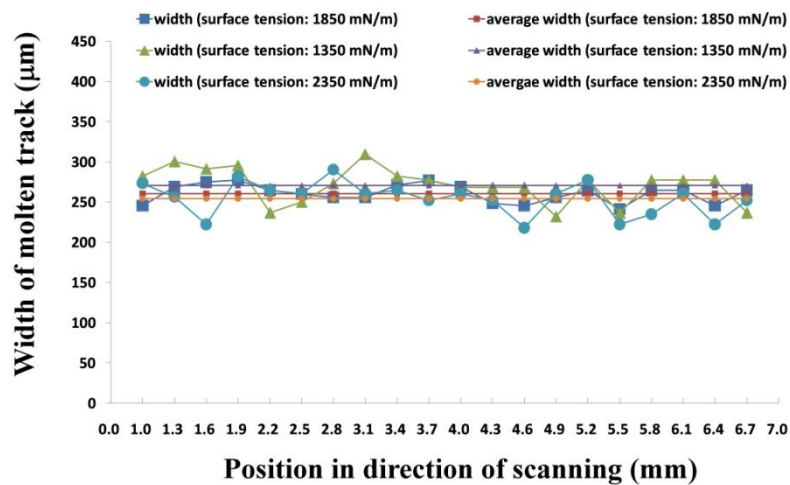


Fig.IV-4.5. Effect of surface tension on width of molten track

The width of molten track with different properties are presented in Fig.14 and Fig.15, respectively. It turns out average widths of molten track with different surface tensions and viscosities are nearly the same. In other words, the variation of surface tension and viscosity has little influence on balling phenomenon in SLM process. This is because the coalescence process of molten metallic grains is too fast. According to Frenkel's model, it only takes less than 0.001s for two molten Ni-alloy grains with diameter of 130 µm to join as one bigger grain. Therefore, in case of metallic SLM process, the parameters have much larger influence than material properties.

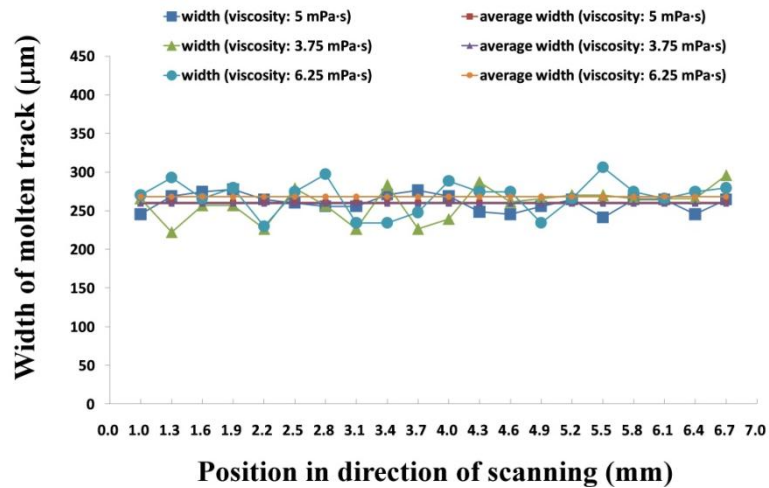


Fig.IV-4.6. Effect of viscosity on width of molten track

4.2. Test simulation of SLS process

In order to demonstrate the capability of our model, we implemented a test simulation. The test model is simulating the SLS process for fabricating a small letter "D" as shown in Fig.IV-4.7(a). Still, PA12 grain with size of 50µm is used for simulation and the global model applied here is the same as in the section IV-2.

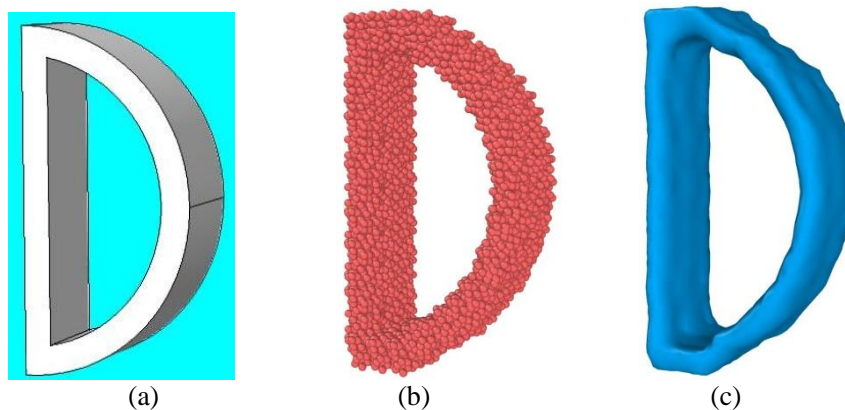


Fig.IV-4.7. Illustration of letter "D": (a) diagram; (b) processing part by SLS; (c) part with constructed surface

The temperature field of powder bed at different layers are presented in Fig.IV-4.8, in which the temperature evolution of powder bed during SLS process can be clearly observed. The temperature of grain in red is higher than the melting point that represents the sintered region. The processing part is shown in Fig.IV-4.7(b), which is directly obtained after laser sintering. Fig.IV-4.7(c) presents the output model with constructive surface which is more clearly to represent the geometry of processing part. The SLS process is not a perfect translation from diagram to processing part, and several defects can be seen in the output model of simulation. Firstly, the stair-step phenomenon can be clearly seen in Fig.IV-4.7(c). This is a well known artifact produced by SLS and other AM systems. Additionally, some loss of definition in the output model is presented. This is caused primarily by two factors: the size of grain is relatively large compared to the dimension of diagram; the laser energy density is high that causes grains outside of the domain of designed diagram to reach temperatures high enough for sintering.

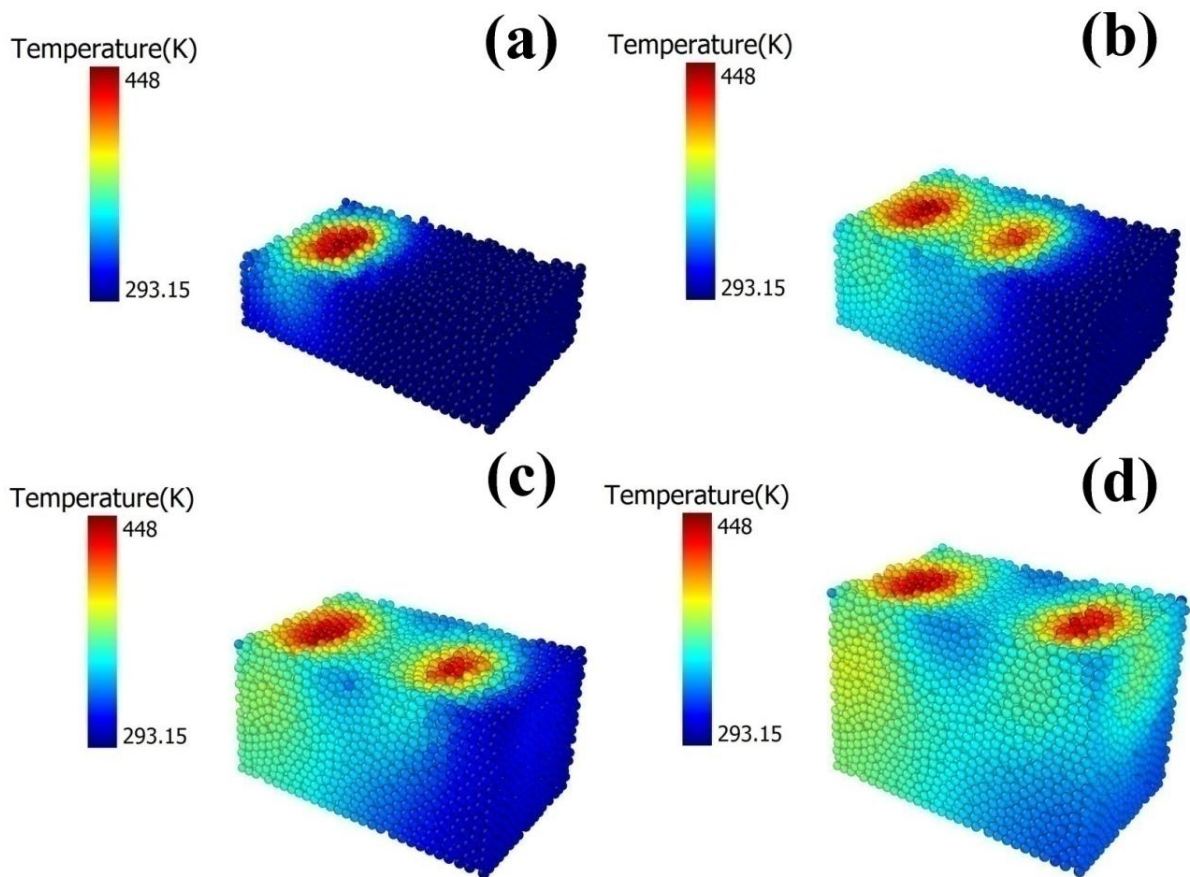


Fig.IV-4.8. Temperature fields of powder bed in different layers for manufacturing process of letter "D":
 (a) 1st layer; (b) 4th layer; (c) 8th layer; (d) 11th layer

5. Conclusions

In this thesis, we have developed a DEM framework for the analysis of particle-based additive manufacturing technologies. This work allows us to express to physical behaviors of discrete particles, which can be suitably adapted to a wide range of processes. In my thesis, this framework has been adapted to the application of a specific additive manufacturing process: the Selective Laser Sintering.

Firstly, the framework is applied to simulate the thermal diffusion of SLS process based on different laser radiation models, in order to study the influence of scattering on the radiative heat transfer and heat conduction in polymer powder bed. The results show the strong effect of scattering on the distribution of laser energy, further, resulting in the variation of region affected by laser and temperature evolution of grains.

Moreover, a global model based on this framework is used to simulate geometries of single sintering line and predict the relative density of sintered line and predict the relative density of sintered sheet. The simulated geometries are in good agreement with experimental results from the literature, which validates our model. The predicted evolution of relative density versus laser energy density also shares the same tendency of the experimental results.

Furthermore, the influences of different parameters on SLS process are simulated and analyzed by this framework. Based on the analysis of the influences of SLS parameters, an optimization is proposed for SLS process with polymer powder bed, which is consistent with the practice of industrial manufacturing.

Finally, our model is applied to model the balling phenomenon and implement a test simulation. The results of the section IV-4 conclude that this numerical framework is capable of capturing the spatially and temporally varying distribution of heat and displacement within the additively manufacturingd object. It is observed that the results of the DEM simulations replicate the geometry of diagram, while also exhibiting features that are characteristic of the physical additive manufacturing process.

In conclusion, this DEM framework will allow the functional validation of the SLS methodology as using a data-driven mixed experimental/numerical technique. The geometric predictions of DEM can be regarded as a reference for the optimization methodology. This framework has a great potential for the design, characterization and certification of additively manufacturingd components.

Reference

- [1] L. Dong, 2007, Simulation et Modélisation du Frittage Selectif par Laser Après la Methode des Elements Finis, Ph.D. Thesis, Université Louis Pasteur, Strasbourg, France.
- [2] Nelson J.C., 1993, Selective laser sintering: A definition of the process and an empirical sintering model. PhD Thesis, University of Texas at Austin, USA.
- [3] Denis DEFAUCHY, 2013, "SIMULATION DU PROCEDE DE FABRICATION DIRECTE DE PIECES THERMOPLASTIQUES APR FUSION LASER DE POWDER", Ph.D. Thesis, Arts et Métiers PatisTech, Paris, France.
- [4] Dong, L., Makradi, A., Ahzi, S., Remond, Y. (2007). Finite element analysis of temperature and density distributions in selective laser sintering process. *Materials Science Forum*, 553, 75-80.
- [5] Dong, L., Makradi, A., Ahzi, S., Remond, Y., Sun, X. (2008). Simulation of the densification of semicrystalline polymer powders during the selective laser sintering process: Application to Nylon 12. *Polymer Science Series A*, 50, 704-709.
- [6] Patrice Peyre, Yann Rouchasse, Denis Defauchy and Gilles Regnier, 2015, "Experimental and numerical analysis of the selective laser sintering (SLS) of PA12 and PEEK semi-crystalline polymers", *Journal of Materials Processing Technology*, 225:326-336.
- [7] Alessandro Franco, Michele Lanzetta and Luca Romoli, 2010, " Experimental analysis of selective laser sintering of polyamide powders: an energy perspective", *Journal of Cleaner Production*, 18:1722-1730.
- [8] Yan, C., Shi, Y., Hao, L. (2011). Investigation into the Differences in the Selective Laser Sintering between Amorphous and Semi-crystalline Polymers. *International Polymer Processing*, 16, 416-423.
- [9] Rietzel, D., Aquite, W., Drummer, D., Osswald, T. (2011a). Polymer powders for Selective Laser Sintering – Production and Characterization. 44th Conference on Manufacturing Systems, Madison (WI).
- [10] Dupin, S., 2012. Etude fondamentale de la transformation du polyamide 12 par frittage laser: mécanismes physico-chimiques et relations microstructures/propriétés. Thèse de Doctorat, INSA de Lyon.
- [11] Peter Mercelis and Jean-Pierre Kruth, 2006, Residual stresses in selective laser sintering and selective laser melting, *Rapid Prototyping Journal*, Vol. 12 Iss 5 pp. 254 - 265.
- [12] M.F. Zaeh, M. Ott. 2011. Investigations on heat regulation of additive manufacturing processes for metal structures. *CIRP Annals - Manufacturing Technology* 60, 259-262.
- [13] Ahmed Hussein, Liang Hao, Chunze Yan, Richard Everson. 2013. Finite element simulation of the temperature and stress fields in single layers built without-support in selective laser melting. *Materials & Design* 52, 638-647.
- [14] Zarringhalam H., (2007). Investigation into crystallinity and degree of particle melt in selective laser sintering. PhD Thesis, Loughborough University.
- [15] Suk-joong L Kang, 2005, Sintering: densification, grain growth& microstructure, Elsevier, Oxford, UK.
- [16] Smoluchowski M., "DreiVorträgeüber Diffusion, BrownscheMolekularbewegung und Koagulation von Kolloidteilchen". *Physik. Z.*, 1916, 17: 557–571, 585–599.
- [17] Pokluda O., Bellehumeur C. T. and Vlachopoulos J. Modification of Frenkel's model for sintering, *AIChE Journal*, 1997, 43:3253-3256.
- [18] Cho S.J., Kang S.J. and Yoon D.N., 1986, Effect of entrapped inert gas on pore filling during liquid phase sintering, *Metallurgical and Materials Transactions A*, 17(A):2175-2182.
- [19] Tontowi, A., Childs, T. (2001). Density prediction of crystalline polymer sintered parts at various powder bed temperatures. *Rapid Prototyping Journal*, 7, 180-184.
- [20] Pham, D., Dotchev, K., Yusoff, W., 2008, Deterioration of polyamide powder properties in the laser sintering process. Part C: *Journal of Mechanical Engineering Science*, 222, 2163-2176.
- [21] Bourel, D.I., Marcus, H.L., Barlow, J.W. and Beaman, J.J. (1992), "Selective laser sintering of metal and ceramics", *Int. J. Powder Met.*, Vol. 28 No. 4, pp. 369-81.
- [22] Tolochko, N.K., Sobolenko, N.V., Mozharov, S.E. and Yadroitsev, I.A. (1996), "Peculiarities of laser sintering of loose powder layers of metall/polymer type", *Physics and Chemistry of Treatment of Materials*, No. 5, Moscow, pp. 13-17.
- [23] Gu D. and Shen Y., 2009, "Balling phenomena in direct laser sintering of stainless steel powder: Metallurgical mechanisms and control methods", *Materials and Design*, 30: 2903-2910.
- [24] I. Yadroitsev, I. Smurov, 2010, Selective laser melting technology: from the single laser melted track

stability to 3D parts of complex shape, *Physics Procedia* 5:551–560.

[25] Tien, C. L., and B. L. Drolen: "Thermal radiation in particulate media with dependent and independent scattering," in *Annual Review of Numerical Fluid Mechanics and Heat Transfer*, vol. 1, Hemisphere, New York, pp. 1-32, 1987.

[26] Rayleigh, L.: "On the light from the sky, its polarization and colour," *Philos. Mag*, vol. 41, pp. 107-120, 274-279, 1871 (reprinted in *Scientific Papers by Lord Rayleigh*, vol. I: 1869-1881, no. 8, Dover, New York, 1964).

[27] Mie, G. A.: "Beitrage zur Optik triiber Medien, speziell kolloidaler Metallosungen," *Annalen der Physik*, vol. 25, pp. 377-445, 1908.

[28] A.V. Gusarov, I. Smurov, 2010, Radiation Transfer in Metallic Powder Beds Used in Laser Processing, *J. Quantitative Spectroscopy & Radiative Transfer*, Vol. 111, pp. 2517-2527.

[29] L. Wang, S. L. Jacques and L. Zheng, 1995, MCML-Monte Carlo Modeling of Light Transport in Multi-Layered Tissues, *Computer Methods and Programs in Biomedicine*, Vol. 47, pp. 131-146.

[30] Partee B., Hollister S.J., Das S., 2006, Selective Laser Sintering Process Optimization for Layered Manufacturing of CAPA® 6501 Polycaprolactone Bone Tissue Engineering Scaffolds, *Trans. ASME, J. Manufacturing Science and Engineering*, 128:531-540.

[31] Schmidt M., Pohle D., Rechtenwald T., 2007, Selective Laser Sintering of PEEK, *Annals of the CIRP*, 56/1:205-208.

[32] Alessandro Franco, Michele Lanzetta and Luca Romoli, 2010, " Experimental analysis of selective laser sintering of polyamide powders: an energy perspective", *Journal of Cleaner Production*, 18:1722-1730.



FOLIO ADMINISTRATIF

THESE DE L'UNIVERSITE DE LYON OPEREE AU SEIN DE L'INSA LYON

NOM : **LIU**

(avec précision du nom de jeune fille, le cas échéant)

DATE de SOUTENANCE : **28/02/2017**

Prénoms : **Xin**

TITRE : **Numerical Modeling and Simulation of Selective Laser Sintering in Polymer Powder bed**

NATURE : **Doctorat**

Numé rod'ordre : 2017LYSEI012

Ecole doctorale : **MEGA de Lyon**

Spécialité : **Thermique et Energétique**

RESUME :

La fabrication additive est l'un des secteurs industriels les plus en développement ces dernières années. L'une de ces technologies de fabrication les plus prometteuses est la fusion laser sélective (SLS), et relève d'un intérêt croissant aussi bien industriel que académique. Néanmoins, beaucoup de phénomène mis en jeu par ce procédé demeure non encore bien compris, entravant ainsi son développement pour la production de pièces de bonne qualité pour des applications industrielles. L'objectif de cette thèse est de développer un cadre de simulation numérique permettant la simulation du procédé SLS pour des poudres de polymère afin de comprendre les multiples et complexes phénomènes physiques qui se produisent lors du frittage laser et d'étudier l'influence des paramètres du procédé sur la qualité du produit final. Contrairement aux approches classiques de modélisation numérique, basées sur la définition de matériaux homogène équivalents pour la résolution des équations de bilan, nous proposons une simulation globale du procédé du frittage laser de poudres, en utilisant la méthode des Eléments Discrets (DEM). Cela consiste en un couplage entre quatre sous-modèles : transferts radiatif dans le milieu granulaire semi-transparent, conduction thermique dans les milieux discrets, coalescence puis densification.

MOTS-CLÉS :

Fabrication additive, fusion laser sélective, polymères, modélisation multiphysique, simulation numériques, méthode des éléments discrets, méthode de Monte-Carlo Modifiée.

Laboratoire (s) de recherche : **CETHIL**

Directeur de thèse: **M'hamed BOUTAOUS**

Président de jury : **Claire BARRES**

Composition du jury :

BOUTAOUS M'hamed	Maître de conférences HDR	INSA-Lyon	Directeur de thèse
XIN Shihe	Professeur des Universités	INSA-Lyon	Co-directeur de thèse
REGNIER Gilles	Professeur des Universités	ENSAM-Paris	Rapporteur
SCHMIDT Fabrice	Professeur des Universités	MINES-Albi	Rapporteur
BARRES Claire	Maître de conférences HDR	INSA-Lyon	Examineur
BERGHEAU Jean-Michel	Professeur des Universités	ENISE-St.Etienn	Examineur